Development of Absorbent Materials in Ammonia Synthesis

A thesis submitted for the degree of Doctor of Philosophy in Inorganic Chemistry

Kirsty Purchase

St Anne's College

Declaration

I confirm that this is my own work and the use of all material from other sources has been properly and fully acknowledged.

Kirsty Purchase

Abstract

Ammonia sorbents are important for both the synthesis and transport of so-called green ammonia. Though $MgCl_2$ is currently the most commonly used absorbent for ammonia it has a number of deficiencies and so new materials are needed targeting fast sorption and desorption speed and high temperature and cycling stability.

13X zeolites underwent ion exchange and were studied for ammonia adsorption. The sodium ions in the 13X structure were replaced by protons, magnesium or lanthanum ions. In each case, the ammonia capacity was increased by the ion exchange, most significantly for magnesium, with fast, stable adsorption. Protons generated strong Brønsted acid sites which gave ammonia that was stable at high temperatures, lanthanum generated Lewis acid sites which gave weakly bound ammonia stable only at low temperatures and magnesium generated a combination of strong Brønsted acid and weak Lewis acid sites giving low and high temperature ammonia. In each material the locations of the ammonia binding sites were identified using SXRD, supported by modelling.

Lanthanum ion exchange was shown to cause structural disruption due to the size of the lanthanum ions. This disruption was shown to be related to lanthanum content but detrimental to capacity. The acidity of the lanthanum zeolites could be tuned using varying lanthanum content.

A variety of layered materials, including $MgCl_2$, were studied in greater detail. Treatment of $MgCl_2$ using acetone was found to significantly improve the absorption rate at detriment to the ammonia capacity; this was proposed to be due to reordering of exfoliated $MgCl_2$ layers or nanopore generation. This treatment was found to be unstable with both time and cycling and attempted alternative methods of stable layer disruption were unsuccessful. Instead, layers were

exfoliated and supported on zeolite which gave fast, stable sorption even at high temperatures and low pressures.

Acknowledgements

Firstly, I would like to thank my supervisor, Professor Edman Tsang, for his ideas, advice and guidance throughout the course of my DPhil. I would also like to thank Siemens and the Engineering and Physical Sciences Research Council for providing funding for this research.

I would like to thank Dr Alberto Roldan Martinez at Cardiff University for his collaboration with modelling, Dr Nick Rees at Oxford University for his help with NMR and Dr Robert Jacobs at Oxford University for his help with N_2 physisorption. I would like to thank Dr Amber Thompson and Dr Kirsten Christensen for their maintenance of the crystallography facilities and training. In addition, I would like to thank Christopher Foo (Oxford University), Dr Tsz-woon Benedict Lo (The Hong-Kong Polytechnic University), Dr Lin Ye (Fudan University), Dr Pu Zhao (Oxford University) and Dr Tatchamapan Yoskamtorn (Oxford University) for their assistance in collecting SXRD patterns and advice on refining these patterns. I would like to thank the beamline scientists at I-11, Diamond Light Source and BL02B2, Spring-8.

I would like to thank all members of the Tsang group, past and present, for providing help and advice during my time with them. In particular, Tugce, Lizzie, Ian, Tim, Josh, Jiri, Simson, Tianyi, Kukkik, Will and Iris for discussions and friendship throughout my project.

I would like to thank all the staff at the Inorganic Chemistry department for their help, especially David Dancer, Alex Garzon Gonzalez, Nenad Vranjes, Aga Borkowska and Alison Chesworth-Wing.

I would like to thank my friends from Uddingston, St Andrews and Oxford who have supported and distracted me as required and made sure my free time has been well spent. Last but not least, I want to thank my family for their continual support, encouragement, pep talks and love.

List of Abbreviations

AMOST – Aqueous miscible organic solvent treatment

AT – Acetone treated

BAS - Brønsted acid sites

BET - Brunauer, Emmett and Teller

Beq - Isotropic displacement factors

CIF - Crystallographic information file

COF -Covalent-organic-framework

DFT - Density functional theory

DTGA - Differential thermogravimetric analysis

ET - Ethanol treated

GOF – Goodness of fit

IGA – Intelligent gravimetric analysis

LDH – Layered double hydroxides

MAC - Multi-analyser crystals

MOF - Metal-organic-framework

NMR – Nuclear magnetic resonance

PXRD – Powder X-ray diffraction

PSD – Position sensitive detectors

SAPO – Silicon aluminium phosphate

SOF - Site occupancy factor

SS-NMR – Solid state nuclear magnetic resonance

SXRD - Synchrotron powder X-ray diffraction

TGA - Thermogravimetric analysis

TPA – Terephthalic acid

TPD – Temperature programmed desorption

XRD - X-Ray diffraction

ZIF – Zinc imidazolate framework

Contents

1. Introduction

1.1. Ammonia

Ammonia is widely considered one of the most important chemicals worldwide. Industrially, it is produced on a huge scale, consuming 1.8-3% of the total global energy.[1] Ammonia is used as a feedstock in a number of chemical processes though its primary use is in nitrogen based fertilizers.[2]

Plants require a nitrogen source as part of their growing process. Although the atmosphere consists of 80 % nitrogen it is present as inaccessible nitrogen gas.[2] Ammonia (consisting of 82 % nitrogen by weight) is a viable chemically reactive and thus useable nitrogen source allowing nitrogen to be used by plants and improving yields.[2]

The importance of ammonia-based fertilisers cannot be overstated. As of 2010, the use of ammonia fertilizers exceeded 150 million metric tonnes.[3] The introduction of ammonia-based fertilizers has allowed for a huge population growth as their use leads to significant improvement in crop yields and increasing efficiency in agricultural processes. In the 100 years following the introduction of ammonia-based fertilizers, the number of humans supported per acre of arable land more than doubled, a change made possible as a result of ammonia production.[2]

Although it is difficult to quantify exactly how much of the crop yield increase can be attributed to ammonia, independent estimates put it at between 30-50%.[2] Using this figure, it has been calculated that approximately 27% of the world's population in this time has been supported by ammonia corresponding to 4 billion people who would not exist without its development and use.[2] With regards to the current population, an estimated 44% of them rely on ammonia fertilizers.[2]

Currently, populations worldwide are continuing to increase coupled with increasing average global temperatures.[2] It is widely accepted that this increasing temperature will also cause increased flooding.[4] This will change the land available for arable farming and is predicted to cause problems with food security.[4] The combination of growing populations and decreasing areas for farming mean that fertilizers will become more important than ever.

Though the main use of ammonia has previously been as a fertilizer, there is currently a huge amount of interest in alternative uses of ammonia. Broadly speaking the main proposed uses for ammonia are in fertilizers, as an energy vector and as a fuel (either the ammonia itself or as a source of hydrogen).

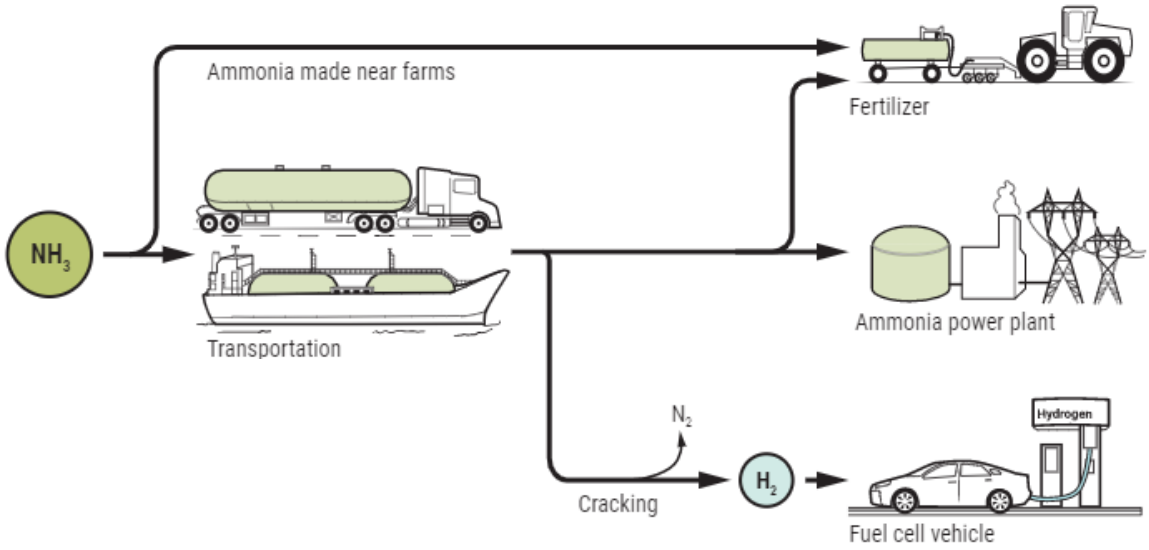

Figure 1-1: Schematic of potential uses for ammonia including transport, fertilizer, ammonia power plants and in fuel cell vehicles (after cracking to hydrogen).[5]

Ammonia sorbents are important, not only in ammonia synthesis, but also for transportation of ammonia. There is currently an extensive ammonia distribution network including pipelines and rail, road and maritime transportation.[1]

1.2. Ammonia as an Energy Vector

One use of ammonia which is increasingly studied is its potential use as an energy vector. This becomes more and more important as renewable alternatives to fossil fuels are sought.

One problem with renewable energy sources such as solar or wind energy is their intermittent supply[1] i.e. it is not always sunny or windy when the energy from these sources is required. To combat this, some way of storing the energy is required so it can be used when it is needed. There are many potential methods of energy storage and it is a huge field. Commonly, energy is stored using batteries, where the charge discharge cycle is used to smooth the erratic supply from renewable sources.[1]

Another method of capturing the energy from renewable sources is the use of alternative fuels. The emitted energy from e.g. wind can be used to generate a fuel. One well studied example of this process is the photochemical splitting of water to give hydrogen as a fuel. However, hydrogen is a dangerous fuel due to it being flammable and explosive and storage is problematic as it is a gas.[6] Other commonly proposed energy vectors are hydrocarbons, generally very short chain hydrocarbons.[6] Systems involving methane and methanol are common.[6]

One possible energy vector with many advantages is ammonia. It contains three hydrogen atoms per molecule so it can provide a hydrogen source following the use of a simple ammonia decomposition catalyst. Hydrogen storage in the form of ammonia avoids the safety problems associated with the explosive and flammable nature of hydrogen.[6] Furthermore, there is already a well-established transportation network for ammonia and so there is already significant investment into ammonia based green energy systems.[1]

One such project involving ammonia is the recent green hydrogen project between Air Products, ACWA and NEOM, using Haldor Topsoe ammonia technology.[7] The project will use solar and wind power to generate hydrogen which is then converted to ammonia and can be transported before being converted back to hydrogen to be used as a fuel. This system aims to produce 1.2 million tons of green ammonia per year, which will be converted to hydrogen with a focus on supplying hydrogen fuel cell buses and trucks. This project alone would lead to a reduction in CO_2 emissions of over 3 million tons each year.

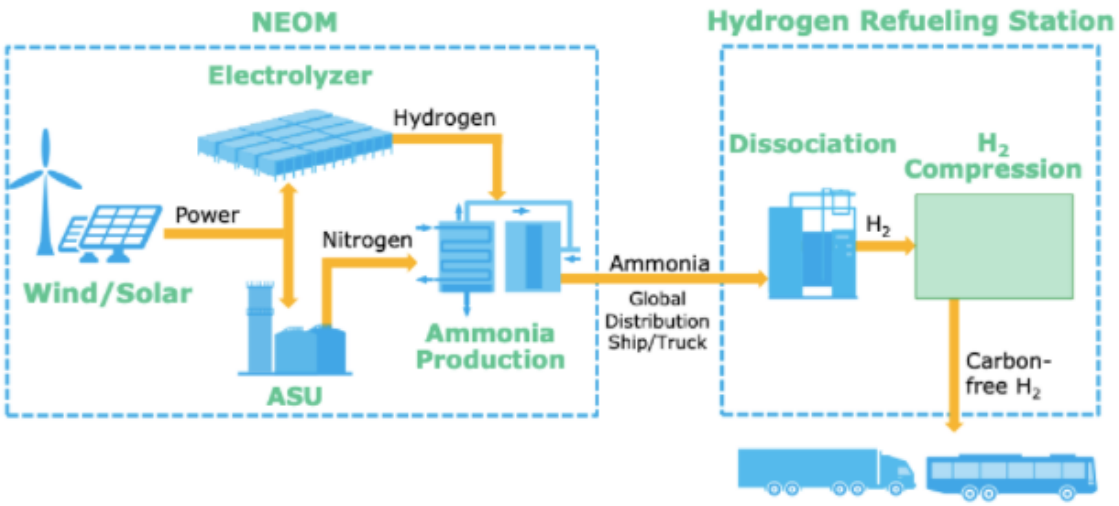

Figure 1-2: A schematic of the NEOM green ammonia project, powered by renewable energy. The ammonia is distributed and then carbon free hydrogen can be generated at the point of use.[7]

This project emphasises how important ammonia is to decarbonising economies. Saudi Arabia is investing significantly in new green technologies in an attempt to reduce the dependence of the Saudi Arabian economy on oil revenues. This $5 billion dollar plant in one of the first of many projects focusing on green energy.[7]

Another country which is investing in green ammonia systems is Australia. Similarly to Saudi Arabia, Australia is well suited for solar powered ammonia production. Australia has invested in the Asian Renewable Energy Hub which will include the world's largest wind and solar electricity plant making green ammonia.[8] Renewable energy sources (initially focusing on wind and solar)

will be used to synthesise ammonia from water and air. This ammonia will then be both used locally and exported internationally to countries including Japan and Korea, to be utilised as hydrogen. Projects such as this emphasise the opportunities ammonia storage opens up; it allows for solar energy to be stored and used across the globe. The Australian government has committed AUS£570 million over the next 10 years for projects supporting their domestic hydrogen industry.[8]

The versatility of such processes is highlighted by the announcement by Yara, a Norwegian firm, that they will fully electrify one of their already existing ammonia production plants.[9] This plant will be powered by hydro[9], showing that green ammonia production is applicable to a wide variety of countries.

The focus of countries such as Norway and Saudi, which have historically been high producers of oil, on green energy systems emphasises the attraction of such systems and their ongoing importance.

Ammonia sorbents can be an important part of such systems, either in the synthesis or transportation stages, as will be discussed in more detail later.

1.3. Ammonia in Transport Applications

One possible area where ammonia as an energy vector has possible useful applications is in transport applications. A move away from petroleum-based fuels would help to meet the goal of decreasing carbon containing emissions. Though fuels such as natural gas and methanol (produced from natural gas) are often studied, due to their high energy capacity and already existing distribution networks[6], this is very short sighted. Natural gas is non-renewable and these

fuels still emit carbon dioxide so focussing on such fuels only postpones the change to a green fuel.

Ammonia is a good option as it does not contain carbon and so the burning of it does not give off carbon dioxide. Although ammonia is currently produced from fossil fuels, alternative methods are being developed which would allow for green ammonia (discussed in greater detail in 1.5). The main drawback to ammonia as a fuel is its toxicity.[6] Overcoming this by adsorbing ammonia into a non-toxic material for storage would make ammonia an excellent candidate for a fuel source.

One area where ammonia has seen particular interest is the maritime sector. The International Maritime Organization published analysis stating that ammonia will be "the primary zero carbon fuel choice adopted by the shipping industry" and reported that this will require an investment of $1.4 trillion between 2030 and 2050.[10] This majority of this investment will go towards green ammonia plants as it is estimated that over 900 million tons of ammonia will be needed to meet the 2050 demand.[10] This is over five times the current ammonia output.[10] This demonstrates just how significant the potential need for ammonia storage technology is.

Another possible use of ammonia in green transport is as a hydrogen source. Hydrogen would be a useful fuel as its combustion gives only water making it a perfect green fuel. However, hydrogen storage has many barriers. Commonly proposed storage materials are MOFs, complex metal hydrides and borohydrides. Unfortunately, these materials are all deficient in some way; MOFs require unfeasibly low operating temperatures, complex metal hydrides cannot currently achieve high enough capacities and borohydrides show extremely poor reversibly of adsorption.[6] An ammonia store, coupled with a decomposition catalyst, could allow for safer production of hydrogen for combustion. In the previously discussed NEOM project ammonia is used both as an

energy vector (to “transport” the energy from solar power nationally or internationally) and then as a hydrogen source for transport applications.

1.4.The Haber Process

Currently, ammonia is produced via the Haber process, shown below.

$$3N_2 + H_2 \rightarrow 2NH_3 \qquad \text{(Equation 1)}$$

Patented in 1908 as a method of reacting nitrogen and hydrogen to give ammonia, the Haber process gained its creator Fritz Haber a Nobel prize and revolutionised agricultural processes. Although the initial process was developed by Haber, further work by engineer Carl Bosch, adapted the process and allowed it to be used on an industrial scale.[11]

1.4.1. Kinetics and Thermodynamics

The above mentioned process is an exothermic reaction and so releases significant heat.[12] This means the reaction would be favoured at low temperatures however, as the reaction is very slow at low temperatures (due to the difficult nitrogen dissociation step) this is not used industrially. As the reaction involves the production of two gaseous molecules from four gaseous molecules, Le Chatelier’s principle predicts that high pressure would increase the proportion of products.[12] This is why high pressures are used in industry.

1.4.2. Current Industrial Process

The Haber process uses an iron or ruthenium catalyst, coupled with very high temperatures and pressures to produce ammonia.[12] In industrial operations, the Haber process is extremely energy intensive. As the pressure of the system decreases as the reaction progresses, the reaction must take place at a high pressure (150-300 bar).[12] The reaction is exothermic so would be favoured at low temperatures, however, the reaction is very slow at low temperatures and so high

temperatures are required. This problem is further compounded by the fact that catalysts generally require high temperatures to perform efficiently. Industrially, the Haber process operates at 400-500 ^{o}C. Despite this, the reaction has a low efficiency, with a single pass conversion of 15-25% due to the thermodynamic limitations. This means that many recycle steps are needed which increases the energy used in the process further.[12]

1.4.3. Catalysts

There are two prominent catalysts studied in relation to the Haber process. The catalysts provide an alternative energy pathway from the reactants to the products and so lower the temperature needed for the reaction to take place. This is a particular necessity for the Haber process, where the splitting of a nitrogen molecule is a very difficult reaction.

Catalysis can be split into two main fields; heterogeneous and homogeneous catalysis.[13] Heterogeneous catalysis is where the catalyst and the reactants exist in different states (almost exclusively a solid catalyst and liquid or gaseous reactants) and homogenous catalysis where the catalyst and the reactants are in the same state (generally both liquids).[13] Heterogenous catalysis has a number of advantages over homogenous catalysis; the catalysts are normally stable under extreme conditions (e.g. of temperature or pressure) and the difference in states between the catalyst and reactants allows for facile separation of the catalyst at the end of the reaction. This, in turn, means that the catalyst can be reused or recycled more easily than a homogenous equivalent.[13]

Given the very high pressures and temperatures necessary in the Haber process, heterogenous catalysts are the obvious choice. The two main types of catalysts studied for use in the Haber process are iron based and ruthenium based catalysts, each having different advantages based on the system in question.[12]

When considering the reaction to produce ammonia it is clear that there are a number of processes involved. Both molecular nitrogen and hydrogen must be split followed by reaction to give the ammonia molecules. Of these processes, it is well documented that the splitting of nitrogen is the rate determining step for the ammonia production reaction.[12] Hence, this is the initial focus for catalyst development in the Haber process, as this is where the greatest improvement is achievable. Shown below is a plot of the turn over frequency against the dissociative chemisorption energy of various transition metal elements, giving a typical volcano plot.[14] The reaction is a compromise when it comes to the dissociative chemisorption energy. A low value suggests that the ammonia will not stay on the catalyst for long enough to react while too high a value means that the dissociated ammonia will be bound too tightly and not leave the surface.

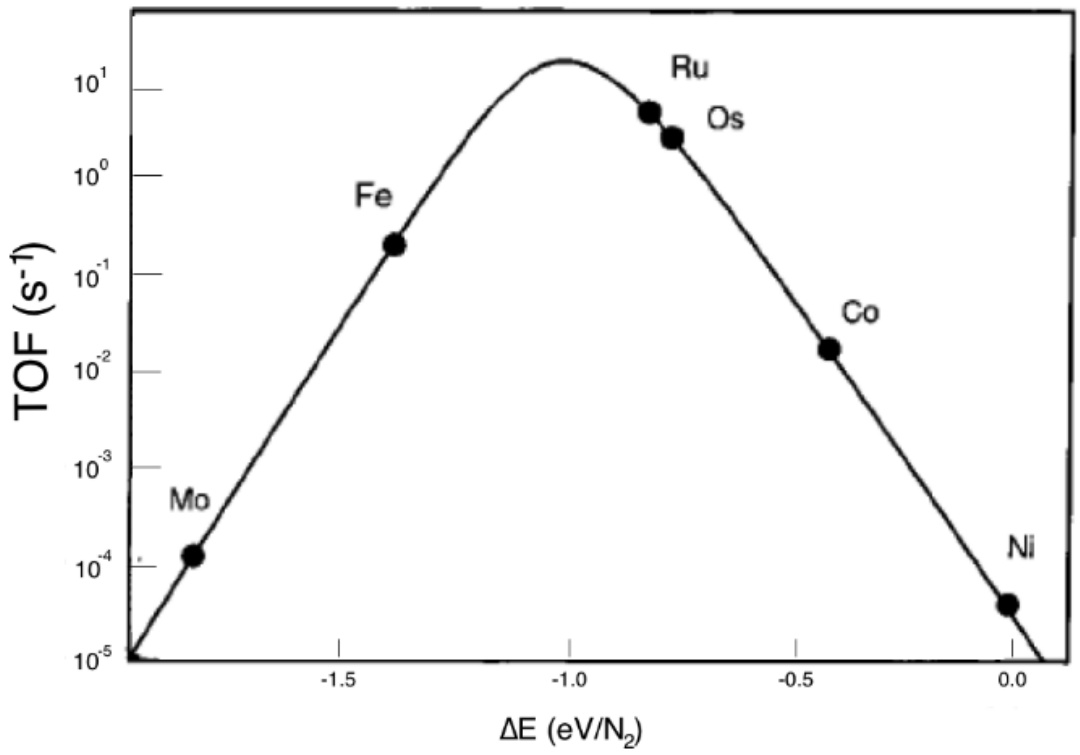

Figure 1-3: Volcano plot showing the relative efficiencies of various metals for ammonia synthesis (adapted from [14]).

As is shown above, ruthenium and iron are the optimal combination of long enough residence time on the catalyst surface and low enough binding to allow for further reaction of the dissociated nitrogen. This is evidenced by the peak in turnover frequency at these points.

While iron and ruthenium show similar nitrogen dissociation abilities there are a number of other relevant factors which determine which metal is used in the catalysts for various conditions.

Iron based catalysts have the overwhelming advantage of low price.[12] Given the scale on which ammonia is produced this is a significant consideration. Iron has a high availability and its processing is well studied and relatively easy. Combined with its good activity, these factors make iron-based catalysts the most commonly used catalysts for ammonia production.

As is seen from the above volcano plot, ruthenium also shows good activity for nitrogen dissociation and hence ammonia synthesis. The increased activity compared to iron means it is a suitable catalyst for milder ammonia synthesis conditions such as lowered temperatures and pressures. One main drawback with using a ruthenium catalyst is that they are more prone to poisoning that iron catalysts and so very pure nitrogen and hydrogen sources must be used.[12]

1.5. Towards a New Ammonia Synthesis Process

Although widely used, there are a number of problems with the current Haber process and so many possibilities for new technologies.

One of the main drawbacks is the extremely high energy use and associated carbon dioxide emissions.[12] It is widely known that atmospheric carbon dioxide causes global warming. This has been related to climate issues including flooding, drought and other extreme weather events.[4] These sorts of events cause a number of deaths, have great economic impact and result in

significant changes of the lives of people affected. It is estimated that an extra 250,000 deaths will occur each year as a result of climate change between 2030 and 2050 and in 2018 climate events had economic costs in the region of tens of billion US dollars.[4]

With ammonia production producing over 1% of all global carbon dioxide emissions[15], it is clear that there is a great motivation for decreasing the energy use in ammonia production plants. A great deal of research has been focussed on this.

The main problem with improving ammonia production is the inherent thermodynamics and kinetics of the reaction necessitating high temperatures and pressures in its current form. However, the introduction of more efficient ruthenium catalysts has changed this. Their high efficiency means that lower temperatures and pressures, which are impossible with iron-based catalysts, can be used.

To further reduce the emissions from ammonia production, renewable sources of the reactant gases required can be used. Atmospheric nitrogen is already used but renewable energy sources, such as wind or solar power, can be used to obtain hydrogen via the electrochemical splitting of water. This also has the advantage of giving a very pure hydrogen source which is necessary to avoid poisoning of the ruthenium catalyst.

Another means of improving the efficiency of the ammonia production process is through the use of sorbents, which is the focus of this work. Absorption of ammonia as it is produced has been shown to improve the efficiency of ammonia synthesis through limiting the reverse reaction (where ammonia is decomposed) and shifting the equilibrium.[16] This is an extremely promising area and so a more thorough understanding of how this process works is needed to aid the development of new sorbents.

1.6.Sorbents

1.6.1. Adsorption versus Absorption

Initially, the difference between adsorption and absorption must be discussed. Both are processes by way of which a molecule, atom or ion interacts with a secondary material. Adsorption is a surface process where the atoms/molecules/ions bind to the surface of the adsorbent. Absorption involves the atoms/molecules/ions permeating the bulk of the absorbent. Clearly there will be ambiguity in some materials, particularly those where the surface is not particularly well defined but these will be the general definitions used in this thesis. Sorbents will be used a general term referring to both adsorbents and absorbents and sorption used for non-specific adsorption or absorption.

1.6.1. Le Chatelier's Principle

The use of sorbents to improve the efficiency of catalytic processes is proposed to be at least partially governed by what is known as Le Chatelier's Principle, which states that a system moves to counteract a change upon it, i.e. if temperature of a system is increased, a reaction equilibrium will shift in such a way to lower the temperature. When using sorbents, the ammonia produced by the catalyst is removed from the system by the sorbent. This prevents the backward reaction, shifts the equilibrium on the catalyst surface and pushes the system to produce more ammonia.[16] This is a further way of lowering the necessary conditions for ammonia production or alternatively improving the ammonia production under the same conditions.

1.6.2. Gas Behaviour

How the gas, in this case ammonia, interacts with the solid must be considered when trying to improve sorption properties.

First, the kinetic behaviour of the ammonia can be considered. The kinetic model describes gas molecules as being in ceaseless, random motion with negligible size (i.e. their diameters are orders of magnitude smaller than the distances they travel between collisions). The molecules are assumed to only interact through brief, infrequent, elastic collisions.[17] Collisions with the sorbent material are relevant here. Collision flux describes the number of collisions between the gas and an area over a period of time on an area and time basis.

$$Z_w = \frac{p}{(2\Pi mkT)^{1/2}} \qquad \text{(Equation 2)}$$

where Z_w is the collision flux, p is the pressure, m is the mass of a molecule, k is Boltzman's constant and T is the temperature.

Also important here is the transport properties of ammonia. Diffusion refers to the migration of matter from a region of high concentration to a region of low concentration.[17] Many diffusion coefficients are reported in the literature, however, Fick's law of diffusion is commonly used to describe experimental data. Experimentally, concentrations are often measured and so Fick's first law of diffusion can be defined as

$$J(c) = -D^t(c)\,\nabla c \qquad \text{(Equation 3)}$$

where J(c) is the concentration flux, D^t is the Fick diffusion coefficient and ∇c is the change in concentration with respect to position.[18]

This law describes how the diffusion of a gas is driven by the gradient of concentration and the diffusion coefficient. Diffusion coefficients are commonly calculated computationally.[19]

1.6.3. Surfaces

As adsorption is a surface phenomenon, many of the recent breakthroughs in surface science offer insight into the adsorption process and how to study it.

1.6.3.1. The Langmuir Isotherm

It is known that the coverage of an adsorbate on a material's surface at equilibrium depends on the gas pressure (provided temperature is constant).[20] This relationship is described by an adsorption isotherm, commonly the Langmuir isotherm. This is often used to describe systems such as high surface area solids adsorbing gas, as is often the case in heterogeneous catalysis or gas storage.

Associative adsorption is the simplest type of adsorption and can be described by the Langmuir isotherm.[20]

$$M_{(g)} + S \rightleftarrows MS \qquad \text{(Equation 4[20])}$$

Where M is the adsorbing gas molecule, S is a surface site and MS is a molecule adsorbed on a surface site. Rate constants of k_a and k_d can be assigned to the adsorption and desorption processes (the forward and backward reactions, respectively).

The rate of adsorption varies as such;

$$\text{Rate of Adsorption} = k_a P(1-\theta) \qquad \text{(Equation 5[20])}$$

Where k_a is adsorption rate constant, P is pressure and θ is the portion of monolayer sites occupied (i.e. 1-θ represents the fractional monolayer coverage of unoccupied sites).

This demonstrates how the rate of adsorption is high at high pressures, high k_a values and when there are many unoccupied sites.

The rate of desorption is described as follows;

$$\text{Rate of Desorption} = k_d\theta \qquad \text{(Equation 6[20])}$$

Where k_d is the desorption rate constant and θ is the portion of monolayer sites occupied.

The above shows that the rate of desorption is not directly dependent on the pressure of the system, although as θ varies with pressure there is an indirect relationship.

At equilibrium, the rate of adsorption and desorption are equal and so the following holds;

$$k_a P(1-\theta) = k_d \theta \qquad \text{(Equation 7[20])}$$

which can be rearranged to give;

$$\theta = \frac{N_s}{N} = \frac{KP}{1+KP} \qquad \text{(Equation 8[20])}$$

where N_s is the number of occupied surface sites, N is the total number of sites, K is k_a/k_d (i.e. the equilibrium constant) and P is the pressure.

This equation represents the Langmuir adsorption isotherm which allows for prediction of monolayer adsorbate coverage changed with pressure.[20] A similar equation exists for dissociative adsorption, which occurs when a molecule dissociates on a surface; this is not expected to occur under the conditions studied here and so is not discussed further.

The Langmuir isotherm model relies on a number of assumptions[20]; firstly that the surface is uniform, the adsorption sites are equivalent and each adsorption site can be occupied by just one molecule. A dynamic equilibrium is assumed to exist between the gas and the adsorbed layer at the pressure and temperature. The adsorbing molecules are assumed to be continually colliding with the surface and any collision with a vacant site leads to the formation of a bond while any collision with a filled site causes the adsorbate to return back to the gas phase. It is assumed that there is no movement between sites once a molecule is adsorbed and finally, the enthalpy of adsorption is taken to remain constant for each site, no matter the coverage. Although these

assumptions do not hold under all circumstances, the Langmuir isotherm generally models associative adsorption well.

1.6.3.2. The BET Isotherm

The main drawback to the Langmuir adsorption isotherm is that it does not apply when layers thicker than monolayers are forming.[20] The adsorption of gas molecules on to an already adsorbed monolayer will show very different behaviour to gas molecules adsorbing on clean surfaces. To model this, Brunauer, Emmett and Teller proposed a further model, now known as the BET model which extends the Langmuir Isotherm for multilayer adsorption. [20]

Again, the model makes assumptions[20]; the first layer is assumed to show Langmuir behaviour and later layers form consecutively (e.g. layer two forms on layer one, layer three on layer two and so on). At equilibrium, the rates of condensation and evaporation are taken to be equal for each layer. Furthermore, the enthalpy of adsorption of the first layer is equal to the Langmuir case while the enthalpy of adsorption is assumed to be equal and opposite to the enthalpy of vaporisation for later layers. These assumptions give the BET equation;

$$\frac{P}{V(P_o - P)} = \frac{1}{V_m C} + \frac{(C-1)P}{V_m C P_o} \qquad \text{(Equation 9[20])}$$

where V is the volume of gas adsorbed at pressure P, V_m is the monolayer adsorption volume, P_o is the pressure at which the material is saturated with adsorbate and C is the BET constant.[20]

This is commonly exploited to calculate surface areas of solids, using N_2 physisorption, though can be used in other contexts, such as determining thermodynamic properties of reactions between gases and solids.

1.6.3.3. Classifications of Isotherms

Langmuir and BET are two of the five types of isotherm that were initially classified by Brunauer, Denning, Denning and Teller.

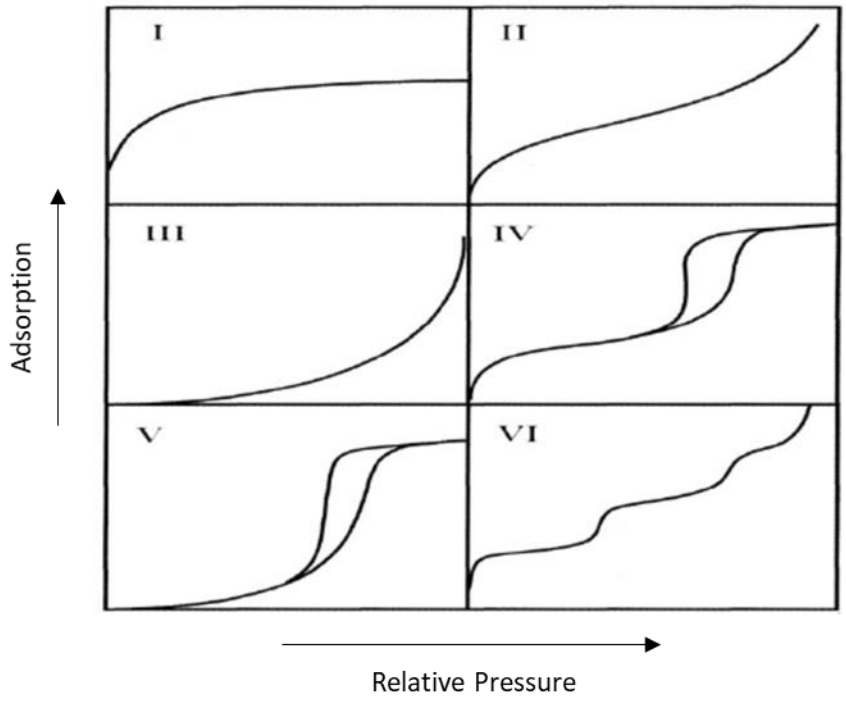

Figure 1-4: The five types of isotherm, classified by Brunauer, Denning, Denning and Teller.[21]

Type I closely resemble Langmuir isotherm behaviour (when the asymptote is a result of the limited number of sites being filled) but also describes filling of micropores within a solid (where the filling of the pores is the limiting factor).[20] These isotherms are most commonly seen here and are typical for zeolites.

Type II isotherms occur when adsorption takes place on non-porous materials or materials with very large pores, where unrestricted multiplayer adsorption can take place. [20] The characteristic shape occurs because monolayer adsorption occurs first, followed by further layer filling at higher pressures. The BET isotherm can be used to understand such behaviour.

Type III isotherms occur when there is multilayer formation at all pressures due to initial adsorption facilitating further adsorption as the interaction between gas molecules is more favourable than interactions between gas molecules and the surface.[22] This is a relatively uncommon case and is not often seen.[20]

Type IV isotherms are typical of materials with pores of sizes between 15-1000 Å; at these pore size multilayer adsorption and capillary condensation both occur leading to this isotherm shape.[20]

Type V isotherms were the final type identified initially. They are similar to type IV but also show the same effect as in type III where initial adsorption promotes further adsorption due to strong interactions between gas molecules.[22] Similarly to type III, this is an uncommonly seen isotherm.[20]

Further work on isotherms has allowed an additional type of isotherm to be identified. Type VI isotherms show a number of steps, caused by stepwise adsorption onto a well-defined non-porous surface; the height of the steps is proportional to the capacity of the layers.[20]

1.6.4. Sorbent Considerations

There are a number of considerations when it comes to ammonia sorbents. The most obvious consideration is ammonia capacity, either on a volumetric or gravimetric basis. This is a measure of the capacity of the material to take up ammonia. When considering ammonia sorbents for use in Haber process type applications, the ammonia sorbent will always be stationary, and commonly on relatively large scales. This means that the weight or volume capacity is less of a consideration than it would be in, for instance, ammonia storage materials in transport applications.

An extremely important factor in ammonia sorbents is the rate of ammonia sorption. Fast rates of sorption mean the ammonia is quickly removed from the system and so the above described equilibrium shift can occur. If ammonia sorption is too slow then it is unlikely that this equilibrium shift will occur.

The strength of interactions between the ammonia and the sorbent are a critical concern. This is a case of getting the interaction “just right”; too weak an interaction and the ammonia will not be removed from the system and thus the catalyst equilibrium will not be shifted yet too strong an interaction and the ammonia will be very difficult to remove. This is strongly related to the acidity of the studied adsorbent material as ammonia is a basic molecule.

When considering which materials are most appropriate there are a number of structural considerations. Strong ammonia adsorption sites alone are not enough for a good adsorbent, these sites must be fully accessible to the ammonia molecules. This is a consideration for porous materials where the pore structure must be open enough to allow for access of the ammonia molecules. Given ammonia’s small size it is not expected that this will generally be a significant problem but it should be considered none the less.

The stability of the material, both with and without ammonia is a further factor that must be considered. Current Haber conditions are extreme, with respect to both temperature and pressure, and any sorbent needs to be stable under these conditions. This is less of a consideration for transport applications or mild Haber conditions which ideally occur under conditions significantly closer to ambient.

It is clear that different applications will have different priorities with regards to sorbent properties. In Haber process type applications, the sorbent will be stationary and so gravimetric

capacity is less important that volumetric. Priorities for such application include high temperate stability (due to the high operating temperature of the reactors), fast sorption and desorption (as was demonstrated as a need by Cussler's work on the topic[23]) and stability over many cycles (as the sorbent bed will ideally not be regularly replaced). When the sorbent is being used in low temperature ammonia synthesis applications the high temperature stability is no longer a particular consideration though the sorption and desorption speed and stability remain important. Transport applications and operations where ammonia is used as an energy vector have differing priorities. One substantial difference is that these are mobile applications and so the gravimetric capacity is important. For consumer transport applications fast sorption is necessary while for maritime applications this is less of a concern. Again, stable sorption is important for these applications. These differing priorities mean that the materials target for sorption research will be different depending on under what circumstances the final material will be used.

1.6.5. Previous Developments

Some work has already been carried out in the field of sorbents for Haber process type applications. Much of the pioneering work in this area has been carried out by Cussler who, along with Knaebel, first proposed the idea of separation of ammonia using an ammonia sorbent to improve the efficiency of Haber process systems in 1996 and proposed that this could allow for ammonia synthesis under more moderate conditions. Work has continued in the group including the recent development of a pilot plant demonstrating the feasibility of ammonia under low pressure.[24] So far it has achieved production rates of 65 kg ammonia per day.[25]

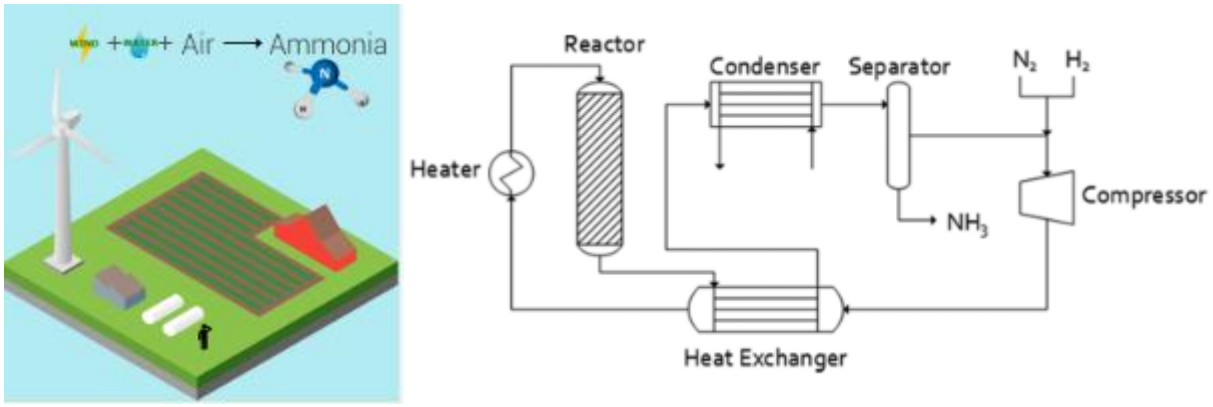

Figure 1-5: The small-scale Haber process proposed by Cussler and colleagues. The N_2 (from air), H_2 (from water) are compressed, heated and then reacted to give ammonia. The ammonia then passes through a condenser and separator to give the product ammonia. The proposed system is powered by wind energy to allow for generation of ammonia on site at, for example, a large farm.[24]

Initial lab experiments showed that a relatively simple system, with a catalyst bed and a separate $MgCl_2$ absorbent bed (shown in Figure 1-6), which gases could be pumped between, allowed the conversion of ammonia to be increased to 95% (in comparison to 20% for typical Haber processes although the kinetics of these systems are not really comparable). This ammonia production was much slower with absorbent due to slow diffusion of ammonia with the absorbent.[26] This demonstrates how fast absorption or adsorption is a target for any new sorbents. They also considered a single bed with mixed catalyst and absorbent (shown in Figure 1-6) which initially did not show good results due to probable poisoning of the catalyst by water in the $MgCl_2$.[26]

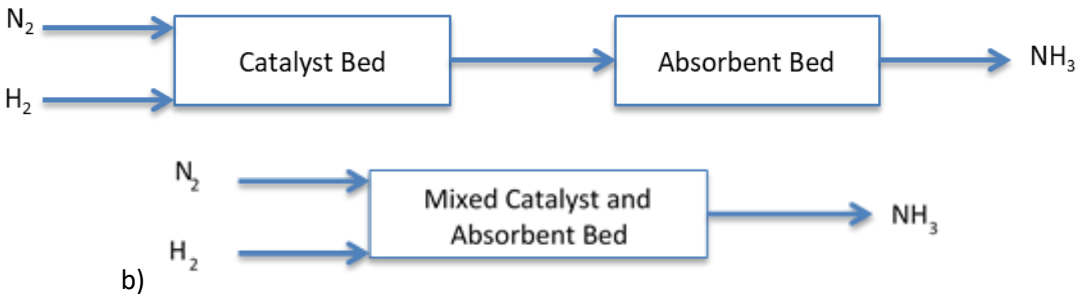

Figure 1-6: Two possible set-ups using absorbents to improve catalyst activity explored by Cussler *et al.*; a) the absorbent bed following the catalyst bed and b) a mixed catalyst and absorbent bed.[26]

In 2016 a small pilot plant in Minnesota was developed based on the above experiments. Ammonia was produced using renewable sources of hydrogen and nitrogen, at lower

temperatures than a conventional Haber plant.[24] An excellent starting point, this work clearly demonstrated that small scale ammonia synthesis from renewable sources is possible.

Since the initial benchmarking experiments carried out on the Minnesota plant, further work has improved understanding and efficiency of ammonia synthesis under milder, greener conditions.

Given the previously discussed limitations caused by slow sorption of ammonia to $MgCl_2$, $MgCl_2$ and $CaBr_2$ loaded on silica and zeolites were trialled with some success.[27,28] 40 % loading of $MgCl_2$ or $CaBr_2$ on silica or zeolite Y showed 60-70 $mg_{NH3}/g_{absorbent}$ (150 ^oC, 4 bar). However, only metal halide-based absorbents have been considered, demonstrating the need for further study of porous material adsorbents.

The effect of reaction temperature, pressure, absorption temperature, and gas transport were studied.[29] Initially, the rate of separation of the produced ammonia was a crucial factor.[29] Once this had been identified and resolved, the limiting factor was found to be the recycling of unreacted products.[30] Later research showed that a mixed bed (iron catalyst and absorbent mixture) avoided this as recycle was not needed.[31]

Work by Cussler also considers the engineering considerations of such systems. In a $MgCl_2$ based system one of the main factors limiting practical use is that desorption of ammonia is very slow, due to poor diffusion of desorbed ammonia from the material. Engineering solutions are proposed; two absorbent beds so one can be absorbing while the other desorbs (as can be seen in Figure 1-7) or desorption purely by pressure swing.[23] It is possible that a chemistry solution is also possible; an sorbent which shows very fast desorption could also overcomes these problems and so zeolites are promising materials to study further.

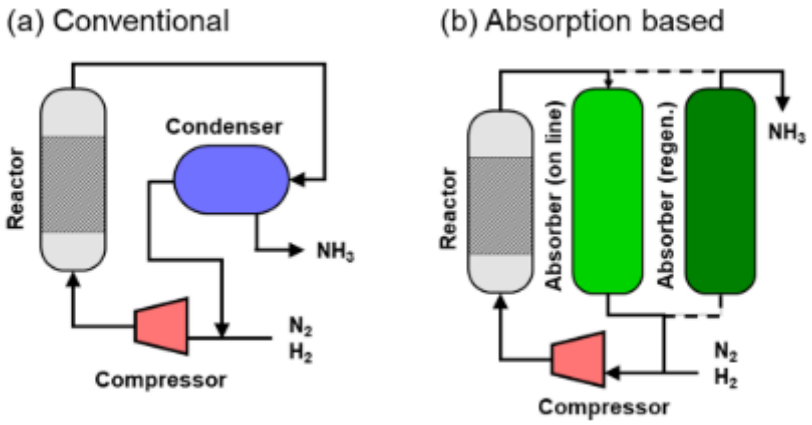

Figure 1-7: Comparison of a) the conventional ammonia synthesis reactor set-up and b) the proposed absorption-based set-up, offering an engineering solution to slow ammonia desorption. In the proposed absorption-based set-up one absorber is absorbing produced ammonia while the other undergoes desorption and is regenerated.

Furthermore, this work also showed the importance of ammonia desorption rates. Cussler and colleagues developed a model to understand what factors limit the potential improvement in ammonia production when using $MgCl_2$. They looked at desorption of ammonia from $MgCl_2$ when the absorbent was below maximum capacity and considered the kinetics of desorption.[23]

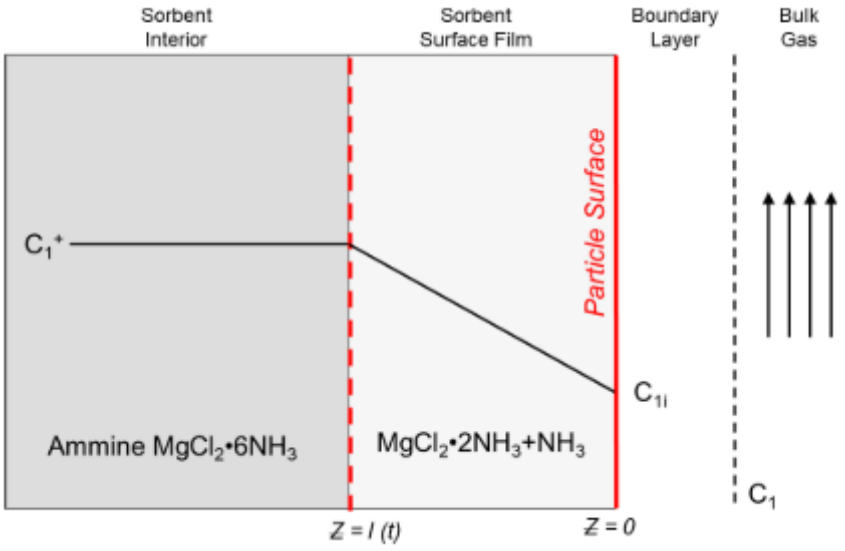

Figure 1-8: Cussler model of concentration within ammonia desorbing $MgCl_2$. The initial bulk concentration of C_1^+ diffuses from the z=l front until the particle surface. The concentration at the particle surface is in equilibrium with the gas phase. [23]

They define the concentrations of ammonia in the sorbent interior section; c_1^+ is the concentration of ammonia at the temperature of absorption and c_1^* is the equilibrium

concentration at the temperature of desorption. The concentration of ammonia in the sorbent surface film section varies with position and time, decreasing until it reaches the particle surface.

They describe this in a more quantitative way. Firstly, the reaction releasing the ammonia from the bulk, in terms of flux:

$$J_1 = k\,(c_1^{+} - c_i^{*}) \qquad \text{(Equation 10}^{23}\text{)}$$

where k is a reaction rate constant (per unit area of the z=l interface) and c_1^{+} is the concentration of ammonia at the temperature of absorption and c_1^{*} is the equilibrium concentration at the temperature of desorption.

This is then equated to the flux across the remainder of the solid where the ammonia is no longer part of the amine bulk:

$$J_1 = \frac{DH}{l}\,(c_1^{*} - c_{1i}) \qquad \text{(Equation 11}^{23}\text{)}$$

where D is the diffusion coefficient of ammonia in the ammonia complex free region, H is the distribution coefficient (the concentration of ammonia in $MgCl_2$ divided by the concentration of ammonia in gas phase in equilibrium with the $MgCl_2$), c_1^{*} is the initial equilibrium bulk concentration and c_{1i} is the surface concentration at the solid- gas interface.

By equating these two flux equations Cussler *et al.* gave an overall desorption flux of:

$$J_1 = \frac{k(c_1^{+} - c_{1i})}{\sqrt{1 + \frac{2\,k^2\,(c_1^{+} - c_{1i})t}{DHc_{10}}}} \qquad \text{(Equation 12}^{23}\text{)}$$

where c_{10} is the ammonia concentration of ammonia in complex with $MgCl_2$ in the sorbent interior region and all other variables are as previously described.

Further examination of this showed that the desorption of ammonia from $MgCl_2$ is limited by the rate of ammonia desorption, the heating rate or the rate of diffusion from the $MgCl_2$.[23] These are the factors which must be targeted to improve the enhancement effect in sorption assisted ammonia production.

Overall, the variety of literature produced by the Cussler group shows that absorption of ammonia can allow for green ammonia production but quick absorption and desorption improves the system and both the operating and desorption temperatures have a significant effect on the practical operations of such systems. For these reasons, it would be beneficial to have a material that can absorb ammonia at the operating conditions of the catalyst[30] and desorb easily.

1.7. New Sorbent Materials

The wealth of literature studying ammonia sorbents provides many possible directions for further research. Here two different classes of materials will be studied: porous materials and layered materials. Though $MgCl_2$ is the most commonly used absorbent, a number of deficiencies have been identified which these materials can potentially overcome. Porous materials show good stability (important for high temperature applications and stability with cycling) and open structures which should lead to fast sorption and desorption (which has been shown to be essential[23]). As $MgCl_2$ is a layered material, other layered materials will be studied with a target of improving diffusion and stability.

1.8. Porous Materials

Porous materials are a well-studied class of materials for adsorption and many catalytic reactions. They benefit from very high surface areas leading to a number of possible active sites and

generally show excellent high temperature stability. Discussed in this thesis are zeolites, SAPOs and activated carbons.

1.8.1. Zeolites

Zeolites are silica alumina-based materials which both occur naturally and are synthesised for commercial purposes. A huge number of zeolite structures are known, with 252 framework codes describing zeolites currently listed by the International Zeolite Association, and more being assigned every year, particularly as computationally aided design of zeolites improves.[32]

Zeolites have a long and varied history, with the first natural zeolite discovered in 1756 by Cronstedt, who understood it to be a new class of minerals.[21] Throughout the 1700s, understanding improved with scientists noting properties including adsorption, ion exchange and dehydration.

Though naturally occurring and synthetic zeolites both exist, naturally occurring zeolites are rarely, if ever, used in industrial settings, partially due to structural defects commonly being present[33]. In contrast, synthetic zeolites have very well-defined structures and are hugely useful in a number of industrial processes. The first synthetic zeolite was prepared hydrothermally in 1862, by St. Claire Deville.[34]

Broadly speaking, the applications of zeolites in industry can be split into three areas: catalysis (primarily in the oil and gas industry), adsorption and ion exchange.

1.8.1.1. Structure

Zeolites consist of a network of silicon and aluminium oxide tetrahedra, joined via oxygen, to give a complex, high surface area network consisting of a system of channels and pores.[13]

A huge variety of zeolites are known, and so zeolites can be chosen to give the desired properties for a particular reaction. Variation in channel width or pore size means zeolites can selectively adsorb molecules based on size or shape.[13]

The basic structure of a zeolite is based on silica tetrahedra. To give functionality, some of the silicon atoms are replaced by aluminium. These tetrahedra join via oxygen to give structural units which then repeat to give a porous network.[35]

As silicon has a charge of 4+ while aluminium has a charge of 3+, the replacement of silicon by aluminium results in a charge unbalance on the material. This unbalance must then be counteracted by the introduction of another ion, commonly sodium.

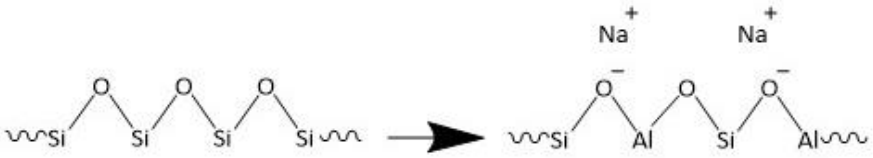

Figure 1-9: Substitution of silicon by aluminium generating charge balancing ions.

These charge balancing ions give rise to many of the interesting and useful properties of zeolites. One such property is Brønsted acidity. When the ion balancing the charge is a hydrogen ion this causes Brønsted acidity in the zeolite, providing a binding or catalytic site for many reactions. This acidity is particularly useful for reaction or adsorbing basic molecules such as ammonia, due to the interaction with the nitrogen lone pair.[36]

The nature of the charge balancing ion can be changed, allowing for many interesting properties to be introduced. Metal ions can be introduced altering the catalytic properties.

1.8.1.2. Synthesis

As naturally occurring zeolites have inconsistent structures, zeolites are commercially synthesised for use in industrial processes.

The first reported synthesis of zeolite materials was by St Claire Deville in 1862. In spite of this, much of the ground-breaking work which led to the zeolite synthesis methods used today was not carried out until the 1940s. The first synthetic zeolite without an equivalent structure in nature was synthesised in 1948 by Barrer who hydrothermally treated both synthetic and naturally occurring aluminosilicates with barium or potassium chloride or bromide to give new materials.[37] Work by researchers at Union Carbide developed such techniques further, pioneering the use of more reactive starting materials, allowing zeolite synthesis under milder conditions. Robert Milton, at Union Carbide, used this technique to develop Zeolite A[38] and Zeolite X[39] and eventually over 20 different zeolites.[34]

Modern day zeolite synthesis is commonly hydrothermal. This involves heating an aqueous mixture of silicon and aluminium sources and a mineralising agent (usually at high pH) to temperatures above 100 ^{o}C in an autoclave. Eventually, the amorphous reactants undergo change to give the crystalline zeolite. Directing agents are also commonly used to generate particular pore structure.[34]

1.8.1.3. Applications

The interesting properties of zeolites make then suitable for many applications with the most commercially important uses being catalysis, adsorption and ion exchange.

Despite moves towards more renewable energy sources, the petrochemical industry is still a hugely important industry. A 2020 report by BP stated that 84.3 % of energy worldwide comes

from fossil fuels[40], with demand for such products increasing in many countries. Products deriving from petroleum products are also important, particularly plastics, and demand for such products continues to rise. A significant portion of petrochemical processes use zeolite catalysts, due to their widely varying structures and flexible acid properties.

The first uses of zeolites as catalysts were in the petrochemical Industry. In 1959, researchers at Carbide developed a zeolite Y based catalyst for use in isomerisation. This was followed in 1962 by Mobil, who used modified synthetic zeolite X to catalyse hydrocarbon cracking, allowing for efficient gasoline production and saving millions of barrels of crude oil.[35] This is one of the most important industrial processes worldwide, with hundreds of thousands of tonnes of zeolite being used every year for catalytic cracking.[35]

Another useful application of zeolites is ion exchange. One early use of this process was developed by Union Carbide in 1977.[35] As discussed, zeolites can contain a number of ions which balance the charge generated by the substitution of silicon by aluminium in the zeolite structure. These ions can be exchanged for other ions within a solution passed through the zeolite pores. This is most commonly applied in detergents, which is the largest zeolite single market by volume, at 72%.[35]

The adsorption properties of zeolites lead to many industrial applications. The ability of zeolites to adsorb molecules was first recognised by Grandjean in 1909 who recorded dehydrated chabazite adsorbing ammonia, hydrogen and air.[35] However, it was not until the 1930s and 1940s when much of the pioneering work on zeolite adsorption was carried out. Barrer was the first to classify zeolites based on size considerations, eventually leading to commercially important zeolite adsorption, particularly by Union carbide. Furthermore, zeolites have a number of properties which make them excellent candidates for gas separation through adsorption. This

effect was first observed by Weigel and Steinhoff in 1925, who observed dehydrated chabazite adsorbing water, methanol, ethanol and formic acid but not acetone or benzene.[35] Developing from this, Union Carbide developed synthetic zeolites, patenting the ISOSIV process which was used to separate paraffins.

The well-defined pore size and high porosity of zeolites mean that they are excellent at separating atoms or molecules based on their size or differing chemical properties. There are three main types of separation that zeolites can exhibit; separation based on different size/shape, separation based on different diffusion or separation based on different adsorption strength. Size exclusion has a zeolite acting as a “molecular sieve”; allowing molecules with a small enough diameter to pass through the zeolite, while larger ones cannot. One such example of this is the use of 3A zeolite to remove water from ethanol, allowing the purified ethanol to be used as a fuel.[41] Various molecules can also be separated by zeolites by exploiting the fact that smaller molecules will diffuse through the porous network more quickly than larger molecules, an effect which occurs to a greater extent at higher temperatures. Hydrogen can be separated from methane in this way[33]. Finally, molecules can be separated based on their different adsorption strengths, due to the acid-base properties of the zeolite. Molecules with higher levels of basicity interact more strongly with acid sites on zeolite and so can be separated from less basic molecules. One examples of this in the separations of carbon dioxide and methane using ZIF-8, as described by Venna.

More recently, there has been a great focus on using zeolites as gas storage materials.

1.8.1.4. Ion Exchange

Ion exchange is one of the most commonly used techniques to alter the properties of zeolites. As was described previously, zeolites contain ions, commonly sodium, which balance the charge

generated by the replacement of silicon by aluminium within the structure. Ion exchange is when these balancing ions are replaced by other ions altering the properties of the zeolites.

One commonly used form of ion exchange is exchanging sodium for protons (via a ammonium ion intermediate) to give Brønsted acid sites which are important catalytic sites in many reactions.[42] Alternatively, metal ions are also commonly used. Exchange of sodium ions by metal ions generally is more favourable due to the fact that this process involved replacing multiple sodium ions with each metal ion due to the differing charges and so is entropically favourable.

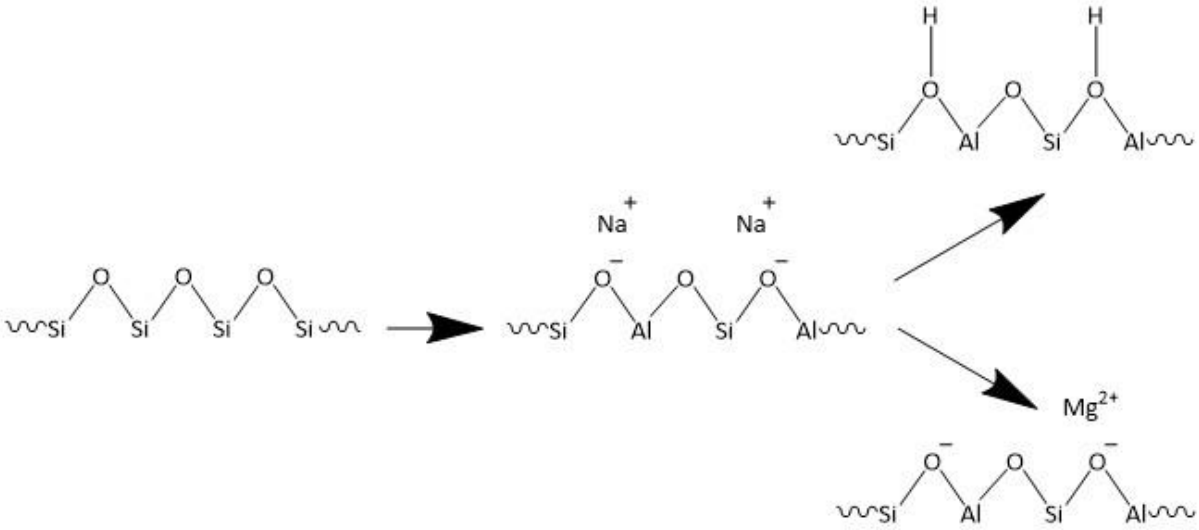

Figure 1-10: Replacement of silicon by aluminium causing a charge imbalance counteracted by sodium ions, which can then be replaced by e.g. protons or magnesium ions.

It is important to note that ion exchange as discussed here does not alter the elements within the framework structure of the zeolite. Altering of the framework elements can be achieved by the introduction of additional elements during the synthesis of the zeolites while ion exchange alters extra-framework species post zeolite synthesis.

1.8.1.5. Acidity

One of the most crucial properties of zeolites which contributes to their widespread use in industry is their tuneable acid properties. Zeolites generally exhibit two types of acidity; Lewis acidity and Brønsted acidity.[36]

Lewis acidity in zeolites occurs as a result of the aluminium in the zeolite which is present outside the framework of the zeolites.[36] High temperature dehydration and steaming of zeolites are two mechanisms by which aluminium is removed from the zeolite framework. These species, known as extra framework aluminium, are Lewis acid sites as they are able to accept a lone pair of electrons, through a now empty orbital.[36] The aluminium can be present as $Al(OH)_3$ or $AlOH^{2+}$, depending on the conditions which generate the extra framework alumina species. Furthermore, these extra framework species can interact with oxygen atoms in the bulk zeolite structure, increasing their Brønsted acidity through a mechanism known as the Brønsted Acid Site Lewis Acid site synergy.

Brønsted acidity in zeolites occurs as a consequence of the replacement of silicon in the zeolite structure by aluminium. When silicon, a tetravalent ion, is replaced by aluminium, a trivalent ion, a charge imbalance is generated across the structure. This imbalance then must be counteracted by an ion, commonly Na^+ or H^+, depending on the synthesis conditions of the zeolite. When H^+ is the counter ion, it is present on one of the O atoms forming a tetrahedra with framework aluminium, the exact location of which is determined by the synthetic conditions.[36] The framework structure has an effect in determining the strength of these acid sites, as does the exact location of the aluminium atom involved.[36] Furthermore, the distribution of these sites, the bonding geometry around them and their ease of access all vary the acidity of the zeolites and hence a thorough understanding of these properties is essential if the acid behaviour of a zeolite is to be understood.

Ammonia is a basic molecule and so the acidity of a zeolite will have a significant effect on the ammonia adsorption properties of the zeolite. There are a number of techniques commonly used to study acidity of zeolites. One technique is temperature programmed desorption (TPD) of probe molecules using thermogravimetric analysis (TGA) which measures the weight change and rate of weight change in a sample as a function of temperature.[43] Weight changes corresponding to processes including desorption, decomposition, oxidation or reduction can be identified. The use of basic probe molecules (commonly ammonia or pyridine) can then give information on the acidity of a zeolite by studying the location and nature of desorption peaks. Unfortunately, TPD cannot alone distinguish between Lewis and Brønsted acid sites.[43] Furthermore, the desorbing molecules may be re-adsorbed as they move through the pore network which can make identification of sites difficult.[43] One further use of TPD is to determine the desorption energy of sites. By varying the heating rate and seeing how to locations of peaks changes, the energy of desorption and thus the acid site strength can be determined.[43] This technique is commonly used in literature; work by Ye *et al.* showed the desorption energies of ammonia in H-ZSM-5 were 7, 21 and 113 kJ mol^{-1} using TPD and so the sites could be classified as weakly binding (e.g. van de Waals interaction between ammonia and framework oxygen), hydrogen bonding and strong Brønsted acid-base adduct formation[44] demonstrating how TPD can be used to calculate zeolite acidity.

Also commonly used to study zeolite acidity is solid state NMR. Often used are ^{29}Si, ^{27}Al, ^{1}H, ^{17}O, ^{15}N and ^{31}P. [43] Aluminium spectra are typically used to determine the relative ratios of tetrahedral and octahedral aluminium. Framework aluminium tetrahedrally bind to oxygen atoms while extra-framework aluminium are octahedral. As these peaks are present in different positions (four coordinate at 60 ppm and six coordinate at 0 ppm), the Al NMR spectra can be used to study Lewis acidity in a zeolite.[43] For example, Bokhoven *et al.* used Al NMR to compare the acidity of

two zeolites; H-USY zeolite showed more extra-framework aluminium, as was shown by an additional peak at 0 ppm, than Na-Y zeolite.[45]

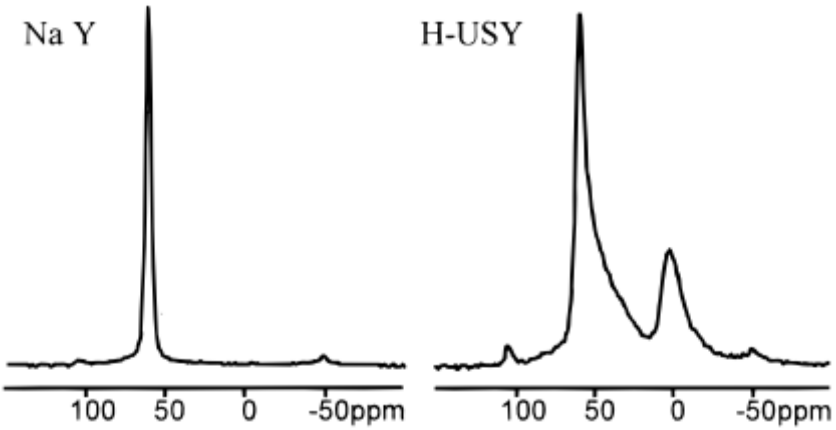

Figure 1-11: ^{27}Al NMR spectra of Na-Y and H-USY, both showing four coordinate Al, indicated by peak at 60 ppm. H-USY shows an additional peak at 0 ppm corresponding to extra-framework aluminium.[45]

Silicon NMR can also give information of the framework as the peak position varies depending on the coordination environment of the atom.[43] The use of Si NMR complements Al NMR and both are often used to study dealumination of zeolites.[43] ^{17}O NMR is sometimes used to study zeolite acidity; it enables the hydroxide groups generating acidity to be directly studied and so is an extremely useful technique. However, the low abundancy of ^{17}O means that enriched zeolites need to be used which makes this technique very costly and so it is less frequently used.[43] The use of probe molecules in NMR can also be used to give information on the acidity of zeolites. Ammines and phosphines are adsorbed on the zeolite and ^{15}N and ^{31}P used to study acidity, as different acid strengths give different chemical shifts for the adsorbed molecules.[43] Though this is a good way of determining acidity of a zeolite, it cannot give information on the location of the acid sites. Complementary techniques are required for this.

One such technique, which allows for the location of acid sites to be determined, is X-ray diffraction (XRD). Many reported zeolite crystal structures were determined using single crystal XRD though the advent of synchrotron X-ray sources means that powder X-ray diffraction is now

commonly used.[36] Most useful when studying acidity is the use of synchrotron X-ray diffraction (SXRD) to determine the location of acid sites and study the interaction of gas molecules with them.

Rietveld refinement of collected SXRD allows for very detailed structural information to be determined.[36] The location of adsorbed probe molecules on the zeolite can be determined and therefore the strength and location of acid sites determined. Commonly used probe molecules are ammonia and pyridine.[36] One of the main drawbacks of this technique is that XRD cannot be used to visualise hydrogen atoms, present in both the acid site and the probe molecules. One way to overcome this is to study the distances between the framework oxygen atoms and the lone pair donor molecule of the probe molecule. This distance is directly related to the acid strength of the binding site and so it does not matter that the hydrogen atoms of the Brønsted acid site cannot be visualised.

One example of this technique in the literature is the elucidation of acid site location in H-ZSM-5 by Ye *et al.*. [44] Ammonia was loaded on H-ZSM-5 and then studied using SXRD. Four ammonia binding sites were assigned and the distances between the nitrogen of the ammonia and the framework oxygen compared. One ammonia (assigned N1) was located 3.358 Å and 3.460 Å from framework oxygen atoms in a bidentate fashion and so was assigned as ammonia very strongly interacting with a Brønsted acid site to give an NH_4^+ species. Two further ammonia (assigned N2 and N3) were found to be located in the sinusoidal channel of H-ZSM-5 and form hydrogen bonding interaction with the strongly bound N1 ammonia. The final ammonia (N4) showed longer distances between it and the other ammonia and so was assigned as a weak physisorption interaction with the zeolite wall. These determined strengths match well with force field calculations and TPD experiments also carried out. Additionally, *in-situ* SXRD studies showed that

the occupancies and bond lengths of the ammonia molecules changed as would be expected given the assigned strengths.

This work demonstrates the value of SXRD to study zeolites. It confirms a previous proposal (based on modelling data) that the Brønsted acid sites in H-ZSM-5 are located in the cross-channel region of the zeolite. Furthermore, this work demonstrates how acidity is not the only factor affecting adsorption and that the spatial arrangement of probe molecules within a zeolite is also important.

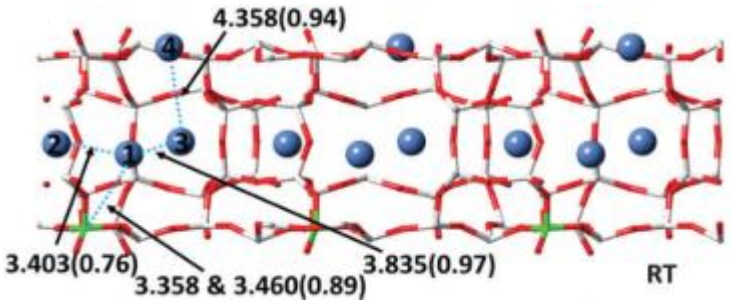

Figure 1-12: Locations of ammonia molecules within H-ZSM-5 with calculated bonding distances, as determined by Rietveld refinement of SXRD. [44]

This technique has since been expanded to other zeolites to great effect. Ammonia adsorbed on Zn-AlPO-5 was studied to determine the location of the acid sites in the AlPO, allowing for the acidity to be tailored. This was then used to improve the selectivity and activity of gamma-valerolactone to pentatonic acid.[46]

It is possible to overcome the inability to visualise hydrogen atoms by using neutron diffraction. This would allow for a fuller picture of zeolite structures and probe molecules to be determined, however, *in-situ* neutron diffraction is difficult and so neutron diffraction and X-ray diffraction are better considered as complementary techniques.[36]

A further difficulty with XRD is that it cannot differentiate between silicon and aluminium atoms due to their very similar size. In fact, there are very few techniques which can be used to

determine the positions of aluminium or silicon in a zeolite. One technique which has been proposed is atom probe tomography which researchers report can be used to determine the distribution of aluminium in ZSM-5.[47] However, this technique does not seem to have been widely used and determining the distribution of aluminium and silicon in zeolites experimentally remains challenging. More commonly used are computational techniques, where the energy of various structures is compared. For example, Fletcher *et al.* screened potential structures of SSZ-13 zeolite, varying the aluminium distribution, using DFT.[48] They found that structures which were previously thought to be impossible (i.e. with Al atoms in close proximity) were viable, which would allow for interesting catalytic activity if achieved experimentally.

1.8.1.6. Examples

Three types of zeolites are studied in this thesis, chosen for their varied properties.

13X is a faujasite type zeolite made of sodalite cages joined via hexagonal prisms generating a framework with large pores.[49] It has a high silicon content which in turn means there are many balancing sodium ions making it a perfect candidate for ion exchange. It has large channels of 13 Å[50] allowing for the inclusion of larger molecules. The extremely open nature of the 13X pore network and small size of ammonia means that the zeolite is very accessible for ammonia.

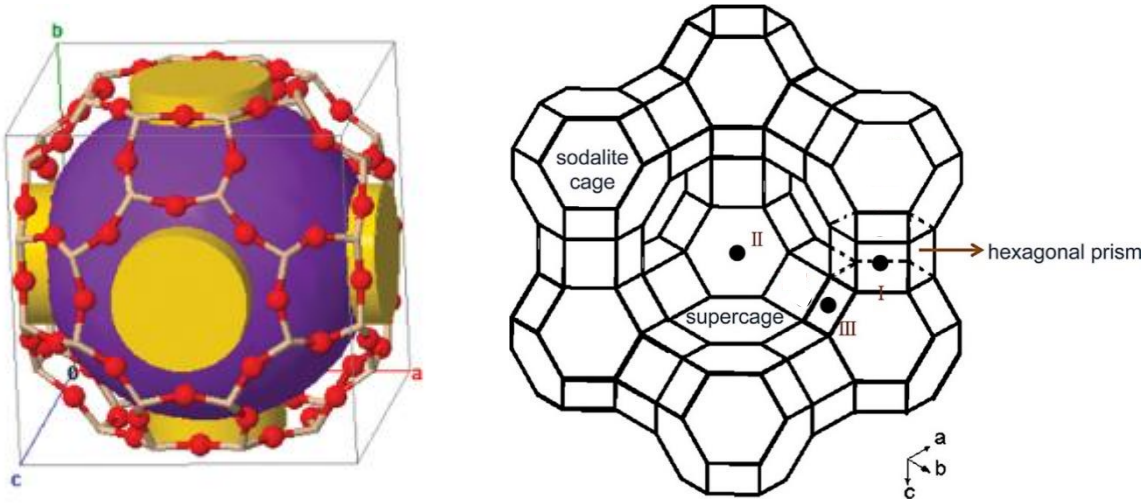

Figure 1-13: Representation of the pore network in a faujasite zeolite. a) The ball and stick model represents the framework (red are oxygen, yellow are silicon/aluminium) and the purple/yellow shapes represent the space within the network.[36] b) The lines represent the Al/Si-O bonds and the circles the possible adsorption sites.[51]

There are three sites which have been identified for possible adsorption. Olson's model identifies three broad classes of sodium sites in Na13X; one located in the hexagonal prisms joining the sodalite cages (site I), one located on the six membered rings on the unjoined hexagonal faces of the octahedra (site II) and one located on the walls of the channels in the supercage and the four ring channels (site III).[49] Studies have shown that the supercage is accessible to ammonia and that ammonia can enter the sodalite cages, thus allowing for access to all sites.[52] This means that all sites are theoretically available for ammonia sorption.

ZSM-5 is a MFI framework zeolite, consisting of pentasil units joined by oxygen atom links to generate a network of straight and sinusoidal channels.[53] The pores here are smaller than in 13X (reportedly less than 6 Å[53]) but still large enough that ammonia can enter.

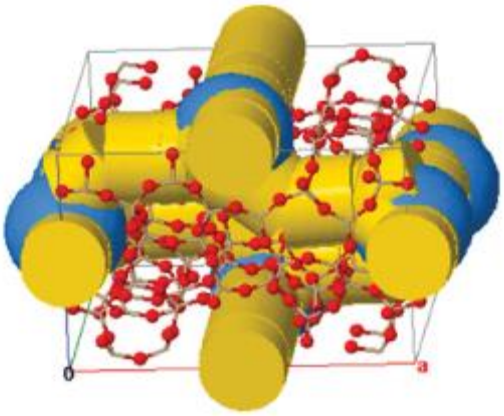

Figure 1-14: Representation of the pore network in a MFI zeolite; the ball and stick model represents the framework (red as oxygen, yellow are silicon/aluminium) and the blue/yellow shapes represent the space within the network.[36]

Mordenite exists as both a naturally occurring and synthetic zeolite. The pore structure is made up of five oxygen rings, joined to give main pores with diameter of 6.6 Å interconnected by 2.8 Å small pores.[54]

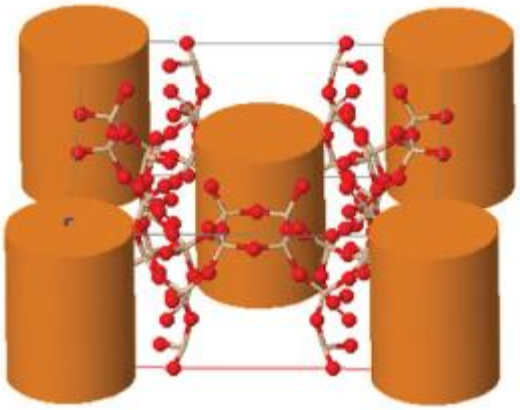

Figure 1-15: Representation of the pore network in a mordenite zeolite; the ball and stick model represents the framework (red as oxygen, yellow are silicon/aluminium) and the orange shapes represent the space within the network.[36]

1.8.2. SAPOs

SAPOs are very closely related to zeolites, and the structural considerations and properties are very similar. As well as the framework silicon and aluminium atoms, SAPOs contain phosphorous atoms, altering the properties of the materials. Syntheses of SAPOs are very similar to those of

zeolites. There are many SAPOs used in industrial processes; SAPO-34 is used in light olefin production, n-hexane isomerisation and NO_x removal.[55]

1.8.3. Activated Carbons

The final class of porous materials discussed here are activated carbons. Activated carbons are extremely high surface area carbon-based materials, often generated from burning carbon containing waste. Activated carbons are used for adsorption of a variety of gases and liquid including CO_2, H_2S, SO_2, HCl, phenol and metal ions.[56] Different functional groups can be present on the carbon surface including alcohols, aromatics and aliphatic chains, which may influence their adsorption capacities.[57] The functional group present in a particular activated carbon can be determined using techniques such as IR. However, in this work, the activated carbon is only used as a support, taking advantage of its high surface area and so this was not studied.

1.9. Layered materials

1.9.1. Metal Halides

A significant portion of the research efforts on ammonia storage to date have focussed on metal halides, with particular focus on the group two halides.

Initially used in heat pumps, metal halides have been extensively studied with works on over 350 ammonia salt complexes collated in 1999 by Touzan.[58]

Kojima *et al.* provide a further excellent review of the breadth of literature studying halides for ammonia absorption.[59] They discuss ammonia sorption on Li, Na, Mg, Ca, Ni, Cu, Zn, Sr, Ba, Ag, Co and Pt halides, with $MgCl_2$ and $CaCl_2$ showing the highest gravimetric densities.

Multiple papers exist comparing various metal halides. Liu *et al.* comprehensively studied $MgCl_2$, $CaCl_2$, $CaBr_2$, $SrCl_2$ and $SrBr_2$ and the corresponding hydrated forms and examined the ability of each of these materials to absorb and desorb ammonia at a variety of temperatures and pressures.[60] They found that $MgCl_2$, $CaCl_2$ and $CaBr_2$ showed the highest capacity at temperatures between 298 K and 473 K at 40 kPa. They found that at higher pressures (60 and 100 kPa) the ammonia absorption was not fully reversible. Hydrated forms of $CaCl_2$ and $SrCl_2$ showed reversible ammonia sorption but their very low capacity means they are of limited use in industry. The poor reversibility of these materials under high pressures has implications for their potential use in Haber type processes, where higher ammonia pressures are expected.

Sharonov compared ammonia sorption on $MgCl_2$, $CaCl_2$ and $BaCl_2$, finding that $MgCl_2$ shows the highest ammonia capacity, followed by $CaCl_2$ and that the sorption capacity peaks at low temperatures in all studied halides.[58]

The conclusion from these works is that magnesium chloride shows the highest gravimetric capacity for ammonia absorption. Therefore, it was used as the standard to which other materials were compared.

1.9.2. $MgCl_2$

Due to the high gravimetric capacity of $MgCl_2$ it is a commonly used and thus well studied ammonia absorption material.[31,61–64]

$MgCl_2$ has the cubic close packed $CdCl_2$ structure with octahedral metal ions, shown in Figure 1-16. Edge sharing magnesium chloride octahedra form the layers which are then held together by weak van der Waals interactions .[65–67]

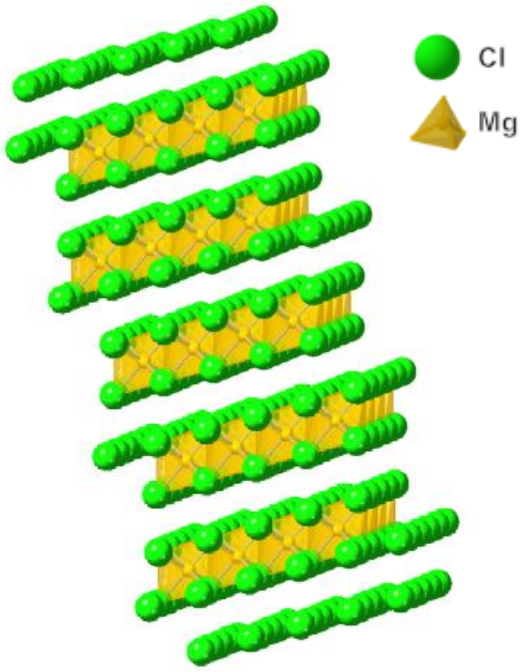

Figure 1-16: Structure of $MgCl_2$[65]

$MgCl_2$ as an ammonia storage compound is well studied in the literature.[61–64,68] $MgCl_2$ is theoretically capable of binding six ammonia molecules per magnesium centre, giving an extremely promising ammonia content of 52 wt%.[68] The structure of $MgCl_2(NH_3)_6$ has been determined to adopt the K_2PtCl_6 structure.[69]

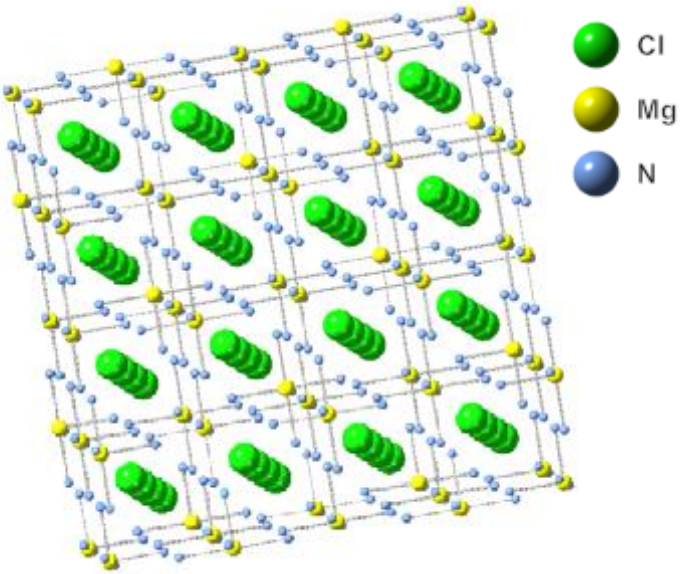

Figure 1-17: Structure of $MgCl_2(6NH_3)_6$. [69] (The H atoms of the ammonia molecules are not shown for clarity.)

The introduction of ammonia into the $MgCl_2$ is not a surface process but is instead absorption to give a new crystal structure. The ammonia molecules diffuse into the lattice of $MgCl_2$ by opening up the weak interaction between the ClMgCl layers to gain access to the Mg^{2+} which ammonia interacts with. It is reported that this hexa-ammonia complex is achieved by the absorption of two ammonia, followed by four ammonia, shown below.[63]

$$MgCl_2 + 2\ NH_3 \rightarrow MgCl_2(NH_3)_2 \qquad \text{(Equation 13}^{63}\text{)}$$
$$MgCl_2(NH_3)_2 + 4\ NH_3 \rightarrow MgCl_2(NH_3)_6 \qquad \text{(Equation 14}^{63}\text{)}$$

The desorption of ammonia is also studied with two mechanisms proposed. The first involves the desorption of four ammonia, followed by one ammonia and then the final ammonia. [62,70]

$$MgCl_2(NH_3)_6 \rightarrow MgCl_2(NH_3)_2 + 4\ NH_3 \qquad \text{(Equation 15}^{62,70}\text{)}$$
$$MgCl_2(NH_3)_2 \rightarrow MgCl_2NH_3 + NH_3 \qquad \text{(Equation 16}^{62,70}\text{)}$$
$$MgCl_2NH_3 \rightarrow MgCl_2 + NH_3 \qquad \text{(Equation 17}^{62,70}\text{)}$$

An alternative mechanism involves three steps each resulting in the loss of two ammonia. [64,68]

$$MgCl_2(NH_3)_6 \rightarrow MgCl_2(NH_3)_4 + 4\ NH_3 \qquad \text{(Equation 18}^{64,68}\text{)}$$
$$MgCl_2(NH_3)_4 \rightarrow MgCl_2(NH_3)_2 + 2\ NH_3 \qquad \text{(Equation 19}^{64,68}\text{)}$$
$$MgCl_2(NH_3)_2 \rightarrow MgCl_2 + 2\ NH_3 \qquad \text{(Equation 20}^{64,68}\text{)}$$

Structural changes with desorption have been identified. Christensen and Nørskov discuss that nanopores are generated during the desorption process increasing the $MgCl_2$ surface area, allowing for easier desorption than would be expected from a non-porous material.[6,71] This bodes well for applications where multiple absorption desorption cycles will be used.

However, there are some problems with ammonia absorption on $MgCl_2$, which we will attempt to overcome here. As discussed previously, the ammonia absorption is not fully reversible at high ammonia pressures.[63] This means that the high capacity cannot be fully used under high ammonia pressure conditions; some ammonia remains bound to the metal centre in the material after attempted regeneration meaning subsequent cycles do not use pure $MgCl_2$ for sorption and so the capacity is gravimetrically lower.[63] Another drawback to $MgCl_2$ as an ammonia absorbent is

that there is significant volume change on absorption. $MgCl_2(NH_3)_6$ is almost half as dense as $MgCl_2$ meaning that the $MgCl_2$ almost doubles in volume on absorption.[72] This has implications for the engineering of any absorbent set-ups or applications where the absorbent volume is important. One solution proposed in the literature is to use supported $MgCl_2$ which shows no volume change as any $MgCl_2$ volume change is limited by the pore size of the zeolite, though this reduced volume change is at the expense of gravimetric capacity.[28] Another drawback with $MgCl_2$ is its poor high temperature capacity. At higher temperatures, much higher ammonia pressures are needed for the maximum ammonia capacity of $MgCl_2$ to be achieved.[23] Ojha *et al.* report that an almost tenfold increase in pressure is needed to achieve the same equilibrium ammonia absorption capacity of $MgCl_2$ when going from 50 to 150 ^oC.[23] This has implications for systems where the absorbent operates at high temperatures, e.g. in the proposed one mixed bed system of Cussler's (see Figure 1-6).

These deficiencies with ammonia absorption on $MgCl_2$ give a number of targets for an improved sorbent. An ideal material would have the high capacity of $MgCl_2$ but with highly reversible sorption and no volume change. A new material should have high ammonia capacity at high temperatures. Furthermore, fast desorption has been shown to be a crucial requirement for improved ammonia capacity.[23]

1.9.3. Layered Double Hydroxides

An alternative class of sorbent materials is layered double hydroxides (LDHs). These are particularly useful materials as the size of molecules that zeolites can adsorb is clearly limited by the pore size of the zeolites. Layered materials, such as layered double hydroxides, can have larger spaced between the layers, hypothetically allowing for larger molecules or greater volume of molecules to intercalate between the layers.

LDHs are a class of materials based on the mineral hydrotalcite. LDHs consist of edge sharing octahedra, formed of metal ions surrounded by octahedral hydroxide ions; these layers show the same structure to those found in brucite, $Mg(OH)_2$. In mineral hydrotalcite these ions are Mg^{2+} and Al^{3+} but these can be replaced by a huge variety of other metal ions to alter the properties of the LDH. Monovalent and tetravalent metal ions can also be introduced, increasing the number of possible structures even further. Yan *et al.* reviewed the variety of elements included in LDHs reported in literature with the following summary.[73] This shows just how flexible the LDH structure is.

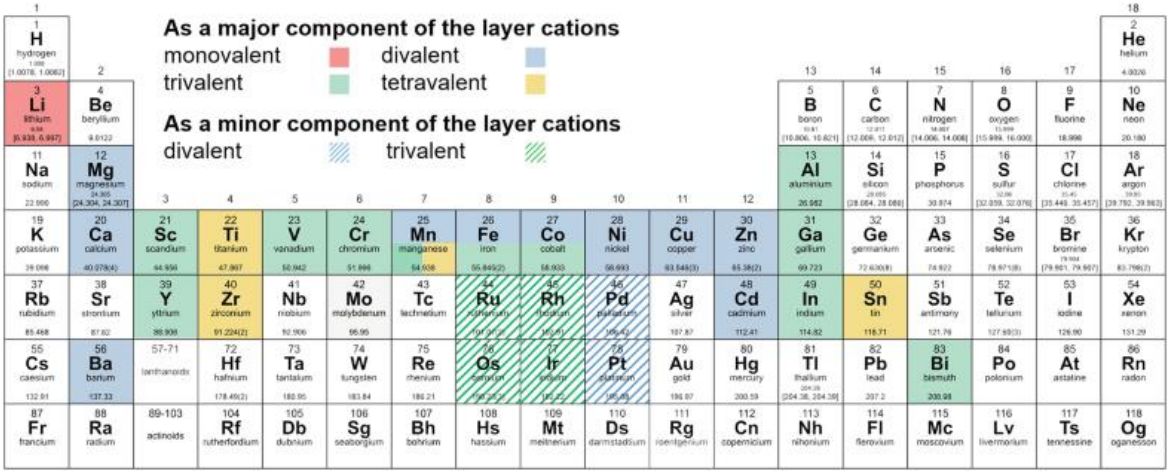

Figure 1-18: Illustration of the variety of elements which can be introduced to LDHs. Elements which have been included as a major component are shown in solid red (monovalent ions), blue (divalent ions), green (trivalent ions) and yellow (tetravalent ions) while elements which have been present only as a minor component are shown in hatched blue (divalent ions) and green (trivalent ions). Adapted from [73].

If only divalent metal ions were present the layers would be neutral, but introduction of trivalent metal ions causes an unbalance. This means the layers have an overall positive charge and so are balanced by interlayers which have a net negative charge. The interlayer species can be from a huge variety of molecules or ions; H_2O, CO_3^-, NO_3^- and Cl^- are common,[74] though metal clusters[75] and large organic molecules are also possible[76].

LDHs have metal ion layers between OH^- layers, similar to $MgCl_2$, with the metal ion surrounded by octahedral hydroxide ions. Further species are present between the OH^- layers, which can vary, including H_2O, CO_3^-, NO_3^- and Cl^- among others.[74]

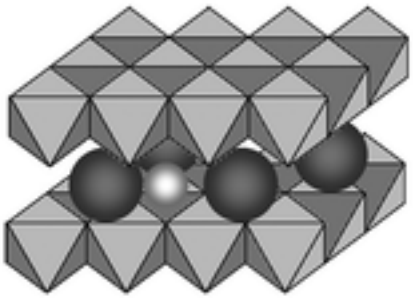

Figure 1-19: LDHs structure (octahedra representing M, OH^- layers, circles representing interlayer species).[77]

There are two main ways in which LDHs are used in adsorption: as prepared or calcined. If LDHs are to be used as prepared, one of the main areas for improvement is the surface area.

A significant benefit of LDHs is that they can be prepared as very thin layer materials ranging from single molecular layers to few layers. As a result, very high surface areas are possible, which means LDHs have wide ranging applications including catalysis, ion exchange and electrochemistry.[74] One promising method of increasing the surface area of an LDH is through organic solvent treatments during synthesis. Work by O'Hare has shown that treatment with acetone can greatly improve the surface area of an LDH though both minimising the number of LDH layers present and the size of the layers.[78] The exact mechanism of this treatment, known as the AMOST method, is not fully understood. It is proposed that the increase in surface area is due to the acetone entering between the LDH layers, disrupting the structure and decreasing the bonding capability between the layers.[79] It has been suggested that the acetone replaces water molecules on the surface of the LDH layers and so significantly decreases the hydrogen bonding interactions between the layers.[79] This means that layers are less capable of aggregating and

stacking, therefor increasing the surface area.[79] This disruption means thin layers or even single layers of LDH are possible giving a much higher surface area, which will be targeted for ammonia adsorption.

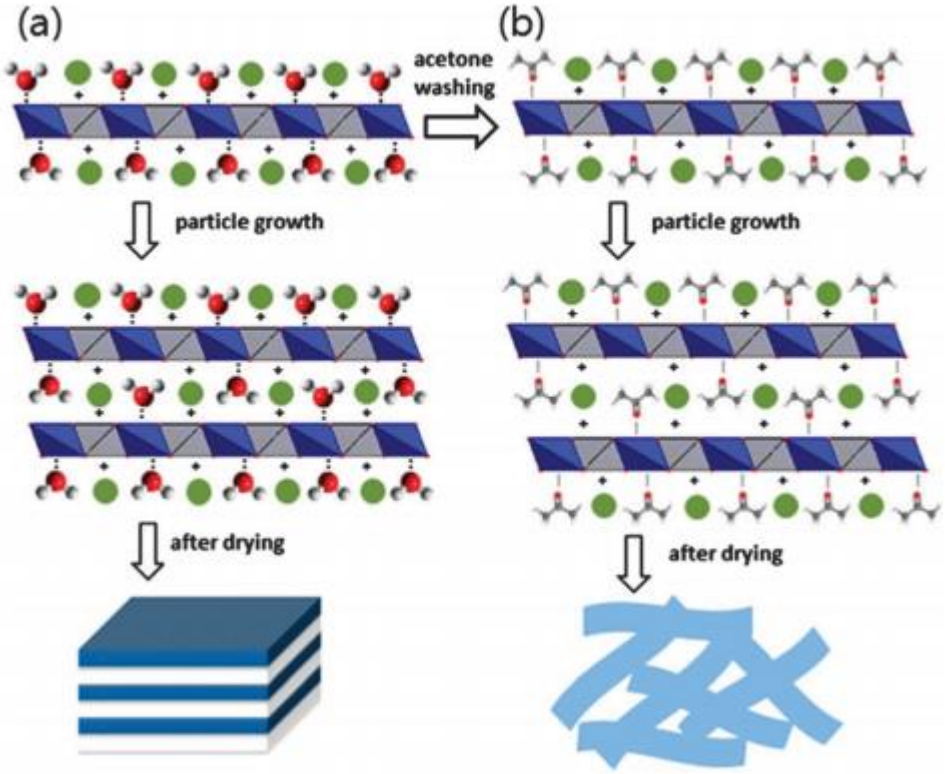

Figure 1-20: Proposed mechanism for increased surface area with AMOST treatment.[79] a) shows the standard synthesis, with water molecules on the LDH surface, interacting between the layers leading to a stacked structure after drying. b) shows the AMOST method, where the acetone molecules replace the surface water, there is decreased bonding interaction between the layers and drying gives unstacked layers.

The main challenge with such treatments is the difficulty in keeping the single layers exfoliated after drying.[79] Almost all previous synthesis methods for single layer LDHs lead to reordering when allowed to completely dry and give a lowered interlayer separation than was present before the exfoliation treatment.[80] The AMOST method shows improvements here,[79] though the potential for reordering should still be considered.

A further related material to LDHs is the equivalent oxide. LDHs can be calcined to give high surface area oxide materials, which can also be trialled as sorbents.

LDHs are commonly used gas adsorbents, frequently for CO_2.[81] The gas molecules are stored in the interlayer region interacting weakly with the metal hydroxide layers. As ammonia sorption in $MgCl_2$ initially also involves the interlayer region, it is hoped that some of the developments around LDHs can be applied to $MgCl_2$ also.

1.10. Aims and Objectives

The aims of this work are to develop new ammonia sorbents, mainly for use in ammonia synthesis applications.

Though $MgCl_2$ is the most commonly used absorbent, a number of deficiencies have been identified. In Haber process type applications the following priorities have been identified; volumetric capacity (as the sorbent will be stationary), thermal stability (due to the high operating temperature of the reactors), fast sorption and desorption (as Cussler[23] identified is essential) and stability over many cycles (as ideally, the sorbent bed will not be regularly replaced). For these reasons, zeolites will first be targeted due to their high temperature stability and open structure, which should lead to fast sorption and desorption. These zeolites will be modified to give a variety of adsorption sites including metal ion sites and Brønsted acid sites in the hope of improving capacity. This adsorption will be studied in detail to understand what factors affect ammonia sorption in such materials and so allowing for better development of future materials.

For low temperature ammonia synthesis applications, high temperature stability is no longer a particular consideration though the sorption and desorption speed and stability remain important. For these applications, layered materials will be studied in greater detail again trying

to improve the materials to give easier diffusion of ammonia through the structure without stability problems. $MgCl_2$ will be modified, primarily through disruption of the layered structure, in an attempt to improve ammonia diffusion through the solid and better the cycling ability. Techniques used in other layered materials, with a focus on LDH techniques, will be used here and a variety of layered materials studied.

In all cases a variety of characterisation techniques will be used to understand the sorption properties of the materials. Gravimetric techniques will used to study the sorption and desorption properties, while techniques such as NMR and BET will allow for structural information. *In-situ* synchrotron X-ray diffraction will be used extensively to identify ammonia positions and understand the binding sites within the sorbents. Modelling techniques will be used to support this. The use of these characterisation aims to give an understanding of what factors improve the ammonia sorption process and how this may be used to tailor future materials.

1.11. Chapter Outline

This thesis consists of six chapters, each studying different aspects of ammonia sorption.

Chapter 2 gives detail of the material syntheses used, technical information on the characterization methods applied and theoretical background of the main instrumental techniques used.

Chapter 3 compares the ammonia capacity of a series of modified 13X zeolites, prepared using H^+, Mg^{2+} and La^{3+} ion exchange to give fast, reversible adsorption. Each zeolite shows different desorption profiles indicating different structural changes as a result of the ion exchange process. Rietveld refinement of *in-situ* TPD SXRD, supported by DFT modelling, NMR, N_2 physisorption and gravimetric techniques, allows for the determination of the structures and the ammonia binding

sites to be identified. H^+ ion exchange generates Brønsted acid sites giving strong ammonia binding, La^{3+} ion exchange causes structural disruption and Lewis acidity giving weaker ammonia binding and Mg^{2+} shows a combination of acidity.

Chapter 4 explores the lanthanum ion exchange process further and how the disorder it causes affects the ammonia capacity. A combination of Rietveld refinement of XRD, NMR, TPD and N_2 physisorption was used to study the effect on temperature, time and concentration on the lanthanum ion exchange process. These experiments show that the lanthanum ion concentration improves ammonia capacity though this can also lead to undesirable dealumination process. Furthermore, a correlation between lanthanum content and acidity is seen.

Chapter 5 is focused on layered materials. First, gravimetric techniques are used to study $MgCl_2$ and $NiCl_2$. Acetone treatment of $MgCl_2$ is shown to greatly improve the ammonia absorption rate and this is shown to be as a result of exfoliation of the layered structure. Alternative methods of layer disruption are attempted, including alternative solvents, dopant elements, pillaring and interlayer species introduction. Finally, supported exfoliated $MgCl_2$ is proposed as a fast, stable ammonia sorbent, particularly at high temperatures and low pressures.

Finally, Chapter 6 summarises the findings of this work and offers possible future lines of study.

Supplementary information, including details of the refined parameters from Rietveld refinements, is given in the appendices.

1.12. References

1. A. Valera-Medina,H. Xiao, M. Owen-Jones, W. I. F. David and P. J. Bowen PJ, *Prog. Energy Combust. Sci.*, 2018, **69**, 63-102.

2. J. W. Erisman, M. A. Sutton, J. Galloway, Z. Klimont and W. Winiwarter, *Nat. Geosci*., 2008, **1**, 636-639.

3. L. K. Boerner, *Chem. Eng. News,* 2019, **97**, 24.

4. S. Hales, S. Kovats, S. Llyod and D Campbell-Lendrum, *Quantitative risk assessment of the effects of climate change on selected causes of death, 2030s and 2050s.*, World Health Organization, 2014.

5. Ammonia—a renewable fuel made from sun, air, and water—could power the globe without carbon, https://www.sciencemag.org/news/2018/07/ammonia-renewable-fuel-made-sun-air-and-water-could-power-globe-without-carbon, (accessed June 2020).

6. A. Klerke, C. H. Christensen, J. K. Nørskov and T Vegge, *J. Mater. Chem*., 2008, **18**, 2304-2310.

7. Saudi Arabia to export renewable energy using green ammonia, https://www.ammoniaenergy.org/articles/saudi-arabia-to-export-renewable-energy-using-green-ammonia/, (accessed December 2020).

8. Australian government to fast-track 26GW hydrogen + ammonia 'Asian Renewable Energy Hub.', https://www.energy-storage.news/news/australian-govt-to-fast-track-26gw-hydrogen-ammonia-asian-renewable-energy, (accessed December 2020).

9. Full electrification: Yara plans 500,000 tons of green ammonia in Norway by 2026, https://www.ammoniaenergy.org/articles/full-electrification-yara-plans-500000-tons-of-green-ammonia-in-norway-by-2026/, (accessed December 2020)

10. Maritime decarbonization is a trillion dollar opportunity, https://www.ammoniaenergy.org/articles/maritime-decarbonization-is-a-trillion-dollar-opportunity/, (accessed December 2020).

11. T. Kandemir M. E. Schuster, A. Senyshyn, M. Behrens and R. Schlogl, *Angew. Chemie Int. Ed*., 2013, **52**, 12723-12726.

12. N. Saadatjou, A. Jafari and S. *Chem. Eng. Commun*., 2014, **202**, 420-448.

13. P. Atkins, T. Overton, J. Rourke, M. Weller and F. Armstrong, *Inorganic Chemistry (5th ed.),* Oxford University Press, Oxford, 2010.

14. C. J. H. Jacobsen, S. Dahl, B. G. S. Clausen, S. Bahn, A. Logadottir and J. K. Nørskov, *J. Am. Chem. Soc*., 2001, **123**, 8404-8405.

15. Ammonia Production causes 1% of total global GHG emissions, https://ammoniaindustry.com/ammonia-production-causes-1-percent-of-total-global-ghg-emissions/, (accessed November 2019)

16. M. Malmali, M. Reese, A. V. McCormick and E. L. Cussler EL, *ACS Sustain. Chem. Eng*., 2018, **6**, 827-834.

17. P. Atkins and J. de Paula J, *Physical Chemistry (9th ed.),* Oxford University Press, Oxford, 2010.

18. B. Smit B and T. L. M. Maesen, *Chem. Rev*., 2008, **108**, 4125-4184.

19. P. Bai, E. Haldoupis, P. J. Dauenhauer, M. Tsapatsis and J. I. Siepmann, *ACS Nano*., 2016, **10**, 7612-7618.

20. G. Attard and C. Barnes, *Surfaces*, Oxford University Press, Oxford, 2011.

21. Z. A. Alothman, *Materials*, 2012, **5**, 2874-2902.

22. S. J. Gregg and J. Jacobs J., *Trans., Faraday Soc*., 1948, **44**, 574-588.

23. D. K. Ojha, M. J. Kale, P. J. Dauenhauer, A. McCormick and E. L. Cussler, *ACS Sustain. Chem. Eng*., 2020, **8**, 15475-15483.

24. M. Reese, C. Marquart, M. Malmali, K. Wagner. E. Buchanan, A. McCormick and E. L. Cussler, *Ind. Eng. Chem. Res*., 2016, **55**, 3742-3750.

25. M. J. Palys, A. McCormick, E. L. Cussler and P. Daoutidis, *Proccesses*., 2018, **6**, 91.

26. H. H. Himstedt, M. S. Huberty A. V. McCormick, L. D. Schmidt and E. L. Cussler, *Am. Inst. Chem. Eng. J*., 2015, **61**, 1364-1371.

27. K. Wagner, M. Malmali, C. Smith, A. McCormick, E. L. Cussler, M. Zhu and N. C. A. Seaton, *AIChE J*., 2017, **63**, 3058-3068.

28. M. Malmali, G. Le, J. Hendrickson, J. Prince, A. V. McCormick and E. L. Cussler, *ACS Sustain. Chem. Eng*., 2018, **6**, 6536-6546.

29. M. Malmali, Y. Wei , A. McCormick and E. L. Cussler, *Ind. Eng. Chem. Res*., 2016, **55,** 8922-8932.

30. M. Malmali, M. Reese, A. V. McCormick and E. L. Cussler, *ACS Sustain. Chem. Eng*., 2018, **6**, 827-834.

31. D. K. Ojha, M. J. Kale, A. V. McCormick, M. Reese, M. Malmali, P. Dauenhauer and E. L. Cussler, *ACS Sustain. Chem. Eng*., 2019, **7**, 18785-18792.

32. International Zeolite Association Database, http://www.iza-structure.org/databases/, (accessed October 2019).

33. A. Farjoo, S. M. Kuznicki and M. Sadrzadeh, *Materials,* 2017, **10**, 1-14.

34. C. S. Cundy and P. A. Cox, *Microporous Mesoporous. Mater*., 2005, **82**, 1-78.

35. E. M. Flanigen, R. W. Broach and S. T. Wilson, *Zeolites in Industrial Separation and Catalysis,* Wiley, Weinheim, 2010.

36. B. T. W. Lo , L. Ye and S. C. E. Tsang, *Chem*., 2018, **4**, 1778-1808.

37. R. M. Barrer, *J. Chem. Soc*., 1948, **0**, 127-132.

38. US Pat., 2 882 243, 1953.

39. US Pat., 2 882 244, 1953.

40. *Statistical Review of World Energy, 2020 (69th Ed.),* BP, 2020.

41. J. C. D. Díaz, I. D. Gil-Chávez, L. Giraldo and J. C. Moreno-Piraján, *E-Journal Chem*., 2010, **7**, 483-495.

42. S. M. T. Almutairi, B. Mezari, G. A. Filonenko, P. C. M. M. Magusin, M. A. Rigutto, E. A. Pidko amd E. J. M. Hensen, *ChemCatChem*., 2013, **5**, 452-466.

43. E. G. Derouane, J. C. Védrine, R. Ramos Pinto, P. M. Borges, L. Costa, M. A. N. D. A. Lemos, F. Lemos and F. Ramoa Ribeiro, *Catal. Rev.,* 2013, **55**, 454-515.

44. L. Ye, B. T. W. Lo, J. Qu, I. Wilkinson, T. Hughes, C. A. Murray, C. C. Tang and S. C. E. Tsang, *Chem. Commun*., 2016, **52**, 3422-3425.

45. J. A. van Bokhoven, A. L. Roest, D. C. Koningsberger, J. T. Miller, G. H. Nachtegaal and A. P. M. Kentgens, *J. Phys. Chem. A*, 2000, **104**, 6743-6754.

46. W-C. Lin, L. Ye, S. Wu, B. Lo, Y-K. Peng, P Zhao, I. McPherson and S. C. E. Tsang, *ChemSusChem*., 2018, **11**, 4214-4218.

47. D. E. Perea, I. Arslan, J. Liu, Z. Ristanovic, L. Kovarik, B. W. Arey, J. A. Lercher, S. R. Bare and B. M. Weckhuysen, *Nat. Commun*., 2015, **6**, 1-8.

48. R. E. Fletcher, S. Ling and B. Slater, *Chem. Sci*., 2017, **8**, 7483-7491.

49. D. H. Olson, *Zeolites*., 1995, **15**, 439-443.

50. M. B. Pourazar, T. Mohammadi, M. R. Jafari Nasr, M. Javanbakht and O. Bakhtiari, *Mater. Res. Express*., 2020, **7**, 035004.

51. L. Zhang, T. N. Pham, J. Faria and D. E. Resasco, *Appl. Catal. A Gen*., 2015, **504**, 119-129.

52. V. Kanazirev and N. Borisova, *Zeolites*., 1982, **2**, 23-28.

53. H. van Koningsveld, J. C. Jansen and H. van Bekkum, *Zeolites*., 1990, **10**, 235-242.

54. W. M. Meier, *Zeitschrift für Krist. – Cryst. Mater*., 1961, **115**, 439–450.

55. T. Doan, K. Nguyen, P. Dam T. H. Vuong, M. T. Le and H. P. Thanh, *J. Chem*., 2019, **2019**, 6197527.

56. M. S. Shafeeyan, W. M. A. W. Daud, A. Houshmand and A. Shamiri, *J. Anal. Appl. Pyrolysis*., 2010, **89**, 143-151.

57. A. P. Ramirez, S. Giraldo, M. Ulloa, E. Flórez and N. Y. Acelas, *J. Phys. Conf. Ser*., 2017, **935**, 012012.

58. V. E. Sharonov and Y. I. Aristov, *React. Kinet. Catal. Lett*., 2005, **85**, 183-188.

59. Y. Kojima and M. Yamaguchi, *Int. J. Hydrogen Energy*, 2020, **45**, 10233-10246.

60. C. Y. Liu and K. Aika, *Ind. Eng. Chem. Res*., 2004, **43,** 7484-7491.

61. M. van der Pal, R. de Boer and J. Veldhuis, *International Symposium on Innovative Materials for Process in Energy Systems*, 2013.

62. C. H. Christensen, R. Z. Sørensen, T. Johannessen, U. J. Quaade, K. Honkala, T. D. Elmoe, R. Kohler and J. K. Norskov, *J. Mater. Chem*., 2005, **15**, 4106-4108.

63. C. Y. Liu and K-I Aika, *Bull. Chem. Soc. Jpn*., 2004, **77**, 123-131.

64. H. Zhu, X. Gu, K. Yao, L. Gao and J. Chen, *Ind. Eng. Chem. Res*., 2009, **48**, 5317-5320.

65. E. Stavrou, Y. Yao, J. M. Zaug, S. Bastea, B. Kalkan, Z. Konopkova and M. Kunz, *Sci. Rep*., 2016, **6**, 30631.

66. A. Ferrari, A. Braibanti and G. Bigliardi, *Acta Crystallogr*., 1963, **16**, 846-847.

67. C. L. Perkins, C. Beall, M. O. Reese and T. M. Barnes, *ACS Appl. Mater. Interfaces*, 2017, **9**, 20561-20565.

68. M. O. Jones, D. M. Royse, P. P. Edwards and W. I. F David, *Chem. Phys*., 2013, **427**, 38-43.

69. I. C. Hwang, T. Drews and K. Seppelt, *J. Am. Chem. Soc*., 2000, **122**, 8486-8489.

70. T. D. Elmøe, R. Z. Sørensen, U. Quaade, C. H. Christensen, J. K. Nørskov and T. Johannessen, *Chem. Eng. Sci*., 2006, **61**, 2618-2625.

71. J. S. Hummelshøj, R. Z. Sørensen, M. Y. Kustova, T. Johannessen, J. K. Nørskov and C. H. Christense, *J. Am. Chem. Soc*., 2006, **128**, 16-17.

72. T. Aoki, H. Miyaoka, H. Inokawa, T. Ichikawa and Y. Kojima, *J. Phys. Chem. C*., 2015, **119**, 26296-26302.

73. H. Yan, X-J. Zhao, Y-Q. Zhu, M. Wei, D. G. Evans and X. Duan, *The Periodic Table II: Catalytic, Materials, Biological and Medical Applications*, Springer International Publishing, Cham, 2019.

74. F. Cavani, F. Trifiro and A. Vaccari, *Catal. Today*, 1991, **11**, 173-301.

75. E. Lopez-Salinas and Y. Ono, *Microporous Mater*., 1993, **1**, 33-42.

76. M. Drezdzon, *Inorg. Chem*., 1988, **27**, 4628-4632.

77. B. Zhao, C. Li and C. Xu, *Catal. Sci. Technol*., 2012, **2**, 1985-1994.

78. C. Chen, A. Wangriya, J. Buffet and D. O'Hare, *Dalt. Transations*, 2015, **44**, 16392-16398.

79. Q. Wang and D. O'Hare, *Chem. Commun*., 2013, **49**, 6301-6303.

80. Q. Wang and D. O'Hare, *Chem. Rev*., 2012, **112**, 4124-4155.

81. Z-Z. Yang, J-J. Wei, G-M. Zeng, H-Q. Zhang, X-F. Tan, C. Ma, X-C. Li, Z-H. Li and C. Zhang, *Coord. Chem. Rev*., 2019, **386**, 154-182.

2. Experimental

2.1. Materials

Unless otherwise specified all starting materials were purchased from Sigma-Aldrich and used as received. The ZSM-5 used was a commercial sample from SINOPEC, China with a Si:Al ratio of 19.25. Gases used were bottle pure gases from BOC.

2.2. Syntheses

2.2.1. 13X Zeolite Modifications

The modified zeolites were prepared using the method commonly used in our group.

Zeolites were prepared via ion-exchange of commercially available Na13X zeolite (Na13X from Sigma Aldrich), with a Si:Al ratio of 1.2. The initial concentration of ions in solution for exchanging was chosen so that all the sodium in the zeolite could be exchanged.

Commercial Na13X (Sigma Aldrich) was used in the ion exchange process due to its high sodium content. To exchange the ions, the zeolite (2 g) was added to a nitrate solution (prepared with 50 mL DI water) and stirred overnight at room temperature. After stirring overnight, the zeolite and solution were separated by centrifuging at 5000 rpm for 5 minutes. The solution was discarded, the zeolite stirred with water (approx. 50 mL) and the mixture centrifuged again. This washing process was carried out a total of three times. The zeolite was then dried at 110 ^{o}C overnight, then calcined at 550 ^{o}C in flowing N_2 (approx. 10mL/min flow rate, 10^{o} C/min ramp rate) for 5 hours.

Table 2-1: Nitrate used and nitrate mass used in ion exchange syntheses.

Zeolite	Nitrate Used	Mass nitrate
H13X	NH_4NO_3 (Sigma Aldrich)	4.00 g
La13X	$La(NO_3)_3.6H_2O$ (Sigma Aldrich)	7.22 g
Mg13X	$Mg(NO_3)_2.6H_2O$ (Sigma Aldrich)	6.41 g
Ni13X	$Ni(NO_3)_2.6H_2O$ (Sigma Aldrich)	7.26 g

2.2.2. Further Lanthanum Modifications

Similar preparations were used to prepare the modified lanthanum zeolites varying the lanthanum concentration, ion exchange temperature, ion exchange time and zeolite, as described below. In each case $La(NO_3)_3.6H_2O$ (Sigma Aldrich) was used as the lanthanum source and the process after ion exchange was the same. After stirring, the zeolite and solution were separated by centrifuging at 5000 rpm for 5 minutes. The solution was discarded, the zeolite stirred with further water and the mixture centrifuged again. This washing process was carried out a total of three times. The zeolite was then dried at 110 ^oC overnight, then calcined at 550 ^oC in flowing N_2 (approx. 10mL/min flow rate, 10^o C/min ramp rate) for 5 hours.

Table 2-2: Nitrate, mass, temperature and duration of lanthanum ion exchange series.

Target	Zeolite Used	Mass of $La(NO_3)_3.6H_2O$ used	Ion Exchange Temperature	Ion Exchange Duration
La13X	Na13X, 2 g (Sigma Aldrich)	7.22 g	25 ^oC	16 hrs
0.5La13X	Na13X, 2 g (Sigma Aldrich)	3.61 g	25 ^oC	16 hrs
1.5La13X	Na13X, 2 g (Sigma Aldrich)	10.83 g	25 ^oC	16 hrs
La13X 40 ^oC	Na13X, 2 g (Sigma Aldrich)	7.22 g	40 ^oC	16 hrs
La13X 60 ^oC	Na13X, 2 g (Sigma Aldrich)	7.22 g	60 ^oC	16 hrs
La13X 24hr	Na13X, 2 g (Sigma Aldrich)	7.22 g	25 ^oC	24 hrs
La13X 48hr	Na13X, 2 g (Sigma Aldrich)	7.22 g	25 ^oC	48 hrs

2.2.3. LDH Syntheses

All LDH materials were synthesised using the following method, previously used by our group.

Mixed nitrate solution, sodium hydroxide solution (1M) and sodium carbonate solutions were prepared in separate vessels. All starting materials were purchased at Sigma Aldrich.

Sodium carbonate was added to 50 mL of water, the nitrates to 50 mL of water and the sodium hydroxide to 100 mL of water.

Table 2-3: Mass of nitrates, sodium carbonate and sodium hydroxide used in LDH syntheses.

Target	$Al(NO_3)_3.9H_2O$	$Mg(NO_3)_2.\ 6H_2O$	$Ni(NO_3)_2.\ 6H_2O$	Na_2CO_3	NaOH
Mg/Al LDH	3.76 g	5.13 g	0.00 g	2.12 g	4 g
Ni/Al LDH	3.76 g	0.00 g	5.82 g	2.12 g	4 g

A 250 mL three neck round bottom flask was equipped with a stirred bar and pH probe and the sodium carbonate solution. A small amount of the sodium hydroxide solution was added to bring the pH to 9. The nitrate solution was added, with concurrent addition of sodium hydroxide to ensure the pH remained between 8.5 and 9.5. This was repeated until all the nitrate solution had been added. The flask was sealed and the solution stirred overnight.

The synthesised LDH and solution were separated by centrifuging at 5000 rpm for five minutes. The solution was discarded, the LDH stirred with further water and the mixture centrifuged again. This washing process was carried out a total of three times. The LDH was then dried at 110 ^oC overnight.

2.2.4. Acetone Treatment of $MgCl_2$

First a saturated solution of $MgCl_2$ was prepared, using the reported solubility of $MgCl_2$. $MgCl_2$ (3 g, Sigma Aldrich) was dissolved in deionised water (7.5 mL) with stirring. Acetone (approx. 40 mL) was added and the mixture vigorously stirred overnight. The treated $MgCl_2$ was then dried at 110 ^oC overnight.

As discussed in greater detail in the results section, AT-$MgCl_2$ showed problems with layer reordering. Unless otherwise specified, a fresh batch of AT-$MgCl_2$ was prepared in advance of testing.

2.2.5. Ethanol Treatment of $MgCl_2$

First a saturated solution of $MgCl_2$ was prepared, using the reported solubility of $MgCl_2$. $MgCl_2$ (3 g, Sigma Aldrich) was dissolved in deionised water (7.5 mL) with stirring. Ethanol (approx. 40 mL) was added and the mixture vigorously stirred overnight. The treated $MgCl_2$ was then dried at 110 ^oC overnight.

To avoid any possible problems with layer reordering, a fresh batch of ET-$MgCl_2$ was used for testing.

2.2.6. Calcium, Nickel and Copper doping of $MgCl_2$

In each doping experiment, the level of dopant was chosen to replace a quarter of the magnesium ions as this was expected to disrupt the layers but not change the structure from the $MgCl_2$ structure. The chlorides were dissolved fully in an excess of water, stirred overnight and then dried at 110 ^oC overnight.

All chlorides were purchased from Sigma Aldrich.

Table 2-4: Mass of chlorides used in doped chloride syntheses.

Target	$MgCl_2$	$CaCl_2$	$NiCl_2$	$CuCl_2$
Ca/$MgCl_2$	0.95 g	0.37 g	0 g	0 g
Ni/$MgCl_2$	0.95 g	0 g	0.43 g	0 g
Cu/$MgCl_2$	0.95 g	0 g	0 g	0.45 g

2.2.7. TPA Pillaring of Mg/Al LDH

Terephthalic acid pillared LDH was prepared using a modified version of the previous LDH synthesis, adapted to follow the pillaring method described by Drezdzon.[1]

The LDH was prepared in the same way as before with the addition of disodium terephthalic acid.

A saturated solution of disodium terephthalic acid (0.83 g) was prepared. 0.5 M NaOH solution was added to bring the pH to above 9 (approx. 50 mL was required). A second solution of $Mg(NO_3)_2.6H_2O$ (3.85 g) and $Al(NO_3)_3.9H_2O$ (2.81 g) in 10 mL of water was prepared. The nitrate solution was added to flask containing 100 mL of water with constant stirring, using the NaOH/TPA solution to keep the pH of the mixture between 8.5 and 9.5. Once all the nitrate solution had been added, the flask was sealed and the solution stirred overnight.

The synthesised LDH and solution were separated by centrifuging at 5000 rpm for five minutes. The solution was discarded, the LDH stirred with further water and the mixture centrifuged again. This washing process was carried out a total of three times. The LDH was then dried at 110 ^oC overnight.

2.2.8. TPA Pillaring of $MgCl_2$

$MgCl_2$ (1.24 g) was fully dissolved in water (10 mL) with stirring. Disodium terephthalic acid (0.83 g) was added and the solution stirred overnight. The solution was dried at 110 ^oC overnight to give a solid.

2.2.9. Introduction of Interlayer Nickel Chloride to LDH

Nickel chloride was introduced between the LDH layers using the method devised by Ono.[2]

First, $[Et_4N]_2[NiCl_4]$ was prepared by dissolving $NiCl_2$ (1.40 g) and Et_4NCl (3.6 g) in hot ethanol (150 mL). The solution was stirred overnight and dried at 110 ^oC.

This product (2.41 g) was dissolved in ethanol (50 mL) and the previously prepared Ni/Al LDH (1 g, see 2.2.3) was added, the flask sealed and the solution stirred overnight. The mixture was filtered, washed with ethanol and dried overnight at 70 ^oC.

2.2.10. Supported $MgCl_2$

Three methods of supporting $MgCl_2$ on high surface area supports were trialled.

$MgCl_2$/C(1) was prepared by adding $MgCl_2$ (0.28 g) and activated C (0.52 g, "Carbon powder, activated, Ash 4% max", Alfa Aesar) to acetone (50 mL) and sonicating for 1 hour, before drying overnight at 160 °C.

$MgCl_2$/C(2) was prepared by adding $MgCl_2$ (0.28 g) to acetone (50 mL) sonicating for 1 hour, before adding activated C (0.52 g, "Carbon powder, activated, Ash 4% max", Alfa Aesar) and sonicating for a further hour. The mixture was dried overnight at 160 °C.

$MgCl_2$/ZSM-5 was prepared by dissolving $MgCl_2$ (0.53 g) in water (50 mL) and adding ZSM-5 (3.00 g). The mixture was stirred overnight then dried overnight at 160 °C.

2.3.Characterisation

2.3.1. Lab Source X-Ray Powder Diffraction (XRD)

Laboratory XRD were performed on PANalytical X'Pert PRO, PANalytical X'Pert PRO Alpha and Rigaku SmartLab diffractometers.

The Panalytical X'Pert PRO diffractometer was operated at 45 kV and 40 mA using Cu K_α radiation (λ = 1.54056). Patterns were recorded between 4 and 70 °, using a step size of 0.017 ° and a step time of 1.03 s/step.

The Panalytical X'Pert PRO Alpha diffractometer was operated at 45 kV and 40 mA using Cu K_α radiation (λ = 1.54056). Patterns were recorded between 4 and 70 °, using a step size of 0.017 ° and a step time of 1.03 s/step.

The Rigaku SmartLab diffractometer was operated at 50 kV and 30 mA using Mo K_α radiation (λ = 0.709317/0.713607). Patterns were recorded between 3 and 50 °, using a scan speed of 0.003 ° and a step time of 0.05 °/min (equivalent to 0.36 s/step). Laboratory XRD on the Rigaku SmartLab were recorded by Dr Tsz-woon Benedict Lo at The Hong-Kong Polytechnic University.

2.3.2. Intelligent Gravimetric Analysis

The IGA is a very powerful gravimetric tool for studying sorption. It consists of a high precision balance (10^{-4} mg resolution), gas inlet and exhaust, furnace (operational up to 500 °C) and vacuum pumping station (with both standard dry scroll pump and a turbomolecular pump).

Prior to experiments the sample (approx. 20 mg) was placed in the sample chamber and the chamber sealed using a copper gasket (using a new gasket each time to ensure complete sealing of the chamber). Pure ammonia gas is connected to the system and the pressure regulated internally. Temperature is regulated by two platinum resistance thermocouples, one located in the sample chamber and one externally, between the furnace tube and the outer chamber casing.

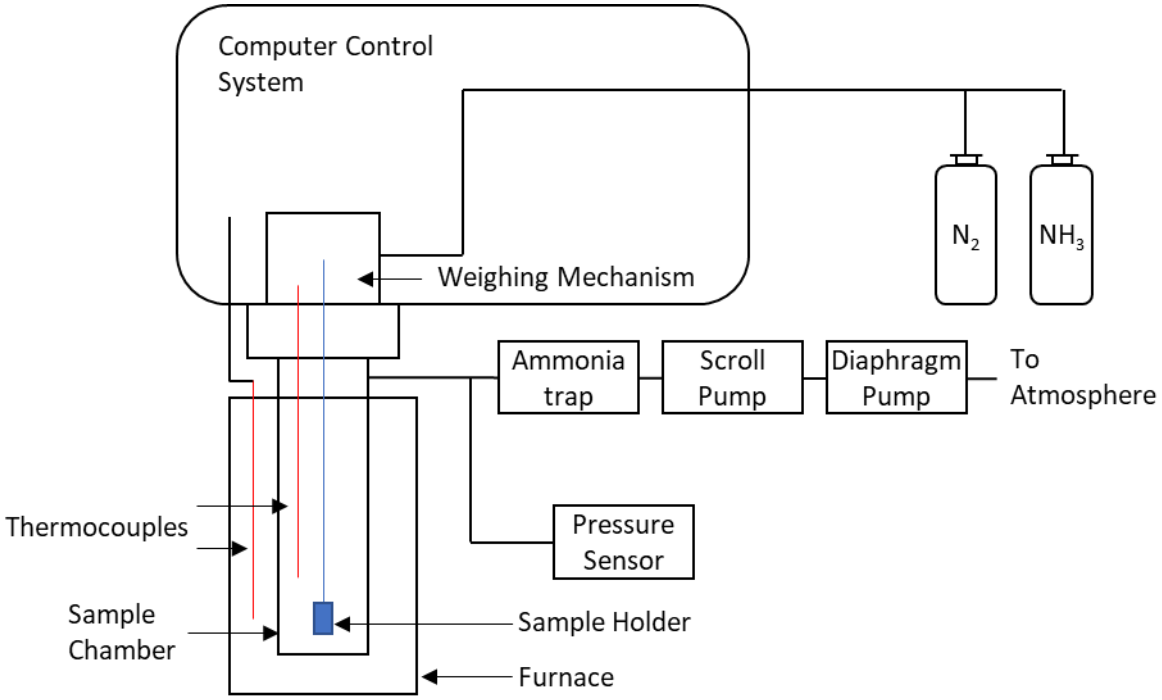

Figure 2-1: Schematic of IGA-002 set-up.

During an isotherm measurement the pressure is increased at a specified rate. Once the chosen set-point is reached this pressure is maintained for a specified time.

After all experiments the ammonia from the system must be removed, so the sample can be safely removed without exposing the user to pure ammonia gas. This is done via a process of repeated flushing with N_2 gas.

The ammonia sorption process was studied using a Hiden Isochema Intelligent Gravimetric Analyser (IGA-002) using pure ammonia (99.9 % purity, BOC). In each experiment approximately 20 mg of sample was used. Samples were loaded in the sample chamber and prior to any sorption each sample was dried at 300 ^{o}C for eight hours, under vacuum (10^{-3} mbar), then cooled to 25 ^{o}C and the initial sample weight accurately recorded. To record an isotherm, ammonia pressure was altered at 200 mbar intervals (ramp rate 10 mbar/min), kept at each pressure for 20 minutes and the sample weight recorded at each step. This was then repeated decreasing the pressure at 200

mbar intervals. To record the sorption rate the ammonia pressure was set at 400 mbar (ramp rate of maximum 100 mbar/min) and the weight change recorded until it stabilised.

2.3.3. Thermogravimetric Analysis (TGA)

TGA was used to study the desorption of ammonia from the materials. Desorption was studied using a TA Instruments Q600 SDT. Ammonia was first loaded using an IGA; clean samples were dried for eight hours at 300 ^{o}C under vacuum then were loaded with ammonia at 400 mbar until the weight stabilized (around 30 minutes). An exact mass (5-20 mg) was placed in an alumina pan in the SDT and the temperature was increased to 800 ^{o}C at a rate of 10 ^{o}C/min under 100 ml/min flowing nitrogen. A TGA curve and its first derivative were simultaneously collected.

2.3.4. N_2 Physisorption

N_2 physisorption measurements were collected in collaboration with Dr Robert Jacobs (Oxford University).

N_2 adsorption and desorption isotherms were determined using a Micrometics Tristar-3000. Isotherms were obtained using ultrahigh purity gases (99.999%). Prior to measurement, the zeolites were first calcined at 550 ^{o}C under flowing N_2. A known mass (0.1-0.2 g) was loaded into the sample cell then dried under vacuum (10^{-5} Torr) at 150 ^{o}C for 12 hours. The isotherms were then measured at 77 K and up to 1 bar; the surface areas were calculated using the BET model (using the initial slope of the isotherm from 0.01 to 0.1 P/P_0), the pore volume obtained using the 0.995 relative pressure point and the microporous properties determined using a t-plot analysis of the adsorption portion of the isotherm.

2.3.5. Al NMR

SS-NMR spectra were collected in collaboration with Dr Nick Rees (Oxford University).

^{27}Al SS-NMR spectra were measured on a Bruker AVIII 400 spectrometer using Larmor frequency of 104.20 Hz. The one pulse method was used with a 10^{o} pulse, a 0.4 s delay time and a scanning number of 6500.

2.3.6. SXRD and Rietveld Refinement

Synchrotron XRD data were collected at Beamline I11, Diamond Light Source, UK and Beamline BL02B2, Spring-8, Japan. SXRD patterns were collected in collaboration with Mr Christopher Foo (Oxford University), Dr Tsz-woon Benedict Lo (The Hong-Kong Polytechnic University), Dr Lin Ye (Fudan University), Dr Pu Zhao (Oxford University) and Dr Tatchamapan Yoskamtorn (Oxford University).

$MgCl_2$ data were collected at Beamline I11, Diamond Light Source; detailed beamline information is provided elsewhere.[3] The energy of the incident X-ray flux was set at 15 keV. The wavelength and the 2θ-zero point were refined using a diffraction pattern obtained from a high-quality silicon powder (SRM640c). For the ammonia-free samples, the sample was ground and loaded in a 0.5 mm borosilicate glass capillary and then dried under vacuum at 423 K for 2 hours. High-resolution SXRD data were achieved by using the multi-analyser crystals (MAC) detectors in the 2θ range 2-78° with 0.001° data binning. Each MAC pattern was collected for an hour to get good statistics.

All other SXRD data were collected at Beamline BL02B2, Spring-8, detailed beamline information elsewhere.[4] The energy of the incident X-ray flux was set at 37 keV. The wavelength and the 2θ-zero point were refined using a diffraction pattern obtained from a Si (1 1 1) double-crystal monochromator. For the ammonia-free samples, the sample was ground and loaded in a 0.5 mm borosilicate glass capillary and then dried under vacuum at 423 K for 2 hours. For the ammonia containing samples, the sample was ground and dried under vacuum (180 ^{o}C, 10^{-3} bar) then

cooled to room temperature and exposed to pure ammonia gas (99.9 % purity, BOC) at approximately 400 mbar for 30 minutes. The sample was then placed in a 0.5 mm borosilicate glass capillary and flame sealed. High-resolution SXRD data of all samples were achieved by using the position-sensitive detectors (PSDs) in the 2θ range 2-78° with 0.001° data binning. Each pattern was collected for 120 s to get good statistics. For the *in-situ* ammonia desorption measurements the samples were heated at a rate of 5 K/min and scans carried out every 100 K.

2.3.7. DFT

DFT simulations were carried out by Dr Alberto Roldan, Cardiff University.

Pristine and modified 13X zeolite and ammonia molecules simulations were performed using the Vienna ab initio simulation package (VASP),[5,6] the PBE density functional,[7] and a kinetic energy cut-off of 550 eV. The inner electrons were represented by projector augmented wave (PAW) pseudopotentials.[8,9] For H13X, all Na atoms were assumed to be removed. For La13X, one La atom substituted three Na atoms from the primitive cell. The periodic simulation cells, and all the atoms in them, were allowed to expand and contract freely upon ionic exchange and NH_3 interaction. The Brillouin zone was sampled by a 0.5 Å-1 k-point mesh, which is dense enough to ensure Pulay stress. Long-range dispersion corrections were included by applying Grimme's DFT-D3 method.[10] Ammonia in the gas phase was relaxed in a box of 15 × 15 × 15 $Å^3$ with a single Γ-centred k-point generated through the Monkhorst–Pack method.[11] The optimization thresholds were 10–5 eV and 0.01 eV/Å for electronic and ionic relaxations, respectively. All the calculations were assessed by diagonalizing the numeric Hessian with a 0.05 Å step, rendering no imaginary frequencies. A Hubbard approach correction (DFT + U) using the method of Dudarev et al. was used on the La 4f-orbitals.[12] The parameters were set to Ueff = 7.5 eV, which better reproduce the reduction of La oxides.[13]

2.3.8. Catalytic Testing

The effect of the sorbent on ammonia production was tested in an ammonia production reactor using a commercial catalyst. Activity was determined using a quartz fixed bed micro-reactor. Commercial catalyst (approx. 100 mg, accurately weighed) was placed in a quartz tubular reactor (5 mm internal diameter) sandwiched between quartz wool. If being used, the absorbent (2000 mg, accurately weighed) was placed in the quartz tubular reactor, downstream of the catalyst bed again sandwiched between quartz wool. In the 0 cm distance experiment there was no quartz wool between the catalyst and absorbent beds. Prior to testing, the catalyst was activated at 773K and the absorbent at 673 K, under a linear flow of nitrogen (52 mL/min). During reaction, a 3:1 mixture of H_2 and N_2 was passed through the reactor at a pressure of 50 bar and flow rate of 52 mL/min. The catalyst was at 743 K and the absorbent at 423 K (Note: the absorbent was not heated; this was residual heat from the catalyst portion of the reactor). After the reaction, any ammonia absorbed on the absorbent was desorbed by heating the absorbent to 673 K under flowing nitrogen (52 mL/min). Throughout, the exit gas was passed through an acid trap (concentrated H_2SO_4 solution) and the ammonia production measured by titrating this solution with NaOH solution and methyl red indicator.

2.4. Data Analysis

TOPAS-Academic Version 6 was used to determine structural information from the diffraction patterns, making use of the Rietveld refinement methods in the software.[14] Initial 13X framework structure and sodium positions were based on the Olson Na13X model.[15] Patterns were refined by optimisation of both scale and lattice parameters. A Chebyschev function with 20 coefficients described the background and a Thompson-Cox-Hastings pseudo-Voigt peak function used to describe the peak shape.

During analysis, the quality of the Rietveld refinements of diffraction data was confirmed by low values of goodness-of-fit (GOF, χ^2) and R factors (R_{wp}, R_p, R_{exp}) and a well fitted pattern with acceptable B_{eq} within experimental errors. The background of these values is discussed in 2.5.3. Furthermore, the determined structure had to make chemical sense and show reasonable errors.

The method used to determine the structure of the zeolites including ammonia has been previously developed in our group.[16–18] First, the unmodified commercial Na13X loaded with ammonia was studied. The 13X starting material is likely to be slightly different to the sample studied by Olson and theoretically the adsorption of ammonia molecules could alter the structure. For these reasons, first, the framework structure of Na13X was determined. As the adsorbed ammonia molecules contain only light elements, they are not expected to contribute significantly to high angle diffraction. Therefore, the high angle region of the diffraction pattern can be used to determine the framework structure. The pattern was initially refined above 30 °. The coordinates (x, y and z) of Al, Si, O and Na were refined. Occupancy of the framework Al, Si and O atoms were fixed at 1, while occupancies of sodium atoms were refined. Isotropic displacement factors (B_{eq}) were allowed to refine with the value of the Al and Si isotropic displacement factors set to be equal and the isotropic displacement factors of the framework O atoms set at twice this while B_{eq} of sodium were set as equal to each other and allowed to refine freely.

Next, this structure used as a basis for the whole pattern refinement containing ammonia. The structures were determined by refining the patterns in areas with significant peaks generally around 5-60 °. Specific ranges for each pattern are listed with the relevant results. The ammonia positions were determined by comparing the observed Fourier electron density map with the one calculated from the refined structure. Discrepancies between the two show where there is additional electron density as a result of the adsorbed ammonia molecules. Only the position of

the N atoms in ammonia were determined due to protons being unable to be visualised by SXRD. Nitrogen atoms were positioned according to this and their exact positions calculated by repeatedly allowing the x, y and z and occupancy parameters to refine, while the framework species were fixed (so called simulated annealing). The R_{wp} value was used to judge the quality of the refinement. The R_{wp} value decreased when ammonia molecules were added indicating a better fit. Additional ammonia molecules were added in the above described way until R_{wp} increased on addition, indicating the quality of refinement was worsening and so no additional ammonia were necessary.

After the position and occupancies of the nitrogen atoms of ammonia had been determined, the previously fixed framework parameters were also allowed to refine. This ensures a global minimum in the refinement fit has been achieved. All atoms had coordinates (x, y and z) refined. Occupancy of the framework Al, Si and O atoms were fixed at 1, while occupancy of sodium and nitrogen atoms were refined. Isotropic displacement factors (B_{eq}) were allowed to refine with the value of the Al and Si isotropic displacement factors set to be equal and the isotropic displacement factors of the framework O atoms set at twice this. Occupancies and isotropic displacement factors were always refined independently of each other as they are correlated.

The room temperature (298K) Na13X-NH_3 refinement was used as a starting point for the higher temperature refinements. The determined Na13X framework structure was used as a starting point for the other ion exchanged refinements, following the above procedure.

Indexing of XRD patterns was carried out using the method developed by A. A. Coelho.[19] The accuracies of indexing was judged using the calculated de Wolff figure of merit, M_N, the origin of which is discussed in 2.5.3.

2.5. Theoretical Background

2.5.1. Intelligent Gravimetric Analysis

One of the most commonly used techniques in this thesis is the study of sorption/desorption isotherms, collected using intelligent gravimetric analysis. This technique exploits the fact that when a material adsorbs or absorbs a gas its weight changes. As discussed previously absorption is a bulk process and adsorption is a surface process, which can be further split into physisorption and chemisorption processes. Physisorption is a long range, weak interaction due to van der Waals type interactions.[22] This bonding is characterised by change in electron density in the adsorbing molecule and the adsorbate separately. During physisorption the free gas is in equillibrium with the adsorbate layer. [22] Chemisorption is a much stronger interaction. In contrast to physisorption, chemisorption is characterised by an exchange of electrons between the adsorbate and adsorbent and so can be understood in terms of traditional covalent or ionic bonding interactions.[22] Each of these processes can be studied using IGA though they cannot be easily differentiated using this technique alone.

An isotherm generated on the IGA gives capacity information and shows how this changes with pressure while also giving more information on the material.

Different isotherm shapes are characteristic of different types of materials. Brunauer, Denning, Denning and Teller initially classified adsorption isotherms into five different types.[20]

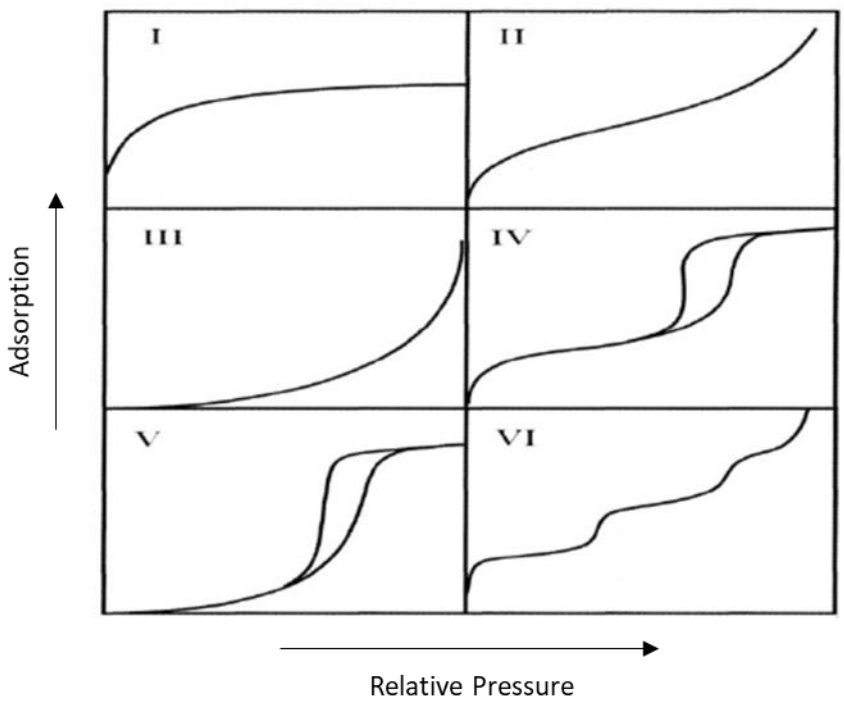

Figure 2-2: The five types of isotherm, classified by Brunauer, Denning, Denning and Teller.[21]

Type I isotherms occur when adsorption is limited to a few layers; this can be chemisorption (when the asymptote is a result of the limited number of sites being filled) or physisorption in microporous materials (where the filling of the pores is the limiting factor).[22] These isotherms are most commonly seen here and are typical for zeolites.

Type II isotherms occur when adsorption takes place on non-porous materials or materials with very large pores, where unrestricted multiplayer adsorption can take place.[22] The characteristic shape occurs because monolayer adsorption occurs first, followed by further layer filling at higher pressures.

Type III isotherms occur when there is multilayer formation at all pressures due to initial adsorption facilitating further adsorption as the interaction between gas molecules is more favourable than interactions between gas molecules and the surface.[20] This is a relatively uncommon case and is not often seen.[22]

Type IV isotherms are typical of materials with pores of sizes between 15-1000 Å; at these pore size multilayer adsorption and capillary condensation both occur leading to this isotherm shape.[22]

Type V isotherms were the final type identified initially. They are similar to type IV but also show the same effect as in type III where initial adsorption promotes further adsorption due to strong interactions between gas molecules.[20] Similarly to type III, this is an uncommonly seen isotherm.[22]

Further work on isotherms has allowed an additional type of isotherm to be identified. Type VI isotherms show a number of steps, caused by stepwise adsorption onto a well-defined non-porous surface; the height of the steps is proportional to the capacity of the layers.[22]

2.5.2. X-Ray Diffraction

X-ray diffraction is one of the most commonly used materials characterisation techniques, giving important structural information about crystalline, bulk materials.

XRD exploits the fact that the distance between repeating units of crystalline materials is similar in magnitude to the wavelength of X-rays. This means that when a material is exposed to a beam of X-rays, the electron cloud of the atoms in the material causes scattering giving a diffraction pattern.[23]

This principle was studied by William Lawrence Bragg and William Henry Bragg, who proposed Bragg's Law to explain the phenomena.

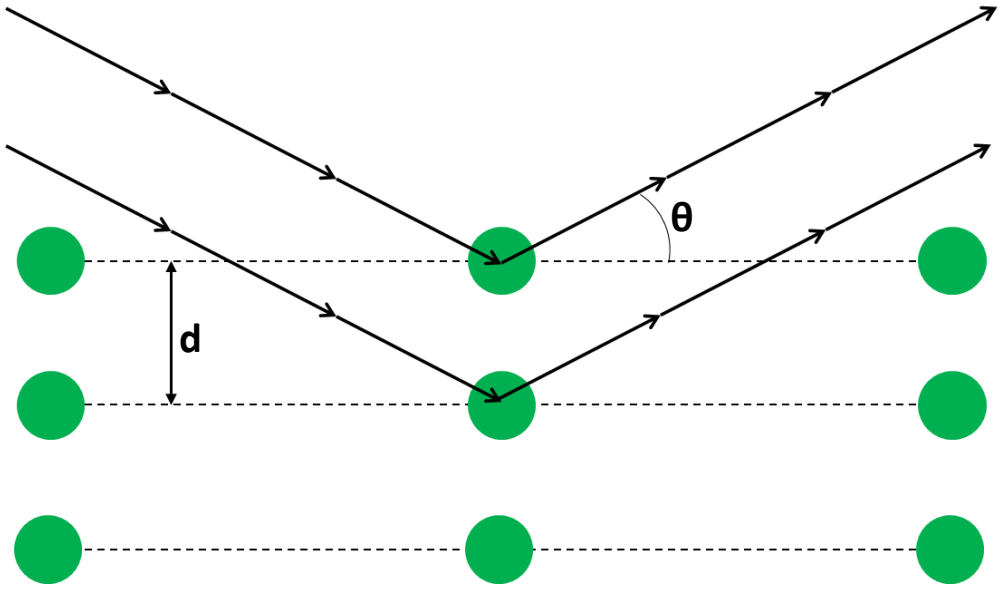

Figure 2-3: Schematic of induced diffraction of an X-ray beam, demonstrating Bragg's Law, adapted from [23].

Bragg's Law can be represented in the following form;

$$n\lambda = 2d\sin\theta \qquad \text{(Equation 21)}$$

where n is an integer, λ is the wavelength of the incident radiation, d is the spacing between the layers and θ is the incident angle of the X-ray beam.[23]

When Bragg's law is satisfied (i.e. when the wavelengths of the incident X-rays are of a similar magnitude to the interplanar spacing) interference occurs and intense peaks are generated at certain angles leading to a diffraction pattern. X-Ray diffraction patterns are characteristic of the unit cell causing the diffraction. The angle of incident radiation can cause constructive interference (where reflections combine in phase and so increase in intensity) or destructive interference (where reflections combine out of phase and so cancel each other out). This causes certain reflections to be missing, known as systematic absences.

During XRD, the X-rays are scattered by the electron density of the atoms within the structure. This means that heavy elements (with greater electron density) strongly scatter electrons while light elements do not.[24] Hydrogen, which has almost no electron density, does not scatter X-rays in any significant way and so the location of hydrogen atoms cannot be determined using X-ray diffraction.[24] For this reason, only the location of the nitrogen atom in ammonia molecules is studied here. Furthermore, there is a decrease in scattering factor as the 2θ angle increases.[24] This can be exploited as it means that at high angles the main contribution to the diffraction pattern will be from heavier elements.

Single crystal and powder X-ray diffraction are both commonly used to determine structures. Powder diffraction has the main advantage of not needing to synthesise a single crystal of the material being studied, which is very difficult for many non-organic reactions.[23] Powder diffraction also gives a good representative pattern of the bulk structure as many particles are present in the studied sample.[24] Furthermore, this quickens data collection times which can be useful for materials which are unstable under X-ray bombardment.[24]

The main drawback to powder diffraction is that, as all orientations are present simultaneously, there is often overlap of peaks within the pattern meaning that determination of the structure is more difficult.[24] Synchrotron radiation provides one possible solution to this.

Synchrotron radiation has vastly improved the ability to determine structures of materials using X-ray diffraction. Laboratory X-ray radiation is generated by bombardment of electrons to a metal target, commonly copper or molybdenum. In a synchrotron, electrons are generated and significantly accelerated to near the speed of light. Due to the curved nature of the synchrotron, electrons change speed and so release energy tangentially, in the form of high brightness x-rays.[24]

Generally, synchrotrons operate with a booster where the electrons increase in energy before passing on to the main storage ring where they can emit X-rays to beamlines where experiments are carried out.

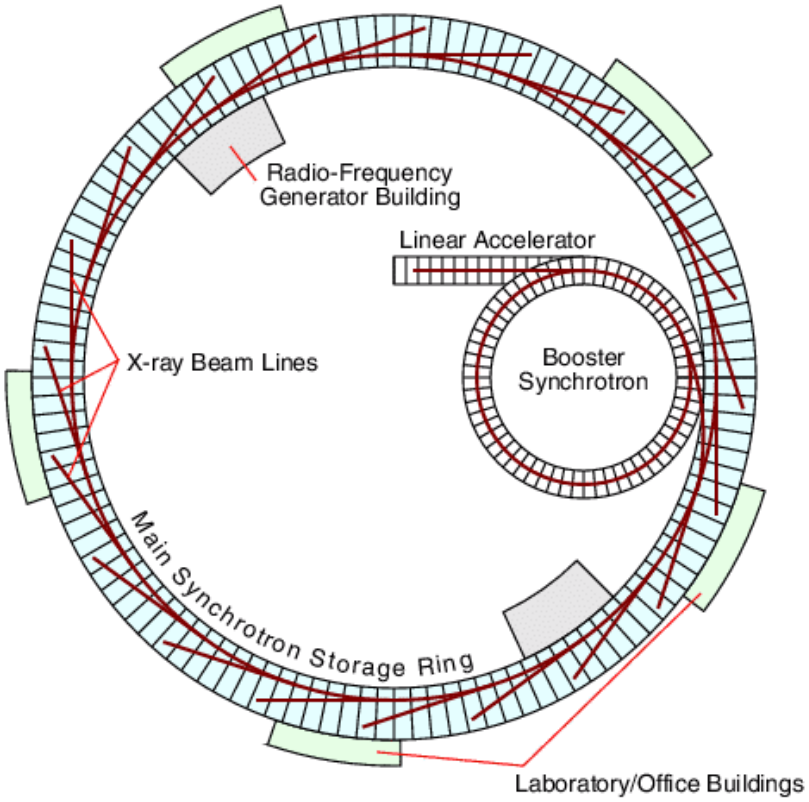

Figure 2-4: Schematic of a typical synchrotron.[25]

Initially, synchrotron radiation was only a by-product of experiments in particle accelerators. Further research found that bending magnets could be used to accelerate the electrons leading to 2nd generation synchrotron facilities. This has since been developed further, with current 3rd generation facilities using insertion devices; undulators and wigglers.[26]

Synchrotron radiation has a number of significant advantages over laboratory source X-rays. Firstly, the X-rays generated are of high brightness, in the order of 10^5-10^{12} more so than laboratory source X-rays. This allows for much shorter experiments and also gives much higher resolution patterns, as a high signal to noise ratio permits small features in the pattern to be

detected.[26] The low angular divergence of the beam means that high angle data can be collected at good resolution while the horizontally polarised beam means the fall in intensity with high 2θ seen in laboratory experiments can be minimised.[26] Synchrotron radiation gives highly tuneable X-ray wavelength which means it can be tailored to the experiment e.g. to avoid X-ray absorption by samples.[26] Finally there are practical applications; the large synchrotron facilities allow for large experimental set-ups or longer term experiments that simply would not be feasible in a lab setting.[26]

2.5.3. Indexing and Refinement of SXRD Patterns

The advent of synchrotron radiation X-ray diffraction allowed for much more useful information to be derived from diffraction patterns. Refinements, mainly Rietveld refinement, allow for structure determination from high quality synchrotron data.[27]

The first step in structure analysis from a diffraction pattern is generally indexing. This allows the space group and lattice parameters of a structure to be determined from the location of the Bragg peaks in a pattern.[28] The space groups of the zeolites studied here are well known and so these patterns were not indexed. When the space group and lattice parameters were to be determined, the method developed by Coelho was used, which judges the indexing using the de Wolff figure of merit.[19] The de Wolff factor accounts for both peaks that are present which would not be expected from the space group and peaks that missing which would be expected from the space group.[19]

The Rietveld refinement method was developed by Hugo Rietveld and can be used to refine parameters such as unit cell parameters, atomic coordinates, atomic site occupancies and thermal parameters. It is a whole-pattern fitting method which exploits non-linear least-squares

to minimise the difference between the observed peak intensities and those calculated from a model pattern based on a postulated crystal strcuture.[29] When carrying out a Rietveld refinement, it is useful to consider the factors which affect the pattern separately, splitting them into group of parameters. Peak position (θ or d) is determined by the crystallographic lattice, space group symmetry and instrumental factors; integrated peak intensity ($|F_{calc,s,p}|^2 \ Corr_{s,p}$) determined by crystal structure and geometric contributions; peak profile ($\phi_{s,p,i}$) determined by instrument and microstructure factors and the background is determined by instrument and scattering influence.[29]

This method generates R-factors which are used to evaluate the quality of the refinement. However, these must be considered in the context of the chemistry of the material. A low R-value which corresponds to a structure which does not make chemical sense is not a good result. Furthermore, the observed pattern and the calculated pattern must be visually compared; if some peaks are a good fit while some are very poor this suggests a problem with the model, no matter the quality of the R-values. These caveats aside, there are a number of R-values commonly used to assess the quality of Rietveld refinements.

$$R_p = \frac{\Sigma_i |I_o - I_c|}{\Sigma_i I_o} \qquad \text{(Equation 22 [29])}$$

$$R_{wp} = \sqrt{\frac{\Sigma_i w_i (I_o - I_c)^2}{\Sigma_i w_i {I_o}^2}} \qquad \text{(Equation 23 [29])}$$

$$R_{exp} = \sqrt{\frac{n-p}{\Sigma_i w_i {I_o}^2}} \qquad \text{(Equation 24 [29])}$$

$$\chi^2 = \frac{{R_{wp}}^2}{{R_{exp}}^2} \qquad \text{(Equation 25 [29])}$$

where I_o is the experimental Bragg peak intensity, I_c is the calculated Bragg peak intensity, w_i is the weighting coefficient at the i^{th} step (equal to $I_{o,ith}^{-1/2}$), n is the number of observables in the data and p is the number of parameters in the refinement.

R_p (Equation 22 [29]) is the profile R-factor and is the most commonly used agreement factor. It simply measures the difference between the observed and calculated intensities. This has the drawbacks of overemphasising any strong reflections and ignoring the effect of any experimental uncertainties.[29] This leads to the weighted profile R-factor, R_{wp} (Equation 23 [29]). This gives a weight to each data point and is directly related to the function which is minimised by Rietveld refinement (the numerator in R_{wp}).[29] R_{exp} (Equation 24 [29]) is a measure of the expected R-factor for a given number of observable and parameters; the best possible R_{wp} that could be expected.[29] χ^2 (Equation 25 [29]) is goodness of fit and compares the ratio of the squares of R_{wp} and R_{exp}.[29]

There is detailed literature discussing the meaning of these factors and how they should be dealt with, particularly by David[30] and Toby[31]. Bearing in mind the previous comments about the need for a chemically sensible solution, there is not a specific point at which R_{wp} values which become acceptably small, however, an R_{wp} of 12 has been proposed as a rough guideline.[28] Other refined patterns of zeolites containing adsorbed species (also studied at Spring-8) have been published with R_{wp} values of between 8 and 13.[32,33]

Paradoxically, better quality data leads to increasing χ^2 values and an apparently worse refinement. This is because the high resolution data contains a greater number of data points which leads to very low R_{exp} values and so increases χ^2.[31] For this reason, χ^2 should not be the sole means by which the quality of a Rietveld refinement is judged for SXRD and instead the similarity between the observed and calculated patterns should be studied along with the R_{wp} value.

2.5.4. Nuclear Magnetic Resonance

Nuclear magnetic resonance (NMR) can give structural information on the framework of zeolite materials. Solid state ^{27}Al NMR is commonly used to study zeolites and is a bulk technique.[34] NMR exploits the fact that when an external magnetic field is applied, the spin of nuclei with non-zero spins (i.e. unpaired electron) aligns. By subjecting the sample to a radio frequency pulse the alignment of these spins can be reversed and the frequency that is needed to cause this studied. These frequencies are dependent on the distribution of electrons around the nucleus and so the NMR frequencies give important chemical structure information.[34] In solid state NMR these interactions are anisotropic as they depend on the orientation of the sample relative to the magnetic field direction and there is not the continuous movement of solution that is seen in liquid state NMR. To reduce the effects of this a technique known as Magic Angle Spinning is commonly used, which decreases peak broadening effects.[34]

Different coordination environments of aluminium in zeolite structures give different peak positions in the NMR spectra due to different shielding effects[28,35] and so aluminium spectra are typically used to determine the relative ratios of tetrahedral and octahedral aluminium. Framework aluminium tetrahedrally bound to oxygen atoms while extra-framework aluminium are octahedral. As these peaks are present in different positions (four coordinate at 60 ppm and six coordinate at 0 ppm), the Al NMR spectra can be used to study Lewis acidity in a zeolite.[36] For example, Bokhoven *et al.* used Al NMR to compare the acidity of two zeolites; H-USY zeolite showed more extra-framework aluminium, as was shown by an additional peak at 0 ppm, than Na-Y zeolite.[37]

2.5.5. Thermogravimetric Analysis

Thermogravimetric analysis (TGA) and differential thermogravimetric analysis (DTGA) can be used to determine the desorption energy of molecules adsorbed or absorbed in a material, such as ammonia on zeolite.

Desorption of ammonia from a zeolite is a first order process.[27] The desorption energy for ammonia desorbed from the zeolites were calculated according to the following equation[38], which is a modified form of the Arrhenius equation which assumes first order desorption:

$$2\ln T_m - \ln\beta = E_{des}/RT_m + \ln E_{des}/AR \qquad \text{(Equation 26[38])}$$

where T_m is the temperature giving maximum desorption in the differential thermogravimetric analysis curve, β is the temperature ramp rate, E_{des} is the desorption energy and A is a constant.

Varying the heating rate a material is exposed to and plotting ($2\ln T_m - \ln\beta$) versus $1/T_m$ for the series of β values allows for the determination of E_{des}.

2.5.6. N_2 Physisorption

N_2 physisorption was used to determine the surface area of the samples.

The N_2 physisorption isotherms are modelled using BET theory, named for Brunauer, Emmett and Teller.[22] This theory is based on the Langmuir theory of monolayer adsorption, expanded to explain multilayer adsorption also. This considers molecules adsorbing on well-defined sites on the surface (one site per molecule) and then adsorbed molecules going on to provide adsorption sites for further molecules. The final adsorbed layer is considered to be in equilibrium with the gas phase.

There are a number of underlying assumptions: the Langmuir model applies to each layer; the gas molecules adsorb in layers infinitely; gas molecules can only interact with adjacent layers; the first gas molecule layer has constant enthalpy of adsorption, which is higher than that of later layers and the enthalpy of adsorption for layer two and beyond is equal to the energy of liquefaction.[22]

This leads to the following equation:

$$\frac{P}{V(P_o - P)} = \frac{1}{V_m C} + \frac{(C-1)P}{V_m C P_o} \qquad \text{(Equation 27[22])}$$

where V is the volume of gas adsorbed at pressure P, V_m is the monolayer adsorption volume, P_o is the pressure at which the material is saturated with adsorbate and C is the BET constant.[22]

Plotting of P/P_o against $1/V[(P_o/P)-1]$ gives a straight line with intercept I and slope A which can then be used to calculate the monolayer adsorption volume. This only holds in the linear region of the graph, at low P/P_o volumes (between 0.05 and 0.35).[22]

$$V_m = \frac{1}{A + I} \qquad \text{(Equation 28[22])}$$

From the monolayer adsorption volume the total surface area can be calculated.[22]

$$S_{total} = \frac{V_m N s}{V} \qquad \text{(Equation 29[22])}$$

where S_{total} the total surface area, N is Avogadro's constant and s is the adsorption cross section of the adsorbing species.[22]

Finally, the BET surface area is simply the total surface area divided by the mass of adsorbent.[22]

2.6. References

1. M. Drezdzon, *Inorg. Chem.,* 1988, **27**, 4628-4632.

2. E. Lopez-Salinas and Y. Ono, *Microporous Mater*., 1993, **1**, 33-42.

3. S. P. Thompson, J. .E. Parker, J. Potter, T. P. Hill, A. Birt, T. M. Cobb, F. Yuan and C. C. Tang, *Rev. Sci. Instrum*., 2009, **80**, 075107-075117.

4. S. Kawaguchi, M. Takemoto, K. Osaka, E. Nishibori, C. Moriyoshi, Y. Kunota, Y. Kuroiwa and K. Sugimotoet, *Rev. Sc.i Instrum*., 2017, **88**, 0851111-0851119.

5. G. Kresse and J. Furthmüller, *Comput. Mater. Sci*., 1996, **6**, 15-50.

6. R. A. Vargas-Hernández, *J. Phys. Chem. A*., 2020, **124**, 4053-4061.

7. J. P. Perdew, K. Burke and M. Ernzerhof, *Phys. Rev. Lett*., 1996, **77**, 3865-3868.

8. P. E. Blöchl, *Phys. Rev. B*., 1994, **50**, 17953-17979.

9. D. Joubert, *Phys. Rev. B. – Condens. Matter. Mater. Phys*., 1999, **59**, 1758-1775.

10. S. Grimme, J. Antony, S. Ehrlich and H. Krieg, *J. Chem. Phys*., 2010, **132**, 154104-154123.

11. H. J. Monkhorst and J. D. Pack, *Phys. Rev. B*, 1976, **13**, 5188-5192.

12. S. Dudarev and G. Botton, *Phys. Rev. B – Condens. Matter. Mater. Phys*., 1998, **57**, 1505-1509.

13. B. Li and H. Metiu, *J. Phys. Chem. C*, 2010, **114**, 12234-12244.

14. J. S. O. Evans, *Materials Science Forum Vol. 651*., Trans Tech Publications, Ltd., Switzerland, 2010.

15. D. H. Olson, *Zeolites.,* 1995, **15**, 439-443.

16. L. Ye, B. T. W. Lo, J. Qu, I. Wilkinson, T. Hughes, C. A. Murray, C. C. Tang and S. C. E. Tsang, *Chem. Commun.,* 2016, **52**, 3422-3425.

17. B. T. W. Lo, L. Ye, J. Qu, J. Sun, J. Zheng, D. Kong, C. A. Murray, C. C. Tang and S. C. E. Tsang, *Angew. Chemie Int. Ed*., 2016, **55**, 5981-5984.

18. W-C. Lin, L. Ye, S. Wu, B. Lo, Y-K. Peng, P Zhao, I. McPherson and S. C. E. Tsang, *ChemSusChem*., 2018, **11**, 4214-4218.

19. A. A. Coelho, *J. Appl. Crystallogr*., 2003, **36**, 86-95.

20. S. J. Gregg and J. Jacobs J., *Trans. Faraday Soc.,* 1948, **44,** 574-588.

21. Z. A. Alothman, *Materials,* 2012, **5**, 2874-2902.

22. G. Attard and C. Barnes, *Surfaces*, Oxford University Press, 2011.

23. M. T. Weller, *Inorganic Materials Chemistry*, Oxford University Press, 2011.

24. W. Clegg, *X-Ray Crystallography,* Oxford University Press, 2015.

25. How do Synchrotrons Work?, http://pd.chem.ucl.ac.uk/pdnn/inst2/work.htm (accessed August 2020).

26. H. Cheng, C. Lu, J. Liu, Y. Yan, X. Han, H. Jin, Y. Wang, Y. Liu and C. Wu, *Prog. Nat. Sci. Mater. Int*., 2017, **27**, 66-73.

27. L. Ye, B. T. W. Lo, J. Qu, I. Wilkinson, T. Hughes, C. A. Murray, C. C. Tang and S. C. E. Tsang, *Chem. Commun.,* 2016, **52**, 3422-3425.

28. B. T. W. Lo, L. Ye and S. C. E. Tsang, *Chem.,* 2018, **4**, 1778-1808.

29. R. E. Dinnebier, A. Leineweber and J. S. O Evans, *Rietveld Refinement*, Walter de Gruyter GmbH, Berlin, 2019.

30. W. I. F. David, *J. Res. Natl. Inst. Stand. Technol*., 2004, **109**, 107-123.

31. B. H. Toby, *Powder Diffr*., 2006, **21**, 67-70.

32. T. Chen, C. K. T. Wun, S. J. Day, C. C. Tang and T. W. B. Lo, *Phys. Chem. Chem. Phys*., 2020, **22**, 18757-18764.

33. A. F. Gualtieri, S. Ferrari, E. Galli, F. di Renzo and W. van Beek, *Chem. Mater*., 2006, **18**, 76-84.

34. P. Atkins, T. Overton, J. Rourke, M. Weller and F. Armstrong, *Inorganic Chemistry (5th ed.),* Oxford University Press, Oxford, 2010.

35. P. V. Wiper, J. Amelse and L. Mafra, *J. Catal*., 2014, **316**, 240-250.

36. E. G. Derouane, J. C. Védrine, R. Ramos Pinto, P. M. Borges, L. Costa, M. A. N. D. A. Lemos, F. Lemos and F. Ramoa Ribeiro, *Catal. Rev.,* 2013, **55**, 454-515.

37. J. A. van Bokhoven, A. L. Roest, D. C. Koningsberger, J. T. Miller, G. H. Nachtegaal and A. P. M. Kentgens, *J. Phys. Chem. A,* 2000, **104**, 6743-6754.

38. A. Corma, V. Fornés, F. V. Melo and J Herrero, *Zeolites,* 1987, **7**, 559–563.

3. Modified 13X for Ammonia Adsorption

Ammonia adsorbents are increasingly important materials as their use in industrial applications such as the Haber-Bosch process and transport applications become more widespread. A wide variety of ammonia storage materials have been studied, amongst them metal halides[1–4], borohydrides[5], zeolites[6,7], COFs[8] and MOFs[9–12]. A variety of metal halides have been studied, including magnesium, calcium, strontium and barium chloride and bromide[13]. Magnesium chloride has one of the highest ammonia storage capacities (52 % ammonia, by weight[14]) of the metal chlorides and so is one of the more widely studied and used ammonia absorption materials. Although widely used it is not an ideal material for all conditions. Absorption on magnesium chloride is more favourable at low operating temperatures[13], it exhibits quite poor reversibility of absorption,[13] has slow absorption times[3] and requires relatively high temperatures for the full desorption of ammonia (up to 400 °C[4]) and undergoes decomposition at high temperatures. Each of these deficiencies can cause difficulties for practical applications, e.g. where fast, reversible, stable, low temperature absorption and desorption is necessary for success.

Porous materials are promising candidates for high temperature ammonia adsorption due to their very high surface area, high temperature stability and extremely tuneable surfaces.[15,16] Although, these materials are expected to show lower gravimetric capacity than $MgCl_2$, they generally show good high temperature stability making them they are potential targets for adsorption assisted ammonia catalysis type systems. Faster adsorption rates would also be beneficial, as would more stable adsorption. $MgCl_2$ shows significant change in volume on ammonia absorption, which is not suitable in all applications and zeolites are expected to be superior in this aspect.

3.1. Initial Screening

First, a number of porous materials were screened for ammonia capacity. Initial materials targeted were zeolites, SAPOs and activated carbon, three classes of materials that are well studied in literature. [15,16] ZSM-5 (Si:Al of 19) and 13X (Si:Al of 1.2) were chosen as initial zeolites. There has been significant previous work in our group on ZSM-5 leading to an understanding of the location, number and type of ammonia adsorption sites within the zeolite.[17] 13X was chosen due to its large pore size and significant number of sodium sites, leading to the potential for a high degree of ion exchange.[18] SAPO-34 was chosen due to a good understanding of its structure[19] and activated carbon as a non-zeolite material for comparison, which is commonly used in adsorption processes.[20]

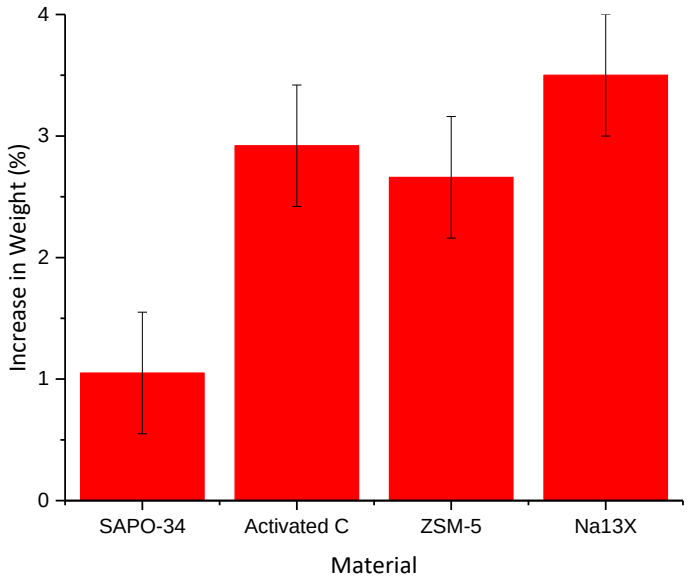

Figure 3-1: Maximum ammonia adsorption capacity measured on a Hidden Isochema IGA-002 using 1000 mbar pure ammonia. Prior to adsorption each sample (approximately 20 mg) was dried at 573 K for eight hours, under vacuum, cooled to 298 K and the initial sample weight accurately recorded. Samples were kept at 298 K and ammonia pressure was increased at 200 mbar intervals, kept at each pressure for 20 minutes and the sample weight recorded.

As is shown in Figure 3-1, each of the porous materials studied showed a relatively low adsorption capacity compared to that of $MgCl_2$. This is to be expected as there are a significantly lower

number of adsorption sites on a gravimetric basis in these materials. Na13X showed the highest capacity with a 3.5±0.5 % increase in weight as a result of ammonia adsorption, compared to 2.9±0.5 % for activated carbon, 2.7±0.5 % for ZSM-5 and 1.1±0.5 % for SAPO-34. This, coupled with the high number of sodium ions present in the structure, meant that Na13X was chosen for further ion exchange studies.

3.2.Ion Exchange of Na13X

Ion exchange is a method used to modify zeolite materials. As discussed in greater detail in the introduction, ion exchange is a process where extra framework ions present in the zeolite (in the case of Na13X, the high number of Na^+ ions) are exchanged with other ions to alter the properties of the zeolite.

4 different ion exchange processes were attempted. H^+ ion exchange was used to generate Brønsted acid sites which should provide a potential strong adsorption site for basic ammonia molecules[21], Mg^{2+} used due to the good capacity of the Mg centre in $MgCl_2$.[1,4,13,14,22], Ni^{2+} used due to the capacity of $NiCl_2$ and to study coordination effects of the transition metal ion and La^{3+} used as it is well known that high coordination environments (of up to 12[23]) are accessible in rare earth elements and so there is a potential for high ammonia adsorption.

3.2.1. Ammonia Adsorption Capacity

Ammonia adsorption desorption isotherms of each of the materials were recorded.

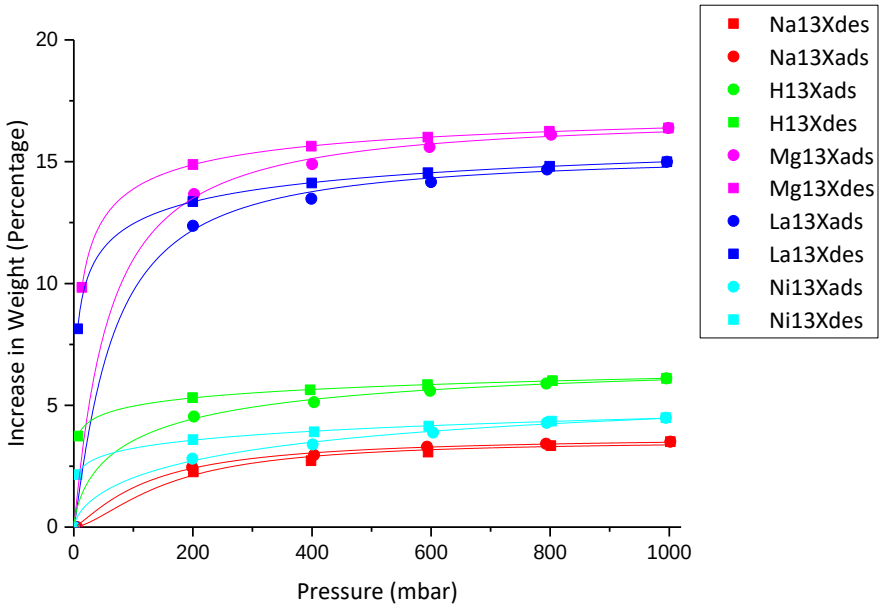

Figure 3-2: Ammonia adsorption isotherms for Na13X, H13X, Mg13X, La13X and Ni13X, capacity measured on a Hidden Isochema IGA-002 using pure ammonia. Approximately 20 mg of sample was placed in the IGA sample chamber, each sample was dried at 573 K for eight hours, under vacuum, cooled to 298 K and the initial sample weight accurately recorded. Adsorption and desorption isotherms were recorded at 298 K by setting the ammonia pressure at 200 mbar intervals, holding at each pressure for 20 minutes and accurately recording the sample weight.

As is clear from Figure 3-2, each of the ion exchange processes has improved the ammonia adsorption capacity of Na13X. Isotherm shape is related to the porosity of the materials and each of the isotherms shows a classic type 1 isotherm, typical of microporous materials such as zeolites[24], indicating that the microporous nature of the zeolites remains in each case.

By comparing the 1000 mbar points of each isotherm the maximum capacity under pure ammonia conditions can be determined. It is important to note that although the ion exchange experiments to synthesise these materials were the same, it is likely that the extent of ion-exchange is different in each material. Each modified zeolite shows a higher capacity than Na13X. Ni13X shows a relatively small increase (5.4 % increase, compared to 3.5 % increase for Na13X) suggesting that the direct coordination effect of transition metal ion with ammonia is not significant. H13X shows a slight improvement (to 6.1 %) indicating that Brønsted acid sites have

been successfully generated, improving the adsorption properties. The highest capacity materials were La13X and Mg13X (15.0 and 16.5 %, respectively) which show good potential for ammonia adsorption materials.

Study of the desorption isotherms of each of the modified samples shows that decreasing pressure alone is not enough to remove the bound ammonia, as is evidenced by the 0 mbar desorption points not reverting to the starting weight of the material. This suggests that there is a relatively strong interaction meaning that the ammonia is not totally desorbed under the standard desorption conditions. Thus, the recyclability of the ammonia over the zeolites was then studied in more detail, as shown in Figure 3-3.

Adsorption capacity is not the only relevant factor in ammonia storage. The rate at which the ammonia adsorbs is also relevant[3], particularly as $MgCl_2$ shows quite slow adsorption (under our typical evaluation it took about 1 hour to reach a steady state, see Chapter 5).

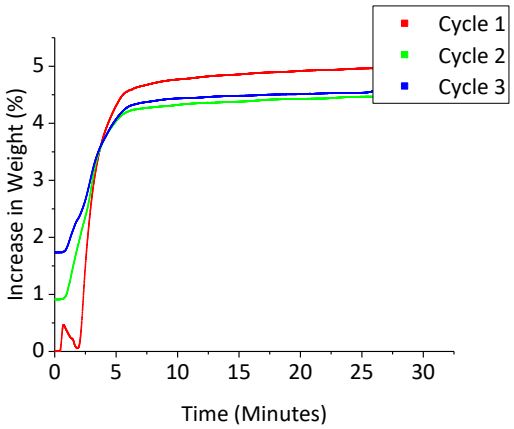

a. Cycles 1, 2 and 3 for H13X.

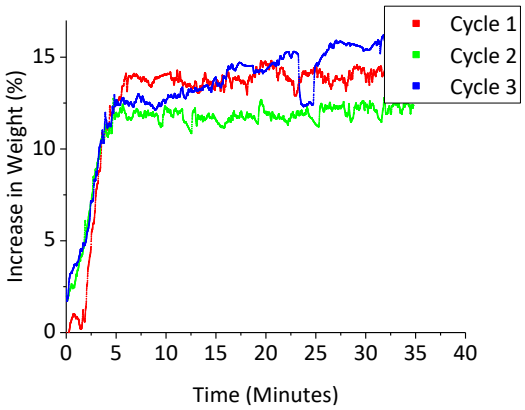

b. Cycles 1, 2 and 3 for La13X. (Apparent noise is due to mispositioned sample holder.)

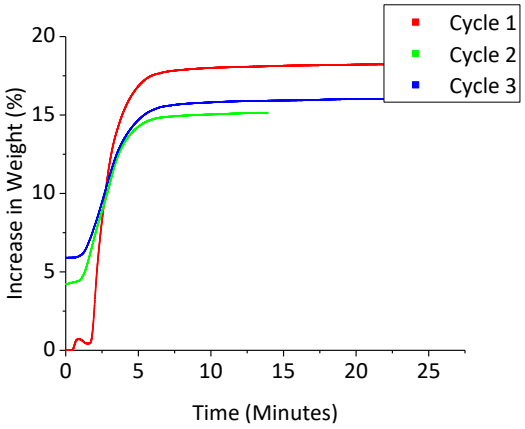

c. Cycles 1, 2 and 3 for Mg13X.

Figure 3-3: Adsorption rate graphs recorded on Hidden Isochema IGA-002 for H13X, La13X and Mg13X. Approximately 20 mg of sample was placed in the IGA sample chamber. Prior to adsorption materials were dried under vacuum at 573 K for 8 hours, and the sample weight accurately recorded at 298 K. For adsorption, pure ammonia gas at 400 mbar was introduced at a rate of 100 mbar/min at 298 K and the pressure kept constant. The weight change in the materials was recorded to track the adsorption. To desorb the ammonia between cycles, the pressure was decreased to vacuum and the temperature increased to 573 K for 8 hours.

It is apparent that the open structure of this modified zeolite gives rapid adsorption. As can be seen from Figure 3-3, each of the ion exchanged zeolites shows a steep slope on approach to the maximum adsorption point. This takes approximately five minutes. There is some decrease in capacity with cycling and some residual ammonia not fully removed by the desorption process used between cycles. Further experiments show that a higher desorption temperature is required to fully remove ammonia (see section 3.2.2).

3.2.2. Desorption Studies

The desorption of each of the above samples was studied to try and understand the nature of the ammonia adsorption and desorption.

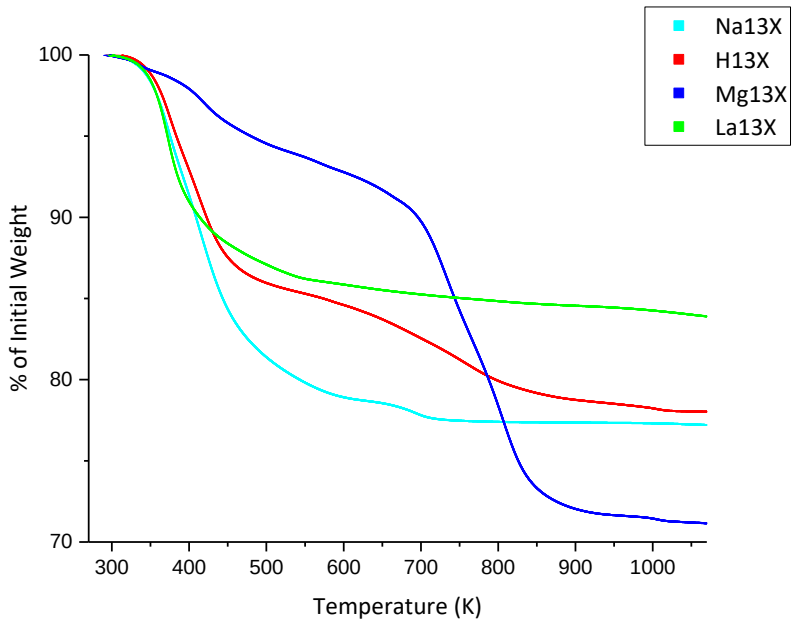

Figure 3-4: Desorption of ammonia on Na13X, H13X, Mg13X and La13X recorded on a TA Instruments Q600 SDT. To load ammonia on H13X, Mg13X and La13X, clean samples were dried for eight hours at 573 K under vacuum, cooled to 298 K then were loaded with ammonia at 400 mbar at 298 K until the weight stabilized (around 30 minutes). The samples were flushed with N_2 before being placed in the SDT. To load ammonia on Na13X the zeolite was dried at 453 K under vacuum for 4 hours, exposed to ammonia at approximately 400 mbar for 30 minutes and placed in the SDT. The temperature was increased to 1073 K at a rate of 10 K/min under 100 mL/min flowing nitrogen and the weight change recorded. In each case, approximately 10 mg of sample was used.

As is clear in Figure 3-4, each of the samples shows a different desorption profile indicating different ammonia interactions. La13X shows the simplest desorption pattern, with only one slope indicating one desorption site at low temperature (<470 K) with 15% in weight lost. Mg13X shows three different downward sloping areas; one from room temperature to approximately 470 K; one from 470 K to 720 K and a final one from 720 K to 820 K. H13X shows two desorption sites; room temperature to 470 K and up to around 670 K. Each of these regions on the graphs

corresponds to desorption although it is important to note that sites with very similar desorption energies may overlap and so cannot necessarily be differentiated based on the SDT data alone.

Further study of the desorption patterns can elucidate information on the energies of each of the desorption sites. Through repeating the above experiments with different heating rates, studying the differential thermogravimetric graph and then using the modified Arrhenius equation shown below, the energy of desorption can be calculated.[25]

$$2\ln T_m - \ln\beta = E_{des}/RT_m + \ln E_{des}/AR \qquad \text{(Equation 1}^{25}\text{)}$$

T_m is the temperature at which there is a maximum in the differential thermogravimetric desorption curve, β is the ramp rate, E_{des} is the desorption energy and A is an Arrhenius constant. Plotting ($2\ln T_m - \ln\beta$) against ($1/T_m$) for a particular series of varying heating rates allows for the determination of E_{des}.

The desorption of ammonia from each sample was studied at 1, 5, 7.5, 10 and 20 K/min.

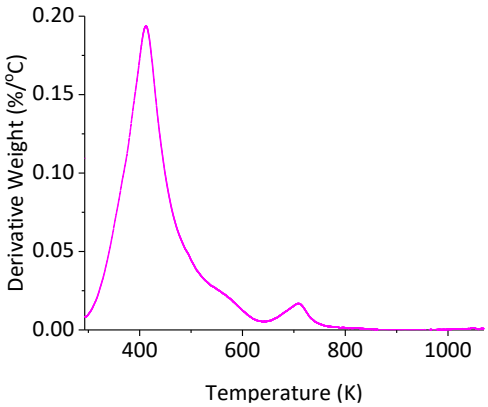

a. Differential thermogravimetric desorption of ammonia on Na13X at 20 K/min heating rate.

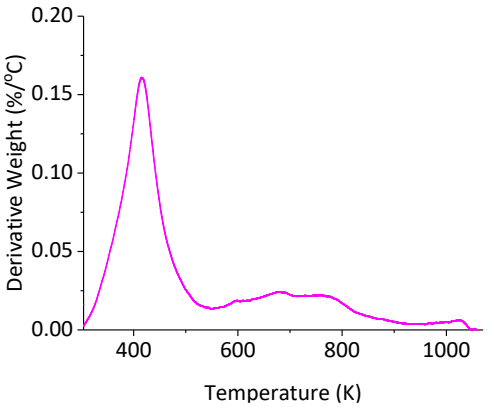

b. Differential thermogravimetric desorption of ammonia on H13X at 20 K/min heating rate.

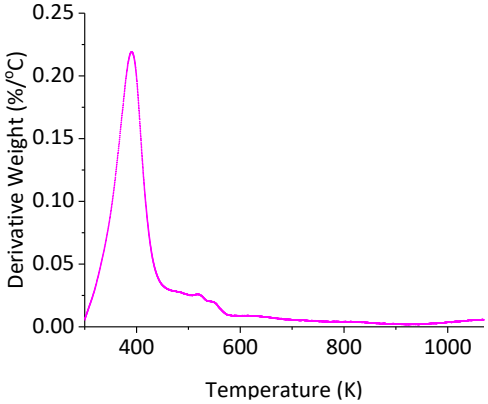

c. Differential thermogravimetric desorption of ammonia on La13X at 20 K/min heating rate.

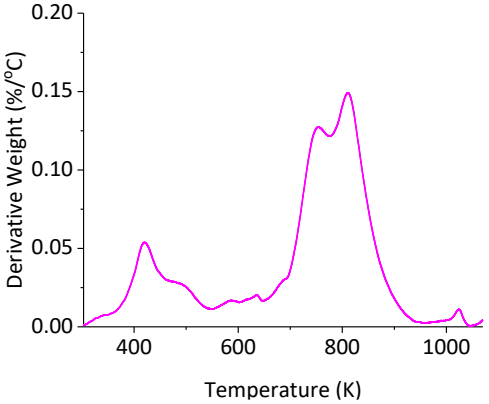

d. Differential thermogravimetric desorption of ammonia on Mg13X at 20 K/min heating rate.

Figure 3-5: Differential thermogravimetric desorption of ammonia from Na13X, H13X, La13X and Mg13X at heating rates of 20 K/min, recorded on a TA instruments Q600 SDT. To load ammonia on H13X, Mg13X and La13X, clean samples were dried for eight hours at 573 K under vacuum at 298 K then were loaded with ammonia at 400 mbar at 298 K until the weight stabilized (around 30 minutes). The samples were flushed with N_2 before being placed in the SDT. To load ammonia on Na13X the zeolite was dried at 453 K under vacuum for 4 hours, exposed to ammonia at approximately 400 mbar for 30 minutes and placed in the SDT. The temperature was increased to 1023 K at a rate of 20 K/min under 100 mL/min flowing nitrogen and the weight change recorded. In each case, approximately 10 mg of sample was used.

The desorption profile of Na13X shows one main, low temperature peak indicative of a weak interaction. The linearization of the peak positions at different heating rates shows the desorption energy of this peak is 1.28 kJ mol^{-1}, confirming this is a very weak interaction. There is also a very small peak at around 700 K. This is probably due to some protonic character in the

commercially available Na13X and only contributes a very small portion of the ammonia storage in Na13X.

As can be confirmed in Figure 3-5.b., H13X has two desorption peaks with the maximum desorption at around 450 K and around 700 K. The linearization of the peak positions at various heating rates gives the desorption energies of these peaks to be 3.29 and 91.98 kJ mol^{-1}, respectively. Comparison of the area under each peak, allows for the relative proportion of ammonia in each site to be estimated; the low temperature peak is 2.5 times the size of the high temperature peak and so 2.5 times as much desorbing ammonia is present in these sites.

According to literature, the strength of the binding sites allows them to be classified into weak, moderate or strong bonds indicative of dispersion, electrostatic or covalent interactions, as was determined by Steiner *et al.*. [26]

Table 3-1: Classification of bond based on bond energies, as determined by Steiner *et al.* [26]

Bond energy (kJ mol^{-1})	**Type of interaction**
< 16	Weak – Electrostatic/dispersion
16 - 63	Moderate – Mostly electrostatic
63 - 167	Strong – Strongly covalent

Comparison of the experimentally determined values with the above Table 3-1, allows the 3.29 kJ mol^{-1} bond to be classed as a weak electrostatic/dispersion type interaction. This is the type of interaction which would be expected when the ammonia is only weakly bound to the zeolite surface without any electron sharing or transfer from the ammonia. In contrast the 91.98 kJ mol^{-1} can be categorized as a strongly covalent bond between adsorbate and solid adsorbent. It has been reported by Ye *et al.*[27] that ammonia adsorption energy on a Brønsted acid site (Al-O(H)-Si) of HZSM-5 is about 113 kJ mol^{-1}. Thus, our measured value is in the same order of magnitude as that of the Brønsted acid site, which is probably generated during the proton ion exchange process with the Na13X (which showed only trace feature in the high temperature region of the

TPD graph). This acid site can, by definition, donate a proton to the ammonia, resulting in an NH_4^+ species which would be expected to have a strong covalent interaction with the newly created O^- species. This NH_4^+ species is clearly a very stable form of ammonia demonstrating that the proton ion exchange process gives an improved, high temperature ammonia adsorbent. This means that H13X is a promising material for use in adsorbent assisted ammonia synthesis applications where the catalyst bed is operating at higher temperatures, where $MgCl_2$ a less viable material.

It is interesting that La13X displays only one, low temperature ammonia desorption, region. The linearization showed the desorption energy of this site was 1.79 kJ mol^{-1}. This is indicative of a weak electrostatic/dispersion interaction i.e. only a surface zeolite interaction, similar to that seen in the parent Na13X material. However, the ammonia capacity in La13X (ca. 15%, see Figure 3-2) is much higher that of Na13X (ca. 3.5%, see Figure 3-2). Thus, there is clearly a dramatic increase in the numbers of weak sites for low temperature ammonia binding (higher desorption peak) meaning that this modified material is very suited to low temperature applications where fast adsorption and desorption can readily taking place and strongly bound ammonia is detrimental. In later section, we will further present evidence for the nature of the sites and explain the increase in the numbers when lanthanide ion is introduced.

From these experiments, it is clear that Mg13X also shows a number of desorption peaks. Similar to La13X there is a low temperature desorption region but the higher temperature peak clearly splits into two very similar peaks. The linearization shows the desorption energy is 9.15 kJ mol^{-1} for the low temperature peak (<470 K) and 83.73 and 108.66 kJ mol^{-1} for the two high temperature peaks (desorption at around 670 K and 770 K, respectively). As would be expected there is still a weak electrostatic/dispersion interaction from ammonia interacting with the zeolite surface (as was seen in other zeolite materials). However, the two high temperature peaks are indicative of some sort of covalent interaction. This desorption peak position and energies of

these high temperature peaks matches well with that of the Brønsted acid site (Al-O(H)-Si) seen in H13X.

In literature, the following reaction is proposed to occur as a result of the polarising nature of the Mg^{2+} ion[28]:

$$Mg^{2+} + H_2O \rightleftarrows Mg(OH)^+ + H^+ \qquad \text{(Equation 2[28])}$$

Through this mechanism, the exchange of magnesium can give strong acid sites which are not seen in the other metal exchanged samples. Therefore, we propose the latter stronger adsorption peaks occur as a result of binding with magnesium hydroxide type species or the simultaneously generated proton. The similar protonic nature of the 'H' for these surface species can cause NH_3 to form the adduct NH_4^+ hence giving a similar desorption regime to ammonia on H13X acid sites. The doubly charged and small size of the Mg^{2+} ion render it extremely polarized to pull the electron density from OH giving to Mg-O(H) with stronger protonic nature than the Al-O(H)-Si site. Na13X should not contain a significant number of Brønsted acid sites however, during the introduction of Mg^{2+} with the liberation of Na^+ during ion exchange of Mg nitrate solution, dissociation of solution water molecules is envisaged to generate terminal OH on Mg^{2+} during the preparation.[28] Interaction with this species, or the simultaneously generated proton would be expected to give the high temperature ammonia desorption species seen in the TPD. This generation of protonic sites has been reported in the case of Zn^{2+} immobilization as Zn-OH on HZSM5[29] which was shown to interact with ammonia as a Brønsted acid site.

In an attempt to understand the reasons for such different desorption behaviour in the modified 13X materials further structural characterisation was carried out.

3.2.3. NMR

Solid state Al NMR is commonly used to study zeolites as it gives valuable information on the coordination environment of the aluminium and shows the presence of extra-framework aluminium sites which generate acidity[30] and so may be useful in ammonia adsorption.

The zeolites were studied without ammonia.

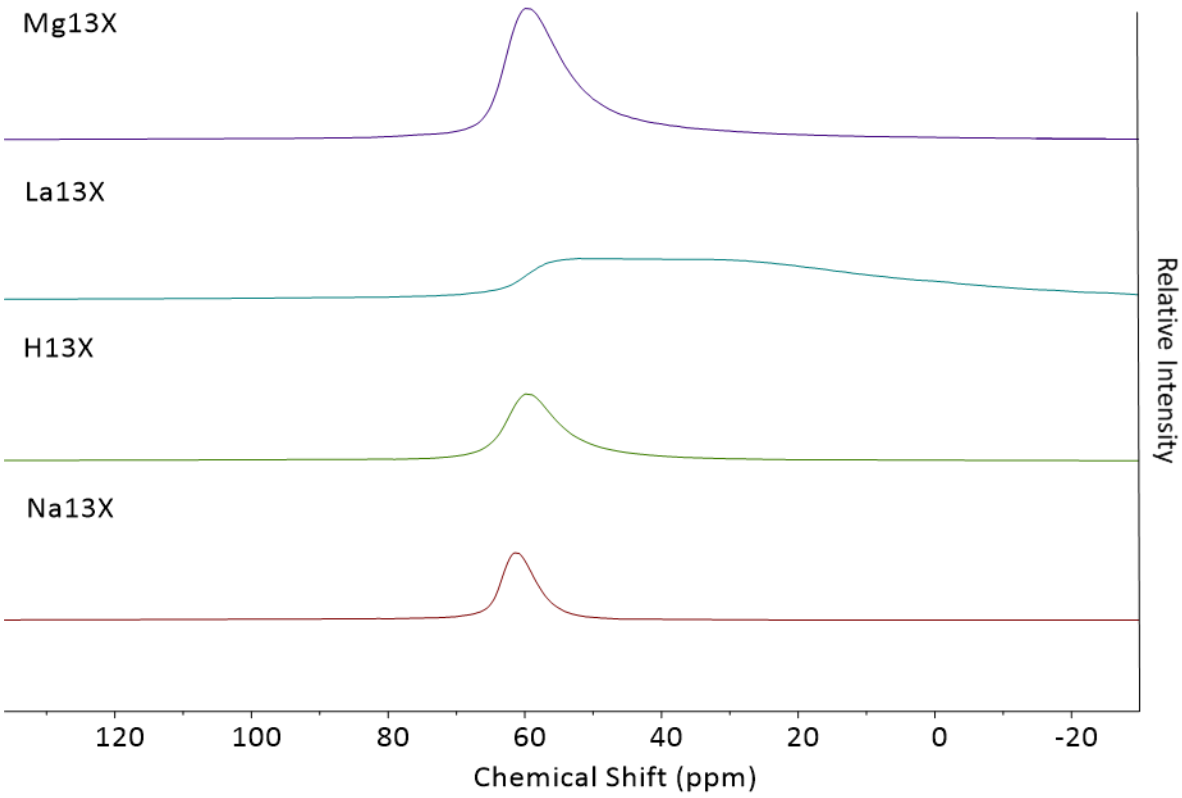

Figure 3-6: ^{27}Al NMR measurements of Na13X, H13X, Mg13X and La13X, recorded on a Bruker AVIII 400 spectrometer, at a Larmor frequency of 104.34 MHz. A one pulse sequence was adopted, with a 10° pulse, a delay time of 0.4 s and a scanning number of 8000. The chemical shift was referenced to an aqueous 1M $AlCl_3$ solution. In each experiment accurately measured 50 mg of sample was used.

As is shown in Figure 3-6, each of the recorded ^{27}Al spectra show only one peak. In the Na13X, H13X and Mg13X this is one sharp peak at around 60 ppm, characteristic of tetra coordinated aluminium.[30] This is typical for a framework alumina species where the aluminium is surrounded by 4 oxygen atoms. None of these samples show extra-framework aluminium species, meaning that any ammonia bonding is through either the framework, the exchanged metal ions or, in the

case of H13X and Mg13X, the generated Brønsted acidity. The NMR spectra also shows that the ion exchange process is mild enough that the general zeolite structure remains.

La13X shows a significantly different ^{27}Al NMR spectra to the other zeolite samples. One broad peak is present, centred around 40 ppm and stretching across the expected values for 4, 5 and 6 coordinated aluminium.[30] This indicates that there are a number of coordination environments present in the La13X sample and so a significant degree of disorder that is not present in the other zeolites. The lanthanum ion exchange process clearly significantly alters the zeolite structure. The ion exchange processes were carried out to be as similar as possible with the metal ion concentration in the exchange solutions chosen so as to allow for complete exchange of the Na^+ ions. However, the ion exchange process appears to be different in different zeolite materials.

In the case of La^{3+}, the ion exchange process does not seem to only liberate three corresponding sodium ions. The tetrahedral aluminium is also somehow liberated to form extra-framework aluminium by the La^{3+} with the dramatic change in coordination environment to 5 (around 30 ppm) and 6 (around 0 ppm)[30], giving structural distortion to create some new Lewis acid sites.

One proposed reason for this drastic difference is that as the exchange process proceeds, the sodium ions are removed and replaced by the new ion. In the case of La^{3+} ion exchange this required three sodium ions to be replaced by one ion. It is possible that the stabilising effect of these ions means that their loss results in a disordered zeolite type material. This effect may be compounded by the fact that each of the exchange processes will be favoured to a different degree. The generation of three sodium ions in solution over one lanthanum ion will be entropically favoured which may account for a greater degree of ion exchange. Furthermore, La^{3+} is a much larger ion than H^+ or Mg^{2+} and so can have a greater disruptive effect.

3.2.4. N_2 Physisorption

BET surface areas, pore volumes and pore diameters were also studied.

Table 3-2: Porosity characterization of Na13X, H13X, Mg13X and La13X, determined using a Micromeritics Tristar-3000. Prior to characterization each sample was dried overnight at 823 K under flowing nitrogen. Samples were then loaded into tubes and further dried at 423 K under vacuum. N_2 adsorption and desorption isotherms were then obtained at 77K.

Sample	Na13X	H13X	Mg13X	La13X
BET Surface area	818.9 m^2/g	510.6 m^2/g	816.2 m^2/g	609.1 m^2/g
t-Plot Micropore Area	730.8 m^2/g	233.2 m^2/g	743.8 m^2/g	544.4 m^2/g
t-Plot External Surface Area	88.0 m^2/g	277.4 m^2/g	72.3 m^2/g	64.7 m^2/g
t-Plot Micropore Volume	0.27cm^3/g	0.10cm^3/g	0.28cm^3/g	0.20cm^3/g
Adsorption Average Pore Diameter (4V/A by BET)	15.8 Å	23.1 Å	16.7 Å	16.9 Å

Using the BET model, the surface areas of each of the modified zeolites were determined and compared to that of the unmodified zeolite. Na13X has a high surface area of 818.9 m^2/g as would be expected from a zeolite. Mg13X resembles Na13X very closely, giving comparable BET surface area of 816.2 m^2/g. The degree of porosity, pore volume and pore size are fairly similar to each other, indicating that the Mg^{2+} ion exchange does not create major structural alterations to the framework.

In contrast, La13X has a lower surface area (609 m^2/g) than the unmodified Na13X zeolite. As previously discussed, it is likely that the introduction of lanthanum ions induces some degree of structural alteration or distortion. The effect of large size and multiple charge of the lanthanum ions may have caused the structural distortion of the parent zeolite. It should be noted that according to structural refinement data (shown later), there is only a relatively low level of lanthanum doping. It is interesting to note that such small doping of lanthanum ions could cause the distortion to give low pore volume (0.20 cm^3/g) but higher average pore size (16.9 Å). This

may be caused by the dealumination process; the extra framework alumina species could block the pores to some degree.

The geometric positions of the lanthanum ions in the zeolite and the original for structural distortion should be further studied.

Unexpectedly, it appears that H13X creates the largest structural changes. It shows the lowest surface area of the modified zeolites at 511 m^2/g. One possible explanation is that the protons are extremely poor at stabilising the zeolite structure. It is anticipated that sodium ions are playing an important role in stabilising this zeolite structure with the high Al to Si ratio and their removal can cause instability. This can be provided by the addition of metal ions in the La13X and Mg13X zeolites but may be difficult in H13X. The substantial losses in internal surface area, pore volume and the dramatic change in pore size, indicate the partial collapse of the crystalline Na13X structure to a more open amorphous form where the disjoint between the amorphous phases alter the defined pore size.

3.3.*In-situ* SXRD Studies

In-situ synchrotron X-ray diffraction studies were used to understand the structure of the unmodified and modified zeolites, how the ammonia interacts with them and how this changes with temperature. Combined with the previously discussed characterisation data this allows for a full picture of the ammonia storage in zeolite materials and how this can be further tailored.

First, the structure of each of the materials, excluding ammonia, were determined. This allowed the structures to be determined before studying the ammonia. Next, the ammonia containing structures were determined and studied as the temperature was increased and the ammonia desorbed.

The structures were determined using Rietveld refinement of the synchrotron data obtained from BL02B2 at Spring-8, Japan.

3.3.1. Refinement of Na13X without Ammonia

Initially, the structure of Na13X was established. Previously, the structure of Na based 13X was determined by Olson[31], whose single crystal zeolite work was ground breaking and crucial to understanding the structures of many zeolites. There are differences between different commercially available Na13X structures, both in the number and location of the sodium ion sites, but Olson's structure is used as a starting point. The position framework atoms were refined, and then the sodium ions added one by one to see if they improved the fitting of the refinement. Finally, any additional sodium sites were located by comparing the observed and the calculated Fourier maps and using any discrepancies as locations possible further sodium sites.

In our commercial Na13X the structure was broadly similar to that of Olson's model. The framework was typical of a faujasite zeolite.[31] Olson's model identifies three broad classes of sodium sites in Na13X; one located in the hexagonal prisms joining the sodalite cages (sites I and I'), one located on the six membered rings on the unjoined hexagonal faces of the octahedra (sites II and II') and one located on the walls of the channels in the supercage and the four ring channels (site III). The sites in the commercial studied sample are closely related to these.

In the Olson model, tetrahedral atom sites are identified as either silicon or aluminium. However, these atoms cannot be differentiated by X-ray diffraction alone, due to their similar size. Instead, the two positions are assigned solely to aluminium or silicon; this minimises Al-O-Al interactions, which are forbidden by Lowenstein's Rule.[32] It is important to emphasise that this is the origin of the tetrahedral atom positions and not any crystallographic finding.

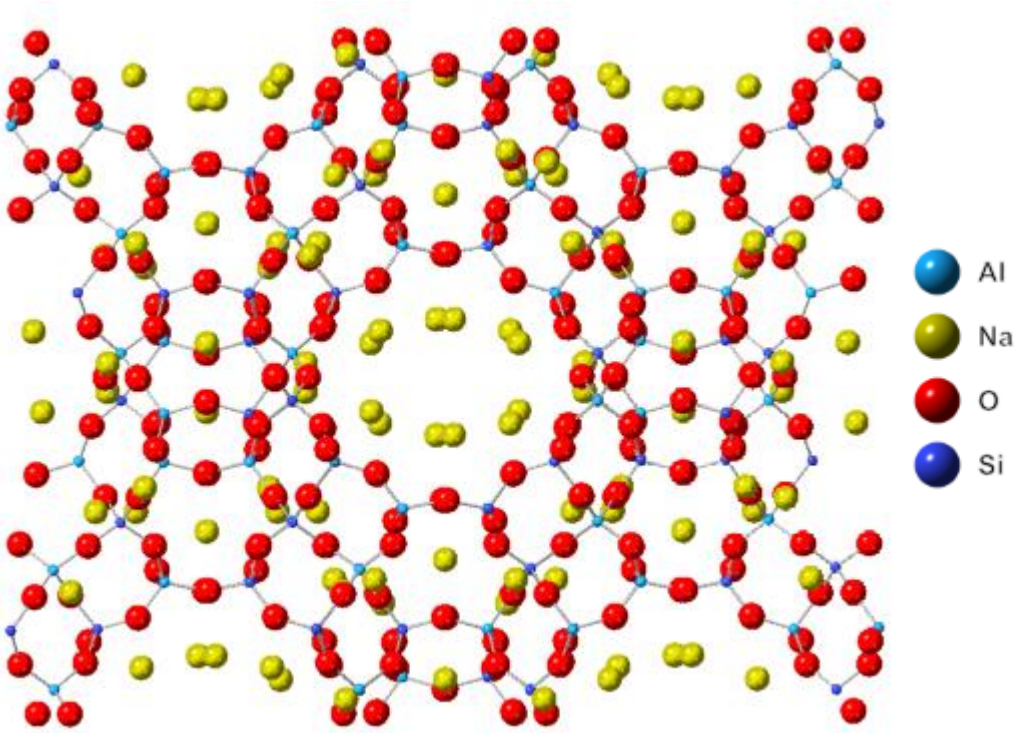

Figure 3-7: Unit cell of Na13X (viewed along 110), as determined by Rietveld refinement of SXRD pattern.

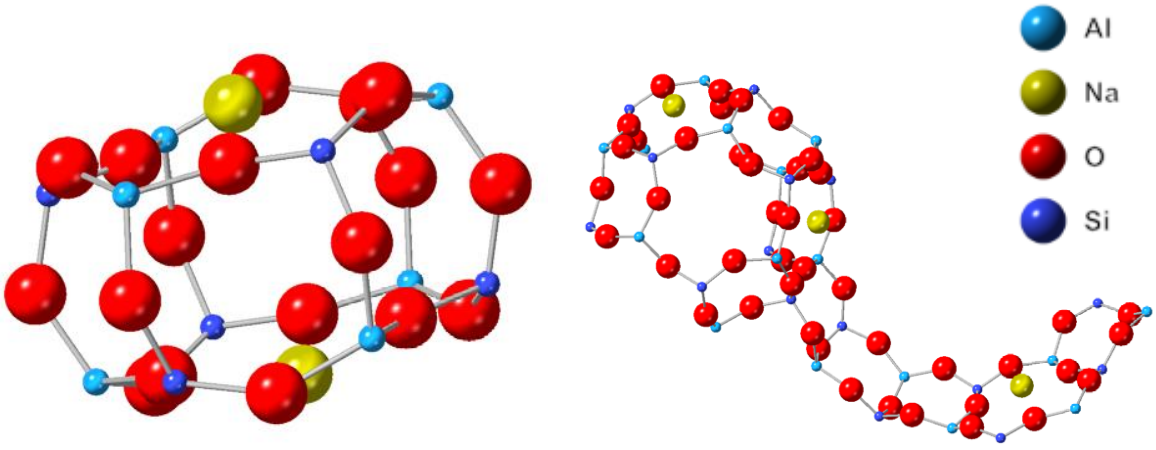

a. Na1, located within hexagonal faces of the prisms which join the sodalite cages.

b. Na2, located in the non-joining hexagonal faces of the sodalite cages.

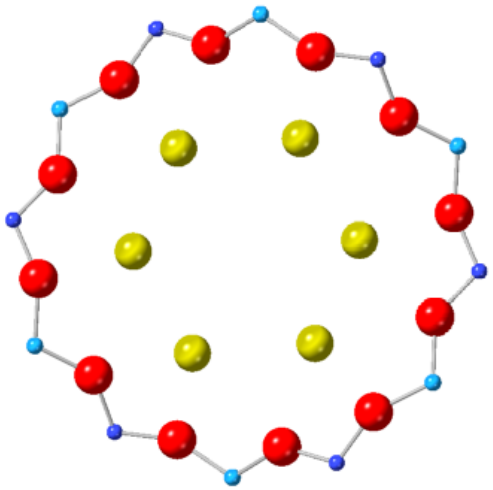

c. Na3, located in the main channel of the zeolite.

Figure 3-8: Locations of the three sodium sites in the commercial, unmodified Na13X zeolite, as determined by Rietveld refinement of SXRD pattern.

There are three sodium sites present in the unmodified Na13X sample. Na1 is located within the faces of the hexagonal faces which form the prisms which join the sodalite cages, a site present in the Olson model. Na2 is also present in the Olson model; the sodium ions are located on the hexagonal faces of the sodalite cages which do not join the cages i.e. the surface of the main pore walls. Finally, there is a third site which is within the main pore of the zeolite.

The occupancy of each of these sites was also determined.

Table 3-3: Occupancies of each Na site, as determined by Rietveld refinement of SXRD pattern.

Site	Occupancy	Equivalent Positions
Na1	0.188(5)	32
Na2	0.301(4)	32
Na3	0.236(10)	96

Each sodium site shows only partial occupancy.

3.3.1. Refinement of Na13X with Ammonia

After the structure of the zeolite framework was established, the location of the ammonia molecules was determined. It is important to note that protons cannot be visualised using XRD and so each ammonia molecule is only shown as a nitrogen atom. The change of the occupancy and location of these sites as temperature was increased was studied *in-situ*.

At room temperature (298K) four ammonia sites were present. All three of the previously identified sodium sites are used in bonding. Both N1 and N4 bind in the main pore of the zeolite, close to the exterior Na3 site. N2 binds to the position closer to the Na2 located on the semi-interior site of the zeolite. Finally, N3 interacts with the interior Na1, a site within the hexagonal prisms which join the sodalite cages.

It is clear the accessibility of the various sites is not a problem, with the ammonia being able to access multiple regions of the zeolite, not just the large main pore of the zeolite. This was expected due to the small size of ammonia. However, one would envisage that a site within the main pore is most easily accessible and so can act as a handling site (gate site) for uptake or download of gaseous ammonia from the macropore and diffusion of the ammonia to and from the other accessible sites.

The ammonia binding was then also studied *in-situ* as the temperature was increased. *In-situ* experiments are extremely useful as they show exactly what is happening in the material as the desorption proceeds and so give useful insights into how the adsorbent works under close to real conditions. The occupancy, binding atom and binding distance of each site were compared at 100 K intervals. By seeing how the occupancy and binding distance of each of the sites changes as temperature is increased, more kinetic information can be gathered on the nature of the binding site.

According to the TPD, the majority of the ammonia is located in sites which desorb below 473 K. (see Figure 3-5), presumably by the weak ion dipole interaction with the Lewis acids as there is no strong protonic site for trapping the ammonia. Although SXRD allows the locations of nitrogen atoms in ammonia to be determined, the precise binding mode to the specific location of the internal surface is not determined. Instead, the nearest atoms are compared although the actual binding site may be the oxygens close to the Na^{+} sites rather than to the cations themselves.

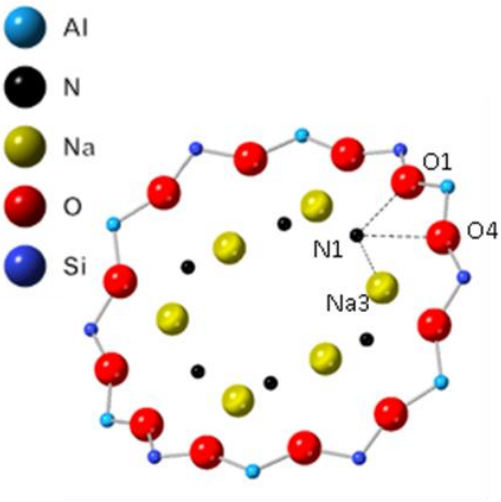

a. Location of N1, in the Na13X zeolite. N1 is closest to Na3, of the main zeolite pore, and is close to O1 and O4.

Temperature	N1 Occupancy	N1 Binding Atom	N1 Binding Distance
298K	0.452(23)	Na3	1.65
373K	0.367(9)	Na3	1.83
473K	0.292(8)	Na3	1.76
573K	0.108(8)	Na3	1.49
673K	0.044(8)	Na3	1.70
773K	0		

b. Occupancy, binding atom and distances (Å) for N1 in Na13X, at increasing temperatures.

Figure 3-9: Site N1, location, occupancy and binding in Na13X, at increasing temperatures, as determined by Rietveld refinement of SXRD pattern.

As can be seen in Figure 3-9, site N1 shows a close interaction with Na3 (less than 2 Å, at all temperature). Single crystal XRD[33], NMR[34] and neutron scattering[35] of ammonia on A type zeolites have shown that cooperative effects between framework oxygen and sodium species can cause very short ammonia sodium bond lengths.

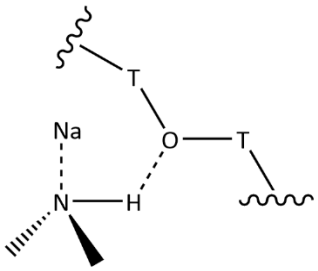

Figure 3-10: Representation of how ammonia orientates to interact with both sodium ions and framework oxygen. Adapted from [35].

As is shown in Figure 3-10 ammonia molecules orientate to interact very closely with sodium ions when nearby oxygen species are also present; a lone electron pair on ammonia interacts with the Na^+ ion and the protons of ammonia interacts with oxygen though the ammonia proton. This

reportedly gives N-Na distances of around 1.8 Å[33] and so interaction can explain the bond distances of less than 2 Å between the ammonia molecules and sodium ions. There is some variation in binding distances although there is not a linear relationship between distance and temperature.

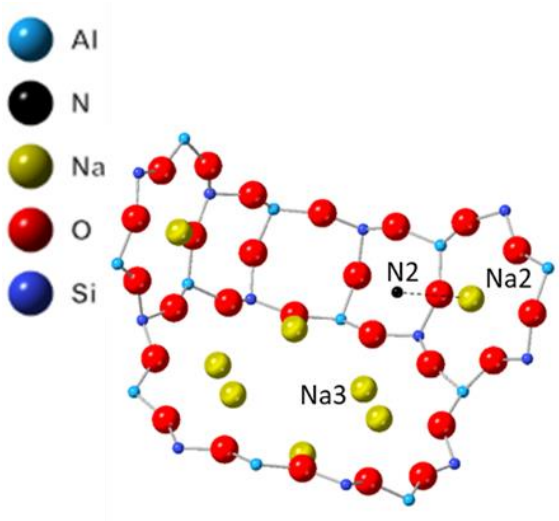

a. Location of N2, located in the main channel of the zeolite, close to both Na2, Na3 and the pore walls.

Temperature	N2 Occupancy	N2 Binding Atom	N2 Binding Distance
298K	0.411(14)	Na2	3.09
373K	0.288(8)	Na2	2.52
473K	0.154(8)	Na2	3.35
573K	0.083(8)	Na2	3.23
673K	0.061(6)	Na2	2.98
773K	0.078(6)	Na2	3.01

b. Occupancy, binding atom and distances (Å) for N2 in Na13X, at increasing temperatures.

Figure 3-11: Site N2, location, occupancy and binding in Na13X, at increasing temperatures, as determined by Rietveld refinement of SXRD pattern.

As can be seen in Figure 3-11, site N2 initially binds to Na2 (semi-interior site) with slightly longer distance compared to those N to Na3 site. Again, this is a weak interaction, probably with both Na and framework oxygen involved.

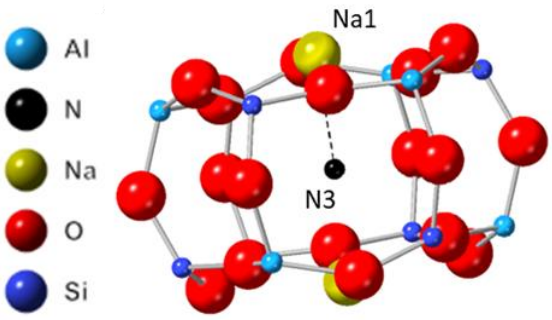

a. Location of N3, located in the centre of the joining hexagonal prism linking the sodalite cage.

Temperature	N3 Occupancy	N3 Binding Atom	N3 Binding Distance
298K	0.168(9)	Na1	2.26
373K	0		
473K	0		
573K	0		
673K	0		
773K	0		

b. Occupancy, binding atom and distances (Å) for N3 in Na13X, at increasing temperatures.

Figure 3-12: Site N3, location, occupancy and binding in Na13X, at increasing temperatures, as determined by Rietveld refinement of SXRD pattern.

As Figure 3-12 shows, site N3 binds with Na2, within the prisms which join the sodalite cages. It shows a low Na-N length of 2.26 Å and is clearly a very weakly bound site shown by the fact it is only occupied at 298K and has completely desorbed by 373K. This is interesting as N3 is also the only site which is in the interior position of the zeolite. It is reported in literature that it is unfavourable for ammonia molecules to be present in this site and that it only occurs to a significant effect at high pressures.[35] The constrained nature of the site, trapped within a very small prisms means it is unfavourable entropically and so easier to desorb than other sites. It is important to consider the fact that N3 is present in the middle of the hexagonal channel, with equidistant Na2 sites on either side and so the binding closer to Na2 is actually binding with two equivalent sodium ions. It should also be noted that the rapid diffusion of N3 to N4 is seen as the increase in the occupancy in N4 from 298K to 373K before the ammonia is desorbed to the gas phase via this gate site.

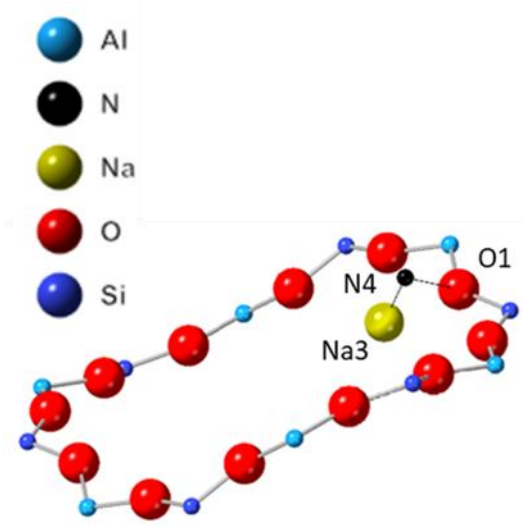

a. Location of N4, located in the main channel of the zeolite, out of plane with the ring.

Temperature	N4 Occupancy	N4 Binding Atom	N4 Binding Distance
298K	0.236(16)	Na3	1.39
373K	0.470(10)	Na3	1.86
473K	0.228(10)	Na3	1.37
573K	0.257(10)	Na3	1.31
673K	0.206(10)	Na3	1.44
773K	0.212(7)	Na3	1.79

b. Occupancy, binding atom and distances (Å) for N4 in Na13X, at increasing temperatures.

Figure 3-13: Site N4, location, occupancy and binding in Na13X, at increasing temperatures, as determined by Rietveld refinement of SXRD pattern.

Similarly to N1, N4 also shows a close interaction with Na3 (less than 2 Å in both cases, at all temperature). This is indicative of interaction with both the sodium ion and the pore wall of the zeolite. Again, there is some variation in binding distances although there is not a linear relationship between distance and temperature.

But Site N4 is somewhat unusual in that it is the only site which does not show a continual decrease in occupancy with increasing temperature and can maintain high degree of occupancy even at 773K. Between 298K and 373 K the occupancy of site N4 actually increases. This is coupled with a decrease in occupancy of all other sites, most significantly site N3. This seems to suggest that ammonia molecules are moving from some of the other sites into N4. Site N4 is acting as a sort of “gate site” which ammonia passes through from other sites before being directly desorbed to the gas phase. This suggests that N4 is a more easily accessible and kinetically more stable site from the others.

3.3.2. Determination of Modified 13X structures

This experiment was repeated with each of the modified zeolites. As discussed previously, each of the zeolites was modified with an aim of fully replacing the sodium ions with the new ion, although this leads to differences in metal ion concentration during the exchange and different entropically favourability in the ion exchange reactions. To establish how much of an effect this has, the sodium ion occupancy of each site was studied.

Table 3-4: Occupancy of sodium sites as determined by Rietveld refinement of SXRD data.

	Na Site 1	**Na Site 2**	**Na Site 3**
Na13X	0.188(47)	0.301(4)	0.236(10)
H13X	0	0.310(5)	0
La13X	0	0.087(4)	0.121(5)
Mg13X	0.135(15)	0	0.242(31)

As is seen in Table 3-4, the sodium occupancy (and so degree of ion exchange) is different in the different prepared zeolites; it is interesting to note that each ion exchange process shows differing loss of sodium sites. Proton ion exchange has caused the complete removal of two of the three sodium sites and had no effect on site two. When the sodium is exchanged for lanthanum, site one ceases to contain sodium while sites two and three both see a partial removal of sodium. Sites Na1 and Na2 are sodalite cage sites and so are near to a high density of oxygen atoms. It is known that rare earth elements, such as lanthanum, preferentially achieve high oxygen coordination[36] and the position of lanthanum ions in these sites allows for this, explaining the preferential ion substitution here. Magnesium ion exchange caused the smallest decrease in sodium occupancies with some sodium remaining in sites Na1 and Na3. Sodium site occupancy is not the only consideration, as ions may also be present in other forms in the structure, offering additional ammonia sites. This explains why Mg13X appears to be the least successful ion exchange process and yet the best ammonia adsorption material.

The locations of the additional ions were also determined. SXRD cannot 'see' protons and so the location of the exchanged protons cannot be directly determined; instead, their presence was indirectly established by looking at the position and strength of the ammonia binding (see 3.4.1).

A number of lanthanum sites were determined, with varying occupancies. The framework structure of the La13X is slightly different to that of the unmodified structure. The bond angles change, bond lengths increase slightly and there is generally a very slight loss of structure. The Na2 site moves slightly further from the pore walls, towards the main pore of the zeolite. This structural change explains why the SS-AlNMR is so different for La13X compared to the other zeolites. However, the space group remains the same and there is not a large change in unit cell parameters.

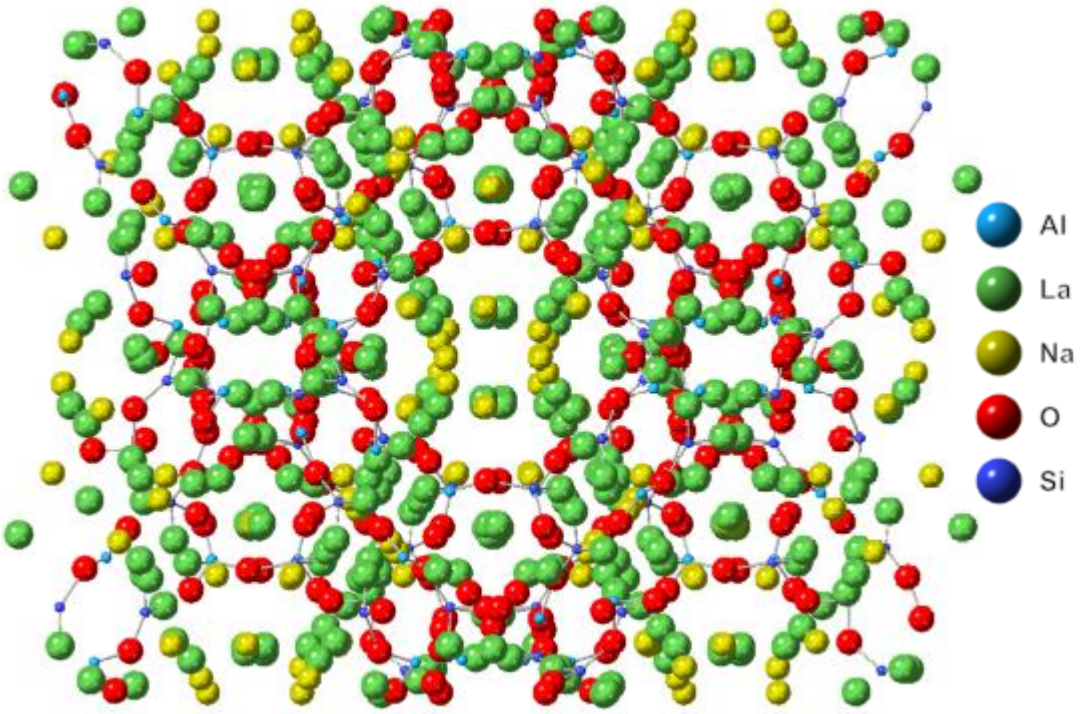

Figure 3-14: Unit cell of La13X (viewed along 110), as determined by Rietveld refinement of SXRD pattern.

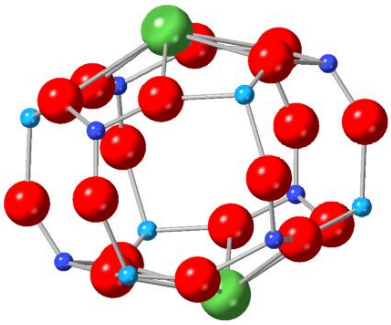

a. La1, located just beyond the hexagonal faces of the prisms which join the sodalite cages.

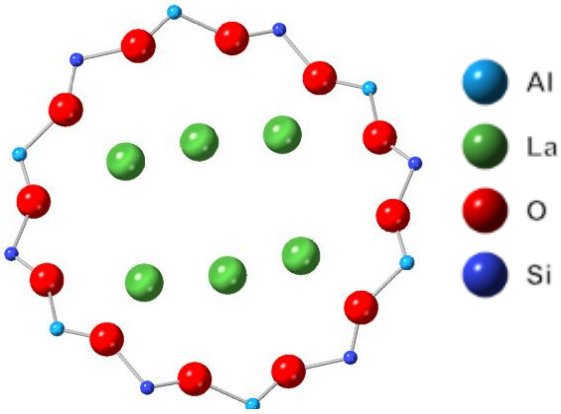

b. La2, located in the main channel of the zeolite.

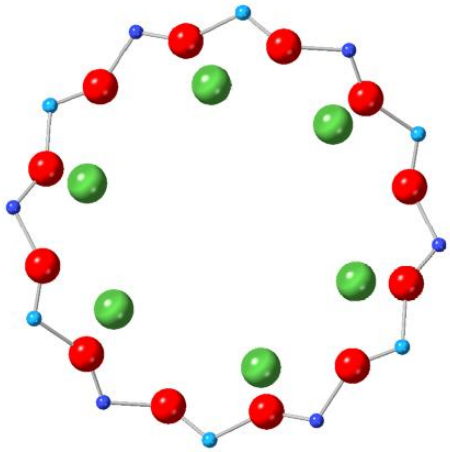

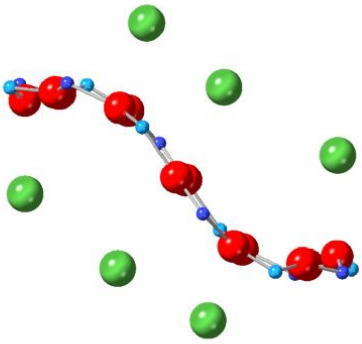

c. La3, located in the main pore of the zeolite, out of the plane of the Al/Si/O ring.

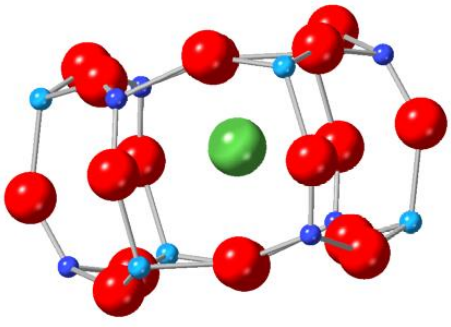

d. La4, located within the joining hexagonal prisms.

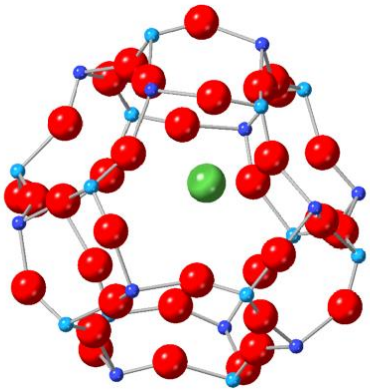

e. La5, located within the sodalite cage.

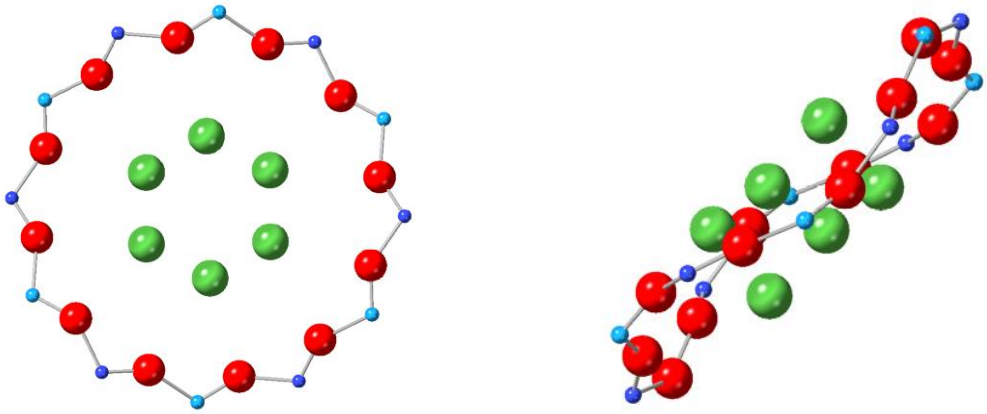

c. La6, located in the main pore of the zeolite, out of the plane of the Al/Si/O ring.

Figure 3-15: Locations of the six lanthanum sites in the La13X zeolite, as determined by Rietveld refinement of SXRD pattern.

The occupancy of each of these sites was also determined.

Table 3-5: Occupancies of each La site, as determined by Rietveld refinement of SXRD pattern.

Site	Occupancy	Equivalent Positions
La1	0.300(0)	32
La2	0.018(1)	96
La3	0.016(0)	96
La4	0.020(1)	96
La5	0.015(1)	96
La6	0.019(1)	96

Six lanthanum sites are present in the La13X unit cell. The highest occupancy site in La1, which is in a roughly similar position to Na1. In the unmodified 13X this was the sodium site where low temperature ammonia bonding occurs. Clearly, the Na ion in the sodalite can be replaced favourably by this rare earth ion due to the high coordination to the nearby oxygen atoms, as is shown by the many near oxygens in the hexagonal face of the sodalite cage, in Figure 3-15.a. Louwen *et al.* used DFT to study the feasibility of La^{3+} ion exchange on zeolite Y[37], which has a very similar structure to 13X. They found that the most stable initial lanthanum ion position is just outside the joining prism of the sodalite cage (equivalent to La1 here), providing this ion is further stabilised by water molecules. If the water molecules were removed, the structure remained the

same, though had a higher energy. This explains why the La1 position here shows the highest lanthanum occupancy.

There are 5 further lanthanum sites present, although each show very low occupancy. Due to the high level of symmetry in the unit cell there are many equivalent positions and so these lanthanum sites each correspond to only 2 La atoms per unit cell. Site La2 is in a very similar position to Na3, while the other lanthanum sites are not direct substitution of any sodium sites.

The magnesium sites generated by ion exchange were determined.

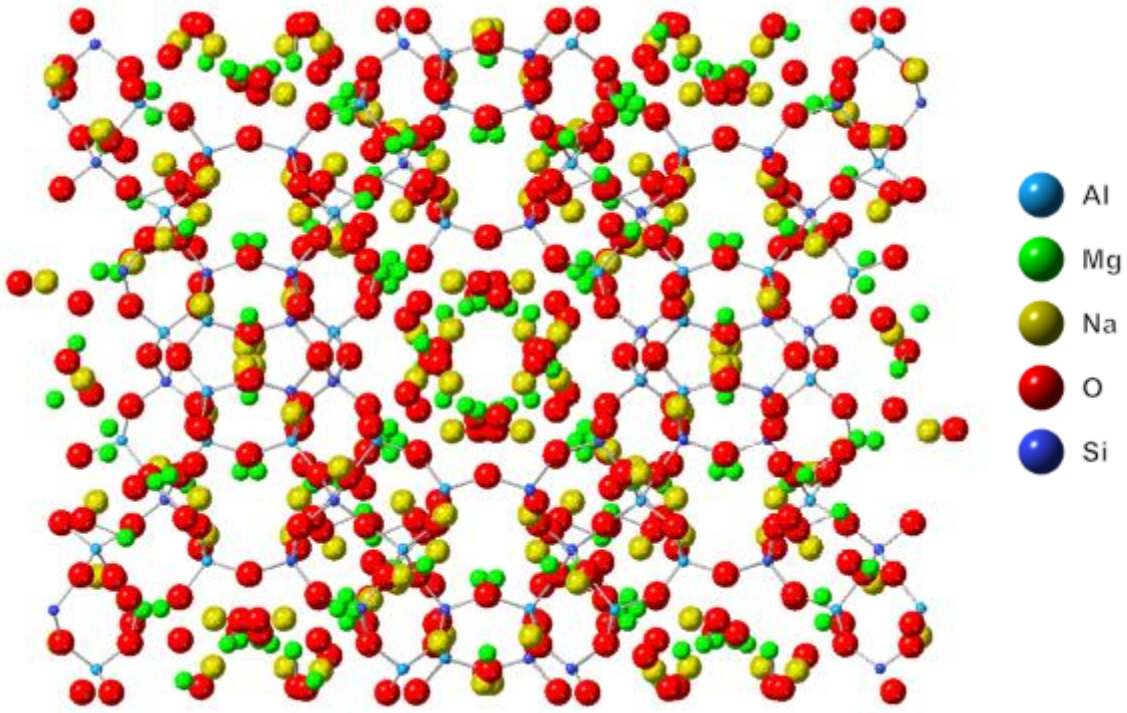

Figure 3-16: Unit cell of Mg13X (viewed along 110), as determined by Rietveld refinement of SXRD pattern.

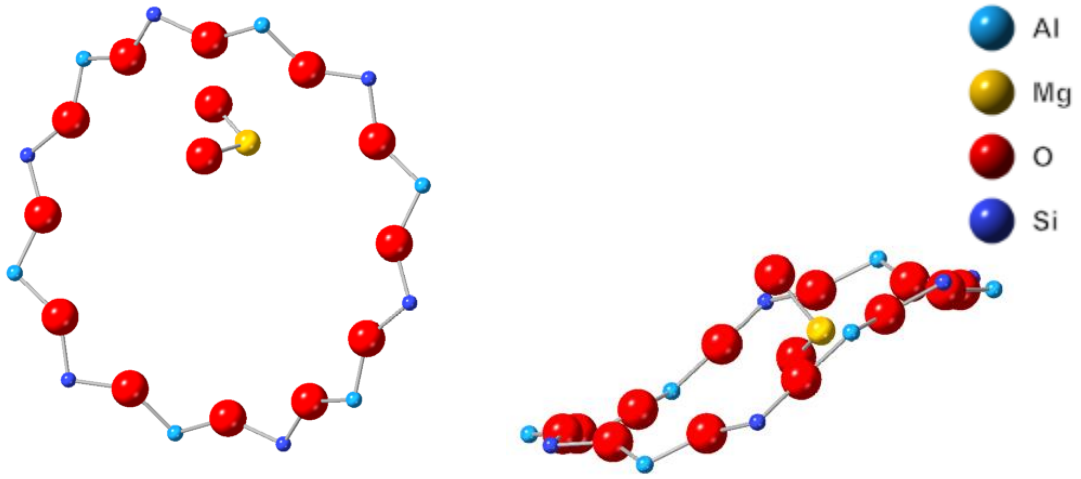

a. Mg1, located in the main pore of the zeolite, binding to two oxygen atoms.

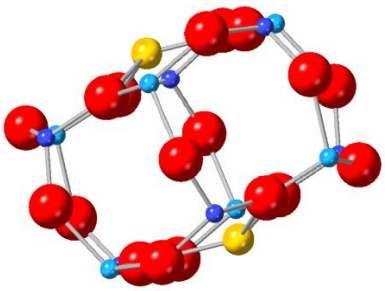

b. Mg2, located within the hexagonal faces of the prisms which join the sodalite cages.

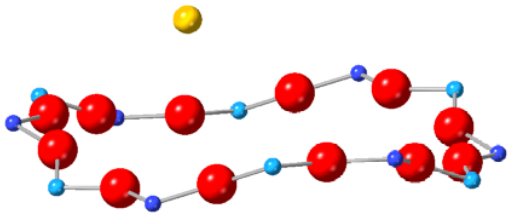

c. Mg3, located within the main pore of the zeolite, out of the plane of the ring.

Figure 3-17: Locations of the three magnesium sites in the Mg13X zeolite, as determined by Rietveld refinement of SXRD pattern.

The occupancy of each of these sites was also determined.

Table 3-6: Occupancies of each Mg site, as determined by Rietveld refinement of SXRD pattern.

Site	Occupancy	Equivalent Positions
Mg1	0.309(20)	96
Mg2	0.188(7)	32
Mg3	0.375(11)	96

There are three magnesium sites present in Mg13X, which show a greater occupancy than the La sites in La13X. Mg1 is located very close to the original Na3 site but given the relevant occupancies of these sites this cannot be strictly an exchange process and instead the magnesium ion is filling some of the vacant sites. Interestingly, Mg1 is binding to oxygen atoms, which was not seen in any of the other materials. This probably accounts for the high temperature storage

which was seen in Figure 3-4, as magnesium hydroxide generation could lead to Brønsted acid type species. As was discussed previously, the polarising nature of the Mg^{2+} ion can split the water used in the synthesis and simultaneously generate magnesium hydroxide species and protons.[28] Furthermore, this generation of protonic sites has been reported in the case of Zn^{2+} immobilization as Zn-OH on HZSM5[29] which was shown to interact with ammonia as a Brønsted acid site. The presence of this hydroxide species suggests protons are probably also formed, although they cannot be visualised using XRD. Again, there is a magnesium site (Mg2) present in the same position as Na1, suggesting that this is a favourable site for exchange. There is a further site, Mg3, within the main pore of the zeolite.

3.4. Ammonia Position Determination

The location of ammonia binding sites in the zeolites, and how this changed over the desorption process, was studied using *in-situ* SXRD. The ammonia binding atoms are established by determining the nearest neighbour.

3.4.1. H13X

First the ammonia sites in H13X were studied, in an attempt to understand the reason for good high temperature stability and to determine to what extent Brønsted acid site formation is important for this.

Five binding sites were identified.

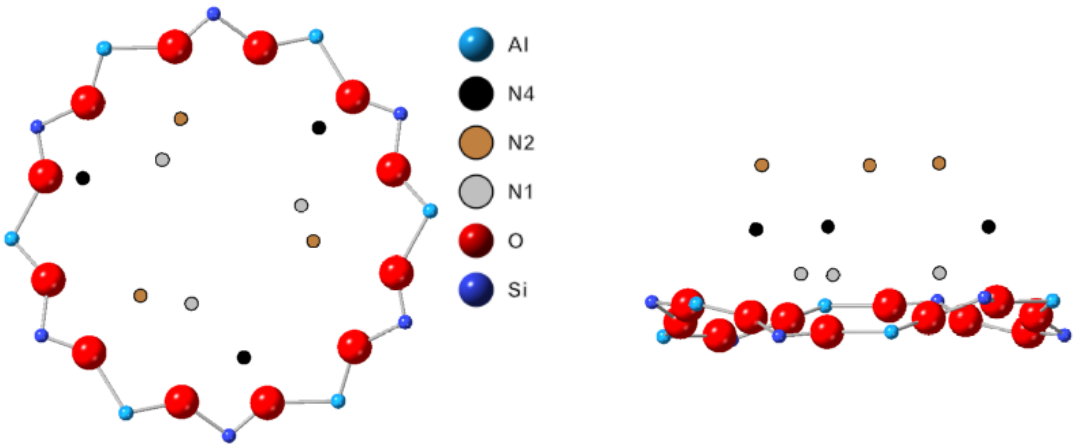

a. N1, N2 and N4, all located within the main channel of the zeolite, at different positions with respect to the Al/Si/O ring.

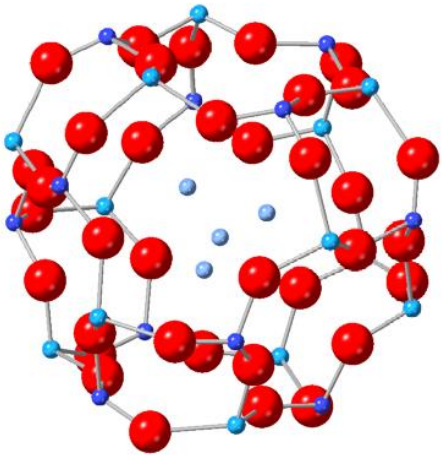

b. N3, located within the sodalite cage.

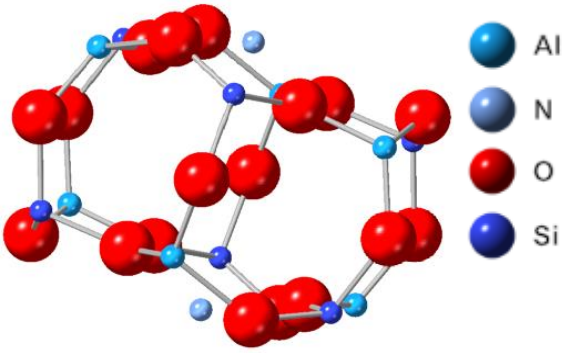

c. N5, located just slightly outwith the hexagonal faces of the prisms which join the sodalite cages.

Figure 3-18: Location of N atoms of ammonia molecules, the H13X zeolite, as determined by Rietveld refinement of SXRD pattern.

As can be seen in Figure 3-18, the majority of sites are present in the zeolite main channel. The binding sites were determined by looking at the closest atom to the nitrogen atoms. As discussed previously, the length of bond between a binding atom and the binding site can be used to classify the type of binding present.

Table 3-7: Classification of bond based on bond energies, as determined by Steiner *et al.* [26]

Bond Length (X-A, where X and A are heteroatoms)	Type of interaction
>3.2	Weak – Electrostatic/dispersion
2.5-3.2	Moderate – Mostly electrostatic
2.2-2.5	Strong – Strongly covalent

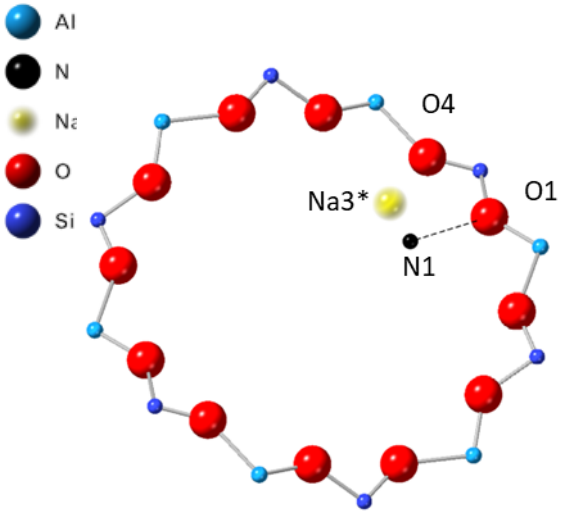

a. Location of N1, in the H13X zeolite. N1 is closest to O1, of the main zeolite pore, and is close to O4 and the previously occupied Na3 site, probably now a Brønsted acid site.

Temperature	N1 Occupancy	N1 Binding Atom	N1 Binding Distance
298K	0.631(15)	O1	2.99
373K	0.628(13)	O1	2.75
473K	0.701(12)	O1	2.87
573K	0		
673K	0		
773K	0		

b. Occupancy, binding atom and distances (Å) for N1 in H13X, at increasing temperatures.

Figure 3-19: Site N1, location, occupancy and binding in H13X, at increasing temperatures, as determined by Rietveld refinement of SXRD pattern.

Site N1, which initially has one of the highest occupancies of each of the ammonia sites, is located within the zeolite channel. The length between the N and the binding O, located in the ring of the pore (2.99 Å initially), suggests that this is a moderate electrostatic interaction which is supported by the stability of the site up to moderately high temperatures. It is anticipated that when Na^+ is replaced with H^+ in the position of Na3, the O1 and O4 between the Al would offer the BAS locations for the NH_3 adsorption as NH_4^+. It can be seen from Figure 3-19, that the ammonia molecule is close to both O1 and O4. Lin *et al.* used SXRD and comparison of bond lengths to study acidity of zeolites.[29] They report ammonia oxygen distances of between 2.0 and 3.5 Å, similar to as found here. Furthermore, they found that the distance between the ammonia

nitrogen and the oxygen from the Brønsted acid site can be related to the strength of this interaction.[29] The lengthening of an O-NH_4^+ interaction corresponds to a lower degree of overlap between the σ_{O-H} orbital and the terminal H atoms from the framework oxygen leading to a more protonated ammonium ion. This means that the interaction between N1 and the framework is weaker than that of, for example, N4, evidenced by N1-O1 having an initial bond distance of 2.99 Å compared to 3.24 Å for N4-O4. This also explains why N1 is unoccupied after 573K.

This allows this site to be identified as one of the low temperature sites seen in the ammonia TPD experiments (Figure 3-5).

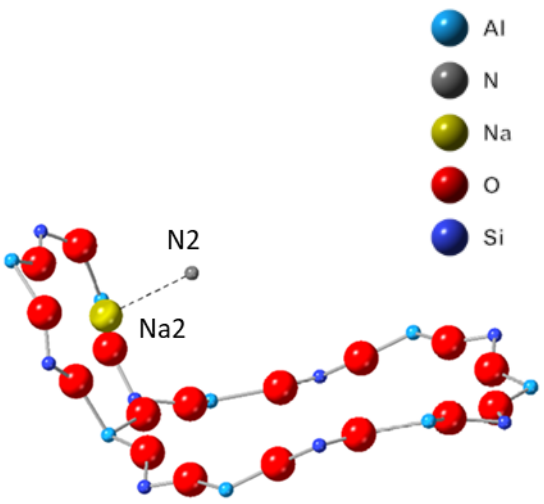

a. Location of N2, in the H13X zeolite. N2 is closest to N2, the sodalite cage face sodium site and is within the main zeolite pore.

Temperature	N2 Occupancy	N2 Binding Atom	N2 Binding Distance
298K	0.290(8)	Na2	2.83
373K	0.218(9)	Na2	2.18
473K	0.195(8)	Na2	1.42
573K	0.203(9)	Na2	2.74
673K	0.151(7)	Na2	2.84
773K	0.061(5)	Na2	2.97

b. Occupancy, binding atom and distances (Å) for N2 in H13X, at increasing temperatures.

Figure 3-20: Site N2, location, occupancy and binding in H13X, at increasing temperatures, as determined by Rietveld refinement of SXRD pattern.

N2 is a similar site to that seen in the unmodified Na13X zeolite, with binding as a weak interaction of ion dipole as the Na2 site is still prevalent (desorption < 470 K, see Figure 3-5). As was seen in Na13X, there are probably complimentary effects where the N2 atom interacts with the Na2 ion while N-H bonds from ammonia interact with the framework oxygens. This means this site is probably the lower temperature peak seen in the TPD experiments (Figure 3-5).

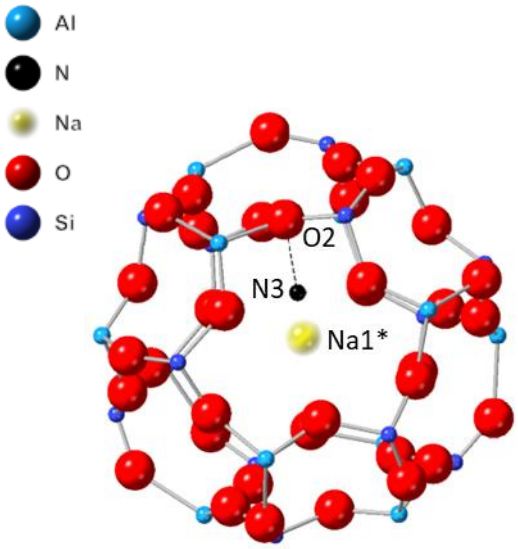

a. Location of N3, in the H13X zeolite. N3 is closest to O2, of the sodalite cage, and is close to the previously occupied Na1 site, probably now a Brønsted acid site.

Temperature	N3 Occupancy	N3 Binding Atom	N3 Binding Distance
298K	0.599(7)	O2	2.93
373K	0.518(7)	O2	3.07
473K	0.417(6)	O2	3.36
573K	0.442(7)	O2	3.06
673K	0.428(6)	O2	3.02
773K	0.380(5)	O2	3.17

b. Occupancy, binding atom and distances (Å) for N3 in H13X, at increasing temperatures.

Figure 3-21: Site N3, location, occupancy and binding in H13X, at increasing temperatures, as determined by Rietveld refinement of SXRD pattern.

Sites N3 is located within the sodalite cage. Prior to ion exchange, O2 was close to Na1, and so it is likely there is now a Brønsted acid site here. The distance between N3 and O2 (2.93 Å) is characteristic of a NH_4^+ species interaction, further confirmed by the high temperature stability of this site, seen by its partial occupancy even at 773 K. The Brønsted acid site effect is probably further emphasised by the fact that the sodalite cage means that there are a number of O atoms in close proximity and so the possibility for multiple binding interactions. This allows this site to be identified as one of the high temperature desorption sites in the TPD experiments (Figure 3-5).

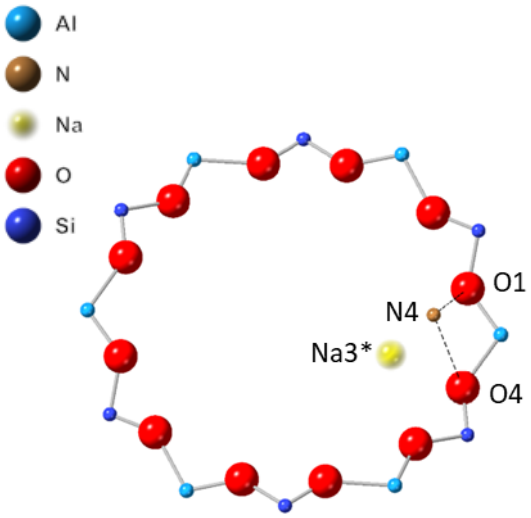

a. Location of N4, in the H13X zeolite. N1 is closest to O1 and O4, of the main zeolite pore, and is close the previously occupied Na3 site, probably now a Brønsted acid site.

Temperature	N4 Occupancy	N4 Binding Atom	N4 Binding Distance
298K	0.221(10)	O4, O1	3.24, 3.37
373K	0.449(15)	O1, O4	3.31, 4.01
473K	0.546(14)	O1, O4	3.17, 3.86
573K	0.752(18)	O1, O4	3.18, 3.56
673K	0.480(15)	O1, O4	3.12, 3.53
773K	0.262(10)	O1, O4	3.08, 3.46

b. Occupancy, binding atom and distances (Å) for N4 in H13X, at increasing temperatures.

Figure 3-22: Site N4, location, occupancy and binding in H13X, at increasing temperatures, as determined by Rietveld refinement of SXRD pattern.

Prior to ion exchange, Na3 was located close to O1 and O4, meaning that a proton is probably located here, providing a possible Brønsted acid site, similarly to N1 and N3. The positioning of N4 between the two oxygen sites and the resulting bond distances (3.24 Å to O4 and 3.37 Å to O1 at 298K) are indicative of strong Brønsted acid binding, allowing this site to be assigned as a high temperature desorption site in the TPD (Figure 3-5). Furthermore, a similar ‘gate’ effect to that in the Na13X sample is seen here. The occupancy of N4 increases with temperature indicating that it is possible for ammonia molecules desorbing from other sites to adsorb to this accessible, kinetically stable site, before being fully removed from the zeolite.

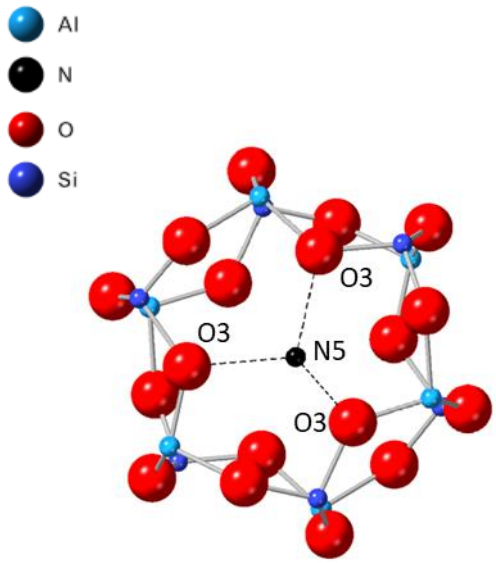

a. Location of N5, in the H13X zeolite. N5 is closest to O3 of the sodalite cage.

Temperature	N5 Occupancy	N5 Binding Atom	N5 Binding Distance
298K	0.669(14)	O3	1.81
373K	0.640(14)	O3	2.04
473K	0.558(9)	O3	2.18
573K	0.528(12)	O3	2.09
673K	0.554(8)	O3	2.22
773K	0.527(7)	O3	2.25

b. Occupancy, binding atom and distances (Å) for N5 in H13X, at increasing temperatures.

Figure 3-23: Site N5, location, occupancy and binding in H13X, at increasing temperatures, as determined by Rietveld refinement of SXRD pattern.

N5 shows little change in occupancy with increasing temperature suggesting a strong interaction. The position of N5, within the prism means that there are likely multiple interactions with the zeolite, stabilising the ammonia further. These factors mean it is very likely the ammonia molecule is covalently bound to a Brønsted Acid OH site, forming an NH^{4+} species. This is supported by the fact that O3 previously was close to Na1; it is likely that the ion exchange has led to a proton being present in this position instead, providing a Brønsted acid site. This corresponds to the very strong ammonia seen in the SDT at high temperatures and modelling data. Sites such as N5 allow for high temperature ammonia storage in applications such as Haber-Bosch type applications.

Clearly the proton exchange of zeolite has improved both the stability and number of the adsorption sites in the zeolite, through the generation of Brønsted acid sites, particularly in N3, N4 and N5 which show very strong ammonia binding and so are assigned to the high temperature

desorption peak present in the TPD (Figure 3-5). The other ammonia sites are weaker interactions; N1 is a very weak interaction between ammonia Brønsted acid site that does not result in a NH_4^+ species while N2 is a dispersion type interaction, as was seen in Na13X. Comparison of the desorption seen here and the TPD (Figure 3-5) gives a good fit; the ratio of desorbed from low temperature site compared to high temperature sites is very close (low:high is 2.46 here, compared to 2.48 from TPD).

The stability of the ammonia sites in the other modified zeolites was compared.

3.4.2. La13X

The SDT of La13X shows less high temperature ammonia storage in the SDT data, likely due to the lack of Brønsted acid sites. La13X shows two ammonia sites within the sodalite cage, one within the joining hexagons and one in the main channel. As discussed, rare earth metal ions such as lanthanum prefer sites with higher neighbouring oxygens in order to attain a more stabilized form. The sodalite cage position of the lanthanum ions offer such stability and so are a preferentially occupied site This differs from H13X where the majority of sites were in the main pore. The occupancy of each site was also studied.

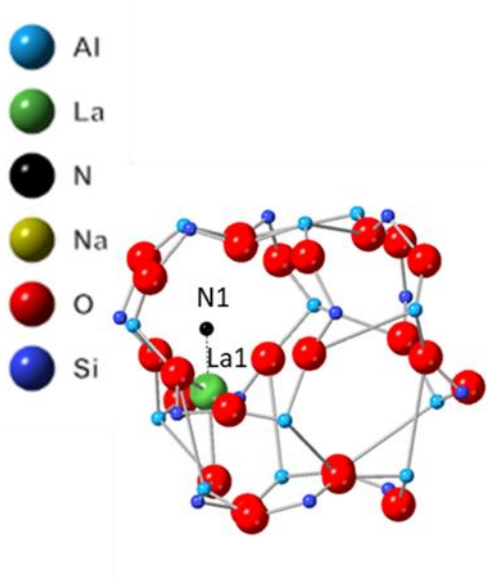

a. Location of N1, in the La13X zeolite. N1 is within the distorted sodalite cage, interacting with La1.

Temperature	N1 Occupancy	N1 Binding Atom	N1 Binding Distance
298K	0.123(78)	La1	1.81
373K	0.103(7)	La1	1.89
473K	0.065(6)	La1	1.56
573K	0		
673K	0		
773K	0		

b. Occupancy, binding atom and distances (Å) for N1 in La13X, at increasing temperatures.

Figure 3-24: Site N1, location, occupancy and binding in La13X, at increasing temperatures, as determined by Rietveld refinement of SXRD pattern.

The TPD of ammonia from La13X (Figure 3-5), showed only low temperature desorption, suggesting the only weak interactions are present.

It is reported in the literature that the unoccupied f orbitals of rare earth elements, such as lanthanum, can act as Lewis acid sites in zeolites despite their diffuse nature.[38,39] This reportedly can lead to very small bond lengths, as low as 2 Å in some systems.[39] It is also likely that the oxygen atoms nearby allow for complimentary bonding effects, as was seen between Na^+ and framework oxygen in Na13X.

N1 interacts with the lanthanum in the sodalite cage, as previously described, with some interaction with sodalite cage oxygen atoms also. The La-N bond length (initially 1.81 Å) is as would be expected from such an interaction[39] particularly given the constrained sodalite cage environment and the framework oxygen effects. The quick desorption of ammonia from this site

(N1 is unoccupied at 573 K) confirm this is a weak interaction, as was seen in the TPD of ammonia from La13X (Figure 3-5).

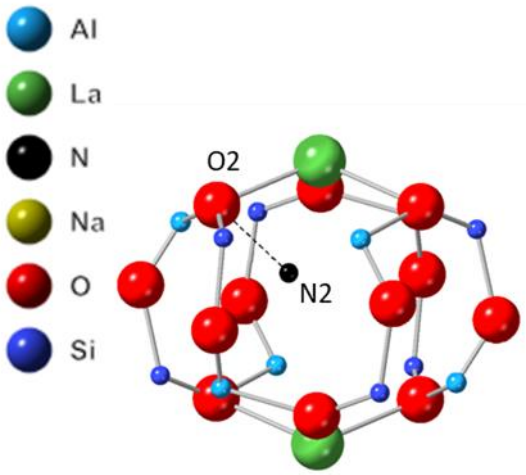

a. Location of N2, in the La13X zeolite. N2 is in distorted hexagonal prisms joining the sodalite cages interacting most closely with the framework oxygen.

Temperature	N2 Occupancy	N2 Binding Atom	N2 Binding Distance
298K	0.222(9)	O2	2.04
373K	0.103(5)	O3	2.23
473K	0.055(3)	O3	2.86
573K	0		
673K	0		
773K	0		

b. Occupancy, binding atom and distances (Å) for N2 in La13X, at increasing temperatures.

Figure 3-25: Site N2, location, occupancy and binding in La13X, at increasing temperatures, as determined by Rietveld refinement of SXRD pattern.

N2 is within the prisms joining the sodalite cages. It is in a similar position to N5-H13X though the lack of Brønsted acid site in La13X results in a significantly lower stability (N2 is unoccupied by 573K) as would be expected emphasising that Brønsted acid character is essential for high temperature stability. It has been previously discussed that it is unfavourable for ammonia molecules to be present in this site, without stabilising Brønsted acid sites,[35] due to the constrained nature of the site. Ammonia trapped here, within a very small prisms, is unfavourable entropically and so easier to desorb than other sites.

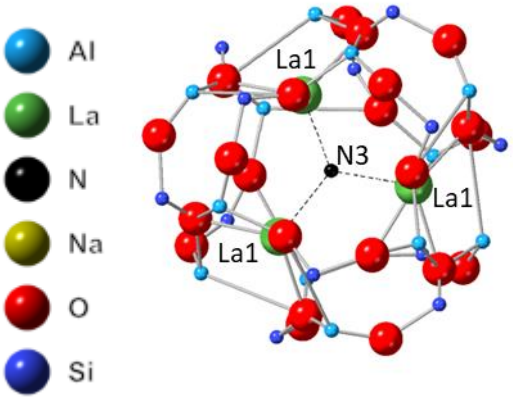

a. Location of N3, in the La13X zeolite. N3 is within the distorted sodalite cage, interacting with La1.

Temperature	N3 Occupancy	N3 Binding Atom	N3 Binding Distance
298K	0.467(4)	La1	2.55
373K	0.457(4)	La1	2.56
473K	0.475(4)	La1	2.56
573K	0.502(3)	La1	2.54
673K	0.494(3)	La1	2.56
773K	0		

b. Occupancy, binding atom and distances (Å) for N3 in La13X, at increasing temperatures.

Figure 3-26: Site N3, location, occupancy and binding in La13X, at increasing temperatures, as determined by Rietveld refinement of SXRD pattern.

N3 is a very similar site to N1; it is also within the sodalite cage and interacts with La1 and framework oxygen. It shows slightly higher occupancy, probably due to its position equidistant from multiple La1 ions but is still completely desorbed by 773K.

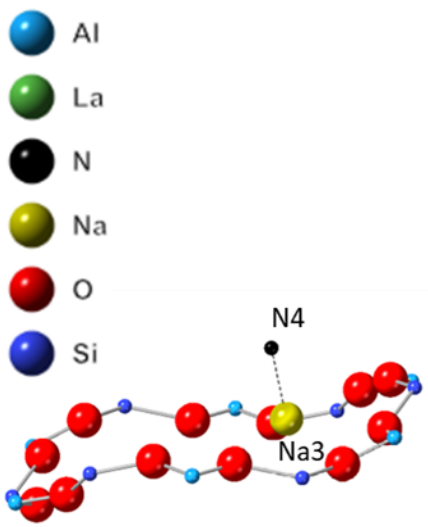

a. Location of N4, in the La13X zeolite. N4 is in the main pore between sodium ions.

Temperature	N4 Occupancy	N4 Binding Atom	N4 Binding Distance
298K	0.131(6)	Na3	2.09
373K	0.127(8)	Na3	2.14
473K	0.138(7)	Na3	2.26
573K	0.127(10)	Na3	1.82
673K	0.098(9)	Na3	2.03
773K	0		

b. Occupancy, binding atom and distances (Å) for N4 in La13X, at increasing temperatures.

Figure 3-27: Site N4, location, occupancy and binding in La13X, at increasing temperatures, as determined by Rietveld refinement of SXRD pattern.

Finally, N4 is the only site close to the macropore, as can be seen in Figure 3-27. This site is similar to the gate sites identified in H13X and Na13X, however without an increasing ammonia occupancy. Its low occupancy and relatively low temperature stability show that this is only a week interaction as was seen in Na13X where there are simultaneous reactions with Na^+ and framework oxygen. This is in contrast to the pore sites in H13X due to absence of protonic character.

All sites are unoccupied at 773K, giving good fit with the TPD of ammonia from La13X (Figure 3-5), showed only low temperature desorption (below 673K).

3.4.3. Mg13X

As a final comparison, the sites and occupancies of Mg13X were prepared. Interestingly, it shows both high and low temperature ammonia in the SDT trace, which is proposed to be a result of the simultaneous generation of magnesium hydroxide and proton species.

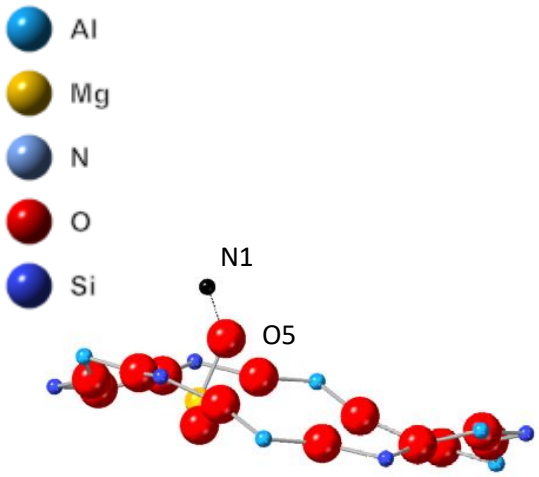

a. Location of N1, in the Mg13X zeolite. N1 is within the main pore of the zeolite, interacting most closely with N4 ammonia, and close to O5 (of MgO).

Temperature	N1 Occupancy	N1 Binding Atom	N1 Binding Distance
298K	0.730(30)	O5	3.66
373K	0.672(26)	O5	3.80
473K	0.507(5)	O5	3.07
573K	0.497(4)	O5	3.06
673K	0.488(8)	O5	3.16
873K	0.464(7)	O5	3.29

b. Occupancy, binding atom and distances (Å) for N1 in Mg13X, at increasing temperatures.

Figure 3-28: Site N1, location, occupancy and binding in Mg13X, at increasing temperatures, as determined by Rietveld refinement of SXRD pattern.

As shown in Figure 3-28, site N1 is located in the main pore of the zeolites and shows the highest initial occupancy of any of the sites. N1 is identified to bond with the oxygen binding to Mg1. None of the other modified zeolite species showed the presence of metal oxide or hydroxide species in the exchanged samples. N1 shows strong binding with O5, with bond lengths of 3-4 Å. This is comparable to binding seen in other Brønsted acid samples, both here and in the literature.[27] As was previously discussed, it is not possible to locate hydrogen atoms using SXRD, however, this bond distance and stability is typical of a Brønsted acid site interaction. This suggests that the magnesium species may in fact be magnesium hydroxide. This accounts for the high temperature desorption region seen in the TPD and explains why it is seen in the Mg13X TPD

but not the La13X TPD; the generation of the hydroxide species is crucial for high temperature ammonia stability in metal ion exchanged zeolites. As can be seen from the Figure 3-28. a. the ammonia is fairly close to the oxygen atoms making up the ring of the main pore. If the generated protons are present here this would strengthen the interaction between the ammonia and the zeolite.

It is possible that this site is acting as a "gate site" as was seen in N4-Na13X and N4-H13X. Ammonia molecules desorbing from other sites deeper in the zeolite can pass to this site before being fully removed from the zeolite.

This high temperature species means that this material is very promising for Haber type applications, where high temperature stability is desirable. Combined with the high capacity, this is a very promising material.

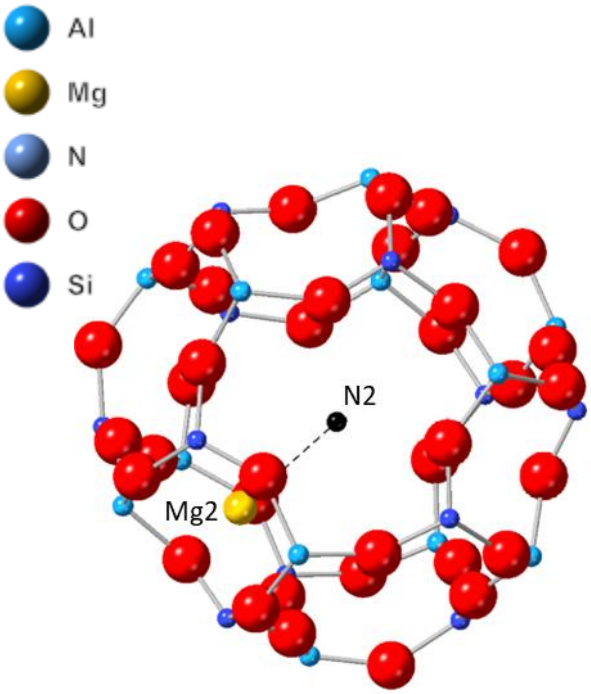

a. Location of N2, in the Mg13X zeolite. N2 is within the sodality cage of the zeolite, interacting most closely with Mg2 (which is located in the hexagonal faces of the prisms joining the sodalite cages).

Temperature	N2 Occupancy	N2 Binding Atom	N2 Binding Distance
298K	0.261(11)	Mg2	2.76
373K	0.262(8)	Mg2	2.78
473K	0.317(9)	Mg2	2.70
573K	0.365(7)	Mg2	2.59
673K	0		
873K	0		

b. Occupancy, binding atom and distances (Å) for N2 in Mg13X, at increasing temperatures.

Figure 3-29: Site N2, location, occupancy and binding in Mg13X, at increasing temperatures, as determined by Rietveld refinement of SXRD pattern.

As can be seen in Figure 3-29, site N2 is located within the sodalite cage, with a fairly low initial occupancy of 0.261(11). Similar sodalite cage sites were seen in the H13X and La13X materials (H13X-N3 and La13X-N1 respectively). Site N2 here and La13X-N1 are both weak interactions between the ammonia and metal site. This is confirmed by this site being unoccupied at higher temperatures (above 673 K) and the relatively long binding distance (between 2.59 and 2.78 Å, depending on temperature). These factors mean that this site can be assigned as the ammonia present in the lower temperature desorption site, as was seen in the TPD pattern. Comparison of this site and the equivalent H13X site (H13X-N3), emphasises the importance of Brønsted acid generation; the Brønsted acid site in H13X greatly increases the stability of this site giving high temperature stability which is not seen here.

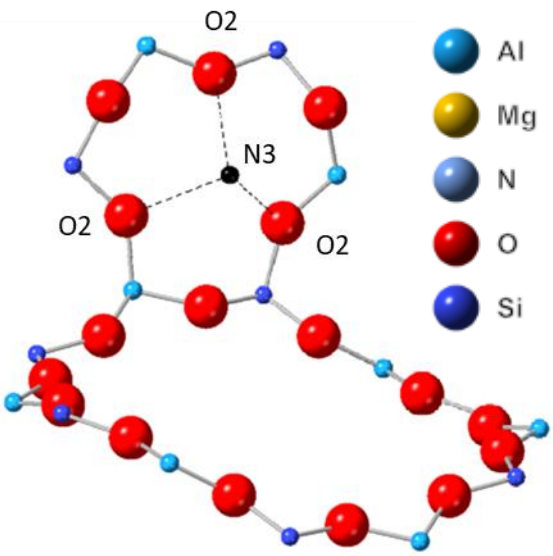

a. Location of N3, in the Mg13X zeolite. N3 is within the main pore of the zeolite, interacting with framework O2 atoms.

Temperature	N3 Occupancy	N3 Binding Atom	N3 Binding Distance
298K	0.464(6)	O2	2.53
373K	0.481(4)	O2	2.52
473K	0		
573K	0		
673K	0		
873K	0		

b. Occupancy, binding atom and distances (Å) for N3 in Mg13X, at increasing temperatures.

Figure 3-30: Site N3, location, occupancy and binding in Mg13X, at increasing temperatures, as determined by Rietveld refinement of SXRD pattern.

Site N3 is a further main pore site, seen in Figure 3-30. Similarly located sites were seen in Na13X (N2-Na13X) and H13X (N2-H13X) though the absence of Na2 in the Mg13X structure means that this N3 site has lowered temperature stability, seen by the site being unoccupied from 473K, and is present slightly closer to the zeolite pore walls. Although the bond length is typical of a moderately strong interaction, the poor temperature stability suggests that this is a weak interaction and the short bond distance is merely a result of the ammonia being held in the centre of the ring to interact with multiple oxygen molecules. The distances and occupancies are similar to those seen in N1-H13X, where there was a weak interaction with a Brønsted acid site. This is possible here, if the magnesium ion exchange generates a proton as expected, though the proton location cannot be unambiguously determined using XRD alone. Nevertheless, this is clearly a weak interaction and can be assigned to the lower temperature region of the ammonia TPD trace (see Figure 3-5).

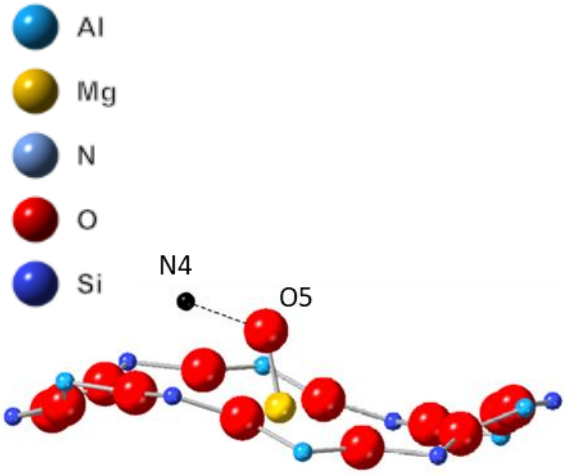

a. Location of N4, in the Mg13X zeolite. N4 is within the main pore of the zeolite, interacting most closely with O5 (which itself interacts with Mg1).

Temperature	N4 Occupancy	N4 Binding Atom	N4 Binding Distance
298K	0.497(31)	O5	1.99
373K	0.523(25)	O5	1.92
473K	0.468(14)	O5	2.17
573K	0.430(12)	O5	1.98
673K	0.649(25)	O5	1.32
873K	0.794(10)	O5	2.00

b. Occupancy, binding atom and distances (Å) for N4 in Mg13X, at increasing temperatures.

Figure 3-31: Site N4, location, occupancy and binding in Mg13X, at increasing temperatures, as determined by Rietveld refinement of SXRD pattern.

N4 is the site which was identified to bond with the oxygen binding to Mg1, as can be seen in Figure 3-31. None of the other modified zeolite species showed the presence of metal oxide or hydroxide species in the exchanged samples. N4 shows strong binding with O5, with bond lengths of around 2 Å. This is indicative of a covalent interaction, which is further supported by the high temperature stability of the ammonia in this site. As was previously discussed, it is not possible to locate hydrogen atoms using SXRD, however, this bond distance and stability is typical of a Brønsted acid site interaction. This suggests that the magnesium species may in fact be magnesium hydroxide. Once again, it is possible that there is also interaction with any generated proton species. This ammonia accounts for the high temperature desorption region seen in the TPD (Figure 3-5) and explains why it is seen in the Mg13X TPD but not the La13X TPD; the generation of the hydroxide species is crucial for high temperature ammonia stability in metal ion exchanged zeolites.

Furthermore, the increasing occupancy with temperature (i.e. between 573 and 673 K) is evidence of this site acting as a “gate site” as was seen in N4-Na13X and N4-H13X. Ammonia molecules desorbing from other sites deeper in the zeolite can pass to this site before being fully removed from the zeolite.

This high temperature species means that this material is very promising for Haber type applications, where high temperature stability is desirable. Combined with the high capacity, this is a very promising material.

3.5. Molecular Modelling

Molecular modelling was also used in an attempt to confirm the ammonia positions determined by SXRD.

3.5.1. H13X

First the framework structure of H13X was calculated. Protons were found in multiple locations. Protons were found on both oxygen sites which make up the main zeolite channel i.e. equivalent to O1 and O4, in the previously numbered structure. Protons were also located on some O2 sites, the oxygen making up the non-linking hexagon faces of the sodalite cages.

The position and nature of the ammonia sites were then also determined. Four ammonia sites were found: two in the main channel of the zeolite, one in the sodalite cage and one within the hexagonal prism linking the sodalite cages.

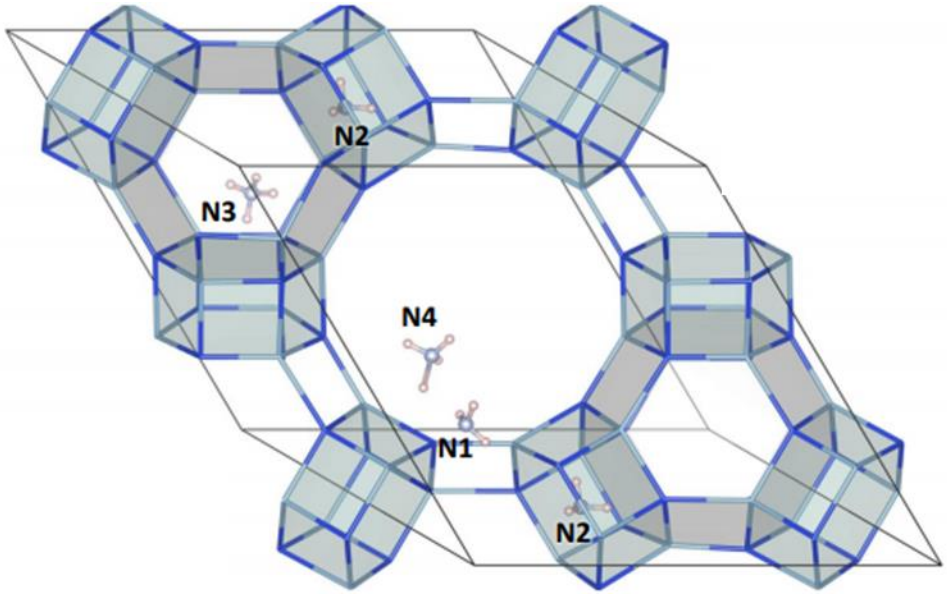

Figure 3-32: Determined NH_3 positions in H13X, calculated using Vienna ab initio simulation package (VASP),[40,41] the PBE density functional,[42] and a kinetic energy cut-off of 550 eV. The stick model represents the zeolite framework, blue circles represent nitrogen atoms and white circles represent the hydrogen atoms.

These positions map well to the ammonia positions determined by Rietveld refinement.

$N1_{modelled}$ is close to the zeolite wall (similar to $N2_{SXRD}$) and is confirmed to be a moderate binding site..

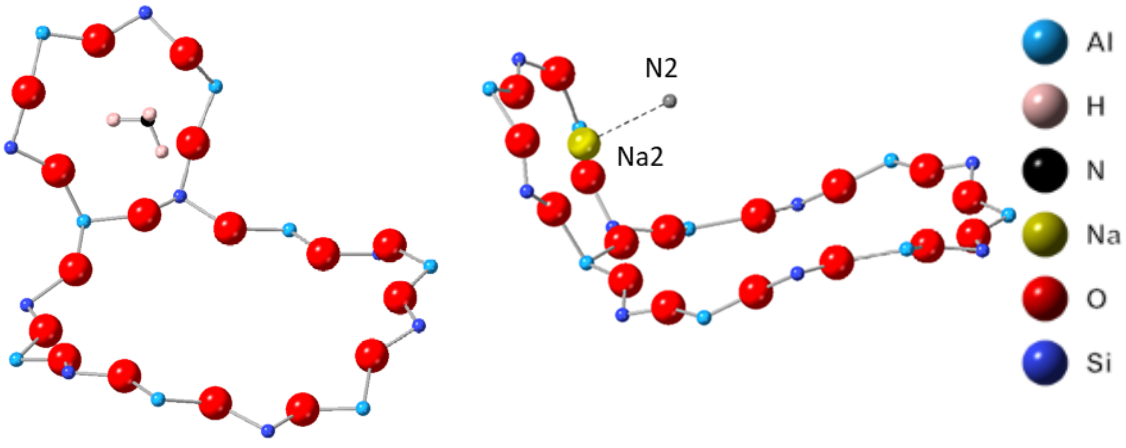

a) b)

Figure 3-33: Comparison of a) $N1_{modelled}$ position to b) $N2_{SXRD}$; both are located within the main pore of the zeolite, close to the hexagonal phase of the sodalite cage.

$N1_{modelled}$ position is very similar to position $N2_{SXRD}$; both are located within the main pore of the zeolite, close to the hexagonal phase of the sodalite cage. One clear difference is the lack of Na2 sodium in the modelled structure, leading to $N2_{SXRD}$ having a further position from the zeolite pore wall. The modelled structure assumed no sodium remained and so this explains this difference, though the general position is the same in the structures from modelling and SXRD. However, bond lengths between the ammonia and the binding site cannot be compared as the binding sodium is completely absent in the modelled structure. Neither of the structures suggest strong ammonia binding as NH_4^+.

$N2_{modelled}$ does not completely match any of the Rietveld structures. $N2_{modelled}$ is located in the centre of the hexagonal prisms joining the sodalite cages. This is a closely related site to $N5_{SXRD}$. Both these sites are identified in Olson's initial structure.[31] Site 1 is located within the centre of the hexagonal prisms while site 1' is located in the centre of the hexagonal faces of the prism. $N2_{modelled}$ is located in site 1 while $N5_{SXRD}$ is in site 1'.

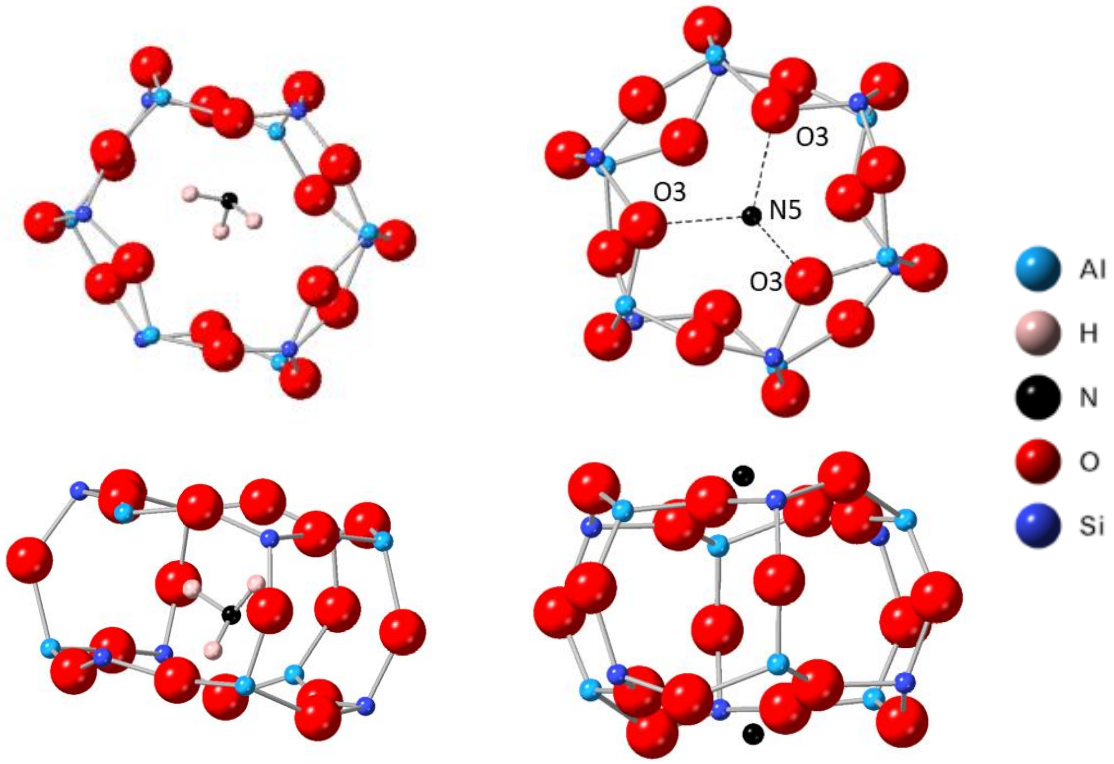

a) b)

Figure 3-34: Comparison of a) $N2_{modelled}$ position to b) $N5_{SXRD}$; $N2_{modelled}$ is located in the centre of the hexagonal prisms joining the sodalite cages while $N5_{SXRD}$ is located in the centre of the hexagonal faces of these prisms.

Though both ammonia molecules are located in the prisms joining the sodalite cages there are some differences. The modelled position of ammonia is within the prism joining the cages while the SXRD position instead shows ammonia within the faces of these prisms. There is also some distortion in the hexagonal prisms in the modelled structure; this was not seen in the Rietveld refined structure or in the NMR of H13X. This may be the cause of the discrepancies in the position between the two structures as this distortion makes the face site less energetically favourable or renders the central prism site accessible to ammonia.

$N3_{modelling}$ corresponds to the previously labelled $N3_{SXRD}$, the strongly bound species which bond length suggested was NH_4^+ species.

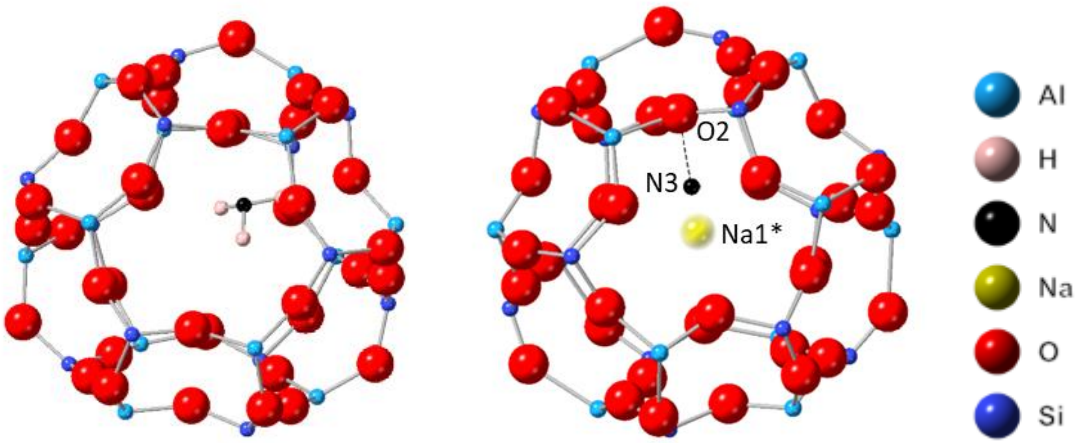

a) b)

Figure 3-35: Comparison of a) $N3_{modelled}$ position to b) $N3_{SXRD}$; both are located within the sodalite cage.

The position of $N3_{modelling}$ corresponds well to the position of $N3_{SXRD}$, though is slightly less central in the sodalite cage. The bond lengths between the ammonia and the equivalent O2 in each structure were compared. $N3_{modelling}$ to O2 had a bond length of 2.85 Å while $N3_{SXRD}$ to O2 was 2.93 Å. This further supports this ammonia position. This ammonia is the first ammonia which the modelling suggested was NH_4^+ which was also suggested by the Rietveld refinement. Both the position and nature of the ammonia site match well between the modelling and the Rietveld refinement.

There is a final $N4_{modelling}$ position. The location of this, within the main pore, almost in plane with the large 12 ring of the zeolite, suggest that this is equivalent to the $N1_{SXRD}$ position.

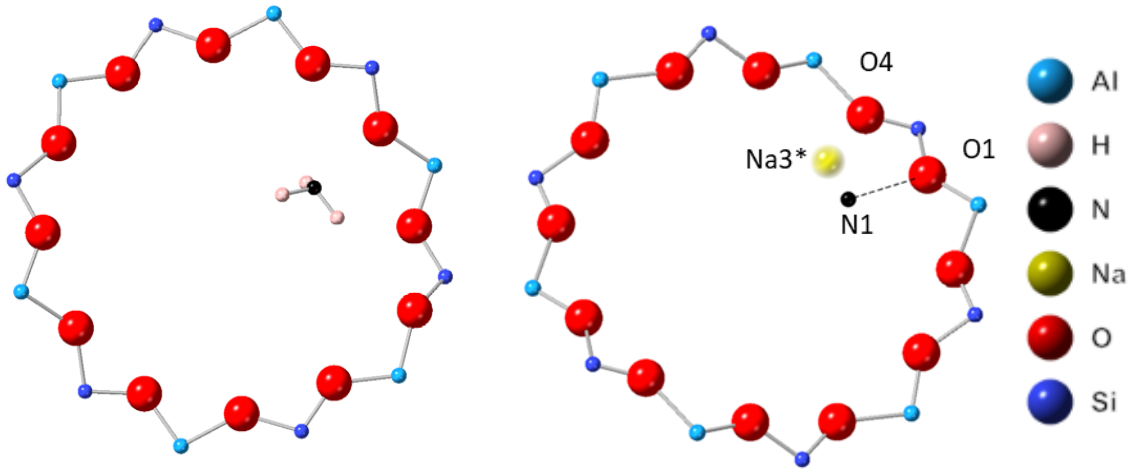

a) b)

Figure 3-36: Comparison of a) $N4_{modelled}$ position to b) $N1_{SXRD}$; both are located within the main pore of the zeolite

Although the position of $N4_{modelled}$ and $N1_{SXRD}$ match fairly well there are some differences. Firstly, $N4_{modelled}$ is an NH_4^+ species while $N1_{SXRD}$ is not. This corresponds to a shorter bond length; $N4_{modelled}$-O1 bond length is 2.58 Å while the Rietveld refined N1-O1 is 2.99 Å. One possible reason for this discrepancy is the previously discussed lack of sodium in the modelled structure. Another possible explanation is that $N4_{modelled}$ is instead more comparable to $N4_{SXRD}$ from the Rietveld refined structure. $N4_{SXRD}$ was also a main pore site, though further out of plane with the 12 ring of the zeolite and was a Brønsted acid site.

On the whole, there is a good fit between the modelled ammonia positions and the Rietveld refined positions. $N1_{modelled}$ was equivalent in position and type to $N2_{SXRD}$ and $N2_{modelled}$ similar in position and type to $N5_{SXRD}$. $N3_{modelled}$ was in the same position as $N3_{SXRD}$ and both were NH_4^+ species. $N4_{modelled}$ was a pore site which could be equivalent to either $N1_{SXRD}$ or $N4_{SXRD}$; it was difficult to tell due to the lack of sodium in the modelled structure.

3.5.2. La13X Structure

The lanthanum exchange zeolite structure was determined and favourable locations for the ammonia molecules found. Sodium was also considered in this model, and so pore sodium remained in the Na3 positions that were determined by Rietveld refinement.

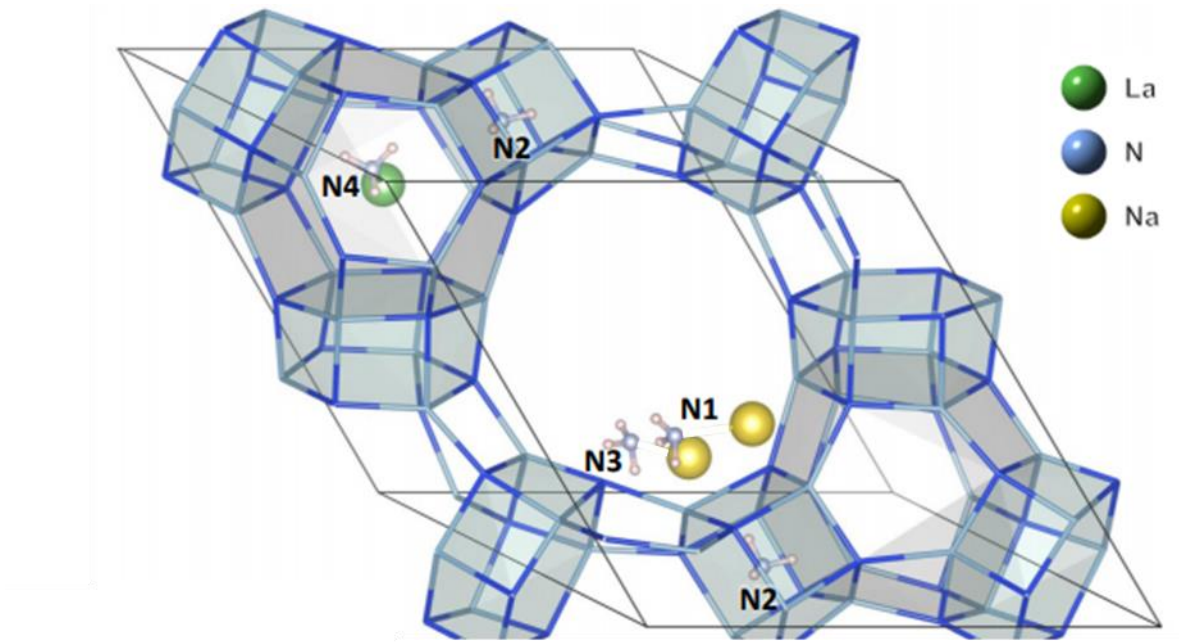

Figure 3-37: Determined NH_3 positions in La13X, calculated using Vienna ab initio simulation package (VASP),[40,41] the PBE density functional,[42] and a kinetic energy cut-off of 550 eV. The stick model represents the zeolite framework, green circles represent lanthanum atoms, yellow circles represent sodium atoms, blue circles represent nitrogen atoms and white circles represent the hydrogen atoms.

Only one lanthanum position was found to be favourable; this lanthanum position was found to be within the sodalite cage. This is broadly equivalent to $La1_{SXRD}$, as previously discussed, which is present in the sodalite cage with the highest occupancy and the lanthanum ion involved in ammonia bonding.

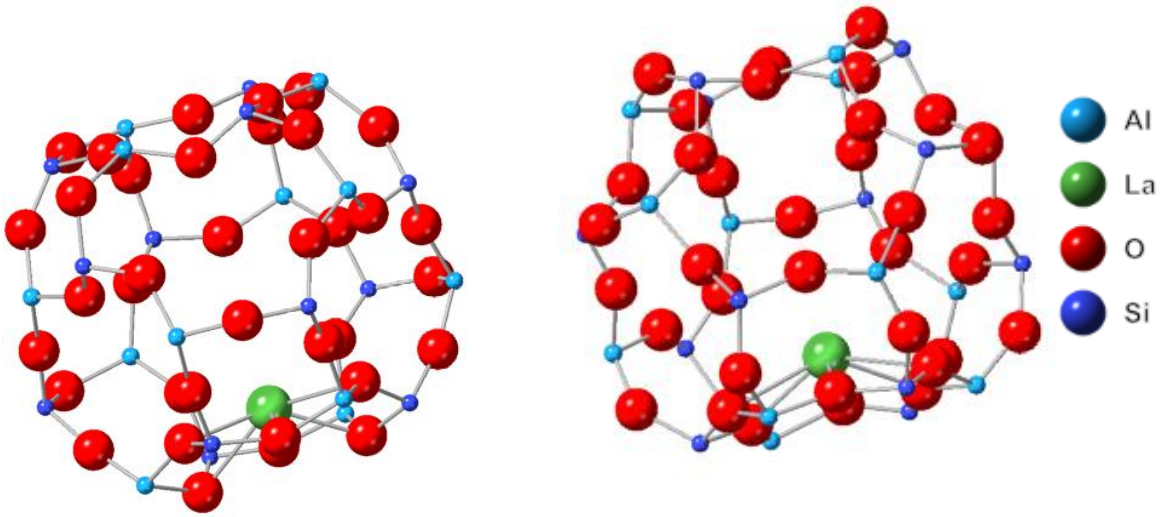

a) b)

Figure 3-38: Comparison of a) $La1_{modelled}$ position to b) $La1_{SXRD}$ determined from Rietveld refinement; both are located within the sodalite cage of the zeolite.

The bond lengths between the La1 and the near oxygens can be compared to judge the closeness of the modelled structure and the Rietveld refined structure. The bond length between $La1_{modelled}$ and the nearest oxygen is 2.48 Å while the SXRD La1-O bond length is 2.54 Å. These almost equivalent distances indicate that the lanthanum position determined by modelling matches the experimental position well.

Again, four ammonia positions were determined, one within the sodalite cage, one within the hexagonal prisms joining the sodalite cage and two in the main pore of the zeolite.

$N1_{modelled}$ and $N3_{modelled}$ are in similar positions in the main pore of the zeolite. Only one main pore ammonia was found in the Rietveld refined structure. By comparing the positions of the modelled ammonia molecules and the distances between the ammonia and framework zeolite atoms, $N3_{modelled}$ is shown to be in a close position to the previously studied $N4_{SXRD}$ site, determined by Rietveld refinement of the SXRD data.

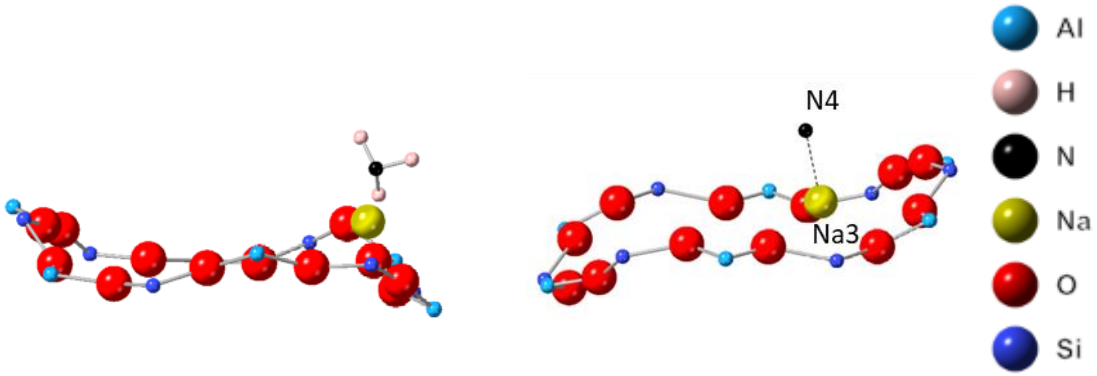

a) b)

Figure 3-39: Comparison of a) $N3_{modelled}$ position to b) $N4_{SXRD}$; both are located within the sodalite cage of the zeolite.

Again, bond lengths between the ammonia and framework species can be used to determine the closeness of the structures. $N3_{modelled}$ showed a binding distance of 2.43 Å to the binding sodium compared to 2.09 Å in the Rietveld refined structure. This difference is likely due to the experimentally prepared samples showing some lanthanum in the pores. Although this was only a small lanthanum content it likely affects the possible ammonia positions and may lead to a shorter required bond length. Furthermore, the modelled data did not assume any disruption in the zeolite structure which was clearly seen in the Rietveld refined structure and further supported by experimental data, such as NMR. These factors may also explain why the Rietveld refined structure shows only one ammonia site while the modelled structure shows two; additional lanthanum ions in the zeolite pore are probably reducing the potential number of ammonia sites here.

$N2_{modelled}$ is in a similar position to $N2_{SXRD}$, within the hexagonal prims joining the sodalite cages.

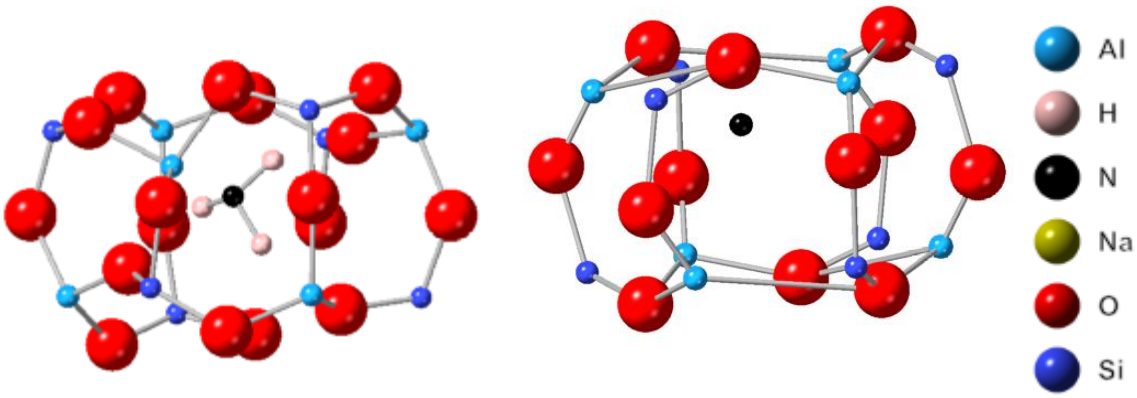

a) b)

Figure 3-40: Comparison of a) $N2_{modelled}$ position to b) $N2_{SXRD}$; both are located within the hexagonal prisms joining the sodalite cages.

The ammonias are clearly in similar position in the modelled and experimental data. Again, bond lengths between the ammonia and the framework species give a good indication of the fit between the two structures. $N2_{modelled}$ is located 2.59 Å from the nearest oxygen, while $N2_{SXRD}$ is 2.04 Å. This is a slight difference, due to the disruption in the experimental La13X structure forcing $N2_{SXRD}$ slightly off centre and so closer to the nearest oxygen atom. Despite this, the position is clearly still within the prism and so the modelled structure supports the experimental data well.

Finally, the $N4_{modelled}$ position was studied. It is located in the sodalite cage, close to the centre. This is a similar position to $N3_{SXRD}$.

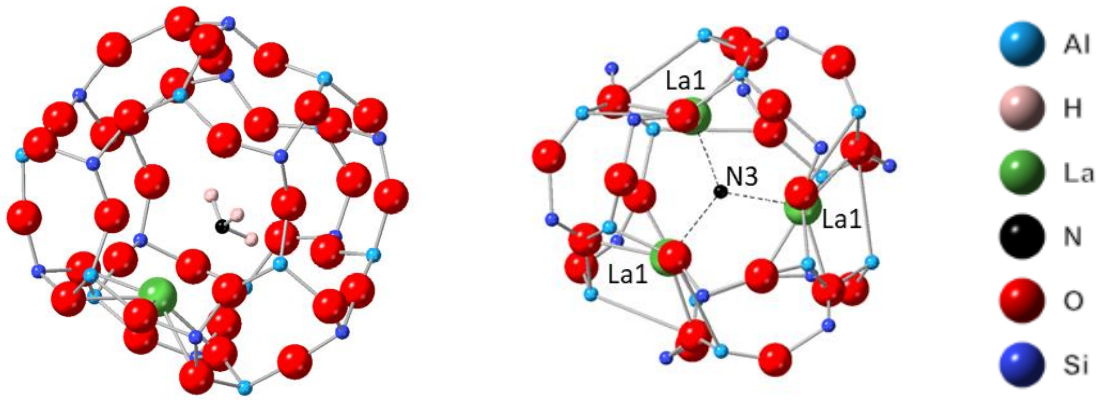

a) b)

Figure 3-41: Comparison of a) $N4_{modelled}$ position to b) $N3_{SXRD}$; both are located within the sodalite cages.

Again, the ammonia positions of the two structures are clearly similar. To confirm this the distance between the bonding lanthanum and the ammonia in the two structures were compared. $N4_{modelled}$ lanthanum distance is 2.68 Å while the equivalent $N3_{SXRD}$ lanthanum distance is 2.55 Å. These are clearly a good fit, indicating that the modelled structure supports the $N3_{SXRD}$ ammonia position well.

Furthermore, none of the ammonia species in the modelled La13X structure were shown to be NH_4^+ species; this matches well with the experimental TPD data and *in-situ* SXRD experiments, which show only weakly bound ammonia and no Brønsted acid site species.

Overall, the modelled structures and ammonia are a good match for the SXRD refinement. The $N3_{modelled}$ position is equivalent to $N4_{SXRD}$ though the lack of lanthanum in the pores in the modelled structure slightly affects the bond distance. $N2_{modelled}$ and $N2_{SXRD}$ are both located in the sodalite cage joining hexagonal prisms and $N4_{modelled}$ and $N3_{SXRD}$ are both located in the centre of the sodalite cage. Moreover, all of the modelled ammonia were low temperature, demonstrating the both the nature and location of the modelled species support the experimental data and Rietveld refinement.

3.6.Conclusions

Crystalline Na13X zeolites contain extremely high Al to Si (Si:Al of 1.2) contents, which are charge balanced by sodium ions. Some of these sodium ions were partially exchanged with cations; namely protons, lanthanum and magnesium and the samples were studied for ammonia uptake. The introduction of these cations all improved the ammonia adsorption capacity particularly for the latter two as compared to the parent Na13X zeolite structure. It is found that Na13X zeolite is mainly characterized with Lewis acid sites for weak adsorption of ammonia (ammonia desorption < 470 K). The crystallinity of Na13X zeolite is substantially decreased when sodium ions are exchanged with protons, however, this partial H13X gave some stronger adsorption sites (ammonia desorption > 670K) for ammonia as a result of Brønsted acid site (Al-O(H)-Si) generation. On the other hand, La13X showed comparable weak adsorption sites but significantly higher capacity for ammonia uptake due to the increase in Lewis acidity of the disordered structure when La^{3+} is incorporated into the zeolite framework. Interestingly, the partial ion exchange of sodium ions of Mg13X gave both weak and strong binding sites for ammonia, indicative the coexistence of both types of adsorption sites which was proposed to be a result of simultaneous generation of magnesium hydroxide and protons. The different affinities and capacities at different temperatures show that ion exchange of cations could be used to tailor this zeolite adsorbent for particular applications.

3.7. Future Work

The fact that the lanthanum disorder has an effect on the ammonia desorption should be studied in further detail. It is unlikely that the level of loading chosen here is optimum and so comparison of varying degrees of lanthanum ion exchange would allow for this effect to be studied in greater detail. To fully understand how ammonia is stored in the zeolites, the whole ammonia molecule

should be studied. Neutron diffraction would allow for the hydrogen atoms in ammonia to be visualised which would give more useful information about the positioning and packing of the ammonia. Neutron diffraction would also allow the Brønsted acid sites to be unambiguously assigned, instead of determining using varying distance of ammonia zeolite interactions.

3.8. References

1. H. Zhu, X. Gu, K. Yao, L. Gao and J. Chen, *Ind. Eng. Chem. Res.,* 2009, **48**, 5317-5320.
2. V. E. Sharonov and Y. I. Aristov, *React. Kinet. Catal. Lett*., 2005, **85**, 183-188.
3. H. H. Himstedt, M. S. Huberty A. V. McCormick, L. D. Schmidt and E. L. Cussler, *Am. Inst. Chem. Eng. J*., 2015, **61**, 1364-1371.
4. C. H. Christensen, R. Z. Sørensen, T. Johannessen, U. J. Quaade, K. Honkala, T. D. Elmoe, R. Kohler and J. K. Norskov, *J. Mater. Chem*., 2005, **15**, 4106-4108.
5. Z. Huang, J. Gallucci, X. Chen, T. Yisgedu, H. K. Lingam, S. G. Shore and J-C. Zhao, *J. Mater. Chem*., 2010, **20**, 2743-2745.
6. C. Y. Liu and K. Aika, *J. Japan Pet. Inst*., 2003, **46**, 301-307.
7. V. P. Shiralkar and S. B. Kulkarni, *J. Colloid Interface Sci*., 1985, **108**, 1-10.
8. C. J. Doonan, D. J. Tranchemontagne, T. G. Glover, J. R. Hunt and O. M. Yaghi, *Nat. Chem*., 2010, **2**, 235-238.
9. H. Jasuja, G. W. Peterson, J. B. Decoste, M. A. Browe and K. S. Walton, *Chem. Eng. Sci*., 2015, **124**, 118-124.
10. C. Petit, B. Mendoza and T. J. Bandosz, *Langmuir*, 2010, **26,** 15302-15309.
11. D. Saha and S. Deng, *J. Colloid Interface Sci*., 2010, **348**, 615-620.
12. A. J. Rieth, Y. Tulchinsky and M. Dinca, *J. Am. Chem. Soc*., 2016, **138**, 9401-9404.
13. C. Y. Liu and K-I Aika, *Bull. Chem. Soc. Jpn*., 2004, **77**, 123-131.
14. M. O. Jones, D. M. Royse, P. P. Edwards and W. I. F David, *Chem. Phys*., 2013, **427**, 38-43.
15. B. T. W. Lo, L. Ye and S. C. E. Tsang, *Chem.,* 2018, **4**, 1778-1808.

16. R. E. Morris and P. S. Wheatley, *Angew. Chemie Int. Ed*., 2008, **47**, 4966-4981.

17. L. Ye, B. T. W. Lo, J. Qu, I. Wilkinson, T. Hughes, C. A. Murray, C. C. Tang and S. C. E. Tsang, *Chem. Commun*., 2016, **52**, 3422-3425.

18. M. B. Pourazar, T. Mohammadi, M. R. Jafari Nasr, M. Javanbakht and O. Bakhtiari, *Mater. Res. Express*., 2020, **7**, 035004.

19. T. Doan, K. Nguyen, P. Dam T. H. Vuong, M. T. Le and H. P. Thanh, *J. Chem*., 2019, **2019**, 6197527.

20. M. S. Shafeeyan, W. M. A. W. Daud, A. Houshmand and A. Shamiri, *J. Anal. Appl. Pyrolysis*., 2010, **89**, 143-151.

21. S. M. T. Almutairi, B. Mezari, G. A. Filonenko, P. C. M. M. Magusin, M. A. Rigutto, E. A. Pidko amd E. J. M. Hensen, *ChemCatChem*., 2013, **5**, 452-466.

22. M. van der Pal, R. de Boer and J. Veldhuis, *International Symposium on Innovative Materials for Process in Energy Systems*, 2013.

23. G. Meyer, *The Rare Earth Elements*, Wiley, Weinheim, 2012.

24. S. J. Gregg and J. Jacobs J., *Trans., Faraday Soc*., 1948, **44**, 574-588.

25. A. Corma, V. Fornés, F. V. Melo and J Herrero, *Zeolites,* 1987, **7**, 559–563.

26. T. Steiner, *Angew. Chemie Int. Ed*., 2002, **41**, 48-76.

27. L. Ye, B. T. W. Lo, J. Qu, I. Wilkinson, T. Hughes, C. A. Murray, C. C. Tang and S. C. E. Tsang, *Chem. Commun*., 2016, **52**, 3422-3425.

28. C. Mirodatos, A. A. Kais, J. C. Vedrine, P. Pichat and D. Barthomeuf, *J. Phys. Chem*., 1976, **80**, 2366-2371.

29. W-C. Lin, L. Ye, S. Wu, B. Lo, Y-K. Peng, P Zhao, I. McPherson and S. C. E. Tsang, *ChemSusChem*., 2018, **11**, 4214-4218.

30. S. Li, A. Zheng, Y. Su, H. Fang, W. Shen, Z. Yu, L. Chen and F. Deng, *Phys. Chem. Chem. Phys*., 2010, **12**, 3895-3903.

31. D. H. Olson, *Zeolites,* 1995, **15**, 439–443.

32. R. E. Fletcher, S. Ling and B. Slater, *Chem. Sci*., 2017, **8**, 7483-7491.

33. R. Y. Yanagida and K. Seff, *J. Phys. Chem*., 1972, **76**, 2597-2601.

34. G. P. Holland and T. M. Alam, *Phys. Chem. Chem. Phys*., 2005, **7**, 1739-1742.

35. A. G. Seel, A .Sartbaeva, A. J. Rammirez-Cuesta and P. P. Edwards, *Phys. Chem. Chem. Phys*., 2010, **12**, 9661-9666.

36. A. Simon, H. Mattausch, M. Ryazanov and R. K. Kremer, *Anorg. Allg. Chem*., 2006, **632**, 919-929.

37. J. N. Louwen, S. Simko, K. Stanciakova, R. E. Bulo, B. M. Weckhuysen and E. T. C. Vogt, *J. Phys. Chem. C,* 2020, **124**, 4626-4636.

38. W. Xiaoning, Z. Zhen, X. Chunming, D. Aijun, Z. Li and J. Guiyuan, *J. Rare Earths*, 2007, **25**, 321-328.

39. K. Suzuki, M. Sugawa, Y. Kikukawa, K. Kamata, K. Yamaguchi and N. Mizuno, *Inorg. Chem*., 2012, **51**, 6953-6961.

40. G. Kresse and J. Furthmüller, *Comput. Mater. Sci*., 1996, **6**, 15-50.

41. R. A. Vargas-Hernández, *J. Phys. Chem. A*., 2020, **124**, 4053-4061.

42. J. P. Perdew, K. Burke and M. Ernzerhof, *Phys. Rev. Lett*., 1996, **77**, 3865-3868.

4. Optimising Lanthanum Ion Exchange

As was discussed in the previous chapter, the lanthanum ion exchange process causes disruption to the 13X zeolite structure. It is not entirely clear why only the lanthanum ion exchange causes such structural disruption and whether the higher ammonia capacity is because of this disruption.

The study of lanthanum ion exchange process has been reported in literature. Lercher and colleagues studied the nature, concentration and location of lanthanum ions in faujasite zeolites using primarily NMR and DFT.[1] They reported that the size of the lanthanum ion hydration shell limits the possible locations accessible to the lanthanum ions during the exchange process. However, raising the temperature allows for entry into the smaller pore of the zeolite e.g. the lanthanum ions can even enter the sodalite cage.[1] After heating (such as with the calcination process used here) lanthanum ions are found in positions where they can coordinate to many oxygen atoms i.e. near to the hexagons which make up the sodalite cage framework. However, research by Gong showed that this process (i.e. lanthanum ions entering the sodalite cages) can also cause structural distortion under some conditions.[2]

To understand this process, and how it affects the subsequent ammonia adsorption capacity of the materials, further experiments were carried out to see the effect of temperature, ion exchange time and lanthanum ion concentration.

4.1. Effect of Temperature

The effect that the ion exchange temperature was studied, comparing exchange at room temperature, 40 °C and 60 °C.

4.1.1. Ammonia Capacity

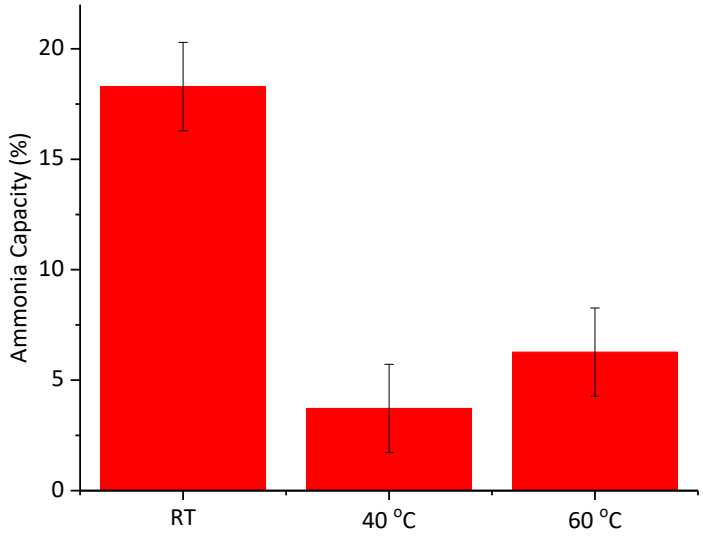

Figure 4-1: Ammonia storage capacity of La13X samples which underwent ion exchange at room temperature (25 °C), 40 °C and 60 °C. Samples (approximately 1 g) were connected to a Schlenk vacuum line and dried at 550 °C under vacuum for 4 hours. The samples were allowed to cool to room temperature and then exposed to pure ammonia gas (approximately 400 mbar) for 45 minutes. To determine capacity the samples were placed in a TA Instruments Q600 SDT. Approximately 10 mg of sample was placed in the SDT. The temperature was increased to 600 °C at a rate of 10 °C/min under 100 mL/min flowing nitrogen and the weight change recorded. The 450 °C sample weight was used to calculate capacity, assuming all weight loss up to this point was due to ammonia. (See Appendix for method validation.)

Figure 4-1 shows the ammonia capacity of the La13X samples which underwent ion exchange at room temperature, 40 °C and 60 °C. The temperature increase has clearly had a detrimental effect on the ammonia capacity of the materials with the 18.3 ± 2.0 % capacity of RT La13X decreasing to 3.7 ± 2.0 % for 40 °C La13X and 6.3 ± 2.0 % for 60 °C La13X. The higher temperature ion exchanges may potentially cause structural breakdown in the zeolites leading to lowered capacity: this was confirmed with further characterisation in later experiments.

4.1.2. Ammonia Desorption

The desorption profiles of the ammonia loaded samples were compared.

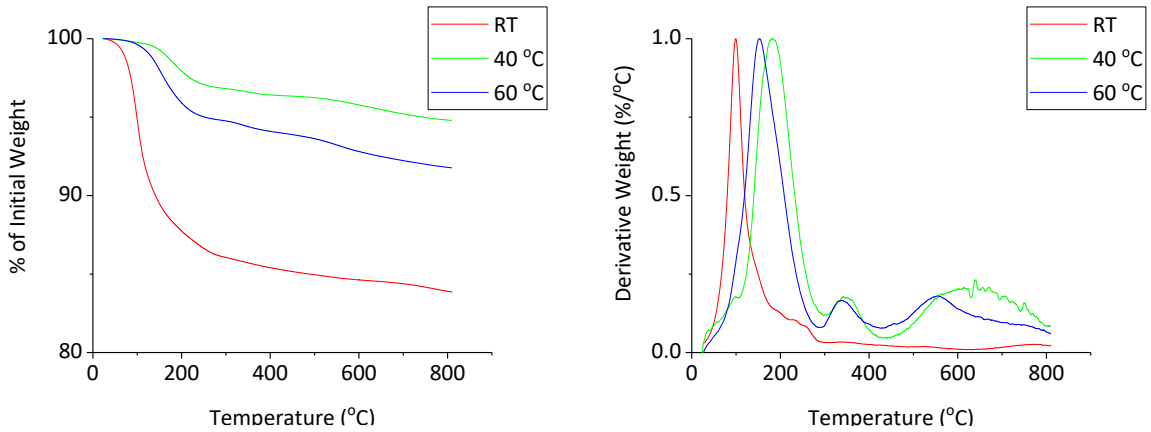

Figure 4-2: Desorption of ammonia on La13X prepared by ion exchange of Na13X at RT, 40 and 60 °C recorded on a TA Instruments Q600 SDT. First the samples were dried under flowing N_2 at 550 °C for five hours, then attached to a Schlenk line. They were dried under vacuum at 550 °C for four hours, cooled to room temperature and then pure ammonia gas was added (around 400 mbar, for 45 minutes.) The samples were placed in the SDT and the temperature was increased to 800 °C at a rate of 10 °C/min under 100 mL/min flowing nitrogen and the weight change recorded.

Figure 4-2 shows the different ammonia desorption patterns for the samples which underwent La^{3+} ion exchange at different temperatures. All samples show the greatest desorption in the low temperature region, although the 40 and 60 °C exchanged samples show desorption peaking at a slightly higher temperature. The RT La13X desorption peak is centred at 96 °C, the 60 °C La13X peak at 154 °C and 40 °C La13X peak at 182 °C. This indicates more weakly bound ammonia when La ion exchange was carried out at RT as compared to 40 and 60 °C. The effect of temperature on lanthanum exchanged Na13X has not been systematically investigated, However, Corma *et al.* reported that increased lanthanum content led to lower ammonia desorption temperature[3] in lanthanum exchanged zeolite Y. From our experiments, higher ion exchange temperatures appear to enhance the strength of ammonia binding in the zeolite. Interestingly, the samples which underwent exchange at higher temperatures also show additional features at high temperatures (500 °C and above). Previously, desorption in this area was attributed to very acidic sties strongly binding to ammonia. The lack of Brønsted acid sites mean it is unlikely that the lanthanum

exchanged zeolite is storing ammonia at temperatures above 350 °C. Instead, it is envisaged that the zeolite structure may have undergone a structural change. It was reported by Triguerio *et al.* that structural instability in zeolites with rare earth elements exchanged can be seen using thermogravimetric techniques.[4] Thus, the TG features at high temperatures in the high temperature exchanged samples can be attributed to the structural changes in the zeolite due to the instability the framework when exchange occurs at elevated temperatures. The higher temperature ion exchange causes structural instability in the zeolite, as is shown by the high temperature peaks in the derivative weight profile, which may also be the reason for the aforementioned decreasing ammonia capacity. Also, the generation of additional sites (e.g. Lewis acid sites through dealumination) could cause a change in acidity.

4.1.3. N_2 Physisorption

To understand any porosity changes, N_2 physisorption was used.

Table 4-1: Porosity characterization of La13X with ion exchange temperatures of RT, 40 and 60 °C determined using a Micromeritics Tristar-3000. Prior to characterization each sample was dried overnight at 550 °C under flowing nitrogen. Samples were then loaded into tubes and further dried at 120 °C under vacuum. N_2 adsorption and desorption isotherms were then obtained at 77K.

Sample	RT	40 °C	60 °C
BET Surface area	609.1 m^2/g	603.3 m^2/g	577.7 m^2/g
t-Plot Micropore Area	544.4 m^2/g	550.4 m^2/g	528.9 m^2/g
t-Plot External Surface Area	64.7 m^2/g	52.9 m^2/g	48.8 m^2/g
t-Plot Micropore Volume	0.204 cm^3/g	0.254 cm^3/g	0.250 cm^3/g
Adsorption Average Pore Diameter (4V/A by BET)	16.9 Å	19.8 Å	20.2 Å

As can be seen in Table 4-1, the temperature that the lanthanum ion exchange process occurs at has an effect on the porosity of the final materials. As temperature increases, the samples show a lower total BET surface area coupled with an increasing pore volume and average pore diameter. The surface area of the zeolites decreases from 609.1 m^2/g when ion exchange is carried out at

room temperature, to 603.3 m²/g when carried out at 40 °C to 577.7 m²/g at 60 °C, respectively. This supports the idea that carrying out the lanthanum ion exchange at higher temperatures increases the disruption caused to the zeolite, leading to a decreased ammonia capacity. Dealumination has been shown to decrease surface area of zeolites.[5]

4.1.4. Al-NMR

Al-NMR was used to determine which ion exchange processes gave disordered aluminium environments and to what extent.

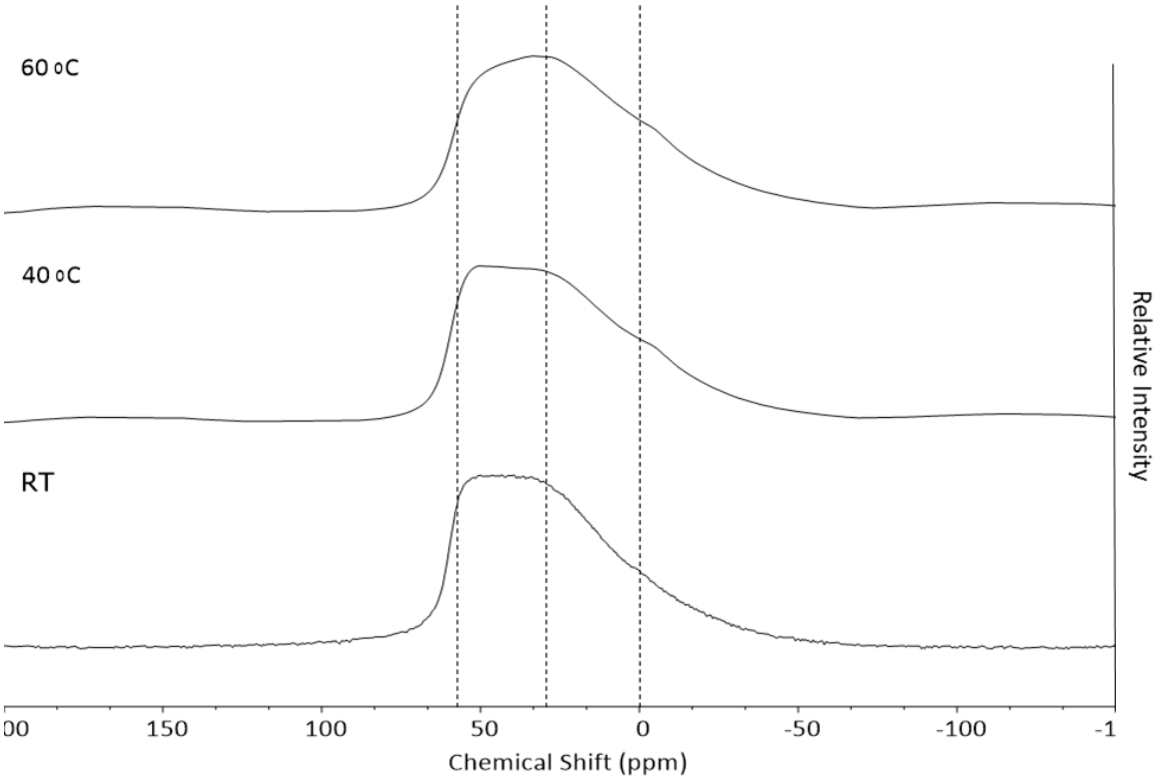

Figure 4-3: ^{27}Al NMR measurements of La13X after ion exchange for at room temperature, 40 °C and 60 °C, recorded on a Bruker AVIII 400 spectrometer, at a Larmor frequency of 104.34 MHz. A one pulse sequence was adopted, with a 10° pulse, a delay time of 0.4 s and a scanning number of 8000. The chemical shift was referenced to an aqueous 1M $AlCl_3$ solution. Dotted lines correspond to 0, 30 and 55 ppm, indicating 6, 5 and 4 coordinate aluminium, respectively.[6]

Figure 4-3 shows the effect that ion exchange temperature has on the ion exchange process using NMR. The three NMR spectra are very similar; each shows a broad asymmetric peak encompassing 55 and 30 ppm indicating that four and six coordinated aluminium is present,

respectively.[6] There is a slight shift compared to literature values, possibly due to very slight differences in the coordination environments.

The broad peak seen in RT La13X becomes more broadened from RT to 40°C and then 60°C, showing a more significant shoulder peak at 0 ppm (higher degree of six coordinated aluminium species). This indicates more 4 coordinated aluminium is generated and so an increasing degree of dealumination has occurred. This supports the TPD and BET data suggesting dealumination. La13X exchanged at 60 °C seems to show an increase in 5 coordinate aluminium; the broad peak is higher in the 30 ppm region, indicative of disordered species such as 5 coordinated aluminium.[7]

Deng *et al.* used ^{27}Al NMR to study the dealumination process of zeolite Y after increasing calcination temperatures. They found that the dealumination process is initially the conversion of four coordinate framework aluminium to six coordinate extra-framework aluminium.[8] The pristine sample showed only a 55 ppm peak, corresponding to four coordinate framework aluminium, while the mildly dealuminated sample also showed an additional peak at 4 ppm, assigned to six coordinate extra-framework aluminium. At higher levels of dealumination there was a further peak at 30 ppm. This was assigned to five coordinate aluminium species. It is interesting to note that this species is only seen at high levels of dealumination; this is reportedly a product of water molecules reacting further with the four coordinated aluminium species.[8] This matches well with the spectra seen here. The increase of the five coordinate aluminium peak relative the four coordinate aluminium peak is seen in the 60 °C sample, indicating that the zeolite here is undergoing a similar dealumination pathway to seen in literature.[8]

There is some evidence in the literature suggesting that an ion exchange equilibria with faujasite type zeolites can be reached at room temperature and that higher temperatures do not show a significant effect.[9] However, this contradicts the changes in the surface areas and TPD data we

observed, which suggested that there was greater dealumination in the higher temperature samples with the increase in extra-framework aluminium.

Often, increasing acidity of zeolite samples is attributed to increased Lewis acidity as a result of the dealumination.[5] This cannot be unambiguously determined from this NMR data. A comprehensive review on Lewis acidity in zeolites by Bokhoven *et al.* shows that there is not a direct correlation between the existence of extra-framework aluminium and Lewis acidity.[10] This is because not all extra-framework species exhibit acidity. Therefore, the fact dealumination occurs cannot alone be used to infer there will be an increase in acidity. Instead, techniques such as TPD are more applicable as a means to study the acidity of zeolites.

4.1.5. XRD

High quality XRD patterns were collected for each sample and used to determine the structure of each of the modified zeolites.

The structures of each of the La13X zeolites is very similar to that of the previously discussed La13X zeolite (Chapter 3). The variations are in the sodium occupancies, lanthanum occupancies and location and occupancies of the ammonia sites. The starting point for the temperature altered ion exchange samples was the previously determined La13X structure which was itself based on the Na13X model by Olson.[11] The site positions, occupancies and isotropic displacement factors were allowed to refine (more detail is available in Chapter 2).

First, the locations of the lanthanum ions were determined at high angles; as ammonia contains only light elements it is not expected that the adsorbed ammonia molecules will affect the diffraction pattern at high angles.

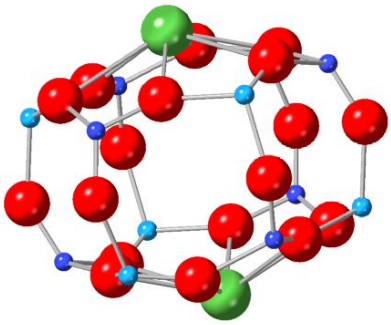

a. La1, located just beyond the hexagonal faces of the prisms which join the sodalite cages.

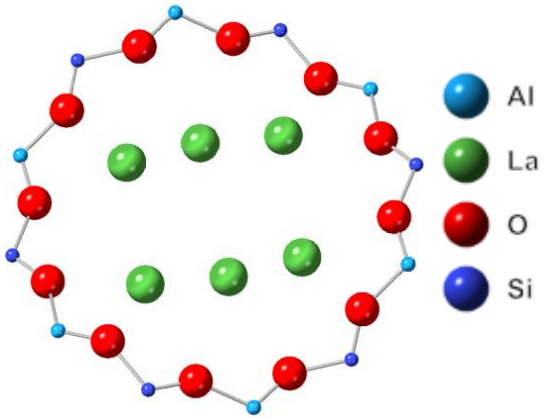

b. La2, located in the main channel of the zeolite.

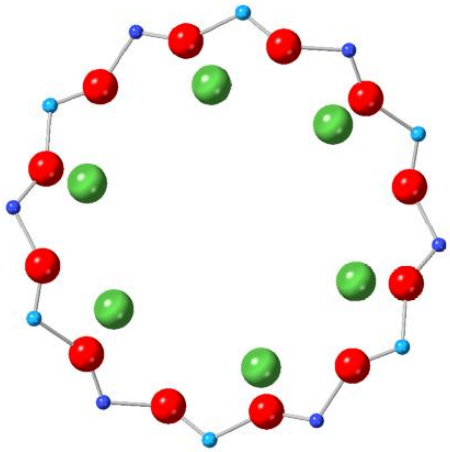

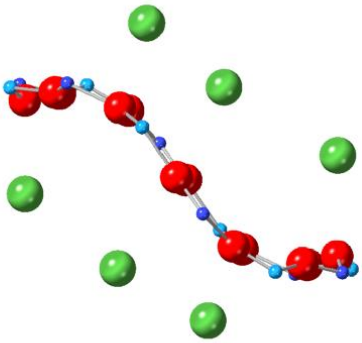

c. La3, located in the main pore of the zeolite, out of the plane of the Al/Si/O ring.

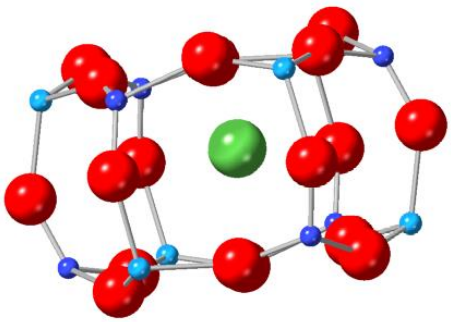

d. La4, located within the joining hexagonal prisms.

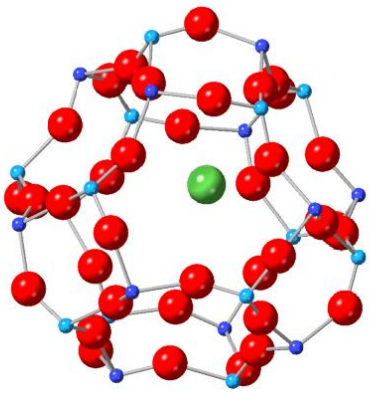

e. La5, located within the sodalite cage.

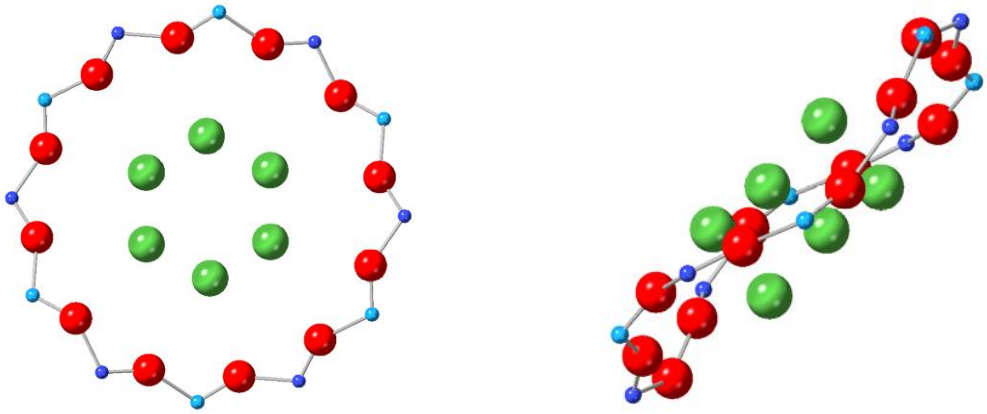

f. La6, located in the main pore of the zeolite, out of the plane of the Al/Si/O ring.

Figure 4-4: Locations of the six lanthanum sites in the La13X zeolite, as determined by Rietveld refinement of XRD pattern. Exact positions are from La13X (16 hours, RT).

The differing occupancies of the lanthanum sites was used to track the ion exchange process between the zeolites.

Table 4-2: Occupancies of each La site, as determined by Rietveld refinement of XRD patterns.

Site	RT La13X Site Occupancy	40 °C La13X Site Occupancy	60 °C La13X Site Occupancy
La1	0.300(0)	0.247(2)	0.245(1)
La2	0.018(1)	0.020(3)	0.012(3)
La3	0.016(0)	0.011(4)	0.017(5)
La4	0.020(1)	0.016(2)	0.014(3)
La5	0.015(1)	0.025(1)	0.027(1)
La6	0.019(1)	0.027(3)	0.031(2)

As can be seen in Table 4-2 the high temperature ion exchange experiments, although partially increasing dealumination, have not led to more efficient ion exchange. Site La1, which shows the highest occupancy and contributes to the ammonia capacity, decreases with higher ion exchange temperatures. With room temperature ion exchange the occupancy is 0.300, at 40 °C the occupancy is 0.247 and at 60 °C the occupancy is 0.245. This demonstrates how the increased disorder (as seen by the decreased surface area and Al-NMR) has not improved the overall ion exchange efficiency.

This is similar to that seen in silver ion exchange of zeolite Y,[12] where dealumination did not correspond to increased ion exchange. It was not previously clear if the improved ammonia adsorption capacity upon introduction of lanthanum (see chapter 3) was the result of the increasing disorder of the structure or due to lanthanum itself. These samples show lower apparent ammonia capacity coupled with higher exchange temperatures causing greater structural disruption. This suggests that the ammonia capacity can be attributed to the lanthanum ion concentration, not the structural disruption.

It seems that the increased dealumination is causing a decrease in the lanthanum occupancies. This can be partially attributed to the fact that the increasing dealumination means there are less interactions between the lanthanum ions and the framework leading to reduced stability. Lanthanum leaching from the structure would be expected if the lanthanum was less stable and such leaching would be entropically favourable, further promoting this pathway. A similar effect was seen in Cu-ZSM-5, where dealumination was coupled with a loss of copper from the structure.[13]

It is likely that the dealuminated extra-framework aluminium also plays a role in the lanthanum occupancies. DFT studies by Liu and colleagues compared the stability of extra-framework species in various locations within faujasite zeolites.[14] They found that although mono-nuclear extra-framework species are found in the main pore of the zeolite, over time the most thermodynamically stable location for extra-framework aluminium species was within the sodalite cage and it was favourable for clusters to form.[14] This could explain the decreased La1 occupancy seen here; increased dealumination leading to more alumina species within the sodalite cage would decrease the space available for lanthanum ions and so decrease the La1 occupancy.

Another interesting observation from the calculated lanthanum occupancies is that the La5 occupancy increases slightly when higher ion exchange temperatures are used. As can be seen in Figure 4-4, this site is located within the prisms joining the sodalite cages – a very constrained site. It is likely that the dealumination makes this constrained site more accessible and so the occupancy increases. However, as this site is not involved in ammonia binding this increased occupancy is not expected to have an effect on ammonia capacity.

The locations of the ammonia molecules were determined and three sites found in each of the high temperature exchanged samples, all also present in the room temperature La13X. The XRD determined capacities were compared to those determined experimentally. At 40 ^{o}C La13X showed a 5.2 % capacity here and a 3.7 ± 2.0 % experimental capacity while 60 ^{o}C La13X showed a 4.4 % capacity here and a 6.3 ± 2.0 % experimental capacity. There are clearly some discrepancies, though it is important to note that the structure in XRD only accounts for the crystalline phases. No extra-framework aluminium was seen in XRD despite it being present so the XRD capacities are not directly comparable.

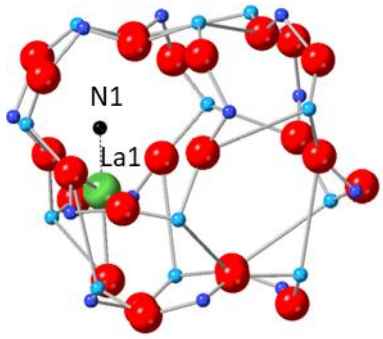

a. N1, in distorted sodalite cage.

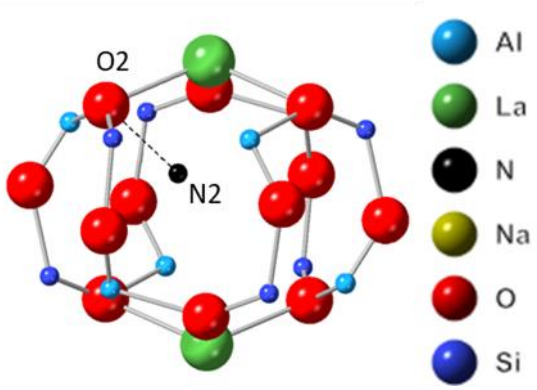

b. N2, in distorted hexagonal prisms joining the sodalite cages, binding to O2 and close to La1.

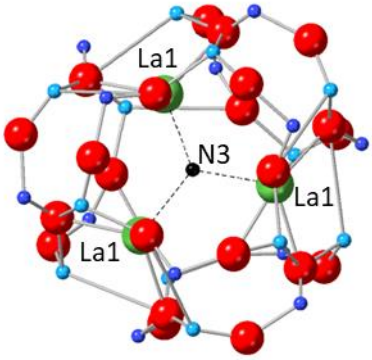

c. N3, in distorted sodalite cage.

Figure 4-5: Location of N atoms of ammonia molecules, the La13X zeolite, as determined by Rietveld refinement of XRD pattern.

Table 4-3: Occupancies of each NH_3 site, as determined by Rietveld refinement of XRD patterns.

Site	RT La13X	40 °C La13X	60 °C La13X
N1	0.123(78)	0.147(19)	0.161(20)
N2	0.222(9)	0.186(23)	0.141(15)
N3	0.467(4)	0.358(14)	0.288(48)
N4	0.131(6)	0	0

Table 4-3 shows the change in occupancies of the ammonia sites when the zeolite undergoes ion exchange at different temperatures. There is no significant change in the occupancy of site N1 between the samples.

As can be seen in Table 4-3, the occupancy of N2 is significantly lower in the higher temperature ion exchange sample; the 0.222 RT La13X occupancy decreases to 0.186 and 0.141 at 40 °C La13X and 60 °C La13X. The occupancy of site N3 decreases to a greater extent with ion exchange

temperature from 0.467 at room temperature, to 0.358 at 40 °C and 0.288 at 60 °C. This is in line with the decreased La1 occupancy. Furthermore, dealumination results in a breakdown of the zeolite framework structure which would be expected to affect the ammonia capacity as there is some degree of interaction with the framework in all ammonia sites. This is especially true of site N2, where the binding site is a framework oxygen, and site N3 where the ammonia is stabilised through multiple interactions. Dealumination here could greatly affect this binding, which explains why these show the greatest proportional decrease. Moreover, dealumination is reported to generate aluminium species preferentially located within the sodalite cage[14]; this would be expected to lower the ammonia capacity as potential vacancies for ammonia become filled with extra-framework aluminium.

One further reason for the lowered occupancy in the high temperature ion exchange samples is the loss of site N4; the gate site that was seen in the previous RT-La13X sample. Clearly, it is more favourable for samples where the ion exchange was carried out at higher temperatures to store ammonia in the sodalite cage sites. This would be expected if the increased dealumination (expected from surface area and literature[12]) gives a more open structure, making these sites more accessible. Furthermore, it is possible that the dealuminated aluminium is present in the pores, though non crystalline and so unidentifiable using XRD. This would also make site N4 unfavourable, as is seen here.

4.1.6. Effect of Temperature Conclusions

It is clear that the temperature at which the ion exchange process takes place has a significant effect on the ammonia capacity of the synthesised zeolite. Higher ion exchange temperatures gave a lower ammonia capacity due to the increased dealumination in the samples. The dealumination could be seen in the change in the Al-NMR spectra, the decreasing BET surface area and an additional high temperature peak in the TPD trace indicative of structural disruption.

XRD showed that this decreased the La1 occupancy which led to a decreased number of ammonia sites. The dealumination is proposed to lower La1 occupancy through decreased interactions between lanthanum and the zeolite framework and blocking by aluminium species. The lower ammonia capacity can also be attributed to these factors.

4.2. Effect of Time

The effect of the duration of ion exchange was studied, by comparing 24 and 48 hour ion exchange times with the standard 16 hours.

4.2.1. Ammonia Capacity

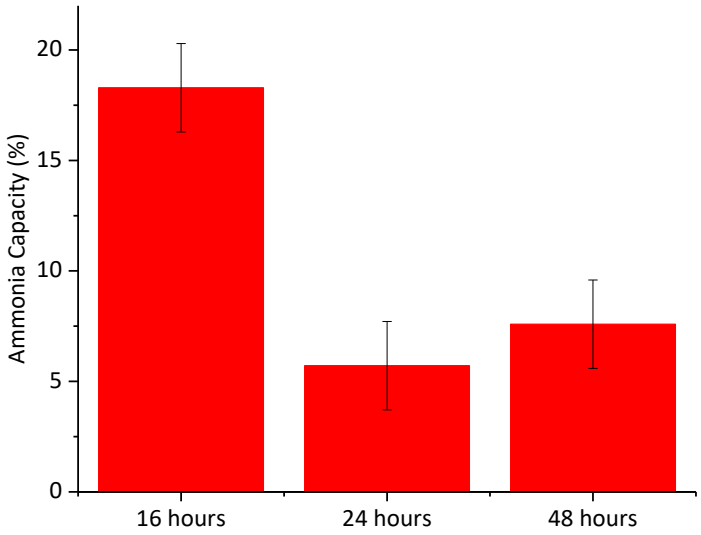

Figure 4-6: Ammonia storage capacity of La13X samples which underwent ion exchange for 16, 24 and 48 hours. Samples (approximately 1 g) were connected to a Schlenk vacuum line and dried at 550 °C under vacuum for 4 hours. The samples were allowed to cool to room temperature and then exposed to pure ammonia gas (approximately 400 mbar) for 45 minutes. To determine capacity the samples were placed in a TA Instruments Q600 SDT. Approximately 10 mg of sample was placed in the SDT. The temperature was increased to 600 °C at a rate of 10 °C/min under 100 mL/min flowing nitrogen and the weight change recorded. The 450 °C sample weight was used to calculate ammonia capacity, assuming all weight loss up to this point was due to ammonia. (See Appendix for method validation.)

Figure 4-6 shows the effect of longer ion exchange times on the ammonia capacity of the La13X samples. The longer experiments have clearly had a detrimental effect on the ammonia capacity

of the materials with the 18.3 ± 2.0 % capacity of 16 hour La13X decreasing to 5.7 ± 2.0 % for 24 hour La13X and 7.6 ± 2.0 % for 48 hours La13X. This may be due to the increased structural changes, as was seen in the high temperature samples. There is evidence in literature that at least 24 hours is required to reach an equilibrium ion exchange point[9]; it is possible that when more La ions are introduced at the equilibrium conditions, they could introduce a structural collapse of the La13X sample due to electrostatic repulsion of La ions within the framework (dealumination). The further characterisation here discusses this further.

4.2.2. Ammonia Desorption

The desorption profiles of the ammonia loaded samples were compared.

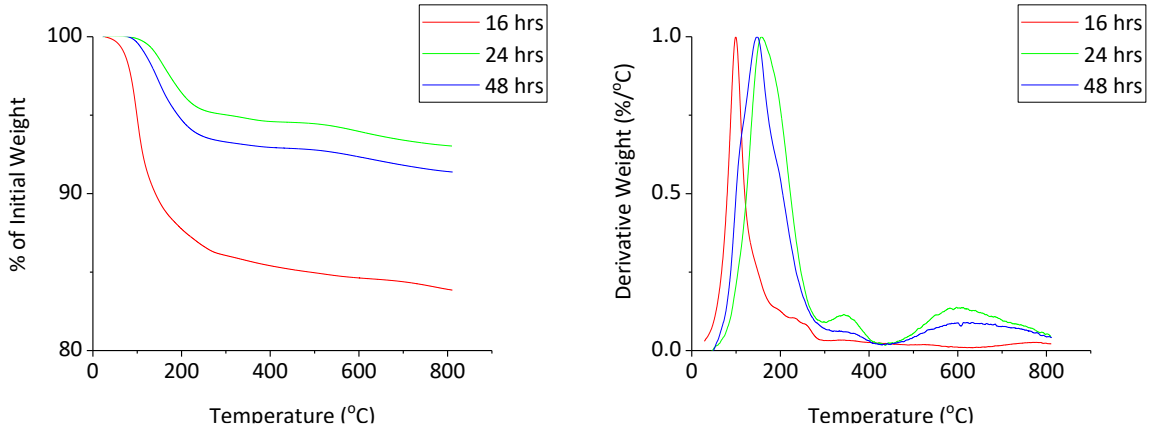

Figure 4-7: Desorption of ammonia on La13X prepared by ion exchange of Na13X for 16, 24 and 48 hours recorded on a TA Instruments Q600 SDT. First the samples were dried under flowing N_2 at 550 °C for five hours, then attached to a Schlenk line. They were dried under vacuum at 550 °C for four hours, cooled to room temperature and then pure ammonia gas was added (around 400 mbar, for 45 minutes.) The samples were placed in the SDT and the temperature was increased to 800 °C at a rate of 10 °C/min under 100 mL/min flowing nitrogen and the weight change recorded.

As can be seen in Figure 4-7 the desorption patterns of the samples ion exchanged for differing times are broadly similar. Longer ion exchange times lead to slightly higher temperature desorption with the room 16 hour La13X peak at 96 °C increasing to 158 °C after 24 hours and 144 °C after 48 hours. This is a less significant change than was seen in the varied temperature samples, suggesting that ion exchange time has less of an effect than temperature on the

strength of the ammonia zeolite interactions. The position of this peak has been shown to be related to lanthanum occupancy, both in literature[3] and in the temperature varied samples. Furthermore, the longer duration ion exchange samples (24 hours and 48 hours) also show an additional peak at high temperature (500 °C and above). This was again attributed to a generated instability in the zeolite structure, as was also reported by Triguerio *et al*.[4] This demonstrates that both longer and higher temperature ion exchange generate structural instability in the zeolite. Also, any generation of additional sites (e.g. Lewis acid sites through dealumination) could cause a change in acidity.

4.2.3. N_2 Physisorption

To understand any porosity changes, N_2 physisorption was used.

Table 4-4: Porosity characterization of La13X with ion exchange times of 16, 24 and 24 hours determined using a Micromeritics Tristar-3000. Prior to characterization each sample was dried overnight at 550 °C under flowing nitrogen. Samples were then loaded into tubes and further dried at 120 °C under vacuum. N_2 adsorption and desorption isotherms were then obtained at 77K.

Sample	16 hours	24 hours	48 hours
BET Surface area	609.1 m^2/g	585.5 m^2/g	611.5 m^2/g
t-Plot Micropore Area	544.4 m^2/g	535.2 m^2/g	554.6 m^2/g
t-Plot External Surface Area	64.7 m^2/g	50.2 m^2/g	56.9 m^2/g
t-Plot Micropore Volume	0.204 cm^3/g	0.258 cm^3/g	0.257 cm^3/g
Adsorption Average Pore Diameter (4V/A by BET)	16.9 Å	20.5 Å	19.7 Å

As shown in Table 4-4 the duration of the ion exchange experiments has an effect on the porosity, however, this is not a clear linear relationship such as is seen with the varying temperature experiments. Between 16 and 24 hours there is a decrease in surface area (from 609.1 m^2/g to 585.5 m^2/g), coupled with an increase in pore volume (from 0.204 cm^3/g to 0.258 cm^3/g) and pore diameter (from 16.9 Å to 20.5 Å) as would be expected with greater structural breakdown over a longer time. However, after a 48 hour ion exchange an increase in surface area was seen (to

611.5 m^2/g), compared to both the 16 and 24 hours samples. This is determined to be as a result of an increase in both micropore surface area. External surface area can be related to the particle size[15] and so the increase in external surface area from 50.2 m^2/g after 24 hours to 56.9 m^2/g after 48 hours would indicate an increasing particle size over time, though this appears to be a competing effect with the decrease in surface area with dealumination.

4.2.4. Al-NMR

Al-NMR was used to determine which ion exchange processes gave disordered aluminium environments and to what extent.

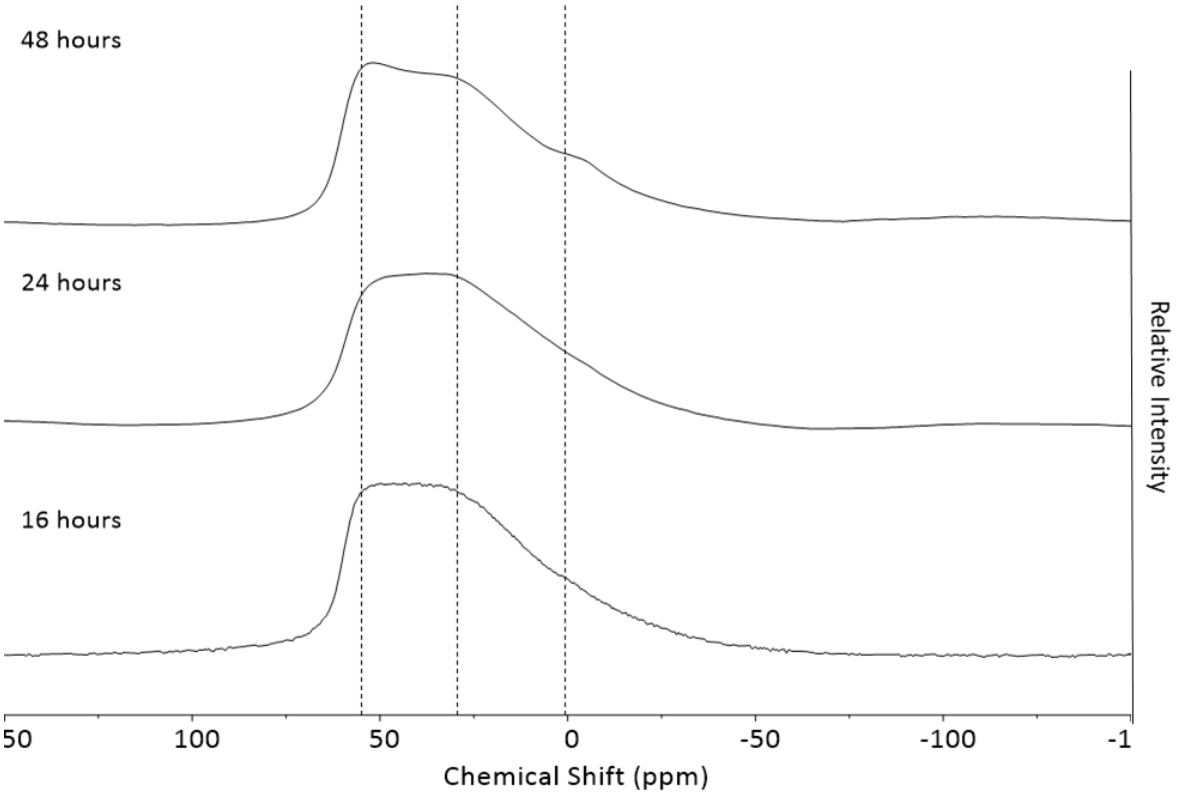

Figure 4-8: ^{27}Al NMR measurements of La13X after ion exchange for 16, 24 and 48 hours, recorded on a Bruker AVIII 400 spectrometer, at a Larmor frequency of 104.34 MHz. A one pulse sequence was adopted, with a 10° pulse, a delay time of 0.4 s and a scanning number of 8000. The chemical shift was referenced to an aqueous 1M $AlCl_3$ solution. Dotted lines correspond to 0, 30 and 55 ppm, indicating 6, 5 and 4 coordinate aluminium, respectively.[6]

As can be seen in Figure 4-8, the NMR spectra show that different ion exchange times has an effect on the aluminium environments present in zeolites. There is little difference between the experiments carried out for 16 and 24 hours which both show four coordinate and five coordinate

aluminium sites (at around 55 and around 30 ppm respectively[6]) in similar amounts and a small asymmetry in the peak suggesting six coordinate aluminium (at around 0 ppm[6]). Some changes are seen between these samples and the 48 hour exchanged sample. There is greater differentiation between the constituent four, five and six coordination peaks in the 48 hours calcined sample. This is indicative of a decreasing number of aluminium environements.[16] The very broad peaks seen in the 16 and 24 hour exchange samples are indicative of distortion of the four, five and six coordinate aluminium sites or intermediate positions between the type of sites[16], as a result of the dealumination process. The greater differentiation between these peaks suggests that the longer ion exchange time give more time for an equilibrium to establish and so intermediate sites between e.g. five and six coordinate aluminium are not present. There is evidence in literature that at least 24 hours is required to reach an equilibrium[9]; clearly longer is required here. The sample which underwent ion exchange for 48 hours shows a more significant peak at 0 ppm, corresponding to extra-framework aluminium[7] and so supports a greater degree of dealumination.

4.2.5. XRD

High quality XRD patterns were collected for each sample and used to determine the structure of each of the modified zeolites. The starting point for the varying time ion exchange samples was the previously determined La13X structure which was itself based on the Na13X model by Olson.[11] The site positions, occupancies and isotropic displacement factors were allowed to refine (more detail is available in Chapter 2). Again, the same lanthanum sites were present in the longer duration ion exchange samples (see Figure 4-4).

The occupancies of the lanthanum sites were studied to track the ion exchange process.

Table 4-5: Occupancies of each La site, as determined by Rietveld refinement of XRD patterns.

Site	16 hr La13X Site Occupancy	24 hr La13X Site Occupancy	48 hr La13X Site Occupancy
La1	0.300(0)	0.241(1)	0.242(3)
La2	0.018(1)	0.015(3)	0.011(3)
La3	0.016(0)	0.020(2)	0.017(2)
La4	0.020(1)	0.020(3)	0.020(3)
La5	0.015(1)	0.024(1)	0.024(1)
La6	0.019(1)	0.016(2)	0.019(2)

As can be seen in Table 4-5, there is slight variation in the lanthanum occupancies in the samples which underwent longer ion exchange. The occupancy of La1, which was determined to lead to the majority of ammonia capacity, decreases from 0.300 after 16 hours, to 0.241 and 0242 after 24 and 48 hours, respectively. It was suggested previously that the increasing dealumination would reduce the stability of lanthanum ions due to decreased interactions with the zeolite framework, leading to lanthanum leaching. This appears to be the case here. It is evident that the higher lanthanum content sample with less structural disruption gives lower desorption temperature. The attempted further inclusion of lanthanum species into the structure using higher temperatures seems to have caused damage in structure hence the resulting dealuminated samples containing lower lanthanum (as it has been leached) and extra-framework aluminium show higher ammonia desorption temperature. Moreover, it was suggested that dealuminated extra-framework aluminium species form preferentially in the sodalite cage.[14] The increased dealumination in these samples may be causing this and so the La1 occupancy decreases.

Two ammonia sites were present in the samples. The determined structure seems to match fairly well with the experimental ammonia capacities; 24 hr La13X showed a 4.5 % capacity here and a 5.7 ± 2.0 % experimental capacity while 60 ^{o}C La13X showed a 6.4 % capacity here and a 7.6 ± 2.0 % experimental capacity.

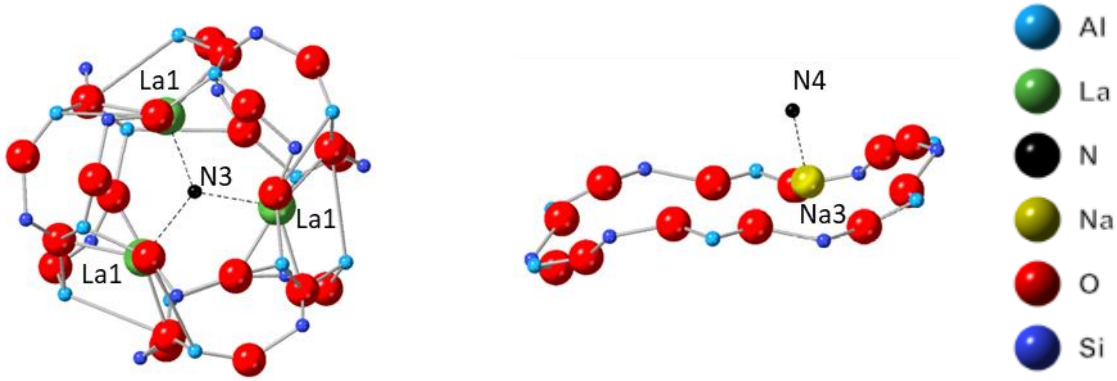

a. N3, in distorted sodalite cage.

b. N4, in the main pore between sodium ions.

Figure 4-9: Location of N atoms of ammonia molecules, the La13X zeolite, as determined by Rietveld refinement of XRD pattern.

Table 4-6: Occupancies of each NH_3 site, as determined by Rietveld refinement of XRD patterns.

Site	16 hr La13X Site Occupancy	24 hr La13X Site Occupancy	48 hr La13X Site Occupancy
N1	0.123(78)	0	0
N2	0.222(9)	0	0
N3	0.467(4)	0.367(11)	0.382(11)
N4	0.131(6)	0.248(26)	0.403(24)

The occupancies of the relevant ammonia sites can be seen in Table 4-6. The N1 site present in the other zeolites was absent from the 24 and 48 hour ion exchanged samples. Instead, N3 is the sole sodalite cage site. The occupancy of N3 decreases with increasing ion exchange time from 0.467 when the zeolite was exchanged for 16 hours to 0.367 and 0.382 when exchanged for 24 and 48 hours, respectively. There are multiple factors which affect capacity in this site. Given this site binds to La1, the occupancy of La1 will affect the possible ammonia capacity. This would partially account for the decreasing occupancy. Furthermore, the degree of dealumination affects the site occupancy. As was seen in the temperature varied samples, greater dealumination affects the ammonia capacity as there is interaction with the zeolite framework as well as the lanthanum binding sites. Moreover, dealumination is reported to generate aluminium species preferentially located within the sodalite cage[14]; this would be expected to lower the ammonia capacity as potential vacancies for ammonia become filled with extra-framework aluminium. The decrease in

N3 occupancy with decreasing La1 occupancy was also seen in the varied temperature ion exchange series, suggesting that the N3 occupancy is correlated with La1 occupancy.

The occupancy of gate site N4 increases in the 24 and 48 hour samples, from 0.131 in the 16 hour sample to 0.248 and 0.403, respectively. The high temperature ion exchange samples showed that increased dealumination made this a less favourable site, though this is not seen here. It is possible that the location of extra-framework aluminium species leads to this difference. It was reported in the literature that extra-framework aluminium is initially present in the main pore and then moves to the sodalite cage.[14] It is possible that the longer ion exchange times used here have allowed for a greater portion of the extra-framework aluminium species to migrate. This would account for the increased N4 occupancy seen here. It is also possible that the less effective lanthanum exchange process means that there can be a greater number of sodium ions remaining and so these are more available for ammonia binding. As these are gate sites it is likely that the other ammonia molecules will pass through these during the desorption process.

4.2.6. Effect of Time Conclusions

The effect of ion exchange duration was studied. Both of the samples which underwent longer ion exchange showed lower ammonia capacity than the standard 16 hour sample. TPD suggests that this was partially due to an increased level of instability in the material which was also shown in decreased surface area. Furthermore, Al-NMR suggested that the samples which were ion exchanged for longer showed greater dealumination coupled with less intermediate species. XRD showed that this decreased the La1 occupancy which led to a decreased number of ammonia sites. The dealumination is proposed to lower La1 occupancy through decreased interactions between lanthanum and the zeolite framework and blocking by aluminium species. The lower ammonia capacity can also be attributed to these factors. It was also proposed that the longer ion

exchange time allows for movement of the extra-framework lanthanum species, altering the most favourable ammonia positions.

4.3. Effect of La^{3+} Ion Concentration

The effect of the lanthanum ion concentration during the ion exchange was also studied, by comparing initial concentrations of 0.5 and 1.5 times the original concentration.

4.3.1. Ammonia Capacity

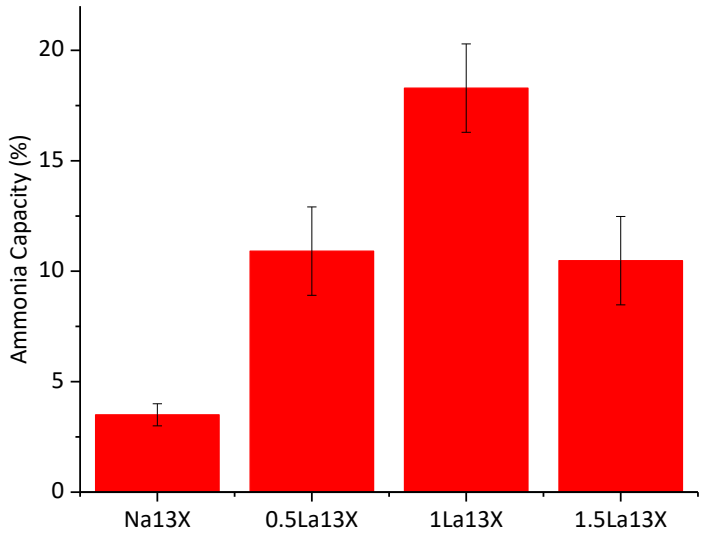

Figure 4-10: Ammonia storage capacity of Na13X, 0.5La13X, 1La13X and 1.5La13X. Samples (approximately 1 g) were connected to a Schlenk vacuum line and dried at 550 °C under vacuum for 4 hours. The samples were allowed to cool to room temperature and then exposed to pure ammonia gas (approximately 400 mbar) for 45 minutes. To determine capacity the samples were placed in a TA Instruments Q600 SDT. Approximately 10 mg of sample was placed in the SDT. The temperature was increased to 600 °C at a rate of 10 °C/min under 100 mL/min flowing nitrogen and the weight change recorded. The 450 °C sample weight was used to calculate capacity, assuming all weight loss up to this point was due to ammonia. (See Appendix for method validation.)

Figure 4-10 shows the ammonia capacity of 13X with varying lanthanum contents. All of the samples containing lanthanum showed higher ammonia capacity than Na13X. The capacity increases from 3.5 ± 0.5 % for unmodified Na13X to 10.9 ± 2.0 %, 18.3 ± 2.0 % and 10.5 ± 2.0 % for

0.5La13X, 1La13X and 1.5La13X, respectively. Clearly, there is an optimum level on lanthanum concentration with both too low and too high lanthanum concentrations lowering the ammonia capacity. There are a number of possible reasons for this. Previously, we have shown that the lanthanum improves ammonia capacity through the creation of additional binding sites within the sodalite cage of the zeolite (see Chapter 3 for further detail). This explains the decreased capacity of almost a half in the 0.5La13X sample compared to 1La13X. There is clearly a different effect leading to the decreased capacity in 1.5La13X. Lercher *et al.* found that the location and number of the lanthanum ion within faujasite type zeolites changes with the concentration of lanthanum ions in ion exchange solution.[1] At high lanthanum ion concentrations the lanthanum ions repel each other during the exchange process. If a similar effect occurs here there would be a lowered lanthanum concentration within the 1.5La13X sample and consequently a lowered ammonia capacity.

It is important to note that the La contents are target values; further experiments would be required to confirm the actual lanthanum contents of the samples which would allow for the lanthanum content to be more directly related to ammonia capacity.

4.3.2. Ammonia Desorption

The desorption profiles of the ammonia loaded samples were compared.

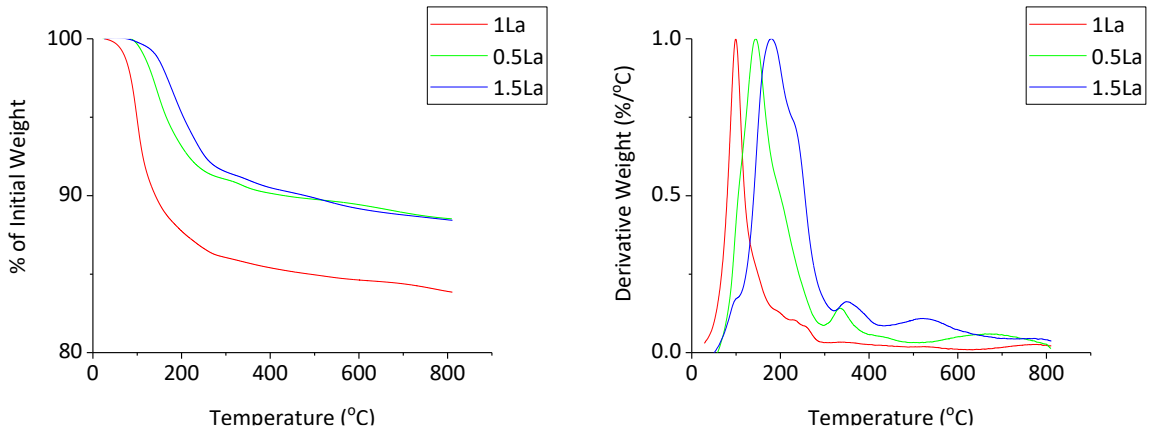

Figure 4-11: Desorption of ammonia on La13X with La ratios of 0.5, 1 and 1.5 times the previous experiments recorded on a TA Instruments Q600 SDT. First the samples were dried under flowing N_2 at 550 °C for five hours, then attached to a Schlenk line. They were dried under vacuum at 550 °C for four hours, cooled to room temperature and then pure ammonia gas was added (around 400 mbar, for 45 minutes.) The samples were placed in the SDT and the temperature was increased to 800 °C at a rate of 10 °C/min under 100 mL/min flowing nitrogen and the weight change recorded.

There are only slight differences between the ammonia desorption on the different lanthanum ratio zeolites, as can be seen in Figure 4-11. Interestingly, 0.5La13X, 1La13X and 1.5La13X all show broadly similar desorption patterns, with derivative weights of each sample all showing that the majority of desorption is low temperature. 1.5La13X shows the highest temperature desorption peaking at 177 °C (compared to 96 °C for 1La13X and 145 °C for 0.5La13X) indicating that the higher level of lanthanum gives more strongly bound ammonia, as Corma *et al.* showed and was seen in the previously discussed samples.[3] Furthermore, there is additional evidence of this concentration effect in the literature; varying lanthanum coordination in zeolite Y slightly increased the ammonia desorption temperature.[2] Interestingly, this work also did not show a linear relationship between lanthanum concentration and ammonia desorption temperature, as was seen here. 1.5La also shows a small high temperature peak as is seen in some of the other samples indicative of the zeolite starting to breakdown. This suggests that the high concentration of lanthanum in the ion exchange solution can cause some instability in the structure though less than e.g. high temperatures or longer ion exchange times.

4.3.3. N_2 Physisorption

To understand any porosity changes, N_2 physisorption was used.

Table 4-7: Porosity characterization of La13X with lanthanum ion concentrations of 0.5, 1 and 1.5 times the initial concentration and the unmodified Na13X, determined using a Micromeritics Tristar-3000. Prior to characterization each sample was dried overnight at 550 °C under flowing nitrogen. Samples were then loaded into tubes and further dried at 120 °C under vacuum. N_2 adsorption and desorption isotherms were then obtained at 77K.

Sample	Na13X	0.5 La13X	1 La13X	1.5 La13X
BET Surface area	818.9 m^2/g	597.0 m^2/g	609.1 m^2/g	617.7 m^2/g
t-Plot Micropore Area	730.8 m^2/g	547.7 m^2/g	544.4 m^2/g	571.9 m^2/g
t-Plot External Surface Area	88.0 m^2/g	49.3 m^2/g	64.7 m^2/g	45.8 m^2/g
t-Plot Micropore Volume	0.272 cm^3/g	0.259 cm^3/g	0.204 cm^3/g	0.265 cm^3/g
Adsorption Average Pore Diameter (4V/A by BET)	15.8 Å	20.0 Å	16.9 Å	19.4 Å

Table 4-7 shows the influence of varying initial lanthanum ion concentration during ion exchange. Na13X is included for a comparison of no lanthanum; it is clear that any lanthanum ion exchange at all has a significant effect on the surface area, pore volume and pore diameter of the materials; more so than variations in lanthanum ion concentration.

Increasing lanthanum ion concentration causes an increasing surface area. 0.5La13X has surface area 597.0 m^2/g and 1La13X a slightly greater surface area of 609.1 m^2/g. This would be expected from greater number of lanthanum ions within the structure giving additional surface area. At lower lanthanum ion concentrations the pores may have larger diameter due to the lack of large lanthanum ions in them.1.5La13X the highest surface area at 617.7 m^2/g, however the large pore diameter and pore volume is close to 0.5La13X, suggesting a low lanthanum ion content.

4.3.4. Al-NMR

Al-NMR was used to determine which ion exchange processes gave disordered aluminium environments and to what extent.

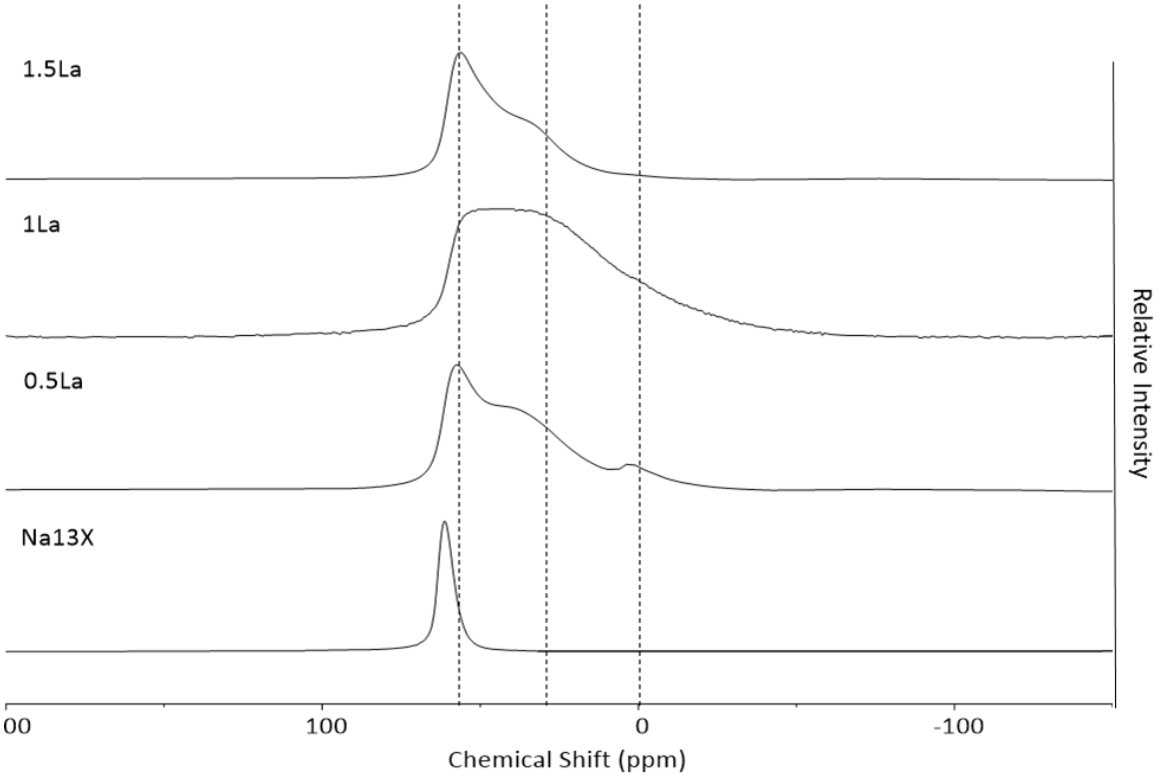

Figure 4-12: ^{27}Al NMR measurements of La13X with relative La of 0.5, 1 and 1.5 and Na13X (i.e. 0 La) for comparison, recorded on a Bruker AVIII 400 spectrometer, at a Larmor frequency of 104.34 MHz. A one pulse sequence was adopted, with a 10° pulse, a delay time of 0.4 s and a scanning number of 8000. The chemical shift was referenced to an aqueous 1M $AlCl_3$ solution. Dotted lines correspond to 0, 30 and 55 ppm, indicating 6, 5 and 4 coordinate aluminium, respectively.[6]

Figure 4-12 shows the effect of La concentration on the disorder after ion exchange.

It is clear that any level of lanthanum ion exchange leads to some degree of disorder of the zeolite structure, as is shown by the change from a single peak in the Na13X sample to multiple or broad peaks in each of the lanthanum modified samples, indicating a variety of aluminium environments[7] corresponding to structural distortion. This suggests that it is not the pH of the ion exchange solution which causes the disorder, as the pH of the 0.5La ion exchange solution is similar to that of the magnesium ion exchange solution discussed in the previous chapter. These experiments confirm that the size of the lanthanum ion and the fact that it causes significant increase in disorder (due to one La^{3+} ion replacing three Na^{+} ions) are the main drivers of the structural breakdown.

However, there does not seem to be a linear relationship between lanthanum ion exchange and the degree of structural changes caused. 1La shows the highest proportion of five coordinate aluminium (with the region between 5 ppm (4 coordinate aluminium^{6}) and 0 ppm (6 coordinate aluminium^{6}) being one roughly symmetrical peak), followed by 0.5La which has some degree of disorder with the main peak corresponding to four coordinate aluminium (55 ppm^{6}) with a shoulder corresponding to five coordinate aluminium and a small peak corresponding to four coordinate aluminium (0 ppm^{6}). Interestingly, 1.5La shows less disorder than the samples with less lanthanum, with only a four coordinate aluminium peak (55 ppm^{6}) with a small shoulder. Gong *et al.* showed that the lanthanum content in the lanthanum site La1 is one factor which has an effect on the degree of dealumination.[2] This suggests that there is less lanthanum present in the La1 site in 0.5La13X or 1.5La13X, compared to 1La13X.

4.3.5. XRD

High quality XRD patterns were collected for each sample and used to determine the structure of each of the modified zeolites. The starting point for the varying lanthanum content samples was the previously determined La13X structure which was itself based on the Na13X model by Olson.[11] The site positions, occupancies and isotropic displacement factors were allowed to refine (more detail is available in Chapter 2).

The structures of each of the La13X zeolites is very similar to the previously discussed La13X zeolite. The variations are in the sodium occupancies, lanthanum occupancies and location and occupancies of the ammonia sites.

Comparing the occupancies of the lanthanum sites is one way to track the ion exchange process. The same lanthanum sites were seen in these samples as in the 1La13X zeolite (see Figure 4-4).

Table 4-8: Occupancies of each La site, as determined by Rietveld refinement of XRD patterns.

Site	0.5La13X Site Occupancy	1La13X Site Occupancy	1.5La13X Site Occupancy
La1	0.232(2)	0.300(0)	0.145(3)
La2	0.019(3)	0.018(1)	0.025(4)
La3	0	0.016(0)	0.094(1)
La4	0.009(1)	0.020(1)	0.019(2)
La5	0.009(3)	0.015(1)	0.010(5)
La6	0.014(2)	0.019(1)	0.019(2)

As shown in Table 4-8, there is varying lanthanum occupancy in the three zeolites. La1 was the site which provided the binding site for the majority of the ammonia. At half lanthanum ion concentration (0.5La13X), the occupancy of La1 is decreased, from 0.300 to 0.232. This would be expected with lower initial concentrations, as there are less lanthanum ions available to exchange with the framework sodium.

Interestingly, the increasing lanthanum concentration in 1.5La13X does not correspond to an increase in La1 occupancy as would be expected but a decrease to 0.145. This corresponds to a significant increase in La3 occupancy, from 0.016 in the 1La13X sample to 0.094 in the 1.5La13X. Site La3 is a main pore site and is it possible that the increase occupancy here is hindering access to the sodalite cage lanthanum sites such as La1, decreasing the ammonia capacity. Furthermore, the relationship between concentration of ion exchange solution and resulting lanthanum concentration has been discussed in literature. Lercher *et al.* found that the probable location of the lanthanum ion changes with the concentration of lanthanum ions in ion exchange solution.[1] They report that at high lanthanum ion concentrations there is greater interaction between the lanthanum ions and so the more constrained positions within the sodalite cage become unfavourable. Either mechanism for lowered La1 capacity would be expected to lead to a decreased ammonia capacity as two of the ammonia sites (N1 and N3) in the unmodified structure are binding to this lanthanum site (see Chapter 3 for more detail) the decrease in occupancy of this site corresponds to a decrease in ammonia capacity.

The occupancy of the lanthanum sites other than La1 and La3 show only slight variation. They generally show a lower occupancy at lower lanthanum ion concentration, as would be expected. It is important to note that these sites did not directly contribute to ammonia bonding in 1La13X.

The lanthanum content in these samples correspond well to the proposed relationship between the lanthanum ions present in the 13X samples and the ammonia desorption temperature; the higher lanthanum content of the samples, the lower the desorption temperature of the ammonia. This is true of all the samples studied here.

Both 0.5La13X and 1.5La13X showed two ammonia sites, both of which are also present in 1La13X. Although the 1.5La13X sample XRD refinement showed a good fit with the experimental value (9.7 compared to 10.5 ± 2.0 % experimentally) the 0.5La13X did not (4.8 compared to 10.9 ± 2.0 % experimentally). It is important to note that the XRD pattern is only of the crystalline phase; any amorphous material in the zeolite sample, which may contribute to capacity, would not be seen by XRD and may account for the discrepancy in these values.

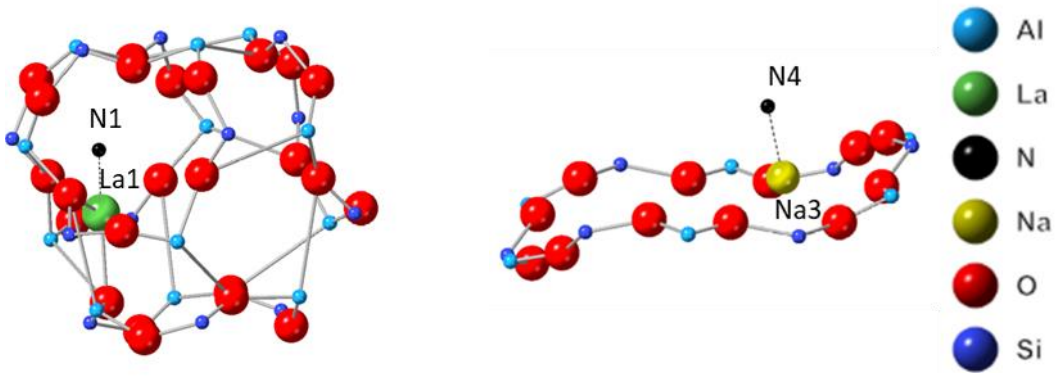

a. N1, in distorted sodalite cage. b. N4, in the main pore between sodium ions.

Figure 4-13: Location of N atoms of ammonia molecules, the La13X zeolite, as determined by Rietveld refinement of XRD pattern. (Labels are the same as in Chapter 3 for clarity)

Table 4-9: Occupancies of each NH_3 site, as determined by Rietveld refinement of XRD patterns.

Site	0.5La13X Site Occupancy	1La13X Site Occupancy	1.5La13X Site Occupancy
N1	0.396(9)	0.123(78)	0.307(9)
N2	0	0.222(9)	0
N3	0	0.467(4)	0
N4	0.254(64)	0.131(6)	0.699(26)

The occupancies of the two sites vary. N1 shows a higher occupancy in both the low and high concentration exchange samples, despite both showing a lower concentration of La1 lanthanum. These are the only samples studied here which show this. This can possibly be attributed to the lack of dealumination seen in these samples. It is possible that dealumination leads to more mobile ammonia within the sodalite cage, lowering occupancies, and so the low dealumination samples can show higher ammonia capacity here. Alternatively, there may now be more space within the sodalite cage. As discussed previously, there are a three possible ammonia sites near to or within the sodalite cage sites in 1La13X (N1, N2 and N3); it is possible that the lack of the N2 and N3 here likely leads to higher occupancy in the N1 sodalite cage site due to a less constrained environment within the sodalite cage. Furthermore, it is proposed that dealumination generates aluminium species preferentially located within the sodalite cage,[14] lowering ammonia occupancy within the sodalite cage. These samples show the least dealumination and so this effect is expected to be minimal here, increasing the N1 ammonia capacity. However, further experiments would be required to confirm these hypotheses.

Site N4 is a main pore gate site, as was seen in the other zeolites. This site binds to sodium and framework oxygen and so the change is unlikely to be directly due to the changing lanthanum content in the samples. Instead, the less effective lanthanum exchange process means that there can be a greater number of sodium ions remaining and so these are more available for ammonia binding. As these are gate sites it is likely that the N1 ammonia molecules will pass through these during the desorption process.

Although the occupancies of N1 and N4 are higher in 0.5La13X and 1.5La13X an in 1La13X the overall ammonia capacity is lower due to the loss of sites N2 and N3. This demonstrates the importance of lanthanum concentration during ion exchange in determining the ammonia capacity of the La13X. Low concentration does not offer enough binding sites while too high concentration also reduces the main ammonia binding site and so lowers the capacity. It seems likely that degree of dealumination is also affecting capacity here.

Similar non-linear relationships between target lanthanum concentration and activity are seen in literature. Xu *et al.* reported that an intermediate lanthanum concentration on zeolite Y gave the best activity of the series of prepared zeolites for fluid catalytic cracking due to varying acidity and stability.[17] Given the ammonia capacity is also related to acidity this matches well with what is seen here.

4.3.6. Effect of La^{3+} Ion Concentration Conclusions

The effect of varying ion concentrations during the ion exchange process was studied. The high levels of dealumination seen in the other samples was not seen here, as can be seen from the Al-NMR. Low La1 concentrations were seen in both samples; in 0.5La13X this was attributed to the lower lanthanum concentration in solution while in 1.5La13X this was attributed to increased lanthanum concentration in other sites blocking access. In both cases this led to a decreased ammonia capacity.

4.4. Conclusions

Various experiments showed how a number of different factors affect the lanthanum ion exchange process of zeolites and what implications this has for ammonia adsorption.

The effect of temperature on the ion exchange process was studied. Higher ion exchange temperatures gave a lower ammonia capacity due to the increased dealumination in the samples. This could be seen in the change in the Al-NMR spectra and the decreasing BET surface area. XRD showed that this decreased the number of ammonia sites and made the sodalite cage sites more favourable in comparison to main pore sites, probably as a result of dealumination and extra-framework aluminium.

Then, the effect that the ion exchange time has on the ammonia capacity was studied. Both of the samples which underwent longer ion exchange showed lower ammonia capacity than the standard 16 hour sample. TPD suggested that this was partially due to an increased level of instability in the material which also shown in decreased surface area. Furthermore, Al-NMR suggested that the samples which were ion exchanged for longer showed increased dealumination. This led to lower La1 occupancy and consequently lower ammonia capacity, due to the decrease in sodalite cage ammonia sites. This was attributed to increased lanthanum leaching due to the more open dealuminated structure and blocking of sites by extra-framework aluminium, which can move to the sodalite cage with time.

The effect of varying lanthanum ion content was also studied. There are two competing processes which affect the capacity here; a too low lanthanum ion concentration during exchange means there is not enough ammonia binding sites while too high lanthanum ion concentration leads to unwanted interaction between the lanthanum ions and blocking of the pores which also leads to a decrease in ammonia binding sites. There is clearly an optimum point which minimises these effects. Further study would allow the ideal concentration to be determined (though it is clearly between 0.5La13X and 1.5La13X, and probably close to 1La13X).

These experiments allow for some more general conclusions about favourable lanthanum ion exchange for ammonia storage. There is a relationship between the La1 occupancy and the ammonia capacity though other factors also influence this. The capacities are also affected by the degree of dealumination. Dealumination can both lower the lanthanum and ammonia capacities as there is lowered interaction between these species and the pore walls and because dealuminated extra-framework species can block access to sites. Clearly, it is not the disorder itself which improves ammonia capacity, as can be seen from the increased temperature ion exchange samples which showed greater dealumination but decreased ammonia storage. Instead, it is the lanthanum ion content in the zeolite which improves activity. Unfortunately, the dealumination process is a side effect of attempts to increase the lanthanum ion concentration within the zeolite. Further methods of increasing lanthanum ion concentration while retaining the zeolite structure should be explored. Stepwise addition of low concentration of lanthanum ions could improve the lanthanum content of the zeolite without a loss of structure which could increase the ammonia capacity even further. Furthermore, a correlation between lanthanum content in the zeolites and ammonia desorption temperature was found; higher lanthanum content corresponds to lower ammonia desorption temperatures.

4.5. References

1. F. Schüßler, E. A. Pidko, R. Kolvenbach, C. Sievers, E. J. M. Hensen, R. A. van Santen and J. A. Lercer, *J. Phys. Chem. C,* 2011, **115**, 21763–21776.

2. C. Deng, J. Zhang, L. Dong, M. Huang, B. Li, G. Jin, J. Gao, F. Zhang, M. Fan, L. Zhang and Y. Gong,*Sci. Rep.,* 2016, **6**, 1–13.

3. A. Corma, V. Fornés, F. V. Melo and J Herrero, *Zeolites,* 1987, **7**, 559–563.

4. F. E. Trigueiro, D. F. J Monteiro, F. M. Z. Zotin and E. Falabella Sousa-Aguiar, *J. Alloys Compd.,* 2002, **344**, 337–341.

5. Y. Wang, T. Yokoi, S. Namba and T Tatsumi, *Catalysts,* 2016, **6**, DOI: https://doi.org/10.3390/catal6010008.

6. W. Qin, Y. Zhou and J. D. Rimer, *React. Chem. Eng.,* 2019, **4**, 1957–1968.

7. S. Li, A. Zheng, Y. Su, H. Fang, W. Shen, Z. Yu, L. Chen and F. Deng, *Phys. Chem. Chem. Phys.,* 2020, **12**, 3895–3903.

8. Z. Yu, A. Zheng, Q. Wang, L. Chen, J. Xu, J-P. Amoureux and F. Deng, *Angew. Chemie,* 2010, **122**, 8839–8843.

9. C. Y. Li and L. V. C. Rees, *Zeolites*, 1986, **6**, 51–59.

10. M. Ravi, V. L. Sushkevich and J. A. van Bokhoven, *Nat. Mater.,* 2020, **19**, 1047–1056.

11. D. H. Olson, *Zeolites,* 1995, **15**, 439–443.

12. M. A. Isa and M. H. Halim, *J. Phys. Conf. Ser.,* 2019, **1349**, 012072.

13. J. E. Schmidt, R. Oord, W. Guo, J. D. Poplawsky and B. M. Weckhuysen, *Nat. Commun.,* 2017, **8**, 1–8.

14. C. Liu, G. Li, E. J. M. Hensen and E. A. Pidko, *ACS Catal.,* 2015, **5**, 7024–7033.

15. B. I. E. Dubois, S. Holgersson, S. Allard and M. E. Malmström, *Acta*, 2011, **82**, 75–82.

16. D. Coster, A. L. Blumenfeld and J. J. Fripiat, *J. Phys. Chem.,* 1994 **98**, 6201–6211.

17. L. Qiu, Y. Fu, J. Zheng, N. Huang, L. Lu, X. Gao, M. Xin, Y. Luo, Y. Shi and G. Xu, *J. Rare Earths,* 2017, **35**, 658–666.

5. Layered Materials for Ammonia Sorption

As discussed in the introduction, magnesium chloride is one of the most commonly used and studied ammonia absorbents[1–3]. Much work has also been done on other group two metal halides[4–6], which will not be reproduced here.

Liu *et al.* comprehensively studied $MgCl_2$, $CaCl_2$, $CaBr_2$, $SrCl_2$ and $SrBr_2$ and the corresponding hydrated forms and examined the ability of each of these materials to absorb and desorb ammonia at a variety of temperatures and pressures.[4] They found that $MgCl_2$, $CaCl_2$ and $CaBr_2$ showed the highest capacity for room temperature ammonia storage. Sharonov compared ammonia sorption on $MgCl_2$, $CaCl_2$ and $BaCl_2$, finding that $MgCl_2$ shows the highest ammonia capacity, followed by $CaCl_2$ and that the sorption capacity peaks at low temperatures in all studied halides.[6]

$MgCl_2$ has the cubic close packed $CdCl_2$ structure with octahedral metal ions. Edge sharing magnesium chloride octahedra form the layers which are then held together by weak van der Waals interactions.[7–9] The introduction of ammonia into $MgCl_2$ is not a surface process but is instead absorption to give a new crystal structure. The ammonia molecules diffuse into the lattice of $MgCl_2$ by opening up the weak interaction between the ClMgCl layers to gain access to the Mg^{2+} which ammonia interacts with. With this in mind, a number of absorbents are studied here with the aim of improving the ease of accessibility for ammonia through disruption of the layered structure.

Techniques which are used in other layered materials, particularly LDHs, will be used here. Work by O'Hare has shown that treatment with acetone can greatly improve the surface area of an LDH though both minimising the number of LDH layers present and the size of the layers[10]; this will be

attempted with $MgCl_2$. Doping of elements into the $MgCl_2$ structure, pillaring and the introduction of interlayer species will be used to introduce disruption to the layered structure.

These materials will be explored for use in Haber type ammonia synthesis systems. Fast ammonia sorption and desorption has been shown to be crucial in such systems[11] and so improvement here will be beneficial for sorbent aided ammonia synthesis.

5.1. Layered Materials Screening

Initially, a variety of different materials were screened; $MgCl_2$ as a standard due to its previously reported high capacity and common use; $NiCl_2$ to determine if the d-orbitals of the transition metal can overlap with the ammonia molecule to raise the temperature stability of absorption or cause any other interesting behaviour; two LDHs (Mg/Al and Ni/Al) due to the well-known ability of LDHs to store a huge variety of molecules between their layers and $GdBr_3$ as lanthanide ions show high possibly coordination numbers potentially giving rise to a high degree of ammonia absorption.

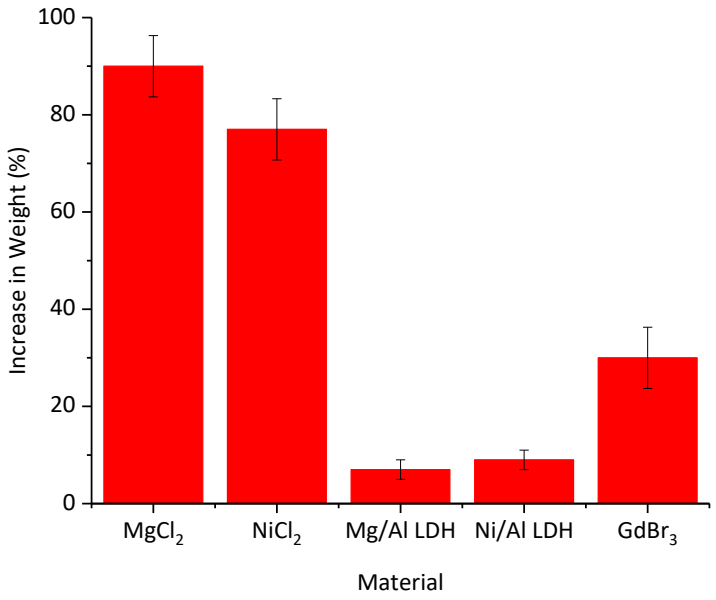

Figure 5-1: Maximum ammonia absorption of $MgCl_2$, $NiCl_2$, Mg/Al LDH and Ni/Al LDH capacity measured on a Hidden Isochema IGA-002 using 1000 mbar pure ammonia. Approximately 20 mg of sample was placed in the IGA sample chamber, each sample was dried at 300 °C for eight hours, under vacuum, the sample cooled to 25 °C and the initial sample weight accurately recorded. Remaining at 25 °C, ammonia pressure was increased at 200 mbar intervals, kept at each pressure for 20 minutes and the sample weight accurately recorded; the maximum capacity shown here is the sample weight at 1000 mbar ammonia pressure. $GdBr_3$ capacity was recorded using pure ammonia gas in a Schlenk line. First the sample was dried at 300 °C, under vacuum, cooled to room temperature and the sample exposed to pure ammonia gas (approximately 400 mbar) for 30 minutes.

As can be seen in Figure 5-1, each of the alternative absorbents tested showed lower absorption than $MgCl_2$, which showed a 90±6 % increase in weight with absorption. $NiCl_2$ showed the next highest absorption with 77±6 % increase, both the Mg/Al LDH and Ni/Al LDH materials showed very low absorption, of 7 and 9±1 % respectively and $GdBr_3$ had an absorption capacity of 30±6 %.

It is expected that in $MgCl_2$, $NiCl_2$ and $GdBr_3$ the ammonia molecules will coordinate to the metal centres, while in the LHD materials they will be present between the layers and not necessarily coordinated to a metal. The above absorption values correspond to a different number of ammonia molecules per metal centre, described below.

Table 5-1: Comparison of actual and theoretical maximum number of ammonia molecules per metal centre, calculated from absorption shown in Figure 5-1.

Absorbent	**$MgCl_2$**	**$NiCl_2$**	**$GdBr_3$**
Ammonia per metal centre	5.5	5.9	7.0
Theoretical maximum ammonia per metal centre	6^{7}	6^{12}	9^{13}

Table 5-1 shows the number of ammonia molecules coordinated to each site. $MgCl_2$ has the lowest coordination number with an average of 5.5 ammonia molecules per magnesium centre, lower than the theoretical maximum of 6. $NiCl_2$ has almost the theoretical maximum number of coordinated ammonia molecules. $GdBr_3$ has the greatest number of ammonia molecules coordinated to each metal centre, with 7.0, showing that the rare earth element can indeed achieve greater coordination as proposed, however, the heavier weight of $GdBr_3$ leads to significantly lower gravimetric absorption. As discussed in the introduction, this low gravimetric capacity is not a problem for all applications; stationary uses of absorbents have other priorities.

Based on the above data, $MgCl_2$ continues to be the highest capacity ammonia absorbent, however absolute capacity is not the only concern, as is discussed in the introduction. Also important is the rate at which the ammonia absorbs and the stability of absorbance across multiple cycles. The absorption rates of the most promising candidates, $MgCl_2$ and $NiCl_2$, were studied for 3 cycles.

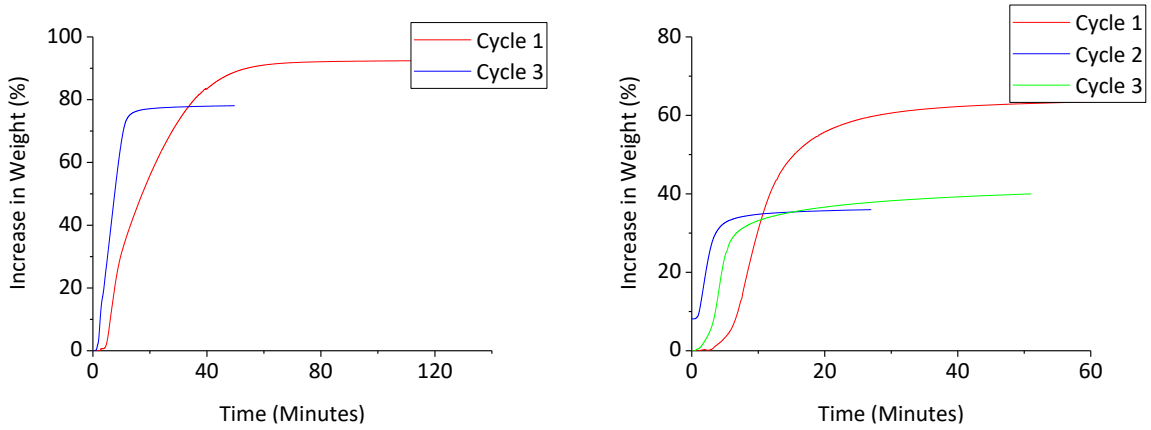

a. Cycles 1 and 3 for NH_3 absorption on $MgCl_2$ b. Cycles 1, 2 and 3 for NH_3 absorption on $NiCl_2$

Figure 5-2: Absorption rate graphs recorded on Hidden Isochema IGA-002 for $MgCl_2$ and $NiCl_2$; cycle 1,2 and 3. (Cycle 2 is missing from $MgCl_2$ due to data corruption.) Approximately 20 mg of sample was placed in the IGA sample chamber. Prior to absorption materials were dried under vacuum at 300 °C for 8 hours, cooled to 25 °C and the sample weight accurately recorded. For absorption, pure ammonia gas at 400 mbar was introduced at a rate of 100 mbar/min at 25 °C and the pressure kept constant. The weight change in the materials was accurately recorded to track the absorption. To desorb the ammonia between cycles, the pressure was decreased to vacuum and the temperature increased to 300 °C for 8 hours.

As can be seen in Figure 5-2, both $MgCl_2$ and $NiCl_2$ show a decrease in ammonia absorption capacity with rate. The $MgCl_2$ capacity decreases to 78 % after three cycles (85% of the cycle one 92 % capacity) while $NiCl_2$ capacity decrease to 36% (57 % of the cycle one 63 % capacity). This agrees with work by Kubota *et al.*[14] and Liu *et al.*,[4] who both reported decreasing ammonia capacity under cycling conditions in metal halides. It is, however, evident that $MgCl_2$ shows both better stability and higher capacity compared to $NiCl_2$ after cycling.

The instability of both materials would not be ideal for industrial applications, where the same absorbent must go through multiple absorption and desorption cycles. It is important to note than compared to industrial scales, 3 cycles is a very small number. It would be useful to test the materials for a significantly greater number of cycles and see how the stability changes. It is likely that materials reach a stable point after a certain number of cycles and it would be good to determine when and at what capacity this stability occurs. Longer term cycling experiments have been reported in the literature. Kubota and colleagues studied the absorption of ammonia on

$NiCl_2$, though only with partial removal of ammonia between cycles, and reported high stability across the first ten cycles.[14] This suggests that partial desorption of ammonia improves the stability of absorption.

Despite the lowered capacity of the cycled materials, the absorption rate increases, as is evidenced by the steeper slope as the absorption approaches the plateau. The structure of both $MgCl_2$ and $NiCl_2$ is clearly changing with cycling to result in such varied capacities and rates.

Hummolshøj et al. studied the absorption and desorption processes of ammonia from $MgCl_2$.[1] They determine that the desorption of ammonia from $MgCl_2.6H_2O$ generates a nanopore systems of smaller, interconnected crystals.[1]

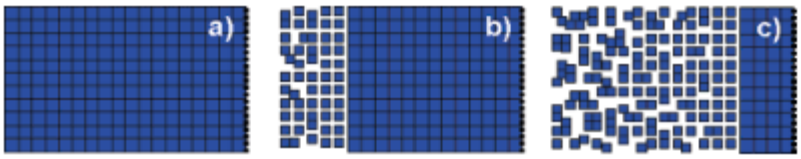

Figure 5-3: Representation of how desorption of ammonia from $MgCl_2.6H_2O$ generates a nanopore system, adapted from [1].

This more open structure, shown in Figure 5-3, would be expected to improve sorption rates, as the additional surface area allows for easier sorption of ammonia to the $MgCl_2$ bulk. However, if this process also generates structural defects it could cause a decrease in ammonia capacity, as was seen in Figure 5-2. Furthermore, the importance of the unit cell size is discussed.[1] With reference to works by Olovsson[15], Jones et al.[16] and Leinewber et al.[17] it is known that the crystal structure of magnesium chloride changes upon absorption of ammonia, and that the inter-layer spacing must increase to accommodate ammonia molecules. Therefore, any increase in interlayer spacing would also be expected to increase the ammonia absorption rate. Some combination of porosity change, particle size change and increasing interlayer spacing are the cause of the

increase absorption rate seen with cycling and further experiments are required to fully understand this.

5.2. Proof of Concept

Before proceeding further, experiments were carried out to study the improvement in ammonia production capacity caused by the use of absorbents. This follows up extensive work in this area carried out by the Cussler group.[3,18–20]

Catalytic testing of a commercial iron catalyst for ammonia synthesis, with and without absorbent beds was used to prove that absorbents improve the overall ammonia production activity. The distance between the absorbent and catalyst beds in a packed reactor tube was also varied.

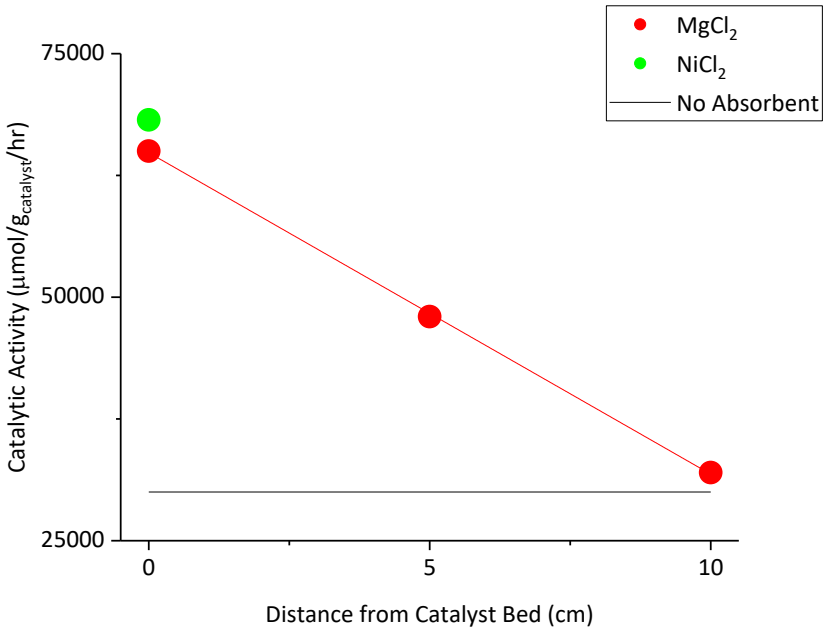

Figure 5-4: Ammonia production over commercial iron catalyst with no absorbent (shown by black line), $MgCl_2$ absorbent or $NiCl_2$ absorbent. Activity was determined using a quartz fixed bed micro-reactor. Commercial catalyst (approx. 100 mg, accurately weighed) was placed in a quartz tubular reactor (5 mm internal diameter) sandwiched between quartz wool. If being used the absorbent (2000 mg, accurately weighed) was placed in the quartz tubular reactor, downstream of the catalyst bed again sandwiched between quartz wool. In the 0 cm distance experiment there was no quartz wool between the catalyst and absorbent beds. Prior to testing, the catalyst was activated at 773K and the absorbent at 673 K, under a linear flow of nitrogen (52 mL/min). During reaction, a 3:1 mixture of H_2 and N_2 was passed through the reactor at a pressure of 50 bar and flow rate of 52 mL/min. The catalyst was at 743 K and the absorbent at 423 K (Note: the absorbent was not heated; this was residual heat from the catalyst portion of the reactor). After the reaction, any ammonia absorbed was desorbed by heating the absorbent to 673 K under flowing nitrogen (52 mL/min). Throughout, the exit gas was passed through an acid trap (concentrated H_2SO_4 solution) and the ammonia production measured by titrating this solution with NaOH solution and methyl red indicator.

From Figure 5-4, it can be seen that the presence of the absorbents has an effect on the catalytic activity. When the $MgCl_2$ absorbent bed is located directly adjacent to the catalyst bed the activity of the catalyst doubles, the ammonia production values significantly increase; from 30,000 µmol/g_{cat}/hr when no absorbent is present, to 65,000 µmol/g_{cat}/hr with the absorbent bed directly adjacent to the catalyst bed. This effect is also seen to a lesser extent when the absorbent bed is separated from the catalyst bed by 5 cm, where an increase in activity to 48,000 µmol/g_{cat}/hr was seen. When the catalyst and absorbent beds are 10 cm apart, the improvement

in activity compared to the absorbent free experiment is negligible, the catalyst activity is only 32,000 μmol/g_{cat}/hr. It is evident that the distance between the catalyst and the absorbent has a significant effect on the degree of improvement of the yield.

This finding builds on work by Cussler, who studied the use of absorbents in ammonia synthesis. When using calcium chloride as an absorbent to separate the catalytically produced ammonia from the gas stream they found that fast separation of ammonia from nitrogen and hydrogen is essential to avoid ammonia decomposition occurring via the reverse reaction.[21] This supports the result here; it is expected that if the ammonia absorbent is far from the catalyst bed then the rate at which ammonia is separated from the reactant gases will be slower and therefore it will be more difficult to exert any changes to the dynamic equilibrium of the system. Furthermore, the rate at which the ammonia is absorbed will also be important.

A similar increase in activity seen with a $NiCl_2$ absorbent bed as was seen with $MgCl_2$; when the two beds are adjacent the activity of the catalyst increases to 68,000 μmol/g_{cat}/hr, compared to 30,000 μmol/g_{cat}/hr when no absorbent is present.

Further experiments are needed to understand this effect fully, and to explore which absorbent factors improve the increased catalytic effect further, particularly to determine whether capacity or absorption rate or some other factor has more of an effect. Given the suggestion in literature is that the rate of absorption has the most significant effect on the increase in catalyst activity when using sorbents[22] this should be further explored. There is also significant scope for optimising the many conditions which can be varied including but not limited to operating conditions and absorbent bed volume, length and density. The results from these experiments are being modelled as part of a collaboration with Dr Wenchan Qi and Professor René Bañares-Alcántara in the Engineering Department, University of Oxford. This will enhance our understanding and allow

us to improve both the catalytic and absorbent systems and lead to a suitable catalyst and sorption technology in ammonia synthesis.

5.3. Kinetic Testing of $MgCl_2$ Absorption

To further understand the absorption process on $MgCl_2$, kinetic experiments were carried out. The capacity for ammonia absorption on $MgCl_2$ was compared at a variety of temperatures. At high temperatures the likelihood of molecular collision between the ammonia and $MgCl_2$ is greater allowing for faster uptake but ammonia molecules already absorbed on $MgCl_2$ also have higher energy enabling them to leave the surface.

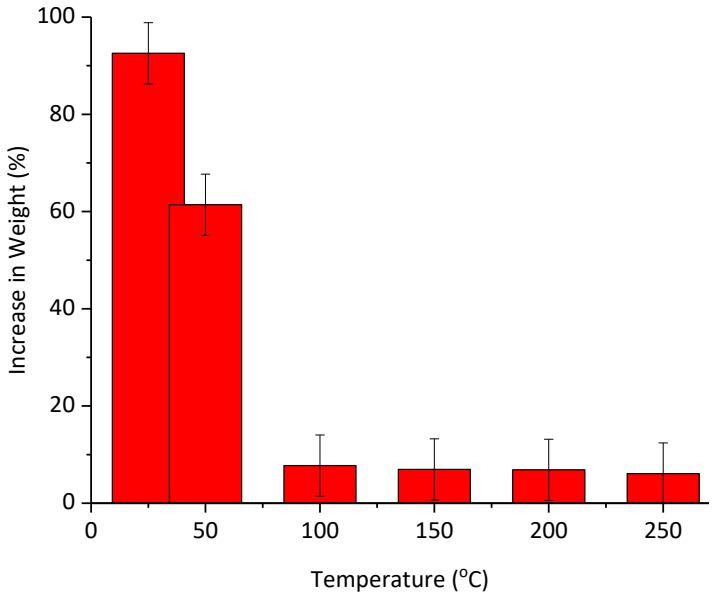

Figure 5-5: Maximum ammonia absorption capacity for $MgCl_2$ at various temperatures recorded on Hidden Isochema IGA-002. Approximately 20 mg of sample was placed in the IGA sample chamber. Prior to absorption materials were dried under vacuum at 300 °C for 8 hours, cooled to 25 °C and the sample weight accurately recorded. For absorption, pure ammonia gas at 400 mbar was introduced at a rate of 100 mbar/min at 25 °C and the pressure kept constant. The weight change in the materials was accurately recorded to track the absorption. (Note: The 25 °C and 50 °C experiments were on completely clean $MgCl_2$. The 50 °C sample was also used for the remaining experiments. To desorb the ammonia between experiments, the pressure was decreased to vacuum and the temperature increased to 300 °C for 8 hours. The temperature was then increased to the target.)

Figure 5-5 shows a clear temperature dependence for ammonia absorption as would be expected. At higher temperatures, more ammonia molecules have the required energy to desorb from the $MgCl_2$ and so there is a lower capacity. The room temperature capacity of $MgCl_2$ of 93±6 % decreases to 61±6 % at only 50 ^oC and even further above 100 ^oC with the capacities at 100, 150, 200 and 250 ^oC being 8, 7, 7 and 6 % respectively. The vast majority of the capacity is lost above 100 ^oC. This is also reported in literature, to an even greater extent with $MgCl_2$ ammonia capacities at 300 ^oC as low at 0.12% being reported.[23] This has significant implications for use of $MgCl_2$ in high temperature industrial applications. Low ammonia capacity at high temperatures may limit the ability of an absorbent to be used industrially, as it will reach the maximum capacity very quickly. These materials may be better suited to lower temperature applications. However, the above catalytic testing (Figure 5-4) shows that even with the absorbent at 423 K there is still an improvement in catalytic activity.

5.4.Acetone Treatment of $MgCl_2$

As repeated cycling showed such an improvement in ammonia absorption uptake rate, other methods of nanopore generation or layer disruption were explored, firstly acetone treatment. This method, developed by Chen et al.[10], uses acetone treatment of LDHs to generate structural disruption and significantly increases the LDH surface area. They found that acetone treatment of LDHs decreased the number of LDH layers present, increasing the surface area without structural changes to the layers themselves. Given $MgCl_2$ also shows a layer structure, this method may improve the $MgCl_2$ surface area and so ammonia capacity.

5.4.1. Ammonia Absorption Rate

A completely saturated solution of $MgCl_2$ was treated with acetone and the dried AT-$MgCl_2$ tested for ammonia absorption capacity.

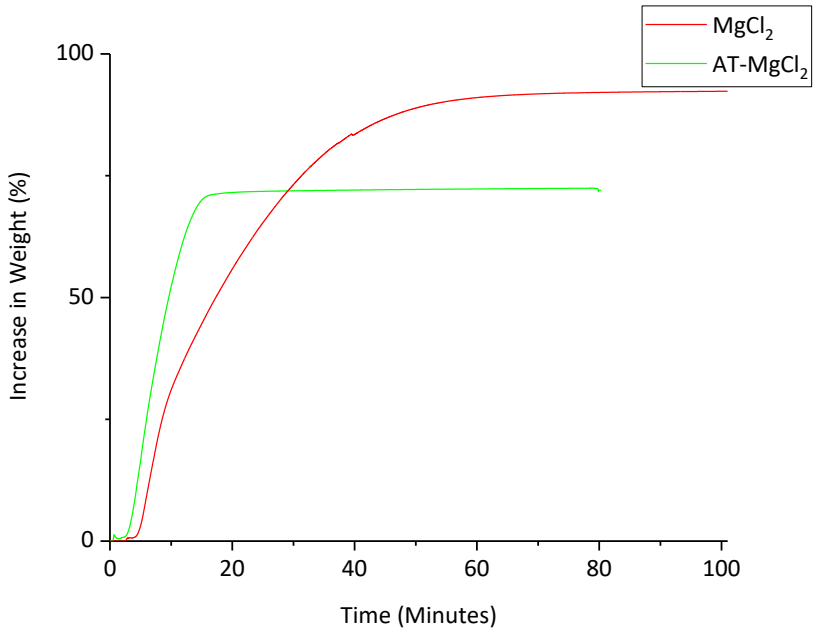

Figure 5-6: Absorption graphs recorded on Hidden Isochema IGA-002 for $MgCl_2$ and AT-$MgCl_2$. Approximately 20 mg of sample was placed in the IGA sample chamber. Prior to absorption materials were dried under vacuum at 300 °C for 8 hours, cooled to 25 °C and the sample weight accurately recorded. For absorption, pure ammonia gas at 400 mbar was introduced at a rate of 100 mbar/min at 25 °C and the pressure kept constant. The weight change in the materials was accurately recorded to track the absorption.

As can be seen in Figure 5-6, the rate of ammonia absorption was much faster in the acetone treated $MgCl_2$ sample, shown by the steeper slope on the approach to the plateau. The maximum absorption capacity of AT- $MgCl_2$ (of 71%) is reached after 16 minutes. It takes $MgCl_2$ 30 minutes to reach this point and 70 minutes to reach plateau. This corresponds to an absorption rate of 0.77 mmol/g/min for $MgCl_2$ compared to 2.61 mmol/g/min for AT-$MgCl_2$. The acetone treatment causes a greater than threefold increase in absorption rate; a significant improvement. Initially, this was attributed to the process increasing surface area of $MgCl_2$ through decreasing the number of layers, as was seen in the initial LDH work by Chen *et al.*,[10] though further characterisation is required to confirm this.

Unfortunately, this increase in rate corresponds to a decrease in the capacity. This is similar to the increased rate, decreased capacity relationship that was seen with ammonia absorption,

desorption cycling (see Figure 5-2). This suggests that the effect of the acetone treatment is similar to that of the ammonia cycling. The change in rate with cycling of $MgCl_2$ was attributed to nanopore generation and changes in the layer ordering, as was described by Christensen and collegues.[1] It is possible that the acetone treatment can also generate nanopores and alter the layers in a similar way. This would be expected if acetone is entering the structure in a similar way to ammonia. Further experiments are required to fully understand the change which the $MgCl_2$ is undergoing due to acetone treatment and if surface area effects or nanopore generation lead to the increase sorption rate.

5.4.2. N_2 Physisorption

Chen et al. proposed that the benefit of the acetone treatment on LDH materials was partly due to increased surface area.[10] N_2 physisorption was used to compare the surface areas in the unmodified and the acetone treated $MgCl_2$ samples, to determine if the increased ammonia absorption rate in AT-$MgCl_2$ was due to increased surface area.

Table 5-2: Porosity characterization of $MgCl_2$ and AT-$MgCl_2$, determined using a Micromeritics Tristar-3000. Approximately 100 mg of sample was accurately weighed. Samples were then loaded into tubes and dried at 423 K under vacuum, for 12 hours. N_2 adsorption isotherms were then obtained at 77K.

Sample	$MgCl_2$	AT-$MgCl_2$
BET Surface area	1.66 m^2/g	7.56 m^2/g

The acetone treatment has indeed increased the surface area, from 1.66 m^2/g to 7.57 m^2/g. This increase in surface area is similar to as was seen in the acetone treatment of LDHs in literature.[10] However, the very low surface area of bulk $MgCl_2$ powder means that even a proportionally great increase in surface area results in a still low surface area. In the nano-porous $MgCl_2$ described by Hummelshøj et al. the BET surface area of the ammonia free sample was 90.5 m^2/g.[1] This is much greater than seen here indicating that any generation of nano-pores in the AT-$MgCl_2$ is not occurring to such a significant extent. This suggests that the layer disruption effect is a greater contributor to the increased ammonia sorption rate in AT-$MgCl_2$. This is not unexpected; it is well

documented that uptake of ammonia to $MgCl_2$ is a bulk absorption process and so surface area effects are expected to be minimal.

Both $MgCl_2$ and AT-$MgCl_2$ have low surface areas when compared to the zeolite samples previously discussed. This demonstrates that there is very little surface sorption taking place. This is confirmed by the fact that AT-$MgCl_2$ has a greater surface area (around four times that of the unmodified $MgCl_2$) and yet did not show an increase in ammonia absorption capacity.

5.4.3. XRD

Both the unmodified and acetone treated $MgCl_2$ were studied using XRD to determine if the differences in absorption properties could be accounted for by structural differences.

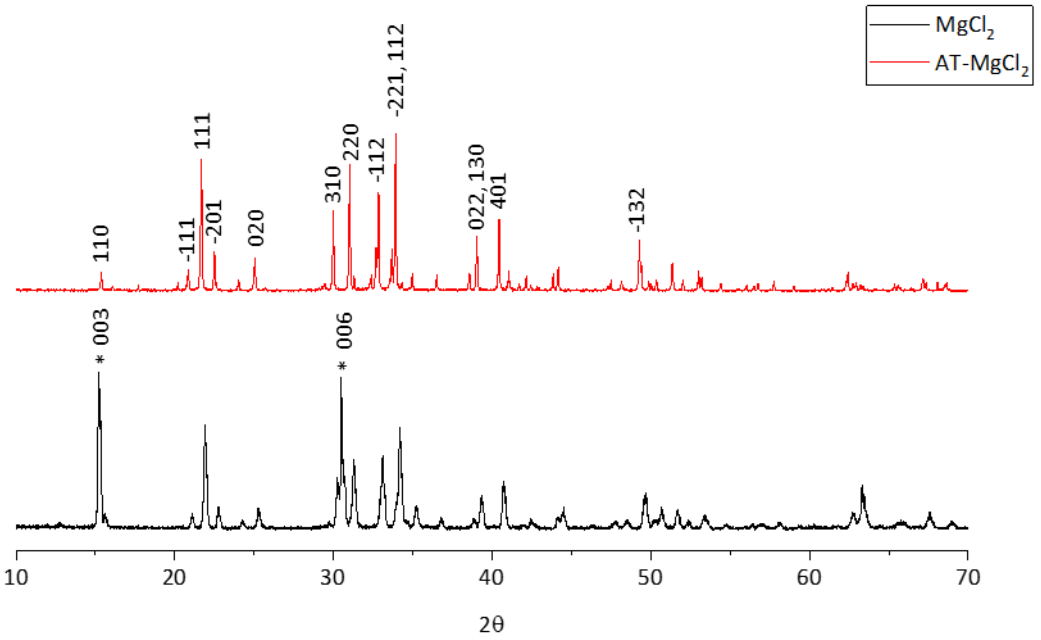

Figure 5-7: XRD patterns of $MgCl_2$ and AT-$MgCl_2$ (freshly synthesized) recorded on a PANalytical X'Pert. Patterns were recorded between 10 and 60 °, using a step size of 0.017 ° and a step time of 1.03 s/step. The * represents $MgCl_2$ peaks, all other peaks are from $MgCl_2.6H_2O$ type structures.

As can be seen in Figure 5-7, there are similarities between the XRD patterns of $MgCl_2$ and AT-$MgCl_2$. Due to the XRD patterns being recorded under ambient conditions and $MgCl_2$ being

hygroscopic the $MgCl_2$ shows a significant number of peaks associated with hydrated magnesium chloride (i.e. $MgCl_2.6H_2O$), which unfortunately significantly overlap with the anhydrous magnesium chloride peaks. However, the 003 and 006 peaks can be assigned to anhydrous $MgCl_2$ in the untreated $MgCl_2$ sample. The other peaks in the $MgCl_2$ pattern and the peaks in AT-$MgCl_2$ are in equivalent positions to those in the XRD pattern of $MgCl_2.6H_2O$. This suggests that the majority of $MgCl_2$ present in the AT-$MgCl_2$ diffraction pattern in hydrated. To understand how the acetone treatment affected the layer spacing, particularly if it has caused exfoliation, SXRD data was used to determine the space group and lattice parameters of each sample, using the method described by Coelho.[24] Prior to scanning the samples were fully dried under vacuum.

Table 5-3: Space group and lattice parameters for $MgCl_2$ and AT-$MgCl_2$ calculated from SXRD (collected at I-11, Diamond and BL02B2, Spring-8, respectively) using the method described by Coelho.[24] M_N represents the de Wolff figure of merit.

Sample	Space Group	a	b	c	α	β	ϒ	M_N
$MgCl_2$	R-3m	3.0416	3.0416	14.7677	90.00 °	90.00 °	120.00 °	15.91
AT-$MgCl_2$	C2/m	9.8606	7.1066	6.0747	90.00 °	93.75 °	90.00 °	19.51

First the space group and lattice parameters of the unmodified $MgCl_2$ were determined, as can be seen in Table 5-3. The space group was R-3m. It is important to note that the hkls in R3, R-3, R32 and R3m are the same as those in R-3m and so technically the pattern could represent any of these space groups. Given the adequate M_N value and wealth of literature discussing the space group of $MgCl_2$ suggesting R-3m[7], this structure can be confidently assigned as this. The lattice parameters were determined, with a, b and c have values of 3.0416, 3.0416 and 14.7677 Å, respectively and α, β and ϒ 90 °, 90 ° and 120 °, respectively.

Similarly, the space group and lattice parameters of AT-$MgCl_2$ were calculated. It is one of C2, Cm or C2/m (all equivalent with regards to hkls). The structure of $MgCl_2.6H_2O$ is fairly well studied and has been determined to have a C2/m structure[25] so it is probable AT-$MgCl_2$ also adopts this structure, with acetone molecules in similar positions to water molecules. This is supported by

the fact the lattice parameters of AT-$MgCl_2$ are very similar to $MgCl_2.6H_2O$ (9.8606, 7.1066 and 6.0747 for AT-$MgCl_2$, compared to 9.8607, 7.1071 and 6.0737 for $MgCl_2.6H_2O$[25]). The M_N value is good and suggests this space group is appropriate.

There is a small amount of water used in the synthesis of AT-$MgCl_2$ to ensure the $MgCl_2$ is in solution. This is not enough to fully hydrate all the $MgCl_2$ used. Either some of the $MgCl_2$ hydrates completely or the water sites are filled with a combination of water/acetone but still adopt the $MgCl_2.6H_2O$ structure. It is possible the hydrated $MgCl_2$ present in the XRD pattern is only one phase present. Single layer $MgCl_2$ or disordered $MgCl_2$ structures would not show on XRD as they are not crystalline. Their presence cannot be ruled out. It is also important to note that these XRD patterns were obtained by synchrotron radiation. This means very minor phases will be detected and so it is not clear what component of the total sample is actually the $MgCl_2.6H_2O$ like phase.

If the crystalline phase seen in XRD has residual water or acetone molecules after drying, this would account for at least some of the lowered capacity. Fully hydrated $MgCl_2$ would have fully coordinated magnesium centres and so could not absorb any further ammonia molecules as they will instead be filled with water molecules. This would suggest that any non-crystalline phase is the reason for the capacity and fast sorption rate. This would be expected if there was single layer $MgCl_2$ present, as the sorption sites would be much easier to access.

5.4.4. Location of Acetone Molecules?

One possible explanation for the lowered ammonia absorption capacity is that the water or acetone molecules used in the exfoliation of layers is binding to the magnesium centres and so there are a reduced number of possible sites for ammonia to bind to. To understand if this was the case, the TPD of AT-$MgCl_2$ was compared to that of unmodified $MgCl_2$.

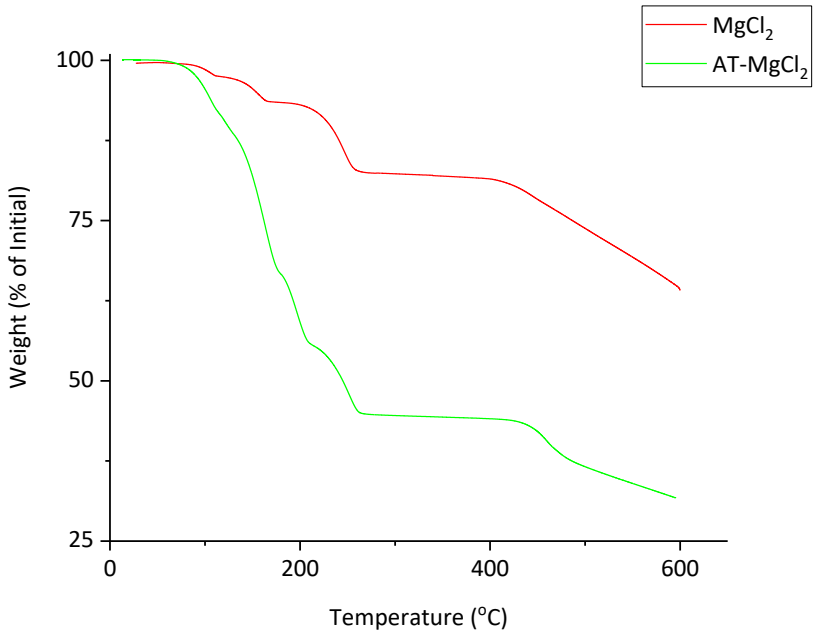

Figure 5-8: Thermogravimetric analysis of $MgCl_2$ and AT-$MgCl_2$ recorded on a TA Instruments Q600 SDT. Approximately 10 mg of sample was placed in the SDT. The temperature was increased to 600 °C at a rate of 10 °C/min under 100 mL/min flowing nitrogen and the weight change recorded.

As can be seen from Figure 5-8, the thermogravimetric patterns of $MgCl_2$ and AT-$MgCl_2$ have significant differences. The slopes up to around 300 °C are attributed to water molecules absorbed under ambient room temperature conditions and, in the case of AT-$MgCl_2$, any remaining acetone molecules. There are three desorption regions for $MgCl_2$ while there are four for AT-$MgCl_2$, with the additional desorption probably due to the acetone having a different interaction with the magnesium centre from water.

The first of the desorption regions of $MgCl_2$ is between room temperature and 115 °C, corresponding to a loss of 2.7 % of the initial weight. A second desorption region is present between 115 and 166 °C, corresponding to a further 4.0 % of the initial weight lost. Finally, the third desorption region, present between 166 °C and 271 °C corresponds to a 10.9 % weight loss.

AT-$MgCl_2$ shows four desorption regions. The first, between room temperature and 110 °C corresponds to a weight loss of 7.5 % of the initial weight. The region between 110 and 173 °C corresponds to a 24.8 %, while between 173 and 206 °C, a loss of 10.9 %. Finally, the highest temperature desorption is between 206 and 262 °C, corresponding to 11.4 % of the initial weight lost.

Neither of the two materials show further desorption after approximately 270 °C until $MgCl_2$ decomposition begins after 400 °C (similarly to the 415 °C decomposition onset reported in literature[26]). Furthermore, each of the materials shows a clear plateau before 400 °C, when decomposition occurs; at this temperature the sample can be assumed to be pure $MgCl_2$ and so the number of coordinated water and acetone molecules can be determined.

The desorption profile of $MgCl_2$ corresponds to a total water content of 1.2 water molecules per magnesium centre ($MgCl_2.1.2H_2O$), with the low temperature desorption (up to 115 °C) region corresponding to 0.18 moles of water, the medium (115 to 166 °C) 0.27 moles and the highest temperature region (166 to 271 °C) 0.74 moles. This is ambiently absorbed water. As both water and acetone are used in the acetone treatment of $MgCl_2$ the exact solvent content cannot be determined. If all the weight loss is assumed to be acetone loss then 2.1 acetone molecules are present per magnesium centre ($MgCl_2.(C_3H_6O)_{2.1}$). However, it is likely that at least some of the weight loss is due to water desorption and so the actual formula contains less acetone.

The TPD of both acetone treated and untreated $MgCl_2$ show desorption only below 300 °C. This shows that the 300 °C overnight drying process prior to absorption measurements is enough to remove any water or acetone from AT-$MgCl_2$ and so the loss of ammonia absorption capacity in AT-$MgCl_2$ cannot be due to acetone filling sites.

5.4.5. Desorption of Ammonia

Also studied was the desorption of ammonia from AT-$MgCl_2$ and $MgCl_2$ to see if there is any difference and understand the absorption sites present. As discussed in 5.4.4, both $MgCl_2$ and AT-$MgCl_2$ appear to both be solely $MgCl_2$ after the 300 °C and so all of the desorption products are attributed to ammonia in both samples.

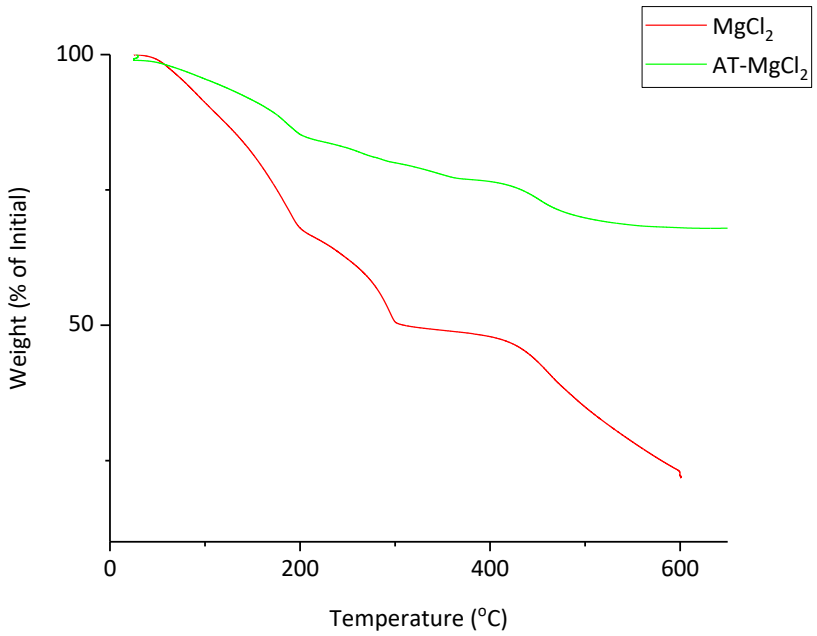

Figure 5-9: Desorption of ammonia on $MgCl_2$ and AT-$MgCl_2$ recorded on a TA Instruments Q600 SDT. To load ammonia on $MgCl_2$ and AT-$MgCl_2$ clean samples were dried for eight hours at 300 °C under vacuum, cooled to 25 °C then were loaded with ammonia at 400 mbar at 25 °C until the weight stabilized (around 60 minutes). The samples were flushed with N_2 before being placed in the SDT. Approximately 10 mg of sample was used. The temperature was increased to 600 °C at a rate of 10 °C/min under 100 mL/min flowing nitrogen and the weight change recorded.

Figure 5-9 shows the difference in ammonia desorption from treated and untreated $MgCl_2$. $MgCl_2$ shows two clear ammonia desorption regions, one between room temperature and 201 °C and one between 201 °C and 302 °C. AT-$MgCl_2$ also shows two desorption regions, one between room temperature and 203 °C and one between 203 °C and approximately 400 °C. It can be seen that the second region shows a less clear plateau, indicating that the ammonia is not fully desorbed before decomposition of the $MgCl_2$ begins.

Based on the initial weight of $MgCl_2$ prior to ammonia absorption, the initial ammonia absorbed $MgCl_2$ material has the formula $MgCl_2.5.5NH_3$ compared to AT-$MgCl_2$ which has initial formula $MgCl_2.4NH_3$.

Both AT-$MgCl_2$ and $MgCl_2$ showed two regions of ammonia desorption. In $MgCl_2$ the low temperature desorption region (between room temperature and 201 ^oC) contained 3.0 NH_3 per Mg centre while the higher temperature region (between 201 and 302 ^oC) contained 2.2 NH_3 molecules. 0.3 NH_3 moles of ammonia remain above 302 ^oC. In AT-$MgCl_2$ the low temperature desorption region (between room temperature and 203 ^oC) contains 1.5 NH_3 molecules per magnesium centre while the higher temperature region (between 203 and 400 ^oC) contains 0.9 NH_3 molecules per magnesium centre. At 400 ^oC, 1.6 moles of ammonia remain in the AT-$MgCl_2$ structure.

The ratios of low to high temperature desorption are similar in both samples although AT-$MgCl_2$ shows slightly less ammonia proportionally in the high temperature desorption region (ratio of low to high temperature ammonia is 1.36 in unmodified $MgCl_2$ and 1.67 in AT-$MgCl_2$). This suggests that there is no significant change in the distribution of possible absorption “sites” available as a result of the acetone treatment; the same bonding seems to be available, just in proportionally lower capacity. This supports the idea of single or few molecular layer $MgCl_2$ being generated by the acetone treatment; there are no extra sites being generated by the acetone treatment process.

It is also obvious that the temperature at which high temperature desorption takes place is higher in AT-$MgCl_2$, shown in the fact that slope does not reach a plateau at 300 ^oC and instead continues to show desorption. There is also significantly more ammonia remaining in the AT-

$MgCl_2$ sample when $MgCl_2$ begins to decompose at around 400 °C. Neither of these properties are very favourable and they will probably have an effect on the cyclability.

$MgCl_2.6NH_3$ has been determined to adopt the K_2PtCl_6 structure[1]. The crystal structure may be considered equivalent to a cubic double perovskite $A_2BB'O_6$[27], with A=Cl, B=Mg, B'=vacancy and O being replaced by ammonia molecules.

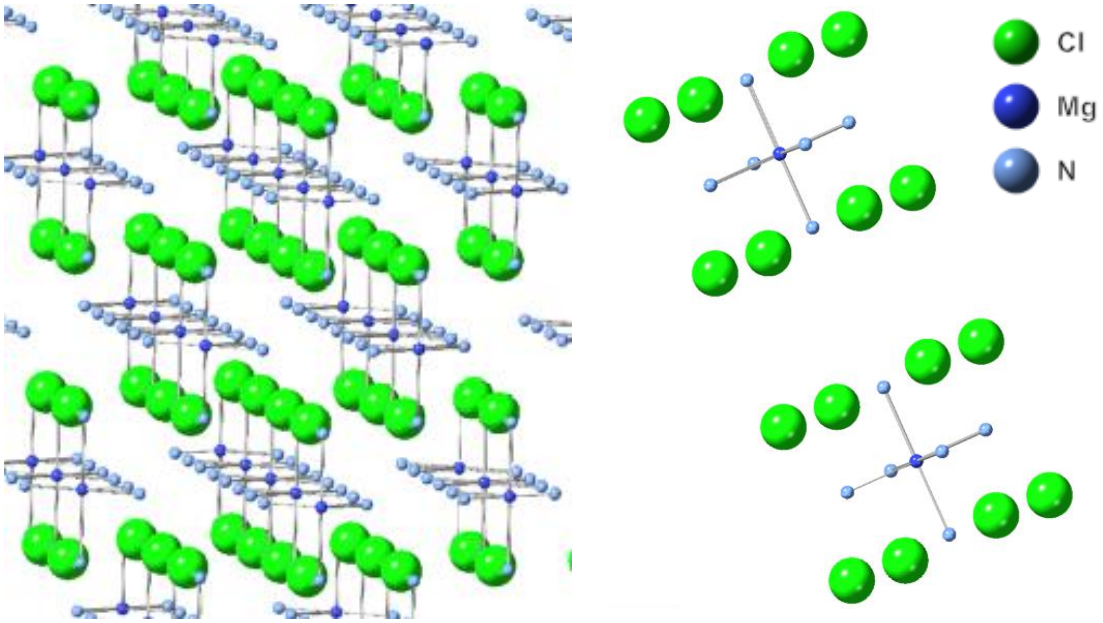

Figure 5-10: $MgCl_2.6NH_3$ structure (H atoms omitted for clarity). Chlorine atoms are shown in green, magnesium in dark blue and N in light blue.

These sites are equivalent and so ammonia in them would be expected to act equivalently. The presence of different desorption sites in ammonia loaded $MgCl_2$ has been discussed in the literature. There is some ambiguity in the literature over how the ammonia desorption from $MgCl_2.6NH_3$ takes place. Zhu and colleagues reported a three stage process with steps at 50-115 °C, 115-200 °C and 200-290 °C, each corresponding to two ammonia molecules desorbing [2]. Alternatively, Christensen reports the desorption first of 4 ammonia up to 220 °C followed by two separate desorption steps of one ammonia molecule, both occurring before 300 and 350 °C [28]. Both of these papers suggest that four ammonia molecules are desorbed in the low temperature region up to around 200 °C, either as a one step or two step process. The results here are a

combination of the two models, with the initial lower temperature desorption (up to 200 °C) holding the majority of the ammonia, similar to the Christensen model.[28] As discussed, the ammonia loaded $MgCl_2$ shows a lower capacity than hypothetically possible (5.5 NH_3 instead of 6 NH_3) and this is due to lower occupancy low temperature site. The higher temperature site contains 2.2 NH_3 molecules similar to as seen by Zhu[2]. AT-$MgCl_2$ shows similar desorption but with lower occupancy in each site.

5.4.6. Instability of AT-$MgCl_2$

In the course of experiments with AT-$MgCl_2$ it became clear that the instability of the acetone treated material made it unsuitable for industrial applications.

Two main types of instability were found: instability over time and instability with cycling.

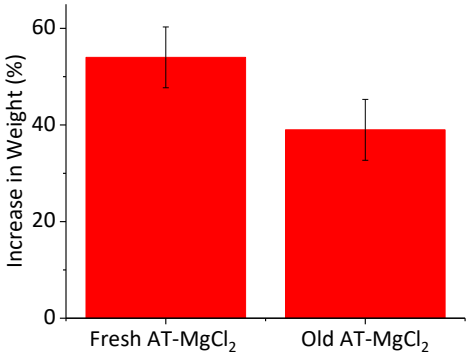

a. Comparison of a freshly prepared AT-$MgCl_2$ (<1 week) and old AT-$MgCl_2$ (>2 months)

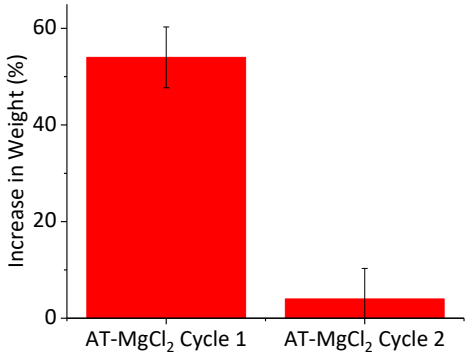

b. Comparison of 1st and 2nd absorption capacity of AT-$MgCl_2$

Figure 5-11: Maximum absorption as recorded on Hidden Isochema IGA-002 for AT-$MgCl_2$ samples. Approximately 20 mg of sample was placed in the IGA sample chamber. Prior to absorption materials were dried under vacuum at 300 °C for 8 hours, cooled to 25 °C and the sample weight accurately recorded. For absorption, pure ammonia gas at 400 mbar was introduced at a rate of 100 mbar/min at 25 °C and the pressure kept constant. The weight change in the materials was accurately recorded to track the absorption. To desorb the ammonia between cycles, the pressure was decreased to vacuum and the temperature increased to 300 °C for 8 hours.

As is clear from Figure 5-11, AT-$MgCl_2$ shows significant problems with stability. First, there is a clear decrease in capacity of AT-$MgCl_2$ over time with the initial 54±6 % capacity decreasing to 39±6 % after 2 months, a loss of 28% of the initial capacity. Although AT-$MgCl_2$ is not studied in literature, there is a great deal of work on 2D materials. This instability is commonly seen in 2D or single layer materials[29]. For example, exfoliated single layer MoS_2 reorders to a bulk material when stored under ambient conditions; this rearrangement is coupled with degradation of the layers themselves leading to a lowered activity.[30] Similarly, exfoliated few layer black phosphorous reorders due to atmospheric moisture, due to it being a very hydrophilic material.[31]

It is likely that there are similar reordering processes taking place in the AT-$MgCl_2$ samples. Even untreated $MgCl_2$ is hydrophilic and so atmospheric water may cause rearrangement as is seen with few layer black phosphrous.[31] A direct rearrangement of the layers to the original $MgCl_2$ structure would be expected to correspond to a return to the initial high ammonia capacity of untreated $MgCl_2$ which is not the case. This indicates that it is not possible for the acetone treated layers to reorder to their original structure. This is similar to what is seen for rearrangement of single layer MoS_2.[30]

These similarities with single or few layer materials suggests that the acetone is exfoliating the layers and that the reason for the increased ammonia sorption rate is due to the magnesium centres being more accessible to ammonia. This shows that layer disruption or exfoliation should be targeted in future materials.

Further instability of AT-$MgCl_2$ is seen with cycling. As is discussed in Figure 5-2, $MgCl_2$ shows a slight decrease in capacity with cycling so a similar decrease in capacity of AT-$MgCl_2$ would not be unexpected. However, the AT-$MgCl_2$ shows a significantly greater decrease in capacity, with

almost all the initial capacity being lost due to cycling. This indicates that there is a further, different process in place here.

Based on comparison with similar literature materials, a likely explanation is that the layers are not reordering to the initial $MgCl_2$ structure but instead to a new structure and therefore are making accessing the magnesium centres difficult. Potential structures are proposed below.

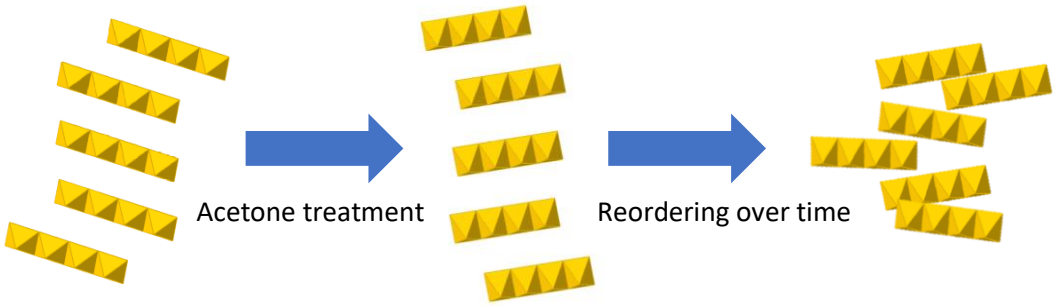

Figure 5-12: Layers of $MgCl_2$ octahedra (shown in yellow) and how the potential structural disruption caused first by acetone treatment and then proposed partial reordering over time.

Figure 5-12 shows possible structures which would explain the decrease in capacity of the acetone treated sample over time. Slight disordering of the layers could render the magnesium centres inaccessible, as shown.

This instability over time does not necessarily mean AT-$MgCl_2$ is not suitable for industrial use. The acetone treatment could be prepared immediately before use or could even be prepared *in-situ*. It is also possible that the reordered layers could be re-exfoliated, as is seen in other layered materials such as MoS_2.[30] This could mean that the initial improvement in capacity is achieved again, although this has not been explored here. The instability of AT-$MgCl_2$ with cycling is more likely to be problematic. As is shown inFigure 5-11.b., there is a significant decrease in capacity in cycle two and almost all of the initial capacity of AT-$MgCl_2$ is lost. It is again likely that the

exfoliated layers are reordering in a disrupted way, meaning that the magnesium centres are no longer accessible, lowering the capacity. The lowered capacity observed with cycling indicates that this material is not suitable for industrial applications, where multiple absorption desorption cycles are necessary.

5.5. Stable Layer Disruption

It is clear from the AT-$MgCl_2$ results that the initial disruption of the layers (i.e. to give better separation) is beneficial for rate of absorption but the instability of the layers means AT-$MgCl_2$ is unsuitable for industrial applications. If a material could be prepared where the $MgCl_2$ layers were disrupted but in a more stable, permanent way and without any loss in capacity, this could be an excellent candidate for fast ammonia absorption. A number of methods of layer disruption were attempted, discussed below.

5.5.1. Alternative Exfoliation Solvents

Two alternative exfoliation solvents were used. Ethanol was used as it is another organic solvent but is larger and more polar than acetone and has different functionality. Due to the previously mentioned similarities with MoS_2 layers, a similar method to that used for single layer MoS_2 was used.

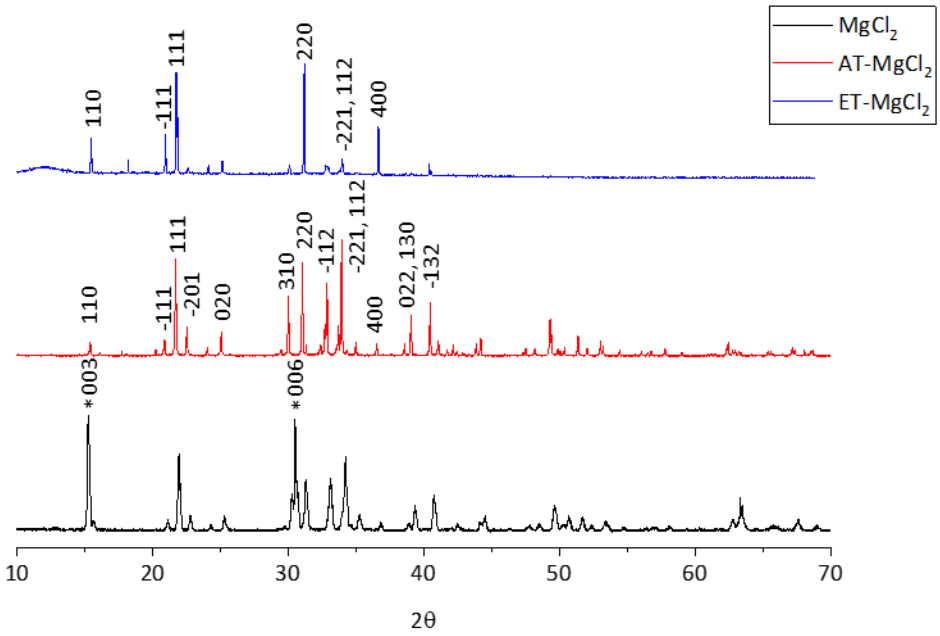

Figure 5-13: XRD patterns of $MgCl_2$, AT-$MgCl_2$ and ET-$MgCl_2$ recorded on a PANalytical X'Pert Alpha. Patterns were recorded between 4 and 70 °, using a step size of 0.017 ° and a step time of 1.03 s/step. The * represents $MgCl_2$ peaks, all other peaks are from $MgCl_2.6H_2O$ type structures.

ET-$MgCl_2$ shows the same $MgCl_2.6H_2O$ structure as AT-$MgCl_2$. Interestingly, there is a variation in the relative peak intensities from that seen in AT-$MgCl_2$. Particularly noticeable is that the 400 peak is greater in intensity in the ET-$MgCl_2$ when compared to the AT-$MgCl_2$ pattern. When carrying out solvent treatments on LDHs, researchers find the relative peak intensities change.[32] After acetone treatment of LDHs the 003 peak in the XRD pattern significantly decreases which they attribute to the generation of nanosheets meaning there is no longer stacking in this direction and so no diffraction. A similar effect may occur here; the increasing relative intensity of 400 may correspond to decreasing coherence in the structure indicating formation of nanosheets. However, the pre-treatment of the ammonia sorbents is expected to remove residual solvent (as was seen in 5.4.4) and so ET-$MgCl_2$ should be studied after drying ensuring no water sorption from the atmosphere to understand if this effect is also present in the dry sample. Unfortunately, as can be seen in Figure 5-13, the ethanol treated sample showed significant reordering under ambient conditions, as indicated by the absence of peaks at high angles. This corresponded to a transition from a powder to a wet, gel-like substance. The conversion of ET-$MgCl_2$ under ambient

conditions to an amorphous material and its extremely hygroscopic nature mean that ET-$MgCl_2$ is not a suitable for ammonia absorption as it is not practical to have an ammonia sorbent which is not stable under atmospheric conditions.

The attempted synthesis of exfoliated $MgCl_2$ with BuLi gave a gel on drying which could not be isolated for further testing.

5.5.2. Introduction of Dopant Elements

One method of introducing disruption was the use of dopant elements. The use of dopants is very common in materials chemistry leading to changes in unit cell sizes and chemical properties. A variety of dopants were tried. The dopants were chosen to study a range of ion sizes. One consideration is whether the dopant will cause disruption in the layers or instead form as a separate phase. It is also possible that the initial $MgCl_2$ structure could tolerate the introduction of the dopant and the structure would not undergo any change. Formulae exist which determine if a structure can tolerate dopants, e.g. in perovskites[33,34], but there is no equivalent work on dopants within $MgCl_2$.

$NiCl_2$ has the same crystal structure as $MgCl_2$[8] which may make it less likely to form as a separate phase as it can be more easily introduced into the $MgCl_2$ structure. $CuCl_2$ and $CaCl_2$ both have different structures from $MgCl_2$ (C2/m[35] and Pnnm[36] respectively). Ion size will also affect whether the structure is changed. Six coordinate Mg^{2+} has an ionic radius of 0.72 Å, while six coordinate Ni^{2+}, Ca^{2+} and Cu^{2+} have ionic radii of 0.69 Å, 1.00 Å and 0.73 Å respectively[37]. These dopants will therefore allow for the effect of both ion size and crystal structure of dopants to be studied.

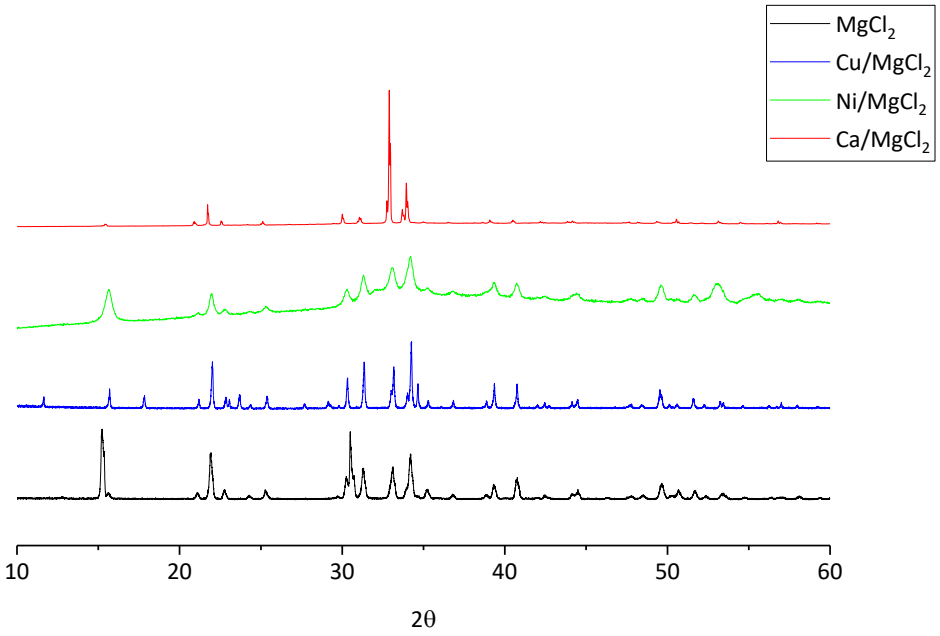

Figure 5-14: XRD pattern comparing $MgCl_2$), $Ca/MgCl_2$, $Cu/MgCl_2$ and $Ni/MgCl_2$ recorded on a PANalytical X'Pert. Patterns were recorded between 4 and 60 °, using a step size of 0.017 ° and a step time of 1.03 s/step.

XRD, shown above in Figure 5-14, shows that each of the doped materials show the same general structure as $MgCl_2$ with each showing hydrated $MgCl_2.6H_2O$ also. In $Cu/MgCl_2$, there is an additional phase present (shown by a small peak at around 11°), suggesting that the copper has not fully entered the $MgCl_2$ structure, most likely due to the different structure of $CuCl_2$ demonstrating this is more important in doping than ion size. However, none of the XRD patterns show significant peak shifting, suggesting there has not been any noticeable increase in layer spacing as a result of the introduction of dopant elements.

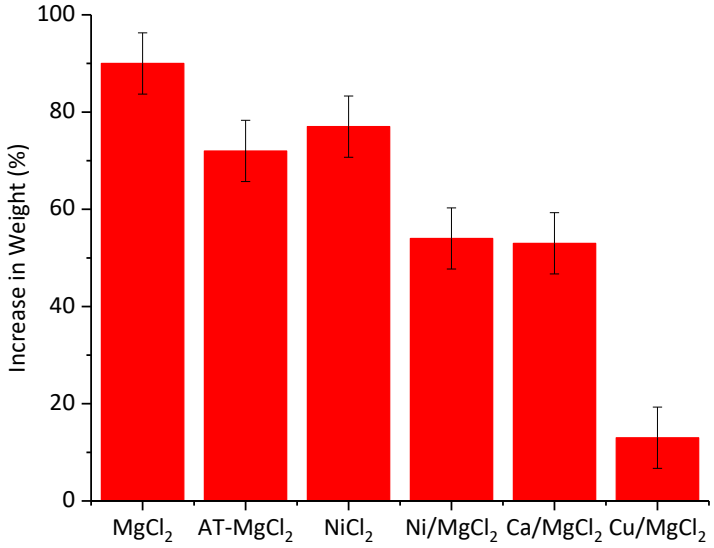

Figure 5-15: Maximum ammonia absorption of $MgCl_2$, AT-$MgCl_2$, $NiCl_2$, Ni/$MgCl_2$, Ca/$MgCl_2$ and Cu/$MgCl_2$ capacity measured on a Hidden Isochema IGA-002 using 1000 mbar pure ammonia. Approximately 20 mg of sample was placed in the IGA sample chamber, each sample was dried at 300 °C for eight hours, under vacuum, cooled to 25 °C and the initial sample weight accurately recorded. At 25 °C ammonia pressure was increased at 200 mbar intervals, kept at each pressure for 20 minutes and the sample weight accurately recorded; the maximum capacity shown here is the sample weight at 1000 mbar ammonia pressure.

As is seen in Figure 5-15, each of the doped materials shows a significantly lower absorption capacity than $MgCl_2$ (90±6 % capacity) or $NiCl_2$ (77±6 %, discussed in greater detail previously, see Figure 5-2). Nickel doped $MgCl_2$ had capacity of 54±6 % and calcium doped $MgCl_2$ has capacity of 53±6 %, both showing a decrease on the unmodified materials. The copper doped material showed the lowest capacity of all the materials, at 13±6 %, suggesting that the different structures of $MgCl_2$ and $CuCl_2$ make the introduction of Cu^{2+} into $MgCl_2$ difficult.

It is clear that doping $MgCl_2$ with other elements does not improve the layer structure of $MgCl_2$ and in fact causes a significant decrease in the ammonia absorption. As the absorption capacity was so low in these materials absorption rate was not studied.

5.5.3. Pillaring

Pillaring was attempted as an alternative method of separating the layers. There has been significant work on pillaring of LDH materials[38], another class of layered materials.

Initially terephthalic acid (TPA) was used as a pillar. It is commonly used in MOFs as a linker where it forms the scaffold separating metal ions, as in UiO-66, MOF-5 and the MIL family[39]. TPA pillaring is also used in LDHs, where the introduction of pillars creates additional catalytic sites and disrupts the layered structure[40]. For these reasons, terephthalic acid was introduced to see if this led to an improvement in sorption capacity or rate.

As the synthesis is well studied[40], TPA pillared Mg/Al LDH was first prepared.

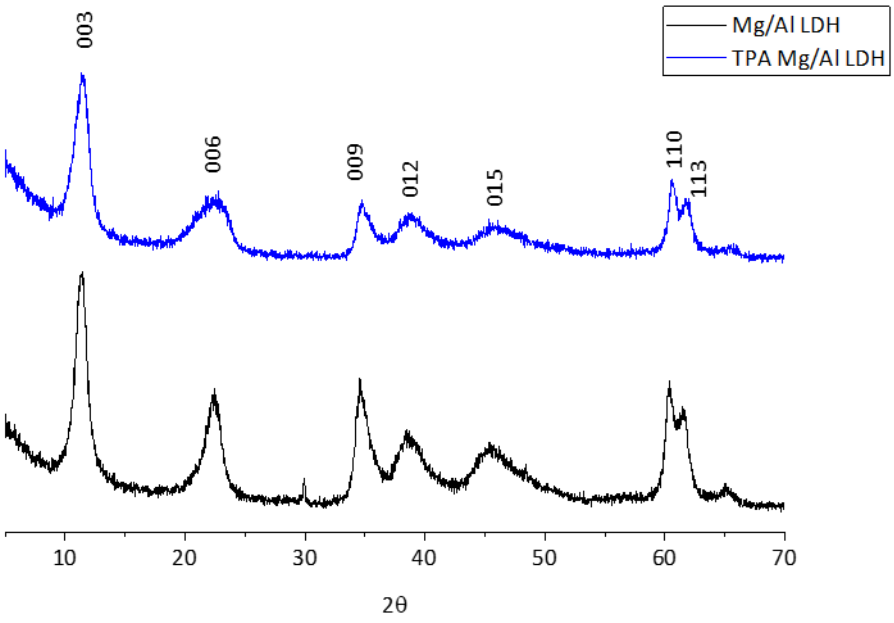

Figure 5-16: XRD patterns of Mg/Al LDH and TPA Mg/Al LDH recorded on a PANalytical X'Pert Alpha. Patterns were recorded between 4 and 70 °, using a step size of 0.017 ° and a step time of 1.03 s/step. Peak hkl assignments adapted from [41].

As is shown in Figure 5-16, the introduction of the TPA pillar did not cause loss of LDH structure. However, there is also no change in peak spacing (which would indicate a change in layer spacing)

and a slight decrease in crystallinity, as evidenced by the broader peaks in the XRD pattern of the pillared LDH. However, this is different to the literature, where TPA pillaring of an Mg/Al LDH almost doubled the spacing between LDH layers, noticeable in XRD patterns.[38] The only difference between the synthesis here and the literature synthesis is the Mg:Al ratio; it is clear that either this affects the ability of the TPA to increase the layer spacing or the TPA was not intercalated between the layers in this sample.

$MgCl_2$ was also treated to introduce pillars.

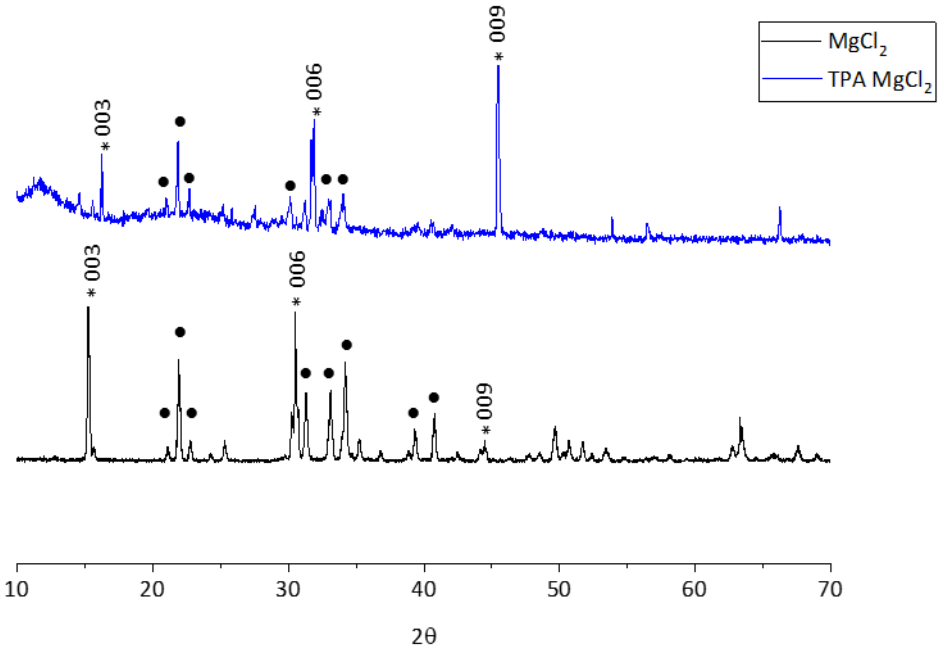

Figure 5-17: XRD patterns of $MgCl_2$ and TPA $MgCl_2$ recorded on a PANalytical X'Pert Alpha. Patterns were recorded between 4 and 70 °, using a step size of 0.017 ° and a step time of 1.03 s/step. * represent $MgCl_2$ peaks and ● represent hydrated $MgCl_2$.

Figure 5-17 shows the XRD of the TPA pillared $MgCl_2$ shows both $MgCl_2$ and hydrated $MgCl_2$ as was seen in each of the modified samples. Interestingly, there is a change in relative intensities of the $MgCl_2$ phases with the 009 peak being significantly larger in the TPA pillared $MgCl_2$. This suggests that there is a change in the layering, leading to greater coherence between the pillared layers. A similar effect was seen when 2-aminoterephthalic acid was intercalated into a Ni/Al LDH.[42] This supports that the layering has changed as a result of pillaring. This is promising for

ammonia sorption; it would be interesting to see if the layers being held apart by the pillars leads to faster or more stable adsorption.

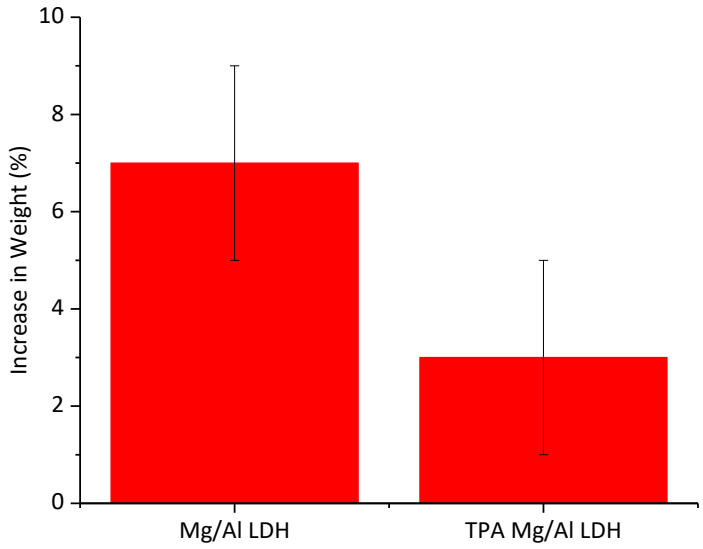

Figure 5-18: Maximum ammonia adsorption of Mg/Al LDH and TPA Mg/Al LDH capacity measured on a Hidden Isochema IGA-002 using 1000 mbar pure ammonia. Approximately 20 mg of sample was placed in the IGA sample chamber, each sample was dried at 300 °C for eight hours, under vacuum, cooled to 25 °C and the initial sample weight accurately recorded. At 25 °C, ammonia pressure was increased at 200 mbar intervals, kept at each pressure for 20 minutes and the sample weight accurately recorded; the maximum capacity shown here is the sample weight at 1000 mbar ammonia pressure.

Unfortunately, as is shown in Figure 5-18, the TPA pillaring of Mg/Al LDH has a negative effect on the ammonia capacity. Unmodified Mg/Al LDH had a capacity of 7 % while the TPA pillared version only had capacity of 3 %; over half of the initial capacity was lost as a result of pillaring. Although the target area for improvement was adsorption rate, this is not useful if it comes at significant detriment to the adsorption capacity.

5.5.4. Introduction of Interlayer Species

Another method of layer separation discussed in the literature is the introduction of interlayer species. This is used in LDH materials. The method developed by Lopez-Salinas and Ono[43] was initially trialled with a Ni/Mg LDH which was used in the screening process and seemed successful

so was also attempted for $MgCl_2$. However, when $MgCl_2$ was used instead of the LDH, the interlayer $NiCl_4$ hydrated very quickly under ambient conditions (as shown by a change in colour and transition from a solid to a liquid) making the material inappropriate for ammonia absorption.

5.5.5. Supported $MgCl_2$ Screening

The possibility of supporting $MgCl_2$ on a high surface area material was also explored. It was hoped that if the $MgCl_2$ was present as a single layer on the surface of a high surface area support then the magnesium centres would be very easy to access, and so sorption would be fast, but as they were anchored to the support there would be no problems with layer rearrangement.

Another benefit of a supported $MgCl_2$ catalyst is that it would be expected to show a constant volume with sorption. $MgCl_2$ increases greatly in volume with absorption of ammonia and it has been shown that this means it is not suitable for use in some industrial settings.[44] $MgCl_2$ on a porous support would not show a change in volume with sorption, as the sorption is taking place within the void of the pores which is already present. In a supported sorbent the ammonia is merely filling previously empty space when it binds to the magnesium compared to unsupported $MgCl_2$ where it must enter the structure and so increases the volume.

Two different classes of support were initially trialled; activated carbon and zeolite. Both are known to have high surface areas and also good high temperature stability.[45]

Two different methods of supporting $MgCl_2$ on supports were used, both using acetone treatment. It was hoped that the acetone treatment would at least partially exfoliate the layers before they were loaded on to the support, giving the previously discussed benefits in rate, without the problems with stability. In one experiment, the saturated $MgCl_2$ solution and support

were both added to acetone at the same time ($MgCl_2$/C(1)). Alternatively, the $MgCl_2$ was treated with acetone and then the support added and the mixture stirred ($MgCl_2$/C(2)).

Initial ammonia sorption capacity results are shown below.

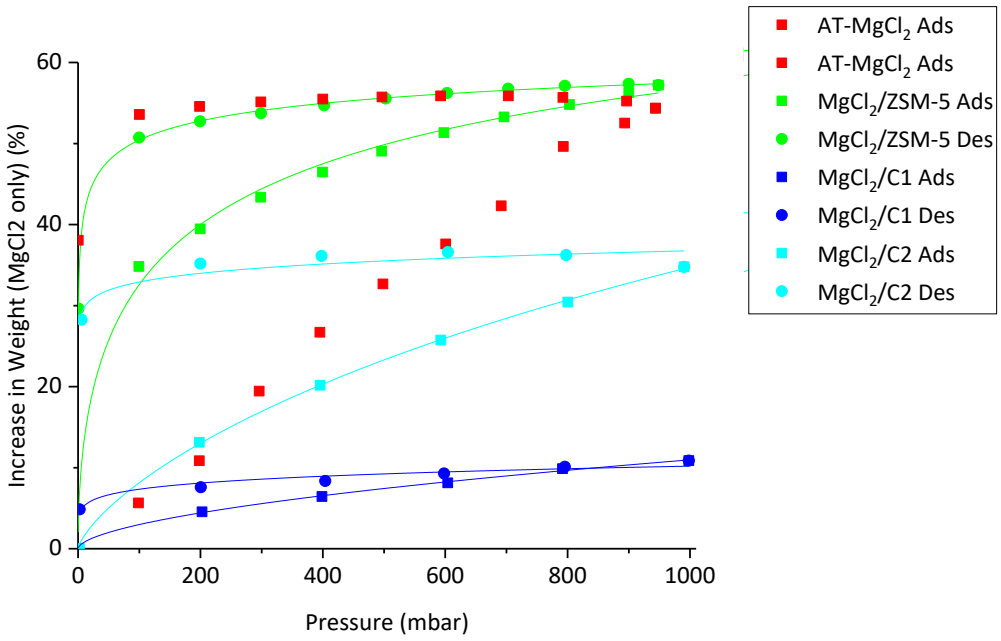

Figure 5-19: Ammonia sorption isotherms for AT-$MgCl_2$, $MgCl_2$/ZSM-5, $MgCl_2$/C(1) and $MgCl_2$/C(2) measured on a Hidden Isochema IGA-002 using pure ammonia. Approximately 20 mg of sample was placed in the IGA sample chamber, each sample was dried at 300 °C for eight hours, under vacuum, cooled to 25 °C and the initial sample weight accurately recorded. Each isotherm was collected at 25 °C. During sorption on $MgCl_2$/C(1) and $MgCl_2$/C(2), ammonia pressure was increased at 200 mbar intervals, kept at each pressure for 20 minutes and the sample weight accurately recorded. During desorption, ammonia pressure was decreased at 200 mbar intervals, kept at each pressure for 20 minutes and the sample weight accurately recorded. During sorption on AT-$MgCl_2$ and $MgCl_2$/ZSM-5, ammonia pressure was increased at 100 mbar intervals, kept at each pressure for 20 minutes and the sample weight accurately recorded. During desorption, ammonia pressure was decreased at 100 mbar intervals, kept at each pressure for 20 minutes and the sample weight accurately recorded. Each of the supported samples is adjusted to only consider the $MgCl_2$ weight, to allow for valid comparison.

As can be seen in Figure 5-19, each of the modified materials still shows a typical type 1 type isotherm, indicating that the $MgCl_2$ loading on the supports has not caused a loss in porosity. This is a good indication, as it was possible that $MgCl_2$ could form as large particles blocking the pores, instead of a single layer as was hoped. Any particles that have formed have not formed to such an extent that the materials are no longer porous.

There is a variation is the ammonia capacity possible in each material. Both activated carbon-based materials show lower sorption than the acetone treated $MgCl_2$ sample, although method 2 of loading $MgCl_2$ gave significantly higher ammonia sorption (maximum capacity of 35 %, based on $MgCl_2$ content) than method 1 (maximum capacity of 11 %). It is clear that the $MgCl_2$ layers first need to be exfoliated before being loaded onto the support. It is likely that the support being present while the layers are exfoliated causes the $MgCl_2$ to bind to the support before the layers are fully exfoliated. It is possible that the acetone treatment has a detrimental effect on the activated carbon support and causes a breakdown of the porosity but this seems less likely.

It is clear than the $MgCl_2$ loading on zeolite shows the best ammonia sorption capacity. When only the $MgCl_2$ weight is considered (as is reasonable given the $MgCl_2$ loading was chosen so as to completely cover the surface of the zeolite) the $MgCl_2$/ZSM-5 sample shows a comparable maximum ammonia capacity to AT-$MgCl_2$ ($MgCl_2$/ZSM-5 showing a maximum capacity of 57 % compared to 54 % for AT-$MgCl_2$). Furthermore, at lower ammonia pressures, the capacity of $MgCl_2$/ZSM-5 is significantly higher than AT-$MgCl_2$ e.g. the 200 mbar capacity for $MgCl_2$/ZSM-5 is 39 % over three times the capacity of AT-$MgCl_2$ which was 11 % at the same pressure. $MgCl_2$/ZSM-5 is clearly a better low temperature sorbent, probably due to the improved diffusion abilities of the material. This supports the previous hypothesis that interlayer spacing and accessibility of magnesium centres are the main factors leading to easy ammonia sorption. This also has implications for possible industrial uses; under conditions where there is likely to be a low ammonia pressure, supported $MgCl_2$ could take up significantly more ammonia than the standard $MgCl_2$ materials. This would be beneficial for consumer transport applications, where pure ammonia gas is likely to cause safety concerns. Sorbents which have high ammonia capacity at low partial pressures of ammonia would be extremely beneficial.

Due to the good sorption capacity of $MgCl_2$/ZSM-5, it was studied in further detail.

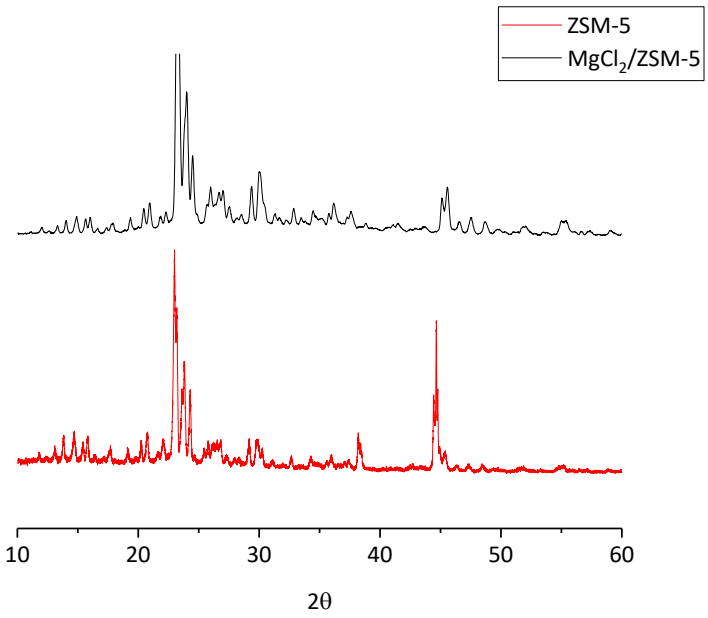

Figure 5-20: XRD patterns of $MgCl_2$/ZSM-5 and unmodified ZSM-5, recorded on a PANalytical X'Pert. Patterns were recorded between 4 and 70 °, using a step size of 0.017 ° and a step time of 1.03 s/step.

As can be seen in Figure 5-20, the XRD patterns of $MgCl_2$/ZSM-5 and unmodified ZSM-5 are similar. $MgCl_2$/ZSM-5 does not show any peaks indicative of $MgCl_2$ species confirming that any $MgCl_2$ is present as a single layer or very small particles. This, combined with the ammonia sorption isotherm, shows there is no $MgCl_2$ particles blocking the zeolite pores.

As the expected benefit from the supported material was fast, stable sorption, the cycling ability of $MgCl_2$/ZSM-5 was also studied.

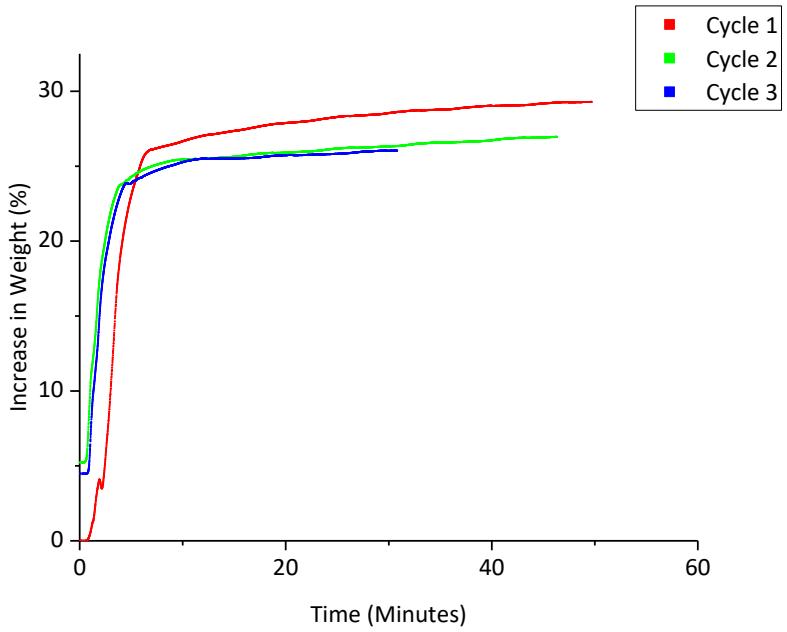

Figure 5-21: Sorption graphs recorded on Hidden Isochema IGA-002 for $MgCl_2$/ZSM-5, with cycles 1, 2 and 3. Approximately 20 mg of sample was placed in the IGA sample chamber. Prior to sorption materials were dried under vacuum at 300 °C for 8 hours, cooled to 25 °C and the sample weight accurately recorded. For sorption, pure ammonia gas at 400 mbar was introduced at a rate of 100 mbar/min at 25 °C and the pressure kept constant. The weight change in the materials was accurately recorded to track the sorption. To desorb the ammonia between cycles, the pressure was decreased to vacuum and the temperature increased to 300 °C for 8 hours.

As can be seen in Figure 5-21, the $MgCl_2$/ZSM-5 sample shows much faster initial ammonia sorption than $MgCl_2$ (Figure 5-2). The zeolite support allows for easy access to the magnesium centres and so gives very fast sorption. It is also a much more stable material with each of the sorption cycles being similar, and no significant decrease in capacity with cycling being seen. Given that fast ammonia sorption and desorption has been shown to be crucial for increased activity in sorption assisted ammonia synthesis[11] this material is very promising. The high stability with cycling is beneficial for industrial applications where many cycles are required.

The rate data clearly shows that the separation of magnesium chloride layers is beneficial for fast sorption with the additional benefit of $MgCl_2$/ZSM-5 giving very stable sorption.

5.5.6. High Temperature Sorption

Zeolites are known for their high temperature stability particularly in industrial applications under high pressures. The high temperature sorption capacity of $MgCl_2$/ZSM-5 was also explored.

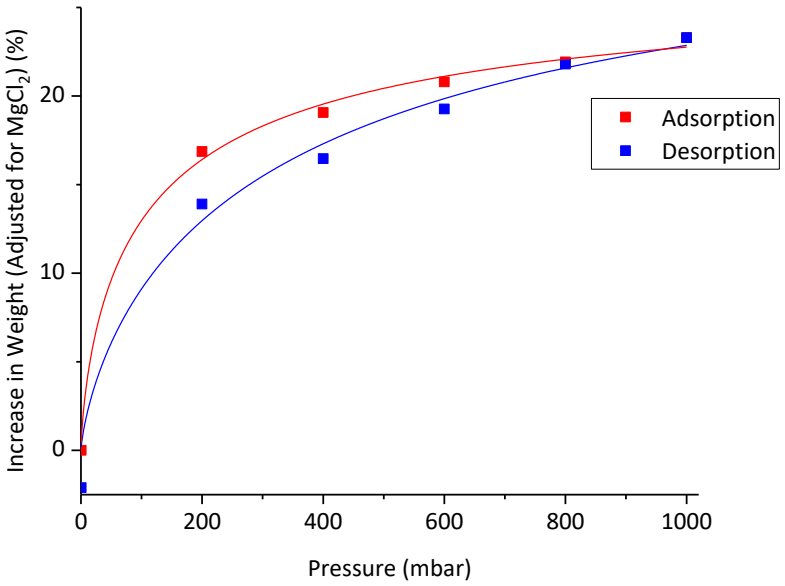

Figure 5-22: High temperature (250 °C) ammonia sorption isotherm for $MgCl_2$/ZSM-5 measured on a Hidden Isochema IGA-002. Approximately 20 mg of sample was placed in the IGA sample chamber, the sample was dried at 300 °C for eight hours, under vacuum, cooled to 250 °C and the initial sample weight accurately recorded. Ammonia pressure was increased at 200 mbar intervals, kept at each pressure for 20 minutes and the sample weight accurately recorded. During desorption, ammonia pressure was decreased at 200 mbar intervals, kept at each pressure for 20 minutes and the sample weight accurately recorded. The weight is adjusted to only consider the $MgCl_2$ weight, to allow for valid comparison with other samples.

As is shown above, $MgCl_2$/ZSM-5 shows much higher sorption capacity at high temperatures than $MgCl_2$ alone, which shows a 400 mbar capacity of 6 wt% (as shown previously in Figure 5-5). $MgCl_2$/ZSM-5 shows a 19 % capacity based on $MgCl_2$ at the same pressure. Interestingly, this is the only sample studied which shows a lower weight after desorption than the initial weight of sorbent. This is probably due to the high temperature meaning ammonia can react with any surface species remaining on the zeolite. Most importantly, this does not affect the capacity of the zeolite. This good temperature stability, combined with very fast sorption, makes it an excellent possibility for industrial Haber type processes. As was previously discussed (in section

5.2), there is a strong relationship between the distance between the absorbent and the catalyst beds and the improvement in absorption capacity. This leads to the possibility of a mixed catalyst sorbent bed, where there is no separation between the catalyst and the sorbent. This is one system proposed by Cussler for improved ammonia synthesis using sorbent assisted Haber process.[3] For these types of set ups it is very important that the sorbent shows high temperature stability and so $MgCl_2$/ZSM-5 is an excellent candidate. $MgCl_2$ supported on zeolite is a promising sorbent for a system of this type and should be further explored.

5.6. Conclusions

$MgCl_2$ was studied in greater detail, as it is the most commonly used industrial ammonia absorbent. Results showed that it shows the higher absorption capacity of the studied layered materials though it shows slow absorption and significantly lowered high temperature capacity. Catalytic testing confirmed the absorbents close to the catalytic bed improve the catalyst activity. Nanopore generation and separation of $MgCl_2$ layers was shown to significantly improve the rate of ammonia absorption. Despite multiple alternative methods being tried it was not possible to exfoliate the layers in a stable way. Instead, $MgCl_2$ layers were supported on zeolites which gave fast, stable sorption. Zeolite supported $MgCl_2$ also gave good high temperature sorption and improved low ammonia pressure sorption, meaning that it shows great potential to be used in a mixed catalyst sorbent bed in industrial Haber applications.

5.7. Future Work

These results show great scope for further experimentation. Alternative methods of supporting $MgCl_2$ could be explored, with the aim of increasing the proportional weight of $MgCl_2$ and thus overcoming the lower ammonia capacity on a gravimetric basis. Testing of the proposed mixed catalyst sorbent bed would confirm that the high temperature sorption capacity of $MgCl_2$/zeolite

is beneficial. There are a number of other applications where $MgCl_2$ is used as a catalyst or absorbent including in Ziegler-Natta catalysts and heat exchangers. Although significantly out with the scope of this project, it would be interesting to see if the stable supported $MgCl_2$ based materials give any benefits in these applications.

5.8. References

1. J. S. Hummelshøj, R. Z. Sørensen, M. Y. Kustova, T. Johannessen, J. K. Nørskov and C. H. Christense, *J. Am. Chem. Soc*., 2006, **128**, 16-17.

2. H. Zhu, X. Gu, K. Yao, L. Gao and J. Chen, *Ind. Eng. Chem. Res*., 2009, **48**, 5317-5320.

3. H. H. Himstedt, M. S. Huberty A. V. McCormick, L. D. Schmidt and E. L. Cussler, *Am. Inst. Chem. Eng. J*., 2015, **61**, 1364-1371.

4. C. Y. Liu and K. Aika, *Ind. Eng. Chem. Res*., 2004, **43,** 7484-7491.

5. C. Y. Liu and K-I Aika, *Bull. Chem. Soc. Jpn*., 2004, **77**, 123-131.

6. V. E. Sharonov and Y. I. Aristov, *React. Kinet. Catal. Lett*., 2005, **85**, 183-188.

7. E. Stavrou, Y. Yao, J. M. Zaug, S. Bastea, B. Kalkan, Z. Konopkova and M. Kunz, *Sci. Rep*., 2016, **6**, 30631.

8. A. Ferrari, A. Braibanti and G. Bigliardi, *Acta Crystallogr*., 1963, **16**, 846-847.

9. C. L. Perkins, C. Beall, M. O. Reese and T. M. Barnes, *ACS Appl. Mater. Interfaces*, 2017, **9,** 20561-20565.

10. C. Chen, A. Wangriya, J. Buffet and D. O'Hare, *Dalt. Transations*, 2015, **44**, 16392-16398.

11. D. K. Ojha, M. J. Kale, P. J. Dauenhauer, A. McCormick and E. L. Cussler, *ACS Sustain. Chem. Eng*., 2020, **8**, 15475-15483.

12. T. J. Huttemaxn, B. M. Foxmax, C. R. Sperati and J. G. Verkade, *Inorg. Chem*., 1965, **4**, 950-953.

13. A. Simon, H. Mattausch, M. Ryazanov and R. K. Kremer, *Anorg. Allg. Chem*., 2006, **632**, 919-929.

14. M. Kubota, K. Matsuo, R. Yamanouchi and H. Matsuda, *J. Chem. Eng. Japan*, 2014, **47**, 542-548.

15. I. Olovsson, *Acta Crystallogr*., 1965, **18**, 889-893.

16. M. O. Jones, D. M. Royse, P. P. Edwards and W. I. F David, *Chem. Phys*., 2013, **427**, 38-43.

17. A. Leineweber, M. W. Friedriszik and H. Jacobs, *J. Solid State Chem*., 1999, **147,** 229-234.

18. M. Malmali, M. Reese, A. V. McCormick and E. L. Cussler EL, *ACS Sustain. Chem. Eng*., 2018, **6**, 827-834.

19. M. J. Palys, A. McCormick, E. L. Cussler and P. Daoutidis, *Proccesses*., 2018, **6**, 91.

20. H. H. Himstedt, M. S. Huberty A. V. McCormick, L. D. Schmidt and E. L. Cussler, *Am. Inst. Chem. Eng. J*., 2015, **61**, 1364-1371.

21. M. Malmali, Y. Wei , A. McCormick and E. L. Cussler, *Ind. Eng. Chem. Res*., 2016, **55,** 8922-8932.

22. M. Malmali, Y. Wei , A. McCormick and E. L. Cussler, *Ind. Eng. Chem. Res*., 2016, **55,** 8922-8932.

23. M. Malmali, G. Le, J. Hendrickson, J. Prince, A. V. McCormick and E. L. Cussler, *ACS Sustain. Chem. Eng*., 2018, **6**, 6536-6546.

24. A. A. Coelho, *J. Appl. Crystallogr*., 2003, **36**, 86-95.

25. P. A. Agron and W. R. Busing, *Acta Crystallogr*., 1985, **C41**, 8-10.

26. Q. Huang, G. Lu, J. Wang and J. Yu, *J. Anal. Appl. Pyrolysis,* 2011, **91**, 159-164.

27. S. V. Halilov, D. J. Singh, M. Gupta and R. Gupta, *Phys. Re.v B – Condens. Matter Mater. Phys*., 2004, **70**, 1-11.

28. C. H. Christensen, R. Z. Sørensen, T. Johannessen, U. J. Quaade, K. Honkala, T. D. Elmoe, R. Kohler and J. K. Norskov, *J. Mater. Chem*., 2005, **15**, 4106-4108.

29. X. Wang, Y. Sun and K. Liu, *2D Mater*., 2019, **6**, 042001.

30. L. Nurdiwijayanto, R. Ma, N. Sakai and T. Sasaki, *Inorg. Chem*., 2017, **56**, 7620-7623.

31. A. Castellanos-Gomez, L. Vicarelli, E. Prada, J. O. Island, K. L. Narasimha-Acharya, S. I. Blanter, D. J. Groenendijk, M. Buscema, G. A. Steela, J. V. Alvarez, H. W. Zandbergen, J. J. Palacios and H. S. J. van der Zant, *2D Mater*., 2014, 1, 025001.

32. Q. Wang and D. O'Hare, *Chem. Rev*., 2012, **112**, 4124-4155.

33. L. Xu, S. Yuan, H. Zeng and J. Song, *Mater. Today Nano*.. 2019, **6**, 100036.

34. X. Zhang, L. Li, Z. Sun and J. Luo, *Chem. Soc. Rev*., 2019, **48**, 517-539.

35. A. F. Wells, *J. Chem. Soc*., 1947, **0**, 1670-1675.

36. C. J. Howard, B. J. Kennedy and C. Curfs, *Phys. Rev. B – Condens. Matter Mater. Phys*., 2005, 72, 2-7.

37. R. D. Shannon, *Acta Crystallogr*., 1976, **A32**, 751-767.

38. A. Béres, I. Pálinkó, I. Kiricsi, J. B. Nagy, Y. Kiyozumi and F. Mizukami, *Appl. Catal. A Gen*., 1999, **182**, 237-247.

39. E. S. M. El-Sayed and D. Yuan, *Green Chem*., 2020, **22**, 4082-4104.

40. M. Drezdzon, *Inorg. Chem.,* 1988, **27**, 4628-4632.

41. K. Klemkaite, I. Prosycevas, R. Taraskevicius, A. Khinsky and A. Kareiva, *Cent. Eur. J. Chem*., 2011, **9**, 275-282.

42. C. S. de Matos, M. M. Nóbrega, M. L. A. Temperini and V. R. L. Constantino, *Appl. Clay Sci*., 2019, **174,** 152-158.

43. E. Lopez-Salinas and Y. Ono, *Microporous Mater*., 1993, **1**, 33-42.

44. M. van der Pal, R. de Boer and J. Veldhuis, *International Symposium on Innovative Materials for Process in Energy Systems*, 2013.

45. R. E. Morris and P. S. Wheatley, *Angew. Chemie Int. Ed*., 2008, **47**, 4966-4981.

6. Conclusions

Ammonia sorbents are important for both the synthesis and transport of so-called green ammonia. Though $MgCl_2$ is currently the most commonly used absorbent for ammonia it has a number of deficiencies and so new materials are needed targeting sorption and desorption speed and high temperature and cycling stability.

First, porous materials were screened; based on these results 13X was studied further. The sodium ions in 13X were exchanged for protons, lanthanum or magnesium and the samples were studied for ammonia uptake. The introduction of these cations all improved the ammonia adsorption capacity particularly for the latter two as compared to the parent Na13X zeolite structure, while also improving adsorption speed and stability. It is found that Na13X zeolite is mainly characterized by Lewis acid sites for weak adsorption of ammonia (ammonia desorption < 200^{o}C). Proton ion exchange gave some stronger binding sites (ammonia desorption > 400^{o}C) for ammonia as a result of Brønsted acid site (Al-O(H)-Si) generation. On the other hand, La13X showed comparably weak dwelling sites but significantly higher capacity for ammonia uptake. Lanthanum ion exchange was shown to cause dealumination in the structure. Interestingly, the partial ion exchange of sodium ions of Mg13X gave both weak and strong binding sites for ammonia, indicative of the coexistence of both Brønsted and Lewis acidity; this was determined to be due to the generation of magnesium hydroxide species. The locations of the sites in each zeolite were studied using SXRD and modelling.

Each of the zeolites achieved the aims of stability with cycling and fast ammonia adsorption. The variety of ammonia strengths seen in the prepared zeolites means that they can be tailored to specific applications; La13X when low desorption temperature ammonia is required and Mg13X where high temperature stability is valuable. This makes them suitable for either low and high temperature Haber applications.

One clear avenue for further study of these materials would be using neutron diffraction to understand how the ammonia molecules orientate with respect to each other and the zeolite framework. This would also allow the Brønsted acid site locations to be unambiguously assigned. There is also scope for optimising the ion exchange process for each sample to potentially increase the ammonia capacity through the generation of additional sites.

The lanthanum ion exchange process was studied in greater detail to understand how the dealumination affected the ammonia capacity of the zeolites. The effect of temperature on the ion exchange process was studied. Higher ion exchange temperatures and longer ion exchange times gave a lower ammonia capacity due to the increased dealumination in the samples. The effect of varying lanthanum ion content was also studied and two competing processes found to affect the capacity. Too low a lanthanum ion concentration during exchange means there is not enough ammonia binding sites while too high a lanthanum ion concentration leads to unwanted interaction between the lanthanum ions and pore blocking which also leads to a decrease in ammonia binding sites. The lanthanum ion content in the zeolite improves activity though the detrimental dealumination process is a side effect of attempts to increase the lanthanum ion concentration within the zeolite. Furthermore, an inverse correlation between lanthanum content in the zeolites and ammonia desorption temperature was found. This suggests that there is room for further optimisation of the ideal lanthanum ion concentration. Furthermore, as the location of the extra-framework aluminium species was found to be important, techniques which could accurately determine its location would be interesting.

Finally, a variety of layered materials, including $MgCl_2$, were studied in greater detail. Treatment of $MgCl_2$ using acetone was found to significantly improve the absorption rate at detriment to the ammonia capacity; this was proposed to be due to reordering of the exfoliated $MgCl_2$ layers or

nanopore generation. This treatment was found to unstable with both time and cycling. Other methods of layer disruption were trialled including alternative exfoliation solvents, doping, pillaring and introduction of interlayer species. It was not possible to exfoliate the layers in a stable way using any of these methods. Instead, $MgCl_2$ layers were supported on zeolites which gave fast, stable sorption. Zeolite supported $MgCl_2$ also gave good high temperature sorption, fast sorption, good cyclability and improved low ammonia pressure sorption, meaning that it shows great potential to be used in a mixed catalyst sorbent bed in industrial Haber applications. Further methods of layer stabilisation could also be trialled.

7. Appendix

7.1.Chapter 3 Supplementary Information

7.1.1. Calculation of Ammonia Binding Energies

Thermogravimetric analysis (TGA) and differential thermogravimetric analysis (DTGA) of the ammonia adsorbed 13X materials were heated to 900 °C in nitrogen by using an TA Instruments SDT Q600 at 1, 5, 7.5, 10 and 20 °C/min heating rates. The desorption energy for ammonia desorbed from the zeolites were calculated according to the following equation, which was adapted from the Arrhenius equation which assumes first order desorption:

$$2\ln T_m - \ln\beta = E_{des}/RT_m + \ln E_{des}/AR$$

where T_m is the temperature giving maximum desorption in the differential thermogravimetric analysis curve, β is the temperature ramp rate, E_{des} is the desorption energy and A is a constant. Plotting ($2\ln T_m - \ln\beta$) versus $1/T_m$ for a series of β values allows the determination of E_{des}.

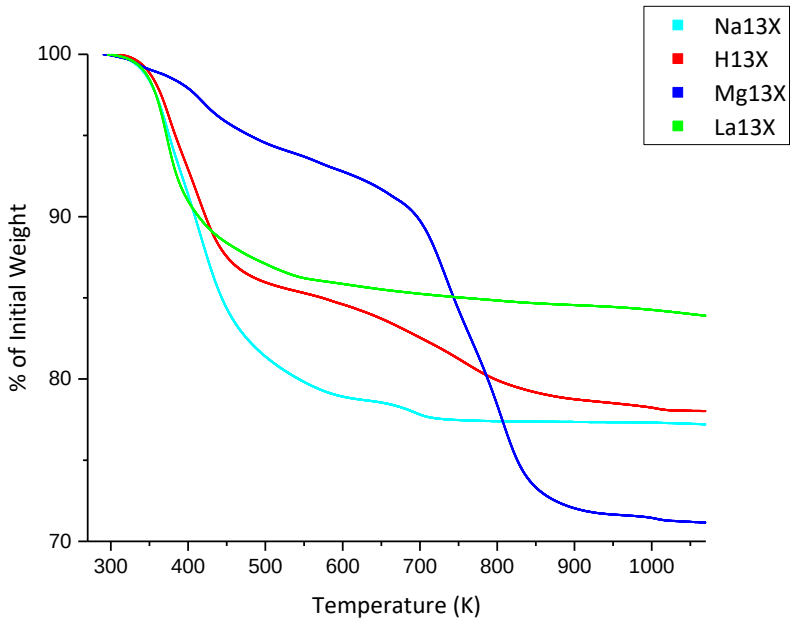

Figure 7-1: Desorption of ammonia on H13X, Mg13X and La13X recorded on a TA Instruments Q600 SDT. Clean samples were dried for eight hours at 300 °C under vacuum then were loaded with ammonia at 400 mbar until the weight stabilized (around 30 minutes) before being placed in the SDT. The temperature was increased to 800 °C at a rate of 10 °C/min under 100 ml/min flowing nitrogen and the weight change recorded.

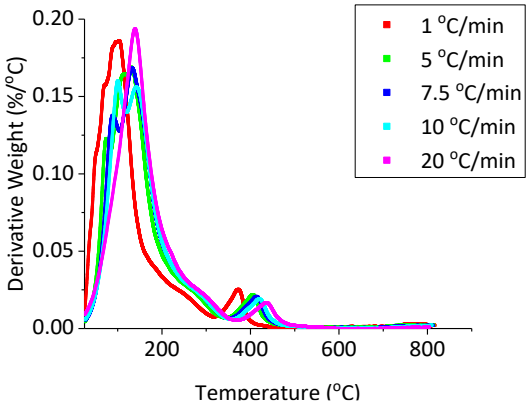

a. Differential thermogravimetric desorption of ammonia on Na13X at 1, 5, 7.5, 10 and 20 K/min heating rate.

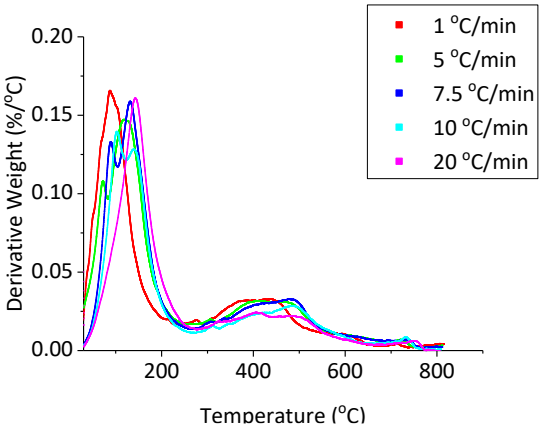

b. Differential thermogravimetric desorption of ammonia on H13X at 1, 5, 7.5, 10 and 20 K/min heating rate.

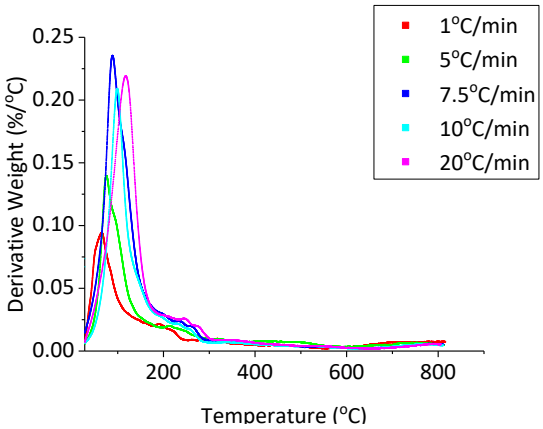

c. Differential thermogravimetric desorption of ammonia on La13X at 1, 5, 7.5, 10 and 20 K/min heating rate.

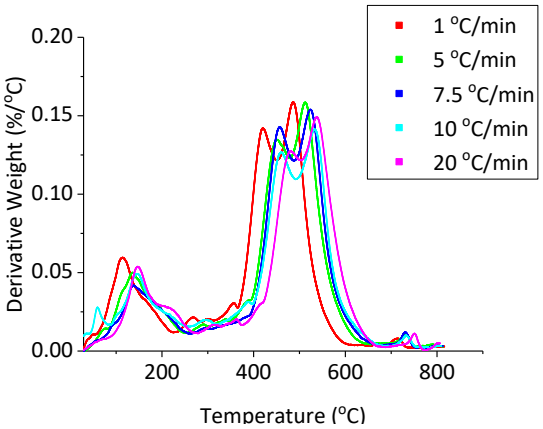

d. Differential thermogravimetric desorption of ammonia on Mg13X at 1, 5, 7.5, 10 and 20 K/min heating rate.

Figure 7-2: Differential thermogravimetric desorption of ammonia from Na13X, H13X, La13X and Mg13X at heating rates of 1, 5, 7.5, 10 and 20 K/min, recorded on a TA instruments Q600 SDT. To load ammonia on H13X, Mg13X and La13X, clean samples were dried for eight hours at 573 K under vacuum then were loaded with ammonia at 400 mbar until the weight stabilized (around 30 minutes). The samples were flushed with N_2 before being placed in the SDT. To load ammonia on Na13X the zeolite was dried at 453 K under vacuum for 4 hours, exposed to ammonia at approximately 400 mbar for 30 minutes and placed in the SDT. The temperature was increased to 1023 K at a rate of 20 K/min under 100 mL/min flowing nitrogen and the weight change recorded. In each case, approximately 10 mg of sample was used.

7.1.2. La13X Cycling

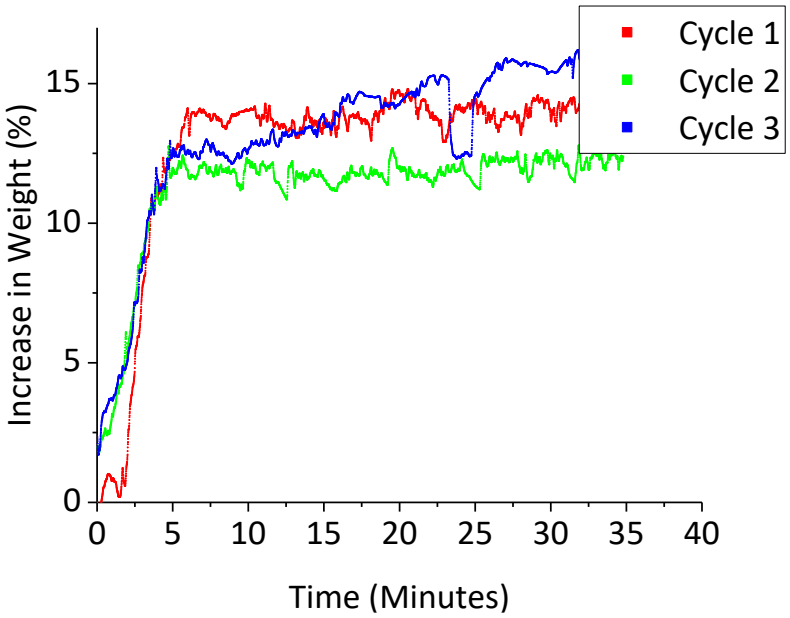

Figure 7-3: Adsorption rate graphs recorded on Hidden Isochema IGA-002 for La13X. Approximately 20 mg of sample was placed in the IGA sample chamber. Prior to adsorption materials were dried under vacuum at 573 K for 8 hours, and the sample weight accurately recorded. For adsorption, pure ammonia gas at 400 mbar was introduced at a rate of 100 mbar/min and the pressure kept constant. The weight change in the materials was recorded to track the adsorption. To desorb the ammonia between cycles, the pressure was decreased to vacuum and the temperature increased to 573 K for 8 hours.

7.1.3. SXRD Patterns

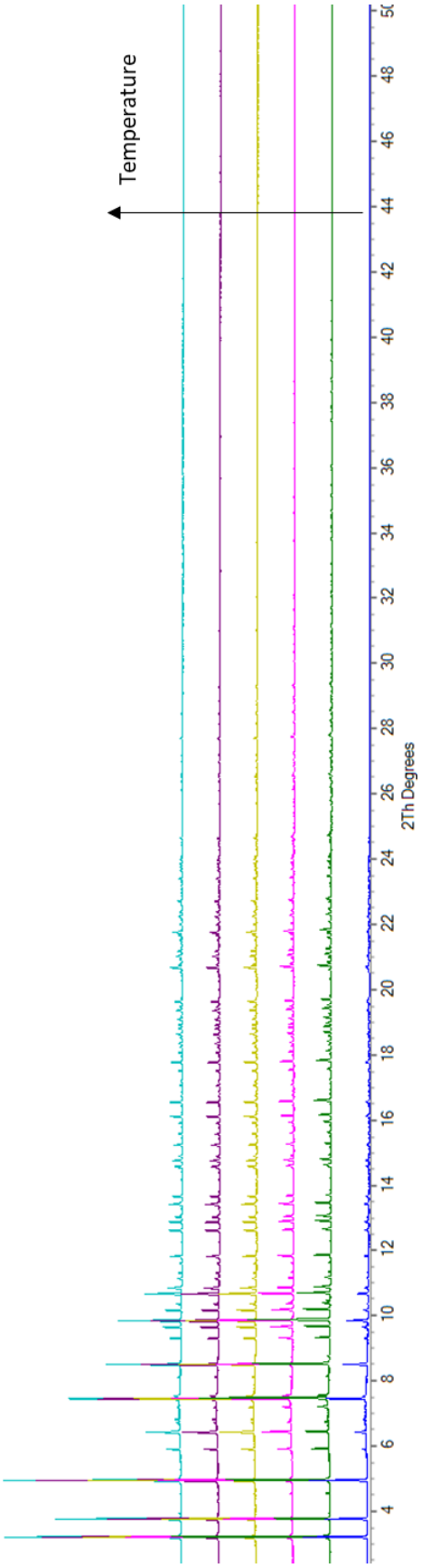

Figure 7-4: SXRD patterns of Na13X with ammonia at various temperatures, recorded at Spring-8, Japan.

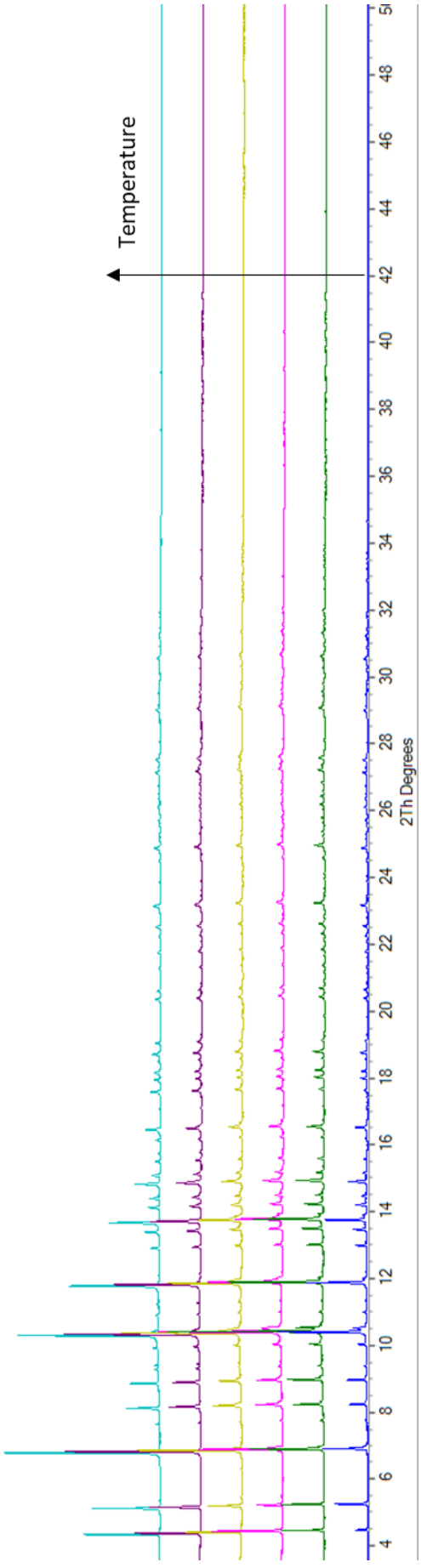

Figure 7-5: SXRD patterns of H13X with ammonia at various temperatures, recorded at Spring-8, Japan.

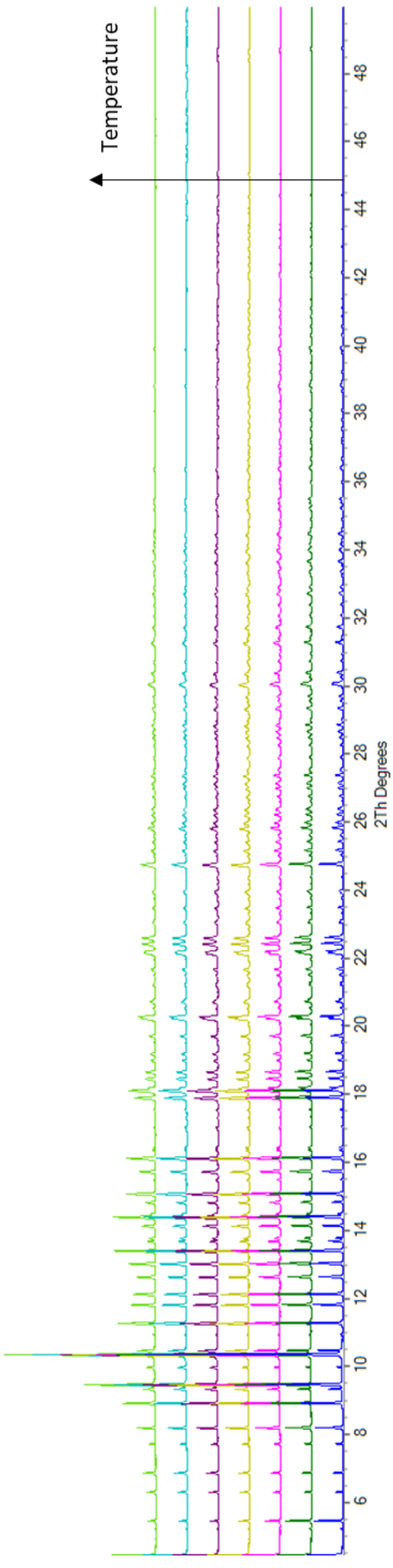

Figure 7-6: SXRD patterns of La13X with ammonia at various temperatures, recorded at Spring-8, Japan.

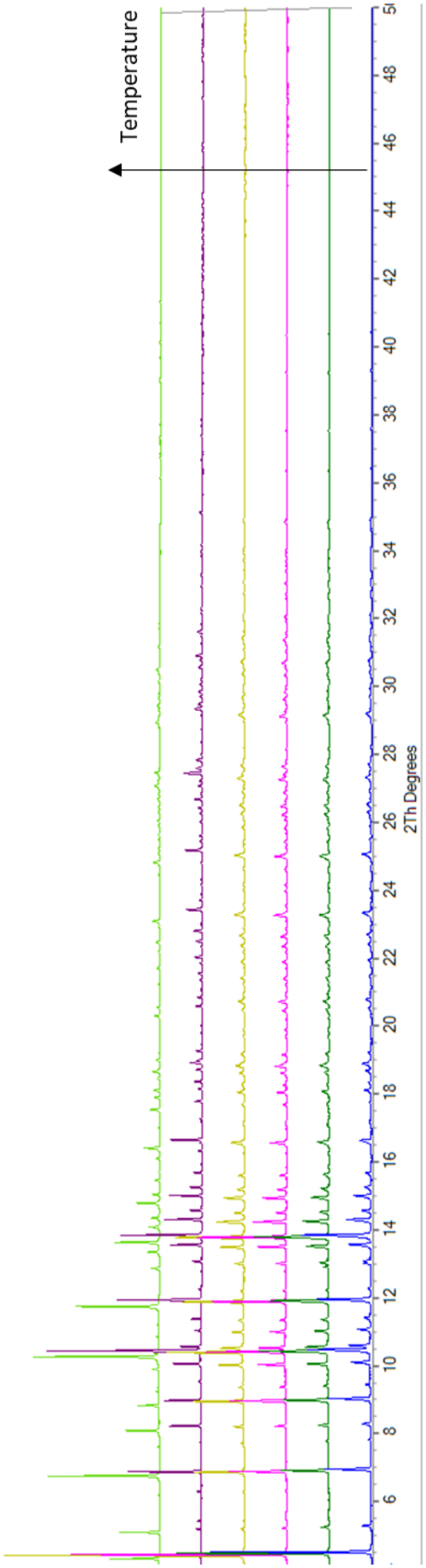

Figure 7-7: SXRD patterns of Mg13X with ammonia at various temperatures, recorded at Spring-8, Japan.

7.1.4. SXRD Refined Crystallographic Parameters

7.1.4.1. Na13X

Table 7-1: Refined crystallographic parameters for Na13X with ammonia at various temperatures, recorded at Spring-8, Japan.

	298 K	373 K	473 K	573 K	673 K	773 K
Crystal System	Cubic	Cubic	Cubic	Cubic	Cubic	Cubic
Space Group	Fd-3 (Origin 2)	Fd-3 (Origin 2)	Fd-3 (Origin 2)	Fd-3 (Origin 2)	Fd-3 (Origin 2)	Fd-3 (Origin 2)
2θ refinement range (°)	5-55	5-55	5-55	5-55	5-55	5-55
Detector	PSD	PSD	PSD	PSD	PSD	PSD
Number of Parameters	84	80	80	80	80	76
Number of hkls	4540	4497	4534	4542	4547	4543
Refinement Method	Rietveld	Rietveld	Rietveld	Rietveld	Rietveld	Rietveld
a (Å)	25.02409 (82)	24.94800 (36)	24.99686 (37)	25.03478 (34)	25.04426 (33)	25.03874 (33)
b (Å)	25.07469 (353)	24.96272 (217)	25.023178 (210)	25.06116 (202)	25.07007 (198)	25.06609 (196)
c (Å)	25.02148 (382)	24.94445 (203)	24.98815 (202)	25.02499 (188)	25.03326 (190)	25.02705 (189)
V (Å^3)	15700(3)	15535(2)	15630(2)	15701(2)	15717(2)	15708(2)
$R_{wp}/R_p/R_{exp}$	4.90195284 /3.77939262/4.35357111	5.88166643 /4.25188077/3.43330497	5.54008363 /4.14620494/3.48848254	5.11948399 /3.85994042/3.55074344	4.93384378 /3.73763971/3.57369988	4.8645262/ 3.68833056 /3.5911877
Gof χ^2	1.124567	1.713121	1.588107	1.441806	1.380598	1.354573
Wavelength (Å)	0.496007	0.496007	0.496007	0.496007	0.496007	0.496007
2θ Zero point (°)	0.0006299	0.0006299	0.0006299	0.0006299	0.0006299	0.0006299

7.1.4.2. H13X

Table 7-2: Refined crystallographic parameters for H13X with ammonia at various temperatures, recorded at Spring-8, Japan.

	298 K	373 K	473 K	573 K	673 K	773 K
Crystal System	Cubic	Cubic	Cubic	Cubic	Cubic	Cubic
Space Group	Fd-3 (Origin 2)	Fd-3 (Origin 2)	Fd-3 (Origin 2)	Fd-3 (Origin 2)	Fd-3 (Origin 2)	Fd-3 (Origin 2)
2θ refinement range (°)	3.5-55	3.5-55	3.5-55	3.5-55	3.5-55	3.5-55
Detector	PSD	PSD	PSD	PSD	PSD	PSD
Number of Parameters	80	80	80	76	76	76
Number of hkls	1680	1665	1649	1649	1650	1651
Refinement Method	Rietveld	Rietveld	Rietveld	Rietveld	Rietveld	Rietveld
a (Å)	24.89537 (85)	24.86524 (105)	24.78695 (134)	24.76879 (158)	24.77860 (113)	24.79783 (81)
b (Å)	24.91911 (363)	24.92984 (342)	24.82472 (487)	24.79697 (584)	24.80372 (480)	24.85002 (340)
c (Å)	24.89787 (391)	24.79868 (404)	24.76256 (482)	24.76865 (619)	24.80819 (436)	24.80309 (321)
V (Å^3)	15446(4)	15372(3)	15237(4)	15213(5)	15247(4)	15284(3)
$R_{wp}/R_p/R_{exp}$	8.70624381/5.77042238 1.086721004	9.21872567/6.16963232/0.823775903	8.55281967/5.41593292/0.819391289	9.71107538/6.10155512/0.838371388	8.26810302/5.31004447/0.846460752	7.20674356/4.86470034/0.85306202
Gof χ^2	8.01148	11.19082	10.43802	11.58326	9.767852	8.448089
Wavelength (Å)	0.689556	0.689556	0.689556	0.689556	0.689556	0.689556
2θ Zero point (°)	-0.00015	-0.00015	-0.00015	-0.00015	-0.00015	-0.00015

7.1.4.3. La13X

Table 7-3: Refined crystallographic parameters for La13X with ammonia at various temperatures, recorded at Spring-8, Japan.

	298 K	373 K	473 K	573 K	673 K	773 K
Crystal System	Cubic	Cubic	Cubic	Cubic	Cubic	Cubic
Space Group	Fd-3 (Origin 2)	Fd-3 (Origin 2)	Fd-3 (Origin 2)	Fd-3 (Origin 2)	Fd-3 (Origin 2)	Fd-3 (Origin 2)
2θ refinement range (°)	3.5-60	3.5-60	3.5-60	3.5-60	3.5-60	3.5-60
Detector	PSD	PSD	PSD	PSD	PSD	PSD
Number of Parameters	98	98	98	90	90	82
Number of hkls	2160	2160	2160	2162	2160	2160
Refinement Method	Rietveld	Rietveld	Rietveld	Rietveld	Rietveld	Rietveld
a (Å)	25.00715 (17)	25.00927 (17)	25.02223 (17)	25.04128 (18)	25.04265 (23)	25.03571 (27)
b (Å)	25.00995 (122)	25.00688 (118)	25.01583 (126)	25.03975 (141)	25.03086 (172)	25.02290 (227)
c (Å)	25.01374 (147)	25.01509 (140)	25.03215 (141)	25.048256 (153)	25.05837 (204)	25.04354 (244)
V (Å^3)	15644(1)	15644(1)	15669(1)	15706(1)	15708(2)	15689(2)
$R_{wp}/R_p/R_{exp}$	5.09256039 /3.5817235 /1.0654293 4	4.93290267 /3.4606983 9/1.067859 18	4.51519815 /3.1546877 5/1.076670 77	4.58950836 /3.1530577 2/1.083266 88	4.97682689 /3.6701706 1/1.091355 24	5.56908005 /4.0758182 3/1.096040 55
Gof χ^2	4.77982	4.619432	4.193667	4.2367291	4.560226	5.081089
Wavelength (Å)	0.688160	0.688160	0.688160	0.688160	0.688160	0.688160
2θ Zero point (°)	-0.00028	-0.00028	-0.00028	-0.00028	-0.00028	-0.00028

7.1.4.4. Mg13X

Table 7-4: Refined crystallographic parameters for Mg13X with ammonia at various temperatures, recorded at Spring-8, Japan.

	298 K	373 K	473 K	573 K	673 K	773 K
Crystal System	Cubic	Cubic	Cubic	Cubic	Cubic	Cubic
Space Group	Fd-3 (Origin 2)	Fd-3 (Origin 2)	Fd-3 (Origin 2)	Fd-3 (Origin 2)	Fd-3 (Origin 2)	Fd-3 (Origin 2)
2θ refinement range (°)	5-55	5-55	5-55	5-55	5-55	5-55
Detector	PSD	PSD	PSD	PSD	PSD	PSD
Number of Parameters	98	98	93	93	89	89
Number of hkls	1650	1650	1648	1636	1603	1655
Refinement Method	Rietveld	Rietveld	Rietveld	Rietveld	Rietveld	Rietveld
a (Å)	24.73186 (133)	24.74727 (95)	24.71908 (74)	24.66299(71)	24.49534(81)	24.77459 (52)
b (Å)	24.74631 (479)	24.75474 (338)	24.76640 (207)	24.72307(29)	24.46707(201)	24.78305 (201)
c (Å)	24.71110 (490)	24.73474 (354)	24.67514 (223)	24.61326(226)	24.42505(301)	24.77612 (238)
V (Å^3)	15124(4)	15153(3)	15106(2)	15008(2)	14638(2)	15212(2)
$R_{wp}/R_p/R_{exp}$	9.71808496 /6.50981238/1.07098303	7.85771147 /5.38296547/1.07345131	7.56842887 /4.98628858/1.08578858	5.86501476 /4.09445702/ 1.08977757	13.8108108 /8.73443733/1.09066944	6.46191421 /4.62967245/1.14568005
Gof χ^2	9.07398592	7.32004459	6.97044437	5.38184573	12.6626917	5.64024329
Wavelength (Å)	0.688160	0.688160	0.688160	0.688160	0.688160	0.688160
2θ Zero point (°)	-0.00028	-0.00028	-0.00028	-0.00028	-0.00028	-0.00028

7.1.5. SXRD Refined Atomic Parameters

7.1.5.1. Na13X

A. 298 K

Table 7-5: Refined atomic parameters for Na13X with ammonia at 298 K, recorded at Spring-8, Japan.

	x	y	z	occ	beq	Equivalent Positions
Al1	-0.05428 (38)	0.03623 (31)	0.12580 (31)	1	1.036(32)	96
Si1	-0.05466 (36)	0.12396 (32)	0.03422 (29)	1	1.036(32)	96
O1	-0.10713 (66)	0.00001 (92)	0.10558 (67)	1	2.073(64)	96
O2	-0.00031 (70)	-0.00257 (70)	0.14256 (28)	1	2.073(64)	96
O3	-0.03645 (30)	0.07356 (64)	0.07230 (63)	1	2.073(64)	96
O4	-0.06699 (30)	0.07616 (60)	0.17833 (67)	1	2.073(64)	96
Na1	0.05083 (28)	0.05083 (28)	0.05083 (28)	0.18793 (474)	2.444 (148)	32
Na2	0.22880 (18)	0.22880 (18)	0.22880 (18)	0.30142 (405)	2.444 (148)	32
Na3	0.43244 (114)	0.30097 (124)	0.16374 (91)	0.23554 (957)	2.444 (148)	96
N1	0.56382 (106)	0.89929 (110)	0.00511 (134)	0.45215 (2279)	5	96
N2	0.18357 (112)	0.71528 (141)	0.20446 (179)	0.41058 (1348)	5	96
N3	0.49025 (5266)	-0.01250 (4959)	0.52053 (707)	0.16810 (938)	5	96
N4	0.90475 (400)	0.15942 (172)	0.85119 (397)	0.23567 (1572)	5	96

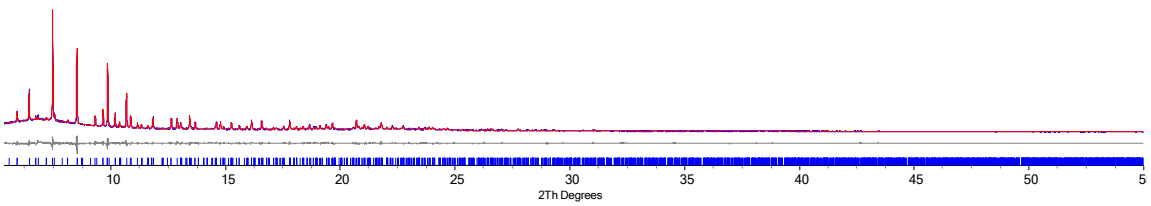

Figure 7-8: Synchrotron PXRD refinement and the crystal structure of ammonia adsorbed Na13X at 298 K. Comparison of the experiment data (blue line) and Rietveld refinement (red line) and the difference between them (grey line).

B. 373 K

Table 7-6: Refined atomic parameters for Na13X with ammonia at 373 K, recorded at Spring-8, Japan.

	x	y	z	occ	beq	Equivalent Positions
Al1	-0.05424 (20)	0.03683 (16)	0.12281 (15)	1	0.954(18)	96
Si1	-0.05402 (20)	0.12576 (14)	0.03490 (18)	1	0.954(18)	96
O1	-0.11231 (23)	0.00184 (37)	0.10237 (21)	1	1.908(37)	96
O2	-0.00019 (31)	-0.00463 (32)	0.14399 (15)	1	1.908(37)	96
O3	-0.03358 (17)	0.07377 (28)	0.06997 (27)	1	1.908(37)	96
O4	-0.06967 (17)	0.07628 (29)	0.17834 (30)	1	1.908(37)	96
Na1	0.05665 (16)	0.05665 (16)	0.05665 (16)	0.19394 (288)	2.568(84)	32
Na2	0.23655 (10)	0.23655 (10)	0.23655 (10)	0.31038 (208)	2.568(84)	32
Na3	0.42021 (68)	0.31207 (65)	0.17396 (55)	0.20543 (523)	2.568(84)	96
N1	0.53718 (69)	0.92890 (66)	0.00968 (88)	0.36734 (909)	5	96
N2	0.19747 (225)	0.74129 (83)	0.19659 (233)	0.28781 (865)	5	96
N3				0		
N4	0.91092 (72)	0.17946 (54)	0.89672 (68)	0.46964 (991)	5	96

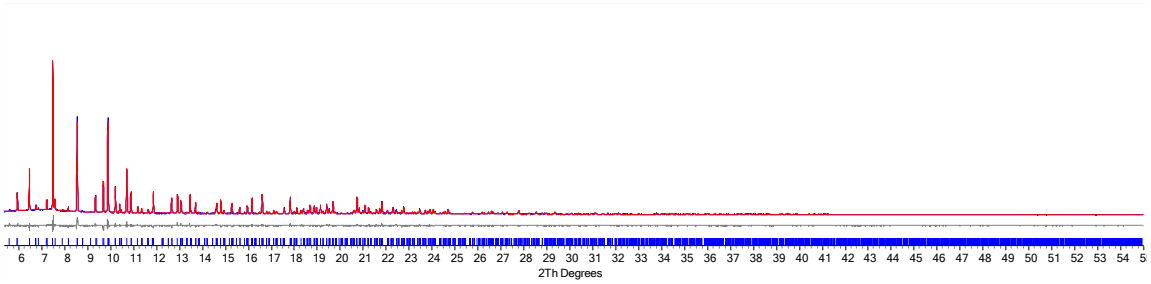

Figure 7-9: Synchrotron PXRD refinement and the crystal structure of ammonia adsorbed Na13X at 373 K. Comparison of the experiment data (blue line) and Rietveld refinement (red line) and the difference between them (grey line).

C. 473 K

Table 7-7: Refined atomic parameters for Na13X with ammonia at 473 K, recorded at Spring-8, Japan.

	x	y	z	occ	beq	Equivalent Positions
Al1	-0.05506 (19)	0.03686 (15)	0.12395 (20)	1	1.174(19)	96
Si1	-0.05418 (19)	0.12524 (20)	0.03498 (16)	1	1.174(19)	96
O1	-0.11146 (24)	0.00441 (34)	0.10234 (21)	1	2.347(37)	96
O2	0.00054 (31)	-0.00420 (31)	0.14165 (16)	1	2.347(37)	96
O3	-0.03447 (17)	0.07437 (30)	0.07097 (31)	1	2.347(37)	96
O4	-0.06988 (16)	0.07472 (34)	0.17902 (33)	1	2.347(37)	96
Na1	0.05126 (18)	0.05126 (18)	0.05126 (18)	0.18883 (267)	3.107(91)	32
Na2	0.23269 (10)	0.23269 (10)	0.23269 (10)	0.31038 (216)	3.107(91)	32
Na3	0.41107 (83)	0.31357 (76)	0.17455 (67)	0.17657 (549)	3.107(91)	96
N1	0.54829 (93)	0.93288 (88)	0.02061 (100)	0.29188 (805)	5	96
N2	0.17687 (224)	0.81857 (147)	0.18276 (262)	0.15371 (826)	5	96
N3				0		
N4	0.90026 (137)	0.16543 (88)	0.87973 (165)	0.22804 (1015)	5	96

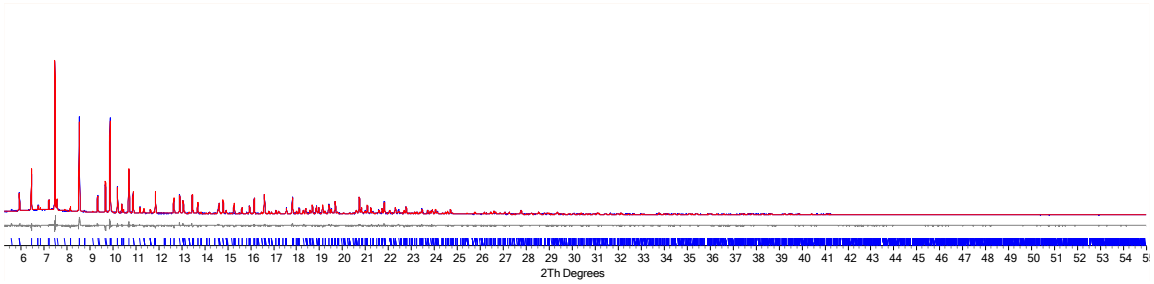

Figure 7-10: Synchrotron PXRD refinement and the crystal structure of ammonia adsorbed Na13X at 473 K. Comparison of the experiment data (blue line) and Rietveld refinement (red line) and the difference between them (grey line).

D. 573 K

Table 7-8: Refined atomic parameters for Na13X with ammonia at 573 K, recorded at Spring-8, Japan.

	x	y	z	occ	beq	Equivalent Positions
Al1	-0.05521 (20)	0.03600 (18)	0.12518 (23)	1	1.422 (19)	96
Si1	-0.05459 (20)	0.12480 (23)	0.03561 (18)	1	1.422 (19)	96
O1	-0.11087 (26)	0.00461 (33)	0.10351 (23)	1	2.844 (38)	96
O2	-0.00011 (33)	-0.00311 (33)	0.14101 (16)	1	2.844 (38)	96
O3	-0.03425 (16)	0.07389 (32)	0.07167 (32)	1	2.844 (38)	96
O4	-0.06868 (16)	0.07288 (36)	0.17904 (36)	1	2.844 (38)	96
Na1	0.04833 (16)	0.04833 (16)	0.04833 (16)	0.19394 (238)	3.091 (82)	32
Na2	0.23101 (9)	0.23101 (9)	0.23101 (9)	0.31038 (212)	3.091 (82)	32
Na3	0.42819 (98)	0.29312 (95)	0.17102 (84)	0.14580 (488)	3.091 (82)	96
N1	0.53445 (305)	0.95109 (176)	0.02054 (298)	0.10816 (838)	5	96
N2	0.18034 (379)	0.82043 (239)	0.19061 (382)	0.08326 (805)	5	96
N3				0		
N4	0.91653 (115)	0.16497 (89)	0.85469 (103)	0.25645 (981)	5	96

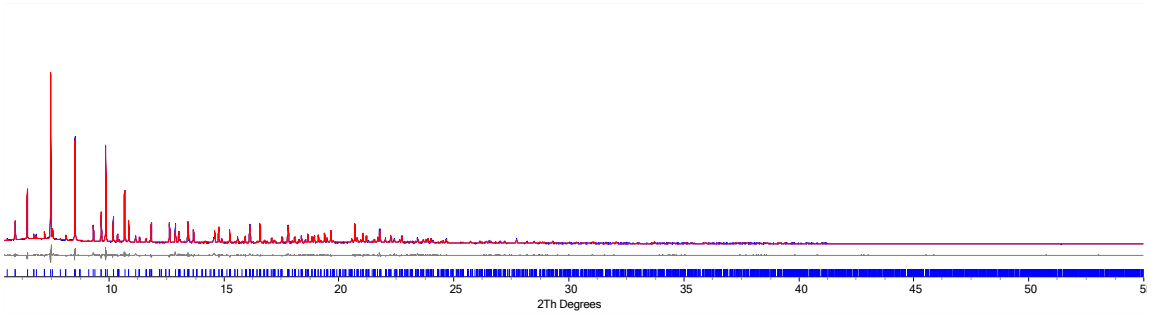

Figure 7-11: Synchrotron PXRD refinement and the crystal structure of ammonia adsorbed Na13X at 573 K. Comparison of the experiment data (blue line) and Rietveld refinement (red line) and the difference between them (grey line).

E. 673K

Table 7-9: Refined atomic parameters for Na13X with ammonia at 673 K, recorded at Spring-8, Japan.

	x	y	z	occ	beq	Equivalent Positions
Al1	-0.05478 (23)	0.03552 (19)	0.12526 (27)	1	1.576 (19)	96
Si1	-0.05501 (22)	0.12510 (26)	0.03597 (19)	1	1.576 (19)	96
O1	-0.11080 (27)	0.00494 (33)	0.10428 (24)	1	3.153 (38)	96
O2	-0.00103 (38)	-0.00219 (37)	0.14030 (16)	1	3.153 (38)	96
O3	-0.03405 (15)	0.07356 (38)	0.07183 (38)	1	3.153 (38)	96
O4	-0.06807 (16)	0.07174 (44)	0.17884 (43)	1	3.153 (38)	96
Na1	0.04791 (15)	0.04791 (15)	0.04791 (15)	0.19394 (226)	2.951 (82)	32
Na2	0.23050 (08)	0.23050 (08)	0.23050 (08)	0.31038 (207)	2.951 (82)	32
Na3	0.42234 (90)	0.30089 (91)	0.16896 (86)	0.13522 (458)	2.951 (82)	96
N1	0.53338 (1206)	0.95880 (396)	0.02645 (1100)	0.04417 (811)	5	96
N2	0.19378 (792)	0.82172 (322)	0.19431 (0773)	0.06142 (617)	5	96
N3				0		
N4	0.90879 (125)	0.15672 (115)	0.86656 (131)	0.20577 (889)	5	96

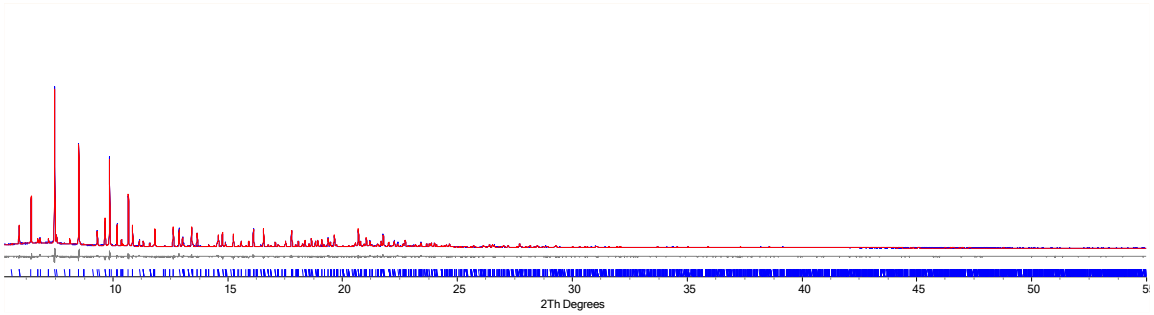

Figure 7-12: Synchrotron PXRD refinement and the crystal structure of ammonia adsorbed Na13X at 673 K. Comparison of the experiment data (blue line) and Rietveld refinement (red line) and the difference between them (grey line).

A. 773 K

Table 7-10: Refined atomic parameters for Na13X with ammonia at 773 K, recorded at Spring-8, Japan.

	x	y	z	occ	beq	Equivalent Positions
Al1	-0.05415 (19)	0.03599 (19)	0.12493 (27)	1	1.767 (20)	96
Si1	-0.05574 (18)	0.12507 (26)	0.03537 (18)	1	1.767 (20)	96
O1	-0.11152 (26)	0.00638 (31)	0.10409 (23)	1	3.534 (39)	96
O2	-0.00092 (39)	-0.00230 (40)	0.14038 (15)	1	3.534 (39)	96
O3	-0.03385 (15)	0.07327 (39)	0.07161 (42)	1	3.534 (39)	96
O4	-0.06752 (16)	0.07143 (41)	0.17824 (34)	1	3.534 (39)	96
Na1	0.04857 (16)	0.04857 (16)	0.04857 (16)	0.19394 (227)	3.750 (91)	32
Na2	0.23065 (9)	0.23065 (9)	0.23065 (9)	0.31038 (212)	3.750 (91)	32
Na3	0.44166 (85)	0.33165 (83)	0.16164 (89)	0.13856 (462)	3.750 (91)	96
N1				0		
N2	0.19448 (495)	0.82628 (243)	0.19467 (486)	0.07831 (615)	5	96
N3				0		
N4	0.90262 (113)	0.15132 (107)	0.87723 (129)	0.21158 (693)	5	96

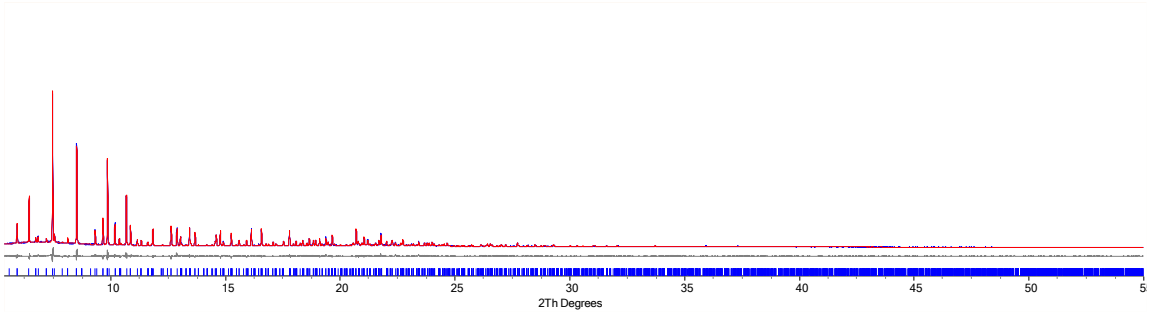

Figure 7-13: Synchrotron PXRD refinement and the crystal structure of ammonia adsorbed Na13X at 773 K. Comparison of the experiment data (blue line) and Rietveld refinement (red line) and the difference between them (grey line).

7.1.5.2. H13X

A. 298 K

Table 7-11: Refined atomic parameters for H13X with ammonia at 298 K, recorded at Spring-8, Japan.

	x	y	z	occ	beq	Equivalent Positions
Al1	-0.05388 (40)	0.03637 (33)	0.12025 (29)	1	1.381 (51)	96
Si1	-0.05171 (38)	0.12434 (31)	0.03663 (35)	1	1.381 (51)	96
O1	-0.10513 (59)	-0.00148 (71)	0.10643 (56)	1	2.762 (102)	96
O2	0.00434 (54)	-0.00122 (59)	0.14309 (27)	1	2.762 (102)	96
O3	-0.02740 (37)	0.07229 (68)	0.07182 (65)	1	2.762 (102)	96
O4	-0.07240 (36)	0.08218 (38)	0.18281 (42)	1	2.762 (102)	96
Na2	0.23717 (22)	0.23717 (22)	0.23717 (22)	0.31038 (486)	3.999 (404)	32
N1	0.53396 (74)	0.89959 (75)	-0.02170 (98)	0.63113 (1531)	5	96
N2	0.19708 (51)	0.69708 (51)	0.19708 (51)	0.28972 (830)	5	32
N3	0.36067 (68)	-0.08817 (178)	0.41877 (145)	0.59896 (719)	5	96
N4	0.86316 (39)	0.18215 (178)	0.86560 (559)	0.22118 (981)	5	96
N5	0.68930 (95)	0.68983 (700)	0.04355 (82)	0.66912 (1419)	5	96

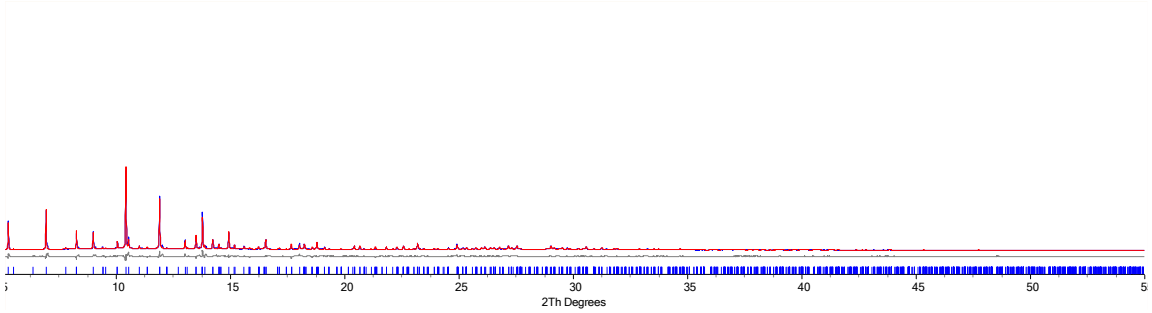

Figure 7-14: Synchrotron PXRD refinement and the crystal structure of ammonia adsorbed H13X at 298 K. Comparison of the experiment data (blue line) and Rietveld refinement (red line) and the difference between them (grey line).

B. 373 K

Table 7-12: Refined atomic parameters for H13X with ammonia at 373 K, recorded at Spring-8, Japan.

	x	y	z	occ	beq	Equivalent Positions
Al1	-0.04935 (29)	0.03548 (30)	0.12475 (25)	1	1.476 (48)	96
Si1	-0.05546 (28)	0.11887 (25)	0.03690 (30)	1	1.476 (48)	96
O1	-0.10958 (46)	-0.00298 (57)	0.10215 (42)	1	2.952 (96)	96
O2	0.00049 (51)	0.00119 (48)	0.14289 (27)	1	2.952 (96)	96
O3	-0.02834 (27)	0.07229 (52)	0.07083 (50)	1	2.952 (96)	96
O4	-0.06819 (30)	0.08269 (41)	0.17931 (44)	1	2.952 (96)	96
Na2	0.24156 (25)	0.24156 (25)	0.24156 (25)	0.31038 (360)	6.297 (372)	32
N1	0.54917 (78)	0.91123 (78)	0.00714 (85)	0.62836 (1304)	5	96
N2	0.20931 (71)	0.70931 (71)	0.20931 (71)	0.21767 (861)	5	32
N3	0.34709 (126)	-0.11568 (88)	0.42230 (72)	0.51750 (682)	5	96
N4	0.85759 (136)	0.21286 (117)	0.83226 (123)	0.44914 (1528)	5	96
N5	0.69011 (827)	0.69102 (31)	0.05104 (261)	0.63947 (1393)	5	96

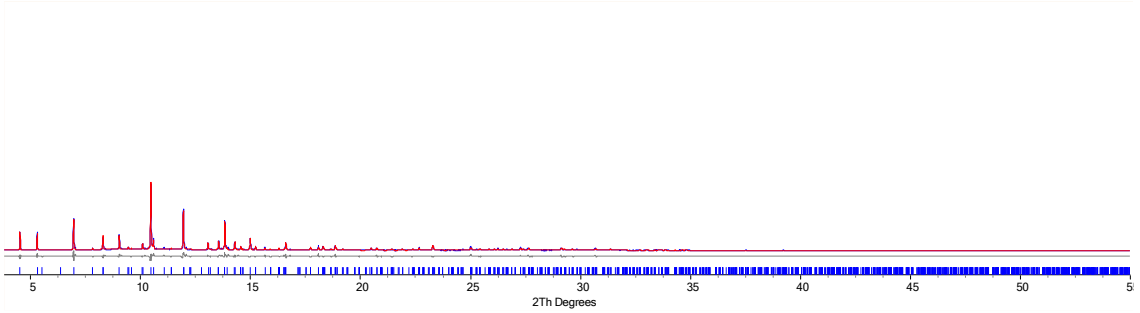

Figure 7-15: Synchrotron PXRD refinement and the crystal structure of ammonia adsorbed H13X at 373. Comparison of the experiment data (blue line) and Rietveld refinement (red line) and the difference between them (grey line).

C. 437 K

Table 7-13: Refined atomic parameters for H13X with ammonia at 473 K, recorded at Spring-8, Japan.

	x	y	z	occ	beq	Equivalent Positions
Al1	-0.05081 (43)	0.03331 (27)	0.12392 (40)	1	1.850 (56)	96
Si1	-0.05405 (43)	0.12118 (40)	0.03954 (28)	1	1.850 (56)	96
O1	-0.11198 (60)	-0.00007 (104)	0.10475 (52)	1	3.699 (11)	96
O2	0.00197 (81)	0.00027 (80)	0.14524 (31)	1	3.699 (11)	96
O3	-0.02767 (42)	0.07171 (74)	0.07405 (69)	1	3.699 (11)	96
O4	-0.07278 (33)	0.07798 (71)	0.17484 (65)	1	3.699 (11)	96
Na2	0.23588 (34)	0.23588 (34)	0.23588 (34)	0.29671 (488)	4.683 (630)	32
N1	0.54263 (65)	0.91519 (65)	0.00504 (96)	0.70105 (1155)	5	96
N2	0.23098 (97)	0.73098 (97)	0.23098 (97)	0.19502 (785)	5	32
N3	0.36750 (198)	-0.10920 (251)	0.41771 (69)	0.41669 (569)	5	96
N4	0.86241 (102)	0.22045 (102)	0.81757 (93)	0.54641 (1390)	5	96
N5	0.69262 (27)	0.69262 (27)	0.05738 (27)	0.55782 (862)	5	32

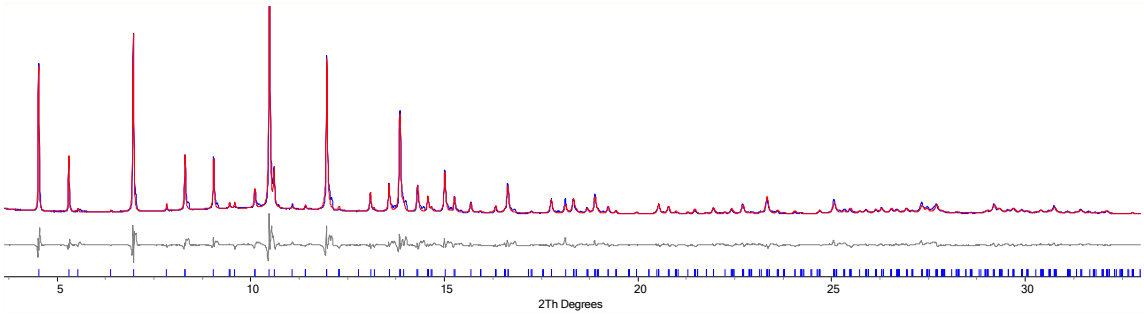

Figure 7-16: Synchrotron PXRD refinement and the crystal structure of ammonia adsorbed H13X at 473 K. Comparison of the experiment data (blue line) and Rietveld refinement (red line) and the difference between them (grey line).

D. 573 K

Table 7-14: Refined atomic parameters for H13X with ammonia at 573 K, recorded at Spring-8, Japan.

	x	y	z	occ	beq	Equivalent Positions
Al1	-0.05227 (66)	0.04050 (36)	0.12558 (47)	1	2.110 (63)	96
Si1	-0.05327 (60)	0.12264 (51)	0.03436 (34)	1	2.110 (63)	96
O1	-0.10819 (91)	0.00383 (101)	0.10490 (80)	1	4.220 (125)	96
O2	0.00104 (88)	0.00508 (86)	0.14273 (39)	1	4.220 (125)	96
O3	-0.02654 (51)	0.07071 (92)	0.07352 (100)	1	4.220 (125)	96
O4	-0.07927 (40)	0.07226 (74)	0.17247 (74)	1	4.220 (125)	96
Na2	0.23645 (28)	0.23645 (28)	0.23645 (28)	0.28430 (383)	3.855 (394)	32
N1				0		
N2	0.19960 (84)	0.69960 (84)	0.19960 (84)	0.20261 (853)	5	32
N3	0.35025 (486)	-0.10535 (414)	0.41972 (117)	0.44215 (675)	5	96
N4	0.91884 (73)	0.21686 (71)	0.77774 (80)	0.75198 (1767)	5	96
N5	0.69633 (35)	0.69633 (35)	0.05367 (35)	0.52772 (1158)	5	32

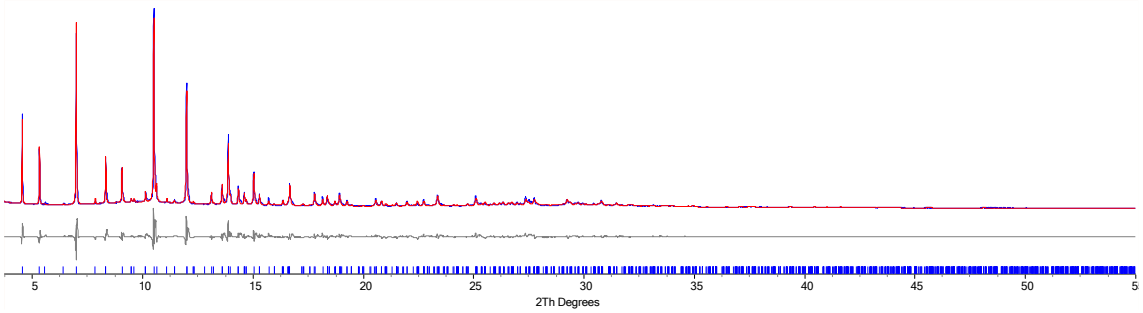

Figure 7-17: Synchrotron PXRD refinement and the crystal structure of ammonia adsorbed H13X at 573 K. Comparison of the experiment data (blue line) and Rietveld refinement (red line) and the difference between them (grey line).

E. 673 K

Table 7-15: Refined atomic parameters for H13X with ammonia at 673 K, recorded at Spring-8, Japan.

	x	y	z	occ	beq	Equivalent Positions
Al1	-0.05189 (48)	0.03848 (35)	0.12788 (34)	1	2.169 (58)	96
Si1	-0.05282 (44)	0.12326 (35)	0.03534 (32)	1	2.169 (58)	96
O1	-0.10865 (61)	0.00128 (75)	0.10241 (56)	1	4.338 (117)	96
O2	0.00125 (65)	0.00438 (65)	0.14555 (31)	1	4.338 (117)	96
O3	-0.03113 (36)	0.07280 (72)	0.07455 (69)	1	4.338 (117)	96
O4	-0.07737 (34)	0.06984 (53)	0.17018 (48)	1	4.338 (117)	96
Na2	0.23376 (27)	0.23376 (27)	0.23376 (27)	0.27414 (356)	6.960 (399)	32
N1				0		
N2	0.19998 (91)	0.69998 (91)	0.19998 (91)	0.15134 (693)	5	32
N3	0.33979 (463)	-0.11434 (96)	0.41288 (420)	0.42826 (593)	5	96
N4	0.91585 (86)	0.21459 (101)	0.77605 (112)	0.47946 (1513)	5	96
N5	0.69635 (26)	0.69635 (26)	0.05365 (26)	0.55439 (796)	5	32

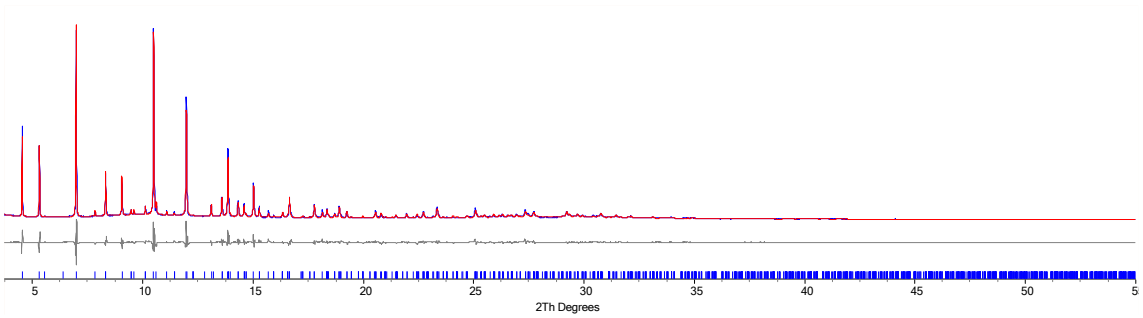

Figure 7-18: Synchrotron PXRD refinement and the crystal structure of ammonia adsorbed H13X at 673 K. Comparison of the experiment data (blue line) and Rietveld refinement (red line) and the difference between them (grey line).

F. 773 K

Table 7-16: Refined atomic parameters for H13X with ammonia at 773 K, recorded at Spring-8, Japan.

	x	y	z	occ	beq	Equivalent Positions
Al1	-0.05012 (33)	0.03521 (28)	0.12763 (30)	1	2.234 (46)	96
Si1	-0.05466 (30)	0.12341 (30)	0.03832 (27)	1	2.234 (46)	96
O1	-0.10786 (50)	-0.00382 (72)	0.10193 (43)	1	4.468 (91)	96
O2	0.00016 (50)	0.00511 (51)	0.14438 (27)	1	4.468 (91)	96
O3	-0.03189 (33)	0.07134 (62)	0.07490 (62)	1	4.468 (91)	96
O4	-0.07382 (28)	0.07843 (51)	0.17690 (52)	1	4.468 (91)	96
Na2	0.23139 (21)	0.23139 (21)	0.23139 (21)	0.25372 (295)	3.255 (446)	32
N1				0		
N2	0.19942 (194)	0.69942 (194)	0.19942 (194)	0.06089 (499)	5	32
N3	0.34565 (243)	-0.12264 (83)	0.41150 (185)	0.38016 (488)	5	96
N4	0.92895 (130)	0.19953 (168)	0.78018 (175)	0.26194 (947)	5	96
N5	0.69497 (24)	0.69497 (24)	0.05503 (24)	0.52699 (711)	5	32

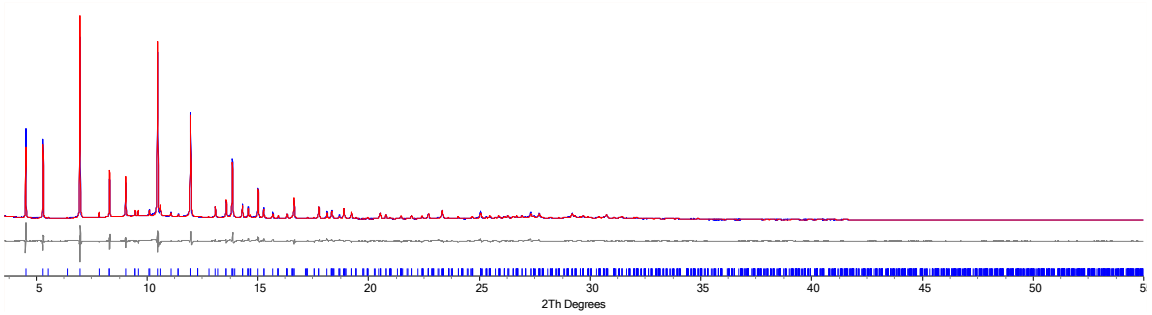

Figure 7-19: Synchrotron PXRD refinement and the crystal structure of ammonia adsorbed H13X at 773 K. Comparison of the experiment data (blue line) and Rietveld refinement (red line) and the difference between them (grey line).

7.1.5.3. La13X

A. 298 K

Table 7-17: Refined atomic parameters for La13X with ammonia at 298 K, recorded at Spring-8, Japan.

	x	y	z	occ	beq	Equivalent Positions
Al1	-0.05490 (20)	0.03776 (20)	0.12564 (22)	1	0.647 (17)	96
Si1	-0.05403 (20)	0.12725 (21)	0.03430 (19)	1	0.647 (17)	96
O1	-0.10106 (27)	0.00328 (43)	0.10709 (30)	1	1.295 (33)	96
O2	0.00633 (24)	-0.00198 (22)	0.13601 (12)	1	1.295 (33)	96
O3	-0.03138 (13)	0.08015 (51)	0.07893 (52)	1	1.295 (33)	96
O4	-0.06992 (12)	0.06671 (30)	0.17802 (30)	1	1.295 (33)	96
Na2	0.32785 (464)	0.24761 (112)	0.32322 (446)	0.08725 (433)	5.548 (688)	96
Na3	0.47627 (135)	0.28950 (156)	0.17615 (107)	0.12075 (516)	5.548 (688)	96
La1	0.06713 (2)	0.06713 (002)	0.06713 (2)	0.29949 (57)	1.892 (17)	32
La2	0.56259 (100)	0.30155 (134)	0.32142 (130)	0.01802 (99)	1.892 (17)	96
La3	0.74911 (315)	0.76321 (160)	0.75354 (424)	0.01636 (30)	1.892 (17)	96
La4	0.17804 (109)	0.03704 (109)	0.30434 (111)	0.01953 (124)	1.892 (17)	96
La5	0.27093 (141)	0.28757 (138)	0.11856 (109)	0.01478 (97)	1.892 (17)	96
La6	0.42170 (108)	0.34848 (105)	0.17953 (102)	0.01925 (91)	1.892 (17)	96
N1	0.27921 (182)	0.37012 (210)	0.90123 (197)	0.12343 (769)	5	96
N2	0.79865 (115)	-0.22926 (128)	1.02065 (123)	0.22175 (904)	5	96
N3	0.58324 (12)	0.16676 (12)	0.58324 (12)	0.46661 (413)	5	32
N4	0.51721 (609)	0.01768 (606)	0.11884 (172)	0.13056 (643)	5	96

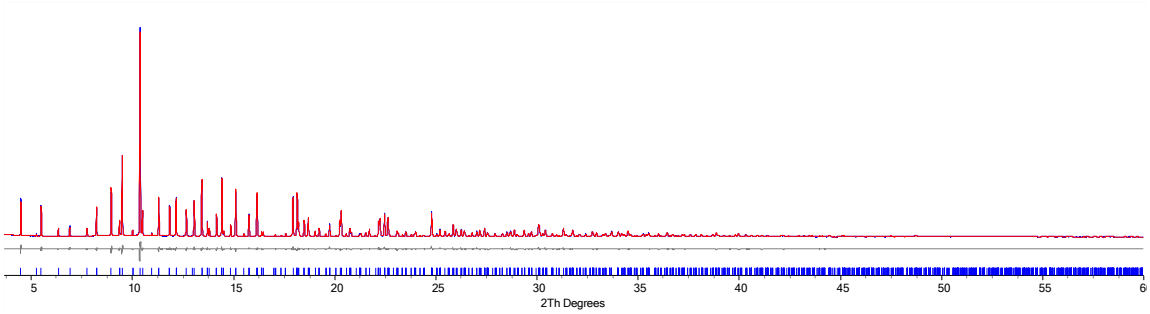

Figure 7-20: Synchrotron PXRD refinement and the crystal structure of ammonia adsorbed La13X at 298 K. Comparison of the experiment data (blue line) and Rietveld refinement (red line) and the difference between them (grey line).

B. 373 K

Table 7-18: Refined atomic parameters for La13X with ammonia at 373 K, recorded at Spring-8, Japan.

	x	y	z	occ	beq	Equivalent Positions
Al1	-0.05514 (21)	0.03778 (21)	0.12521 (21)	1	0.775 (17)	96
Si1	-0.05403 (21)	0.12762 (20)	0.03432 (20)	1	0.775 (17)	96
O1	-0.10191 (30)	0.00348 (45)	0.10688 (31)	1	1.549 (33)	96
O2	0.00565 (27)	-0.00163 (27)	0.13594 (12)	1	1.549 (33)	96
O3	-0.03146 (12)	0.08068 (51)	0.07819 (50)	1	1.549 (33)	96
O4	-0.07023 (12)	0.06764 (40)	0.17857 (39)	1	1.549 (33)	96
Na2	0.32520 (651)	0.24384 (116)	0.32104 (634)	0.08771 (491)	8.065 (795)	96
Na3	0.47279 (182)	0.28780 (204)	0.17493 (106)	0.13200 (564)	8.065 (795)	96
La1	0.06702 (2)	0.06702 (2)	0.06702 (2)	0.30283 (54)	2.003 (17)	32
La2	0.56217 (93)	0.30387 (131)	0.32010 (126)	0.01906 (102)	2.003 (17)	96
La3	0.75221 (1154)	0.76441 (108)	0.75142 (1099)	0.01767 (30)	2.003 (17)	96
La4	0.17883 (84)	0.03121 (76)	0.29428 (78)	0.02656 (102)	2.003 (17)	96
La5	0.27241 (157)	0.28784 (157)	0.11526 (116)	0.01373 (99)	2.003 (17)	96
La6	0.41794 (143)	0.34747 (143)	0.18110 (118)	0.01513 (85)	2.003 (17)	96
N1	0.27939 (215)	0.37401 (235)	0.90080 (233)	0.10302 (743)	5	96
N2	0.76612 (1120)	-0.22928 (984)	1.00975 (244)	0.10261 (450)	5	96
N3	0.58327 (12)	0.16673 (12)	0.58327 (12)	0.45681 (412)	5	32
N4	0.53685 (193)	0.00376 (174)	0.11397 (222)	0.12718 (828)	5	96

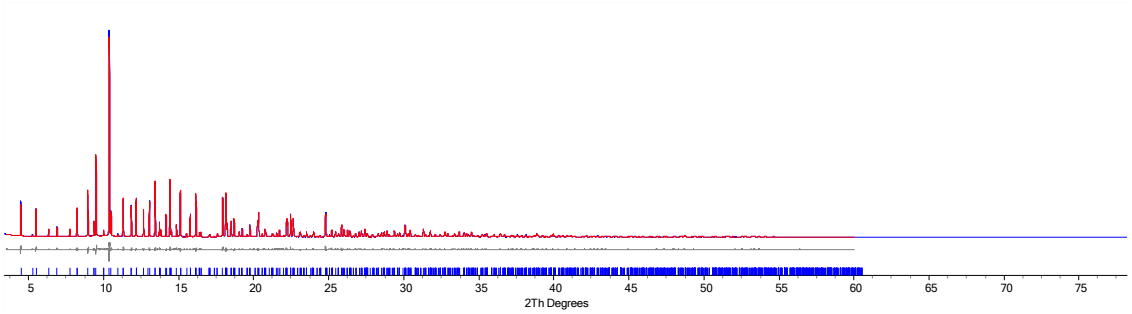

Figure 7-21: Synchrotron PXRD refinement and the crystal structure of ammonia adsorbed La13X at 373 K. Comparison of the experiment data (blue line) and Rietveld refinement (red line) and the difference between them (grey line).

C. 473 K

Table 7-19: Refined atomic parameters for La13X with ammonia at 473 K, recorded at Spring-8, Japan.

	x	y	z	occ	beq	Equivalent Positions
Al1	-0.05362 (20)	0.03794 (18)	0.12461 (19)	1	0.937 (18)	96
Si1	-0.05571 (19)	0.12776 (17)	0.03438 (18)	1	0.937 (18)	96
O1	-0.10679 (38)	-0.00113 (61)	0.10200 (34)	1	1.873 (36)	96
O2	-0.00069 (30)	0.00578 (35)	0.13663 (12)	1	1.873 (36)	96
O3	-0.03232 (13)	0.07933 (60)	0.07898 (59)	1	1.873 (36)	96
O4	-0.06972 (11)	0.06810 (45)	0.17884 (45)	1	1.873 (36)	96
Na2	0.31310 (352)	0.23340 (114)	0.32435 (327)	0.10896 (414)	13.820 (1.012)	96
Na3	0.47600 (202)	0.29130 (181)	0.16529 (137)	0.13417 (659)	13.820 (1.012)	96
La1	0.06700 (2)	0.06700 (2)	0.06700 (2)	0.30133 (58)	2.215 (17)	32
La2	0.56841 (173)	0.35067 (180)	0.32968 (171)	0.01061 (81)	2.215 (17)	96
La3	0.74890 (356)	0.75236 (512)	0.75919 (188)	0.02400 (28)	2.215 (17)	96
La4	0.17730 (166)	0.02888 (150)	0.27385 (157)	0.01362 (87)	2.215 (17)	96
La5	0.26940 (988)	0.27074 (973)	0.11880 (217)	0.00674 (81)	2.215 (17)	96
La6	0.43231 (151)	0.30097 (149)	0.18957 (128)	0.01466 (2)	2.215 (17)	96
N1	0.28756 (324)	0.35460 (1349)	0.89307 (1339)	0.06529 (555)	5	96
N2	0.74842 (627)	-0.25158 (627)	1.00158 (627)	0.05470 (281)	5	96
N3	0.58330 (12)	0.16670 (12)	0.58330 (12)	0.47531 (359)	5	32
N4	0.56670 (203)	-0.00502 (167)	0.09769 (206)	0.13802`66 0)	5	96

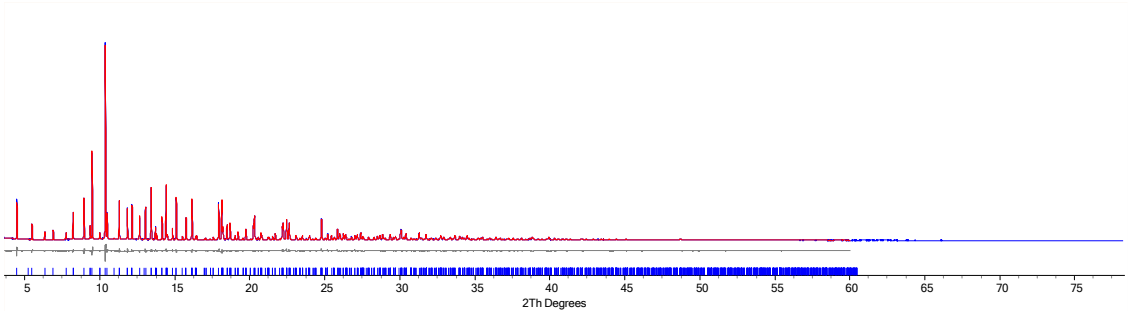

Figure 7-22: Synchrotron PXRD refinement and the crystal structure of ammonia adsorbed La13X at 473 K. Comparison of the experiment data (blue line) and Rietveld refinement (red line) and the difference between them (grey line).

D. 573 K

Table 7-20: Refined atomic parameters for La13X with ammonia at 573 K, recorded at Spring-8, Japan.

	x	y	z	occ	beq	Equivalent Positions
Al1	-0.05598 (32)	0.03614 (32)	0.12587 (25)	1	0.760 (18)	96
Si1	-0.05416 (29)	0.12901 (19)	0.03483 (27)	1	0.760 (18)	96
O1	-0.10819 (33)	0.00211 (50)	0.10165 (28)	1	1.520 (36)	96
O2	0.00411 (56)	0.00237 (54)	0.13546 (16)	1	1.520 (36)	96
O3	-0.03231 (13)	0.07909 (48)	0.07824 (47)	1	1.520 (36)	96
O4	-0.06945 (14)	0.07064 (51)	0.18109 (52)	1	1.520 (36)	96
Na2	0.33161 (944)	0.24345 (168)	0.33265 (982)	0.07644 (450)	10.322 (1.313)	96
Na3	0.45488 (292)	0.26636 (287)	0.15897 (290)	0.07764 (636)	10.322 (1.313)	96
La1	0.06719 (2)	0.06719 (2)	0.06719 (2)	0.33673 (88)	2.193 (16)	32
La2	0.56018 (243)	0.32175 (286)	0.33658 (303)	0.00845 (99)	2.193 (16)	96
La3	0.76071 (1206)	0.75890 (936)	0.76681 (293)	0.02399 (32)	2.193 (16)	96
La4	0.09887 (214)	-0.01545 (430)	0.25978 (433)	0.00911 (83)	2.193 (16)	96
La5	0.29945 (65)	0.20564 (59)	0.11400 (57)	0.05511 (191)	2.193 (16)	96
La6	0.44292 (318)	0.30027 (310)	0.19341 (158)	0.01239 (119)	2.193 (16)	96
N1				0		
N2				0		
N3	0.58439 (11)	0.16561 (11)	0.58439 (11)	0.50216 (296)	5	32
N4	0.52645 (262)	-0.01384 (225)	0.10755 (240)	0.12673 (953)	5	96

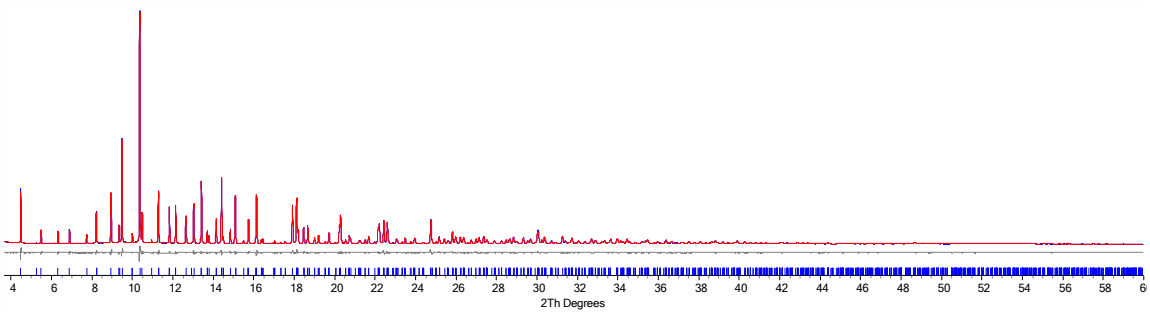

Figure 7-23: Synchrotron PXRD refinement and the crystal structure of ammonia adsorbed La13X at 573 K. Comparison of the experiment data (blue line) and Rietveld refinement (red line) and the difference between them (grey line).

E. 673 K

Table 7-21: Refined atomic parameters for La13X with ammonia at 673 K, recorded at Spring-8, Japan.

	x	y	z	occ	beq	Equivalent Positions
Al1	-0.05651 (25)	0.03630 (37)	0.12714 (35)	1	1.084 (24)	96
Si1	-0.05252 (24)	0.12373 (32)	0.03703 (34)	1	1.084 (24)	96
O1	-0.10655 (42)	0.00511 (49)	0.10100 (41)	1	2.168 (47)	96
O2	0.00187 (74)	0.00062 (82)	0.13650 (19)	1	2.168 (47)	96
O3	-0.03254 (17)	0.08022 (65)	0.07764 (61)	1	2.168 (47)	96
O4	-0.06958 (15)	0.06883 (55)	0.17796 (57)	1	2.168 (47)	96
Na2	0.32060 (1101)	0.25239 (261)	0.32683 (1150)	0.05469 (562	11.993 (2.679)	96
Na3	0.47646 (309)	0.24192 (393)	0.13452 (285)	0.06657 (639	11.993 (2.679)	96
La1	0.06736 (2)	0.06736 (2)	0.06736 (2)	0.33183 (101)	2.425 (20)	32
La2	0.69183 (105)	0.35854 (86)	0.27801 (95)	0.04037 (222)	2.425 (20)	96
La3	0.76781 (667)	0.76542 (560)	0.77829 (144)	0.02588 (44)	2.425 (20)	96
La4	0.20722 (265)	-0.04914 (236)	0.19096 (305)	0.00857 (98)	2.425 (20)	96
La5	0.23599 (1036)	0.23367 (1026)	0.11438 (275)	0.00778 (92)	2.425 (20)	96
La6	0.43225 (230)	0.30130 (243)	0.19157 (170)	0.00978 (74)	2.425 (20)	96
N1				0		
N2				0		
N3	0.58274 (12)	0.16726 (12)	0.58274 (12)	0.49367 (327)	5	32
N4	0.60566 (304)	0.01834 (228)	0.07649 (261)	0.09817 (923)	5	96

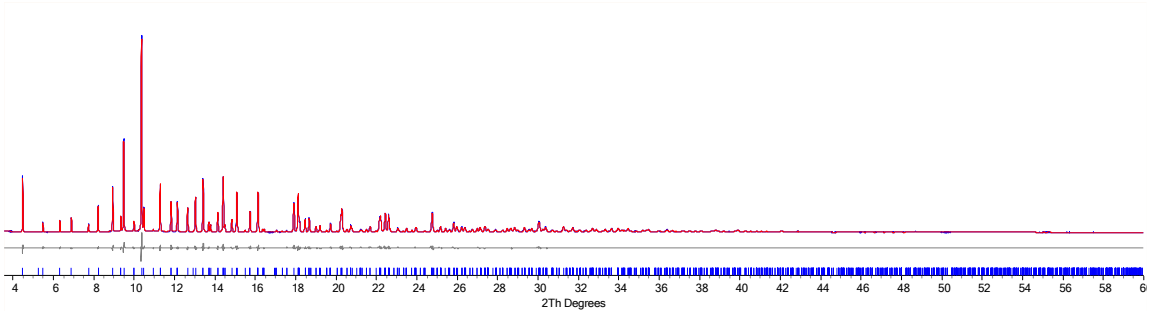

Figure 7-24: Synchrotron PXRD refinement and the crystal structure of ammonia adsorbed La13X at 673 K. Comparison of the experiment data (blue line) and Rietveld refinement (red line) and the difference between them (grey line).

F. 773 K

Table 7-22: Refined atomic parameters for La13X with ammonia at 773 K, recorded at Spring-8, Japan.

	x	y	z	occ	beq	Equivalent Positions
Al1	-0.05421 (32)	0.03908 (24)	0.12329 (26)	1	1.308 (27)	96
Si1	-0.05446 (34)	0.12854 (27)	0.03382 (30)	1	1.308 (27)	96
O1	-0.10602 (45)	0.00590 (50)	0.10236 (43)	1	2.617 (54)	96
O2	0.00407 (47)	0.00007 (48)	0.13633 (15)	1	2.617 (54)	96
O3	-0.03197 (15)	0.08042 (54)	0.07587 (53)	1	2.617 (54)	96
O4	-0.06918 (18)	0.06932 (61)	0.17820 (60)	1	2.617 (54)	96
Na2	0.31336 (785)	0.20996 (238)	0.30759 (770)	0.04510 (461)	3.442 (1.234)	96
Na3	0.43448 (195)	0.28907 (171)	0.19633 (178)	0.07471 (559)	3.442 (1.234)	96
La1	0.06746 (2)	0.06746 (2)	0.06746 (2)	0.32760 (111)	2.940 (26)	32
La2	0.22598 (27)	0.22598 (27)	0.22598 (27)	0.02560 (37)	2.940 (26)	96
La3	0.83187 (126)	0.47046 (151)	0.87733 (134)	0.01475 (103)	2.940 (26)	96
La4	0.07400 (71)	0.08578 (247)	0.16108 (201)	0.05336 (56)	2.940 (26)	96
La5	0.22096 (257)	0.13654 (234)	0.30961 (251)	0.02227 (248)	2.940 (26)	96
La6	0.38683 (240)	0.22645 (207)	0.27685 (234)	0.01215 (103)	2.940 (26)	96
N1				0		
N2				0		
N3				0		
N4				0		

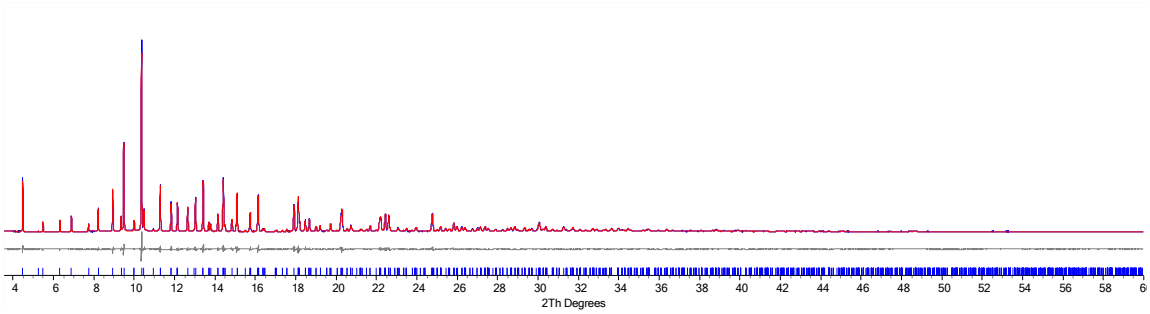

Figure 7-25: Synchrotron PXRD refinement and the crystal structure of ammonia adsorbed La13X at 773 K. Comparison of the experiment data (blue line) and Rietveld refinement (red line) and the difference between them (grey line).

7.1.5.4. Mg13X

A. 298 K

Table 7-23: Refined atomic parameters for Mg13X with ammonia at 298K, recorded at Spring-8, Japan.

	x	y	z	occ	beq	Equivalent Positions
Al1	-0.05344 (45)	0.03583 (41)	0.12554 (36)	1	1.153(49)	96
Si1	-0.05171 (43)	0.12346 (43)	0.03741 (43)	1	1.153(49)	96
O1	-0.10743 (74)	0.00120 (74)	0.10285 (61)	1	2.306(97)	96
O2	-0.00180 (69)	-0.00302 (67)	0.14631 (29)	1	2.306(97)	96
O3	-0.03401 (53)	0.07566 (80)	0.07150 (69)	1	2.306(97)	96
O4	-0.07315 (42)	0.07451 (71)	0.17645 (73)	1	2.306(97)	96
Na1	0.07640 (269)	0.08521 (286)	-0.01548 (169)	0.13580 (1407)	1.405(660)	32
Na3	0.38907 (125)	0.28412 (151)	0.21070 (159)	0.24184 (2122)	1.405(660)	96
Mg1	0.26876 (199)	0.31424 (198)	0.57324 (166)	0.30864 (1978)	10.734 (544)	96
Mg2	0.80952 (63)	0.80952 (63)	-0.05952 (63)	0.18780 (656)	10.734 (544)	32
Mg3	0.87600 (185)	0.35618 (147)	1.07956 (63)	0.37490 (1124)	10.734 (544)	96
O5	0.51032 (207)	0.89131 (105)	-0.00774 (187)	0.45579 (2848)	5	96
O6	0.94436 (95)	0.16062 (81)	0.82910 (115)	0.86683 (2977)	5	96
N1	0.90264 (98)	0.95973 (92)	0.24574 (116)	0.72985 (2950)	5	96
N2	0.66570 (53)	0.08430 (53)	0.58430 (53)	0.26099 (1115)	5	32
N3	0.74839 (34)	0.50161 (34)	0.00161 (34)	0.46444 (554)	5	32
N4	0.12095 (168)	0.78248 (174)	0.19172 (158)	0.49719 (3084)	5	96

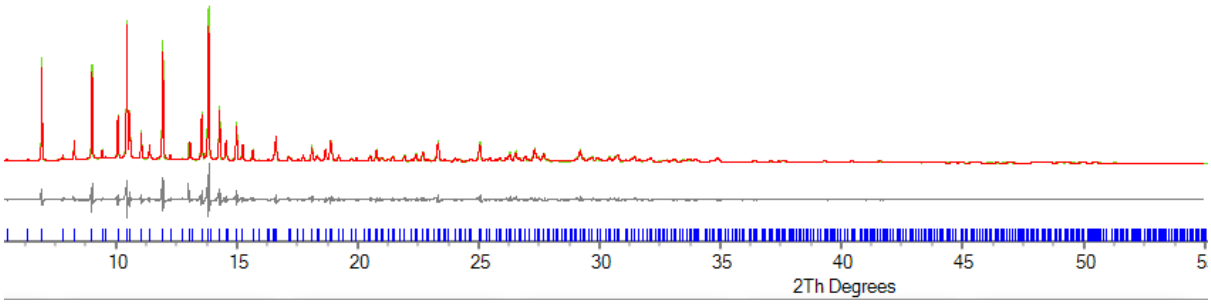

Figure 7-26: Synchrotron PXRD refinement and the crystal structure of ammonia adsorbed Mg13X at 298 K. Comparison of the experiment data (green line) and Rietveld refinement (red line) and the difference between them (grey line).

B. 373 K

Table 7-24: Refined atomic parameters for Mg13X with ammonia at 373 K, recorded at Spring-8, Japan.

	x	y	z	occ	beq	Equivalent Positions
Al1	-0.05387 (30)	0.03595 (34)	0.12452 (35)	1	1.182(38)	96
Si1	-0.05097 (29)	0.12482 (38)	0.03704 (37)	1	1.182(38)	96
O1	-0.10689 (61)	0.00147 (59)	0.10399 (55)	1	2.364(76)	96
O2	-0.00175 (53)	-0.00424 (48)	0.14619 (22)	1	2.364(76)	96
O3	-0.03369 (41)	0.07757 (72)	0.07283 (62)	1	2.364(76)	96
O4	-0.07315 (32)	0.07349 (56)	0.17602 (56)	1	2.364(76)	96
Na2	0.07051 (248)	0.07757 (289)	-0.01447 (146)	0.16765 (1308)	4.597(688)	32
Na3	0.38750 (163)	0.29609 (172)	0.20362 (172)	0.22306 (1304)	4.597(688)	96
Mg1	0.26762 (196)	0.30907 (164)	0.57634 (129)	0.29499 (1654)	12.074 (451)	96
Mg2	0.80870 (53)	0.80870 (53)	-0.05870 (53)	0.18518 (526)	12.074 (451)	32
Mg3	0.86810 (258)	0.36295 (236)	1.07958 (47)	0.36341 (876)	12.074 (451)	96
O5	0.51404 (109)	0.89190 (89)	-0.01089 (110)	0.50392 (1955)	5	96
O6	0.94723 (67)	0.16129 (68)	0.83160 (84)	0.93797 (2613)	5	96
N1	0.90148 (87)	0.96187 (77)	0.24809 (98)	0.67168 (2563)	5	96
N2	0.66433 (46)	0.08567 (46)	0.58567 (46)	0.26221 (841)	5	32
N3	0.74824 (25)	0.50176 (25)	0.00176 (25)	0.48051 (437)	5	32
N4	0.12736 (112)	0.77772 (150)	0.19870 (146)	0.52320 (2466)	5	96

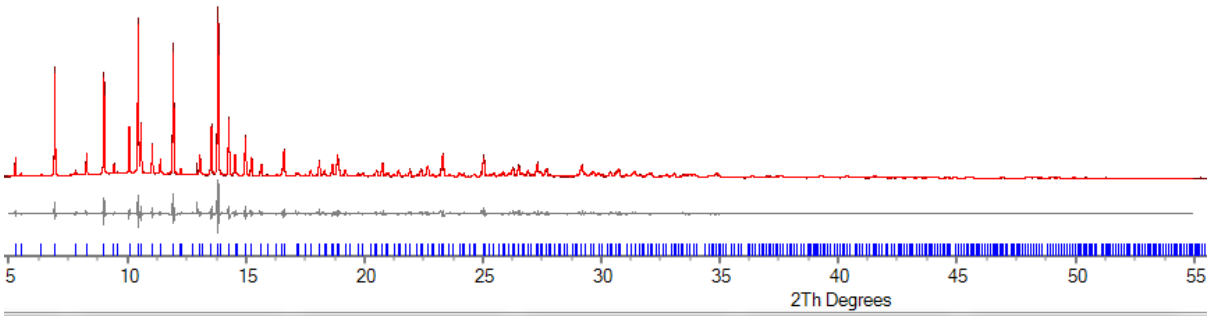

Figure 7-27: Synchrotron PXRD refinement and the crystal structure of ammonia adsorbed Mg13X at 373K. Comparison of the experiment data (pink line) and Rietveld refinement (red line) and the difference between them (grey line).

C. 473 K

Table 7-25: Refined atomic parameters for Mg13X with ammonia at 473 K, recorded at Spring-8, Japan.

	x	y	z	occ	beq	Equivalent Positions
Al1	-0.05105 (24)	0.03702 (22)	0.12540 (21)	1	1.200(35)	96
Si1	-0.05257 (22)	0.12350 (22)	0.03621 (22)	1	1.200(35)	96
O1	-0.10702 (37)	0.00201 (39)	0.10171 (34)	1	2.400(70)	96
O2	0.00011 (37)	-0.00554 (38)	0.14628 (22)	1	2.400(70)	96
O3	-0.03339 (32)	0.07515 (43)	0.07152 (44)	1	2.400(70)	96
O4	-0.07441 (30)	0.07343 (36)	0.17840 (34)	1	2.400(70)	96
Na2	0.06022 (137)	0.08006 (156)	-0.01311 (120)	0.19394 (1159)	5.780(593)	32
Na3	0.39729 (123)	0.30016 (120)	0.18639 (102)	0.24184 (1028)	5.780(593)	96
Mg1	0.24947 (106)	0.28781 (071)	0.58379 (065)	0.55695 (1362)	15.196(449)	96
Mg2	0.81047 (059)	0.81047 (059)	-0.06047 (059)	0.17776 (510)	15.196(449)	32
Mg3	0.88595 (301)	0.36499 (343)	1.07595 (057)	0.28934 (688)	15.196(449)	96
O5	0.51686 (058)	0.86998 (061)	-0.02909 (041)	0.75374 (1337)	5	96
O6	0.92251 (057)	0.15859 (047)	0.79830 (063)	0.91623 (1550)	5	96
N1	0.00423 (4902)	0.00406 (910)	0.25	0.50677 (513)	5	96
N2	0.66314 (30)	0.08686 (30)	0.58686 (30)	0.31674 (905)	5	32
N3				0		
N4	0.15520 (82)	0.77140 (89)	0.19934 (92)	0.46824 (1431)	5	96

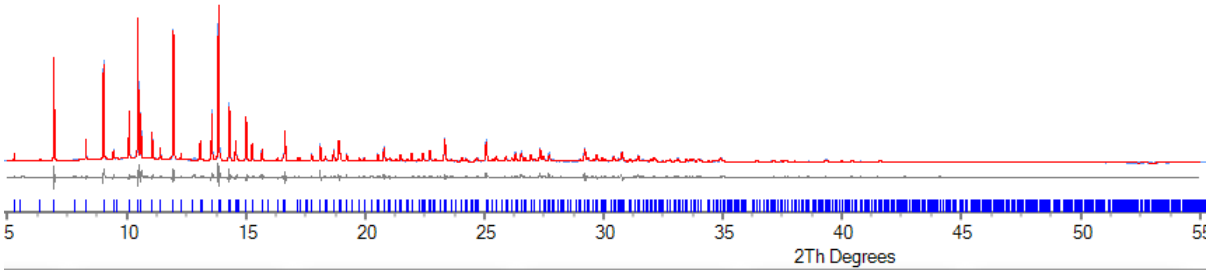

Figure 7-28: Synchrotron PXRD refinement and the crystal structure of ammonia adsorbed Mg13X at 473K. Comparison of the experiment data (pink line) and Rietveld refinement (red line) and the difference between them (grey line).

D. 573 K

Table 7-26: Refined atomic parameters for Mg13X with ammonia at 573 K, recorded at Spring-8, Japan.

	x	y	z	occ	beq	Equivalent Positions
Al1	-0.05018 (20)	0.03772 (18)	0.12542 (17)	1	1.718(26)	96
Si1	-0.05238 (18)	0.12351 (18)	0.03544 (18)	1	1.718(26)	96
O1	-0.10604 (32)	0.00167 (36)	0.10170 (31)	1	3.435(51)	96
O2	-0.00148 (31)	-0.00579 (35)	0.14712 (18)	1	3.435(51)	96
O3	-0.03257 (27)	0.07325 (36)	0.06990 (38)	1	3.435(51)	96
O4	-0.07341 (25)	0.07275 (29)	0.17984 (28)	1	3.435(51)	96
Na2	0.05977 (118)	0.08379 (140)	-0.01471 (108)	0.18246(1017)	5.828(474)	32
Na3	0.38302 (102)	0.29883 (81)	0.19997 (99)	0.24184(866)	5.828(474)	96
Mg1	0.24174 (85)	0.29310 (59)	0.58589 (61)	0.63607(1541)	19.981(444)	96
Mg2	0.81318 (53)	0.81318 (53)	-0.06318 (53)	0.20879(452)	19.981(444)	32
Mg3	0.88274 (437)	0.37469 (489)	1.06846 (56)	0.25669(790)	19.981(444)	96
O5	0.51019 (62)	0.87053 (63)	-0.02630 (46)	0.55268(1147)	5	96
O6	0.92281 (43)	0.16001 (34)	0.80070 (47)	0.91624(1183)	5	96
N1	0.00332 (2874)	0.00356 (2866)	0.25	0.49665 (393)	5	96
N2	0.66239 (21)	0.08761 (21)	0.58761 (21)	0.36511 (650)	5	32
N3				0		
N4	0.16028 (71)	0.77218 (77)	0.20371 (73)	0.42980 (1164)	5	96

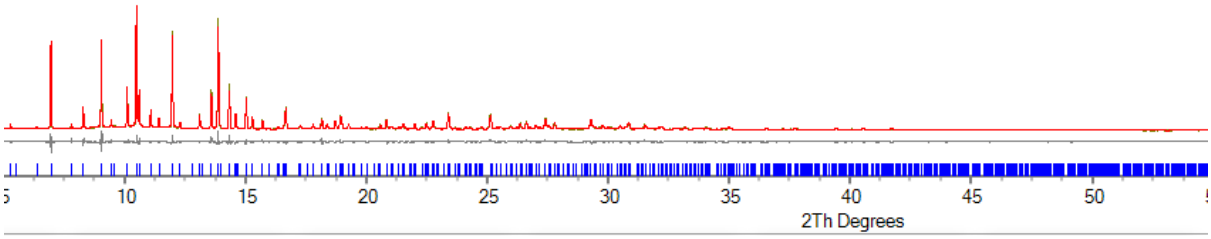

Figure 7-29: Synchrotron PXRD refinement and the crystal structure of ammonia adsorbed Mg13X at 573K. Comparison of the experiment data (green line) and Rietveld refinement (red line) and the difference between them (grey line).

E. 673 K

Table 7-27: Refined atomic parameters for Mg13X with ammonia at 673 K, recorded at Spring-8, Japan.

	x	y	z	occ	beq	Equivalent Positions
Al1	-0.05199 (29)	0.04031 (24)	0.12355 (28)	1	1.322(52)	96
Si1	-0.04963 (30)	0.12758 (26)	0.03680 (27)	1	1.322(52)	96
O1	-0.09474 (46)	0.00810 (54)	0.11019 (46)	1	2.644(103)	96
O2	-0.00010 (56)	-0.00032 (57)	0.14948 (35)	1		96
O3	-0.02472 (48)	0.07540 (51)	0.07392 (53)	1	2.644(103)	96
O4	-0.07492 (47)	0.07522 (52)	0.17237 (52)	1	2.644(103)	96
Na2	0.06722 (215)	0.05327 (283)	0.03112 (177)	0.17442 (1030)	4.418(781)	32
Na3	0.38465 (167)	0.23035 (137)	0.17979 (142)	0.24184 (1289)	4.418(781)	96
Mg1	0.28157 (174)	0.29235 (169)	0.53985 (99)	0.40301 (1240)	13.133(545)	96
Mg2	0.83095 (58)	0.83095 (58)	-0.08095 (58)	0.30092 (766)	13.133(545)	32
Mg3	0.89075 (192)	0.33973 (159)	1.06000 (137)	0.32868 (1527)	13.133(545)	96
O5	0.47394 (93)	0.87413 (131)	0.02682 (101)	0.54549 (1689)	5	96
O6	0.93766 (112)	0.17241 (105)	0.83378 (134)	0.67900 (2263)	5	96
N1	1.00412 (8635)	1.00400 (8653)	0.25	0.48808(79 8)	5	96
N2				0		
N3				0		
N4	0.17308 (122)	0.75323 (100)	0.21300 (83)	0.64872(25 30)	5	96

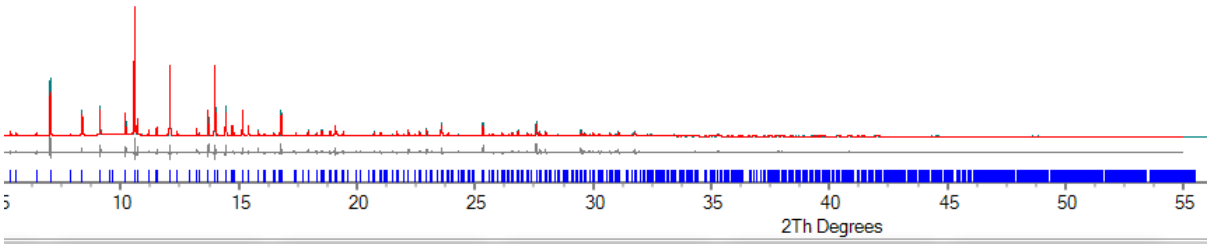

Figure 7-30: Synchrotron PXRD refinement and the crystal structure of ammonia adsorbed Mg13X at 673K. Comparison of the experiment data (blue line) and Rietveld refinement (red line) and the difference between them (grey line).

F. 873 K

Table 7-28: Refined atomic parameters for Mg13X with ammonia at 873 K, recorded at Spring-8, Japan.

	x	y	z	occ	beq	Equivalent Positions
Al1	-0.05561 (21)	0.03971 (22)	0.12328 (21)	1	1.787(45)	96
Si1	-0.04959 (29)	0.12630 (29)	0.03465 (26)	1	1.787(45)	96
O1	-0.11603 (40)	-0.00035 (51)	0.09981 (34)	1	3.575(90)	96
O2	0.00520 (46)	-0.00249 (47)	0.14701 (29)	1	3.575(90)	96
O3	-0.03101 (38)	0.07577 (45)	0.06948 (34)	1	3.575(90)	96
O4	-0.06813 (45)	0.07930 (56)	0.17729 (49)	1	3.575(90)	96
Na2	0.13441 (258)	0.04979 (244)	-0.04504 (298)	0.19394 (2324)	9.665(1.129)	32
Na3	0.37955 (141)	0.35043 (143)	0.15320 (92)	0.24171 (941)	9.665(1.129)	96
Mg1	0.21201 (126)	0.27610 (95)	0.54465 (127)	0.32765 (933)	11.520(251)	96
Mg2	0.80334 (16)	0.80334 (16)	-0.05334 (16)	0.48952 (577)	11.520(251)	32
Mg3	0.94102 (87)	0.39454 (86)	1.13116 (110)	0.44886 (1489)	11.520(251)	96
O5	0.53683 (65)	0.87912 (80)	-0.00846 (66)	0.48321 (957)	5	96
O6	0.93427 (94)	0.16164 (102)	0.78367 (103)	0.57791 (2203)	5	96
N1	0.00904 (540)	0.01148 (508)	0.25	0.46429 (707)	5	96
N2				0		
N3				0		
N4	0.19558 (55)	0.73915 (49)	0.16679 (54)	0.79418 (974)	5	96

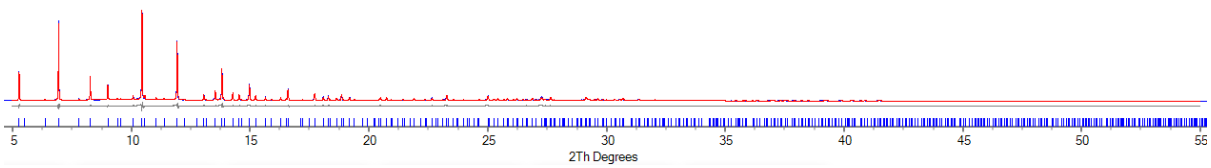

Figure 7-31: Synchrotron PXRD refinement and the crystal structure of ammonia adsorbed Mg13X at 873. Comparison of the experiment data (blue line) and Rietveld refinement (red line) and the difference between them (grey line).

7.2.Chapter 4 Supplementary Information

7.2.1. SXRD Patterns

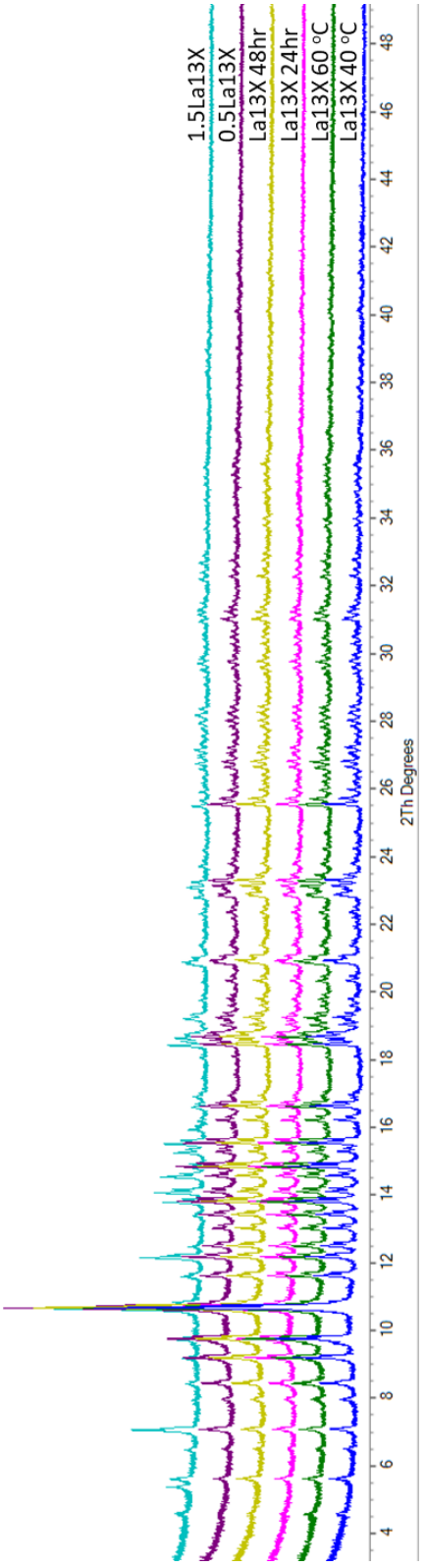

Figure 7-32: XRD patterns of modified La13X with ammonia, recorded on Rigaku SmartLab diffractometer.

7.2.2. SXRD Refined Crystallographic Parameters

Table 7-29: Refined crystallographic parameters for modified La13X with ammonia, recorded on Rigaku SmartLab diffractometer.

	La13X 40 °C	La13X 60 °C	La13X 24hrs	La13X 48hrs	0.5La13X	1.5La13X
Crystal System	Cubic	Cubic	Cubic	Cubic	Cubic	Cubic
Space Group	Fd-3	Fd-3	Fd-3	Fd-3	Fd-3	Fd-3
2θ refinement range (°)	5-40	5-40	5-40	5-40	5-40	5-40
Detector	2D HPAD	2D HPAD	2D HPAD	2D HPAD	2D HPAD	2D HPAD
Number of Parameters	98	98	98	98	98	95
Number of hkls	641	645	644	641	645	651
Refinement Method	Rietveld	Rietveld	Rietveld	Rietveld	Rietveld	Rietveld
a (Å)	24.98960(81)	25.01010(78)	24.99480(96)	24.98937(74)	25.00048(90)	25.05819(110)
b (Å)	24.95725(439)	24.98765(497)	24.99565(584)	24.97233(478)	24.966423(515)	25.04823(571)
c (Å)	25.02826(579)	25.04004(635)	24.99643(739)	25.01255(583)	25.03865(691)	25.07165(680)
V (Å^3)	15609(5)	15649(5)	15617(6)	15609(5)	15628(5)	15737(6)
$R_{wp}/R_p/R_{exp}$	8.63699799/6.85271908/6.42606912	8.76513021/6.92453946/6.50522588	9.21447732/7.23468387/7.15471062	8.76253709/6.88906236/6.60529146	8.78681595/6.94560777/6.57376679	8.73371363/6.87043115/6.76476352
Gof χ^2	1.34405619	1.34739829	1.28788959	1.32659356	1.33664857	1.29105971
Wavelength (Å)	0.709317/0.713607	0.709317/0.713607	0.709317/0.713607	0.709317/0.713607	0.709317/0.713607	0.709317/0.713607
2θ Zero point (°)	-0.00227(18)	-0.00293(20)	-0.00332(22)	-0.00291(19)	-0.00282(22)	-0.00290(24)

7.2.3. SXRD Refined Atomic Parameters

7.2.3.1. La13X 40 °C

Table 7-30: Refined atomic parameters for La13X 40 °C with ammonia at RT, recorded on Rigaku SmartLab diffractometer.

	x	y	z	occ	beq	Equivalent Positions
Al1	-0.05380 (53)	0.03327 (44)	0.12521 (63)	1	0.855(56)	96
Si1	-0.05559 (51)	0.12605 (54)	0.03829 (40)	1	0.855(56)	96
O1	-0.10729 (87)	-0.00488 (96)	0.10403 (77)	1	1.710(112)	96
O2	-0.00086 (77)	0.00412 (78)	0.13776 (32)	1	1.710(112)	96
O3	-0.03132 (28)	0.07511 (74)	0.08154 (74)	1	1.710(112)	96
O4	-0.07118 (37)	0.07081 (125)	0.18114 (122)	1	1.710(112)	96
Na2	0.32505 (457)	0.17512 (174)	0.41971 (562)	0.28832 (1616)	17.200(1.521)	96
Na3	0.33183 (353)	0.29263 (336)	0.22777 (267)	0.15762 (1659)	17.200(1.521)	96
La1	0.06740 (6)	0.06740 (6)	0.06740 (6)	0.24676 (155)	1.977(67)	32
La2	0.52849 (335)	0.24616 (317)	0.33939 (275)	0.01967 (315)	1.977(67)	96
La3	0.84419 (229)	0.84419 (229)	0.84419 (229)	0.01053 (385)	1.977(67)	32
La4	0.20906 (912)	0.20979 (917)	0.46898 (266)	0.01583 (200)	1.977(67)	96
La5	0.23032 (176)	0.24885 (812)	0.25147 (761)	0.02498 (88)	1.977(67)	96
La6	0.41466 (200)	0.23098 (258)	0.18807 (303)	0.02680 (297)	1.977(67)	96
N1	0.28589 (374)	0.35840 (1322)	0.89079 (1312)	0.14655 (1860)	5	96
N2	0.80846 (343)	-0.28592 (379)	0.99110 (468)	0.18623 (2290)	5	96
N3	0.58131 (151)	0.16869 (151)	0.58131 (151)	0.27676 (4029)	5	32

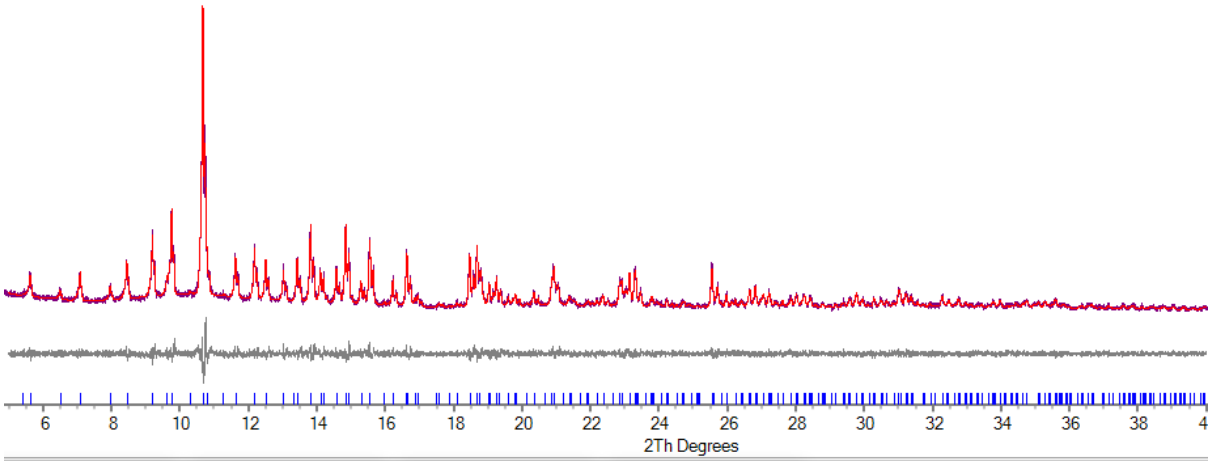

Figure 7-33: PXRD refinement and the crystal structure of ammonia adsorbed La13X, 40°C. Comparison of the experiment data (blue line) and Rietveld refinement (red line) and the difference between them (grey line).

7.2.3.2. La13X 60 °C

Table 7-31: Refined atomic parameters for La13X 60 °C with ammonia at RT, recorded on Rigaku SmartLab diffractometer.

	x	y	z	occ	beq	Equivalent Positions
Al1	-0.05598 (47)	0.03385 (44)	0.12320 (54)	1	0.850(49)	96
Si1	-0.05299 (47)	0.12725 (45)	0.03870 (41)	1	0.850(49)	96
O1	-0.10682 (111)	0.00460 (110)	0.10404 (107)	1	1.700(98)	96
O2	0.00273 (96)	-0.00087 (99)	0.13809 (28)	1	1.700(98)	96
O3	-0.03211 (31)	0.07691 (137)	0.07865 (132)	1	1.700(98)	96
O4	-0.06928 (36)	0.06914 (119)	0.18170 (120)	1	1.700(98)	96
Na2	0.33418 (721)	0.17015 (245)	0.42433 (686)	0.21653 (1817)	18.551(2.762)	96
Na3	0.34493 (397)	0.30428 (432)	0.22322 (292)	0.14813 (1757)	18.551(2.762)	96
La1	0.06721 (7)	0.06721 (7)	0.06721 (7)	0.24503 (140)	1.852(72)	32
La2	0.51132 (809)	0.24778 (840)	0.32064 (364)	0.01203 (254)	1.852(72)	96
La3	0.84010 (146)	0.84010 (146)	0.84010 (146)	0.01699 (514)	1.852(72)	32
La4	0.21476 (566)	0.20293 (601)	0.46020 (349)	0.01410 (253)	1.852(72)	96
La5	0.23437 (149)	0.25483 (1161)	0.25382 (1182)	0.02729 (81)	1.852(72)	96
La6	0.41483 (196)	0.23324 (194)	0.19370 (203)	0.03123 (224)	1.852(72)	96
N1	0.28406 (372)	0.35772 (1591)	0.89219 (1556)	0.16129 (1943)	5	96
N2	0.78888 (801)	-0.25801 (1118)	1.03316 (865)	0.14067 (1536)	5	96
N3	0.58056 (221)	0.16944 (221)	0.58056 (221)	0.20230 (5399)	5	32

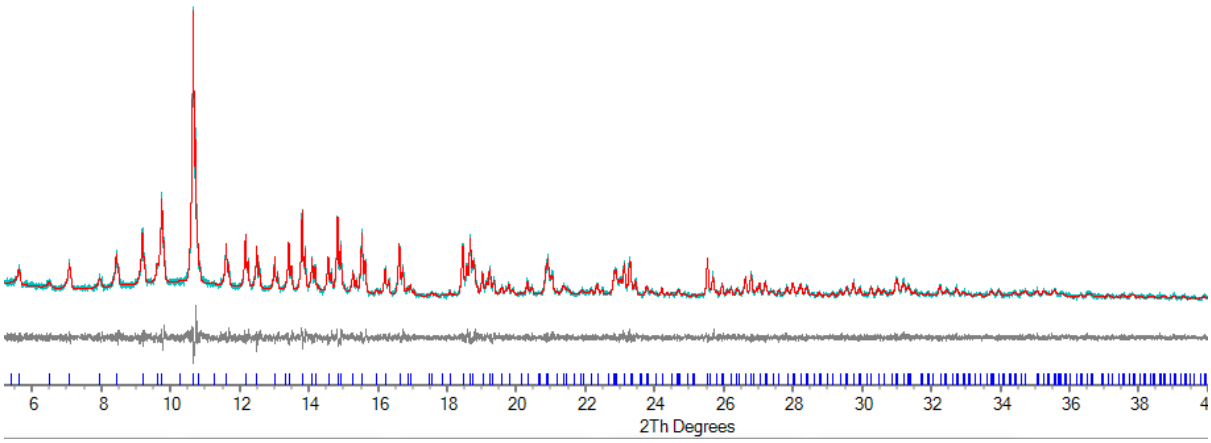

Figure 7-34: PXRD refinement and the crystal structure of ammonia adsorbed La13X, 60°C. Comparison of the experiment data (blue line) and Rietveld refinement (red line) and the difference between them (grey line).

7.2.3.3. La13X 24hrs

Table 7-32: Refined atomic parameters for La13X 24hrs with ammonia at RT, recorded on Rigaku SmartLab diffractometer.

	x	y	z	occ	beq	Equivalent Positions
Al1	-0.05551 (71)	0.03729 (70)	0.12465 (57)	1	0.723(68)	96
Si1	-0.05213 (65)	0.12723 (54)	0.03452 (66)	1	0.723(68)	96
O1	-0.10352 (88)	-0.00718 (99)	0.10625 (96)	1	1.445(136)	96
O2	0.00162 (121)	0.00102 (120)	0.13968 (28)	1	1.445(136)	96
O3	-0.03166 (38)	0.08032 (90)	0.07058 (105)	1	1.445(136)	96
O4	-0.06769 (38)	0.06762 (118)	0.18013 (118)	1	1.445(136)	96
Na1	0.04948 (353)	-0.03020 (428)	-0.00269 (654)	0.11425 (1160)	8.165 (1.378)	32
Na2	0.35980 (314)	0.22790 (343)	0.30634 (411)	0.11751 (1448)	8.165 (1.378)	96
Na3	0.42161 (138)	0.24360 (276)	0.21061 (188)	0.24170 (1978)	8.165 (1.378)	96
La1	0.06757 (7)	0.06757 (7)	0.06757 (7)	0.24064 (143)	1.895(77)	32
La2	0.63103 (507)	0.36854 (454)	0.22021 (456)	0.01458 (254)	1.895(77)	96
La3	0.85621 (846)	0.89284 (824)	0.78784 (277)	0.02021 (203)	1.895(77)	32
La4	0.91362 (587)	0.70480 (302)	0.84358 (644)	0.02007 (259)	1.895(77)	96
La5	0.23810 (377)	0.24917 (1945)	0.25145 (1656)	0.02372 (89)	1.895(77)	96
La6	0.41918 (294)	0.34771 (414)	0.18254 (303)	0.01629 (230)	1.895(77)	96
N3	0.58662 (39)	0.16338 (39)	0.58662 (39)	0.36712 (1087)	5	32
N4	0.55094 (447)	-0.07993 (219)	0.06377 (542)	0.24793 (2586)	5	96

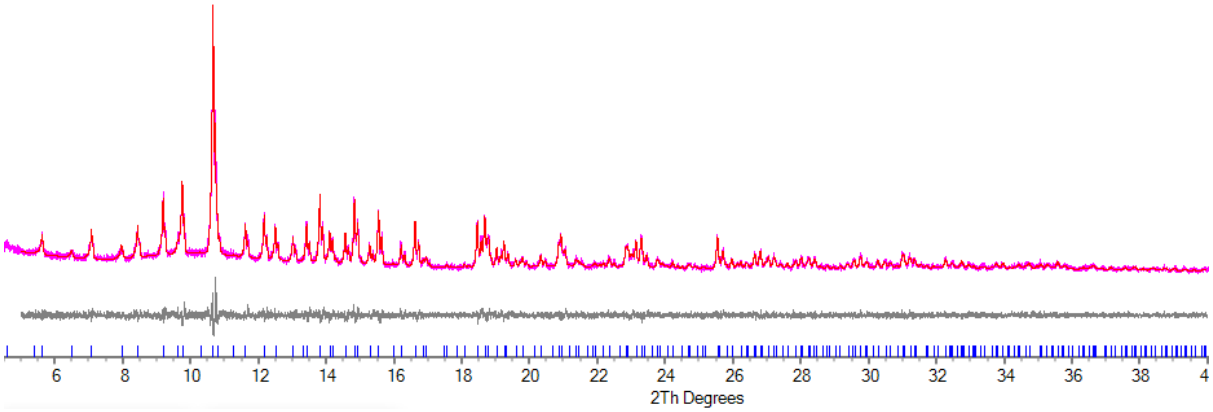

Figure 7-35: PXRD refinement and the crystal structure of ammonia adsorbed La13X, 24hrs. Comparison of the experiment data (pink line) and Rietveld refinement (red line) and the difference between them (grey line).

7.2.3.4. La13X 48 hrs

Table 7-33: Refined atomic parameters for La13X 48hrs with ammonia at RT, recorded on Rigaku SmartLab diffractometer.

	x	y	z	occ	beq	Equivalent Positions
Al1	-0.05220 (59)	0.03436 (48)	0.12329 (49)	1	0.833(57)	96
Si1	-0.05526 (57)	0.12895 (38)	0.03725 (48)	1	0.833(57)	96
O1	-0.10058 (75)	-0.00146 (121)	0.11008 (67)	1	1.666(113)	96
O2	0.00068 (133)	0.00159 (126)	0.13750 (32)	1	1.666(113)	96
O3	-0.03107 (35)	0.07586 (108)	0.07748 (110)	1	1.666(113)	96
O4	-0.06921 (41)	0.07002 (114)	0.18167 (111)	1	1.666(113)	96
Na1	0.02035 (698)	-0.02861 (308)	0.02921 (732)	0.10862 (1050)	4.765 (1.036)	32
Na2	0.30798 (668)	0.22962 (413)	0.32434 (576)	0.06774 (923)	4.765 (1.036)	96
Na3	0.42169 (137)	0.24315 (169)	0.21117 (151)	0.24176 (1350)	4.765 (1.036)	96
La1	0.06734 (6)	0.06734 (6)	0.06734 (6)	0.24188 (166)	1.395(59)	32
La2	0.62691 (516)	0.36102 (518)	0.22521 (483)	0.01090 (257)	1.395(59)	96
La3	0.84970 (373)	0.88768 (330)	0.79290 (265)	0.01695 (234)	1.395(59)	32
La4	0.90111 (259)	0.68325 (277)	0.82398 (269)	0.02007 (259)	1.395(59)	96
La5	0.23775 (169)	0.25567 (866)	0.25821 (769)	0.02372 (89)	1.395(59)	96
La6	0.41716 (251)	0.36129 (222)	0.22133 (276)	0.01862 (190)	1.395(59)	96
N3	0.58517 (45)	0.16483 (45)	0.58517 (45)	0.38195 (1051)	5	32
N4	0.54804 (215)	-0.07481 (147)	0.07424 (205)	0.40316 (2426)	5	96

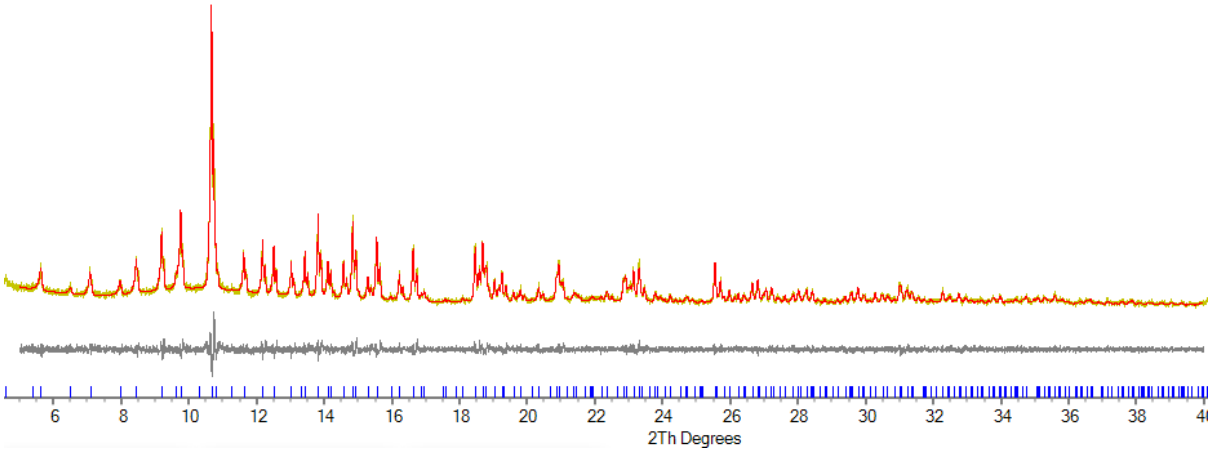

Figure 7-36: PXRD refinement and the crystal structure of ammonia adsorbed La13X, 48 hrs. Comparison of the experiment data (yellow line) and Rietveld refinement (red line) and the difference between them (grey line).

7.2.3.5. 0.5La13X

Table 7-34: Refined atomic parameters for 0.5La13X with ammonia at RT, recorded on Rigaku SmartLab diffractometer.

	x	y	z	occ	beq	Equivalent Positions
Al1	-0.05664 (51)	0.03846 (37)	0.12286 (45)	1	0.742(58)	96
Si1	-0.05263 (47)	0.12785 (38)	0.03366 (42)	1	0.742(58)	96
O1	-0.10148 (64)	0.00156 (114)	0.10839 (71)	1	1.48432(116)	96
O2	0.00534 (66)	-0.00169 (63)	0.13776 (34)	1	1.48432(116)	96
O3	-0.03017 (33)	0.08143 (76)	0.07553 (71)	1	1.48432(116)	96
O4	-0.07033 (36)	0.07112 (125)	0.17984 (131)	1	1.48432(116)	96
Na1	-0.00641 (5968)	0.01461 (3157)	-0.02166 (3914)	0.03353 (1068)	9.610 (2.154)	32
Na2	0.24406 (77)	0.24406 (77)	0.24406 (77)	0.15597 (375)	9.610 (2.154)	32
Na3	0.40480 (424)	0.22996 (460)	0.19398 (524)	0.16793 (4596)	9.610 (2.154)	96
La1	0.06731 (8)	0.06731 (8)	0.06731 (8)	0.23154 (162)	1.984(79)	32
La2	0.57198 (248)	0.31028 (464)	0.32191 (407)	0.01852 (252)	1.984(79)	96
La4	0.20756 (256)	0.04244 (256)	0.20756 (256)	0.00922 (119)	1.984(79)	96
La5	0.27422 (674)	0.23187 (635)	0.07847 (830)	0.00851 (264)	1.984(79)	96
La6	0.34778 (817)	0.40079 (869)	0.15277 (246)	0.01426 (162)	1.984(79)	96
N1	0.33405 (36)	0.41595 (36)	0.91595 (36)	0.39647 (908)	5	32
N4	0.50306 (570)	-0.08058 (364)	0.05348 (434)	0.25353 (6433)	5	96

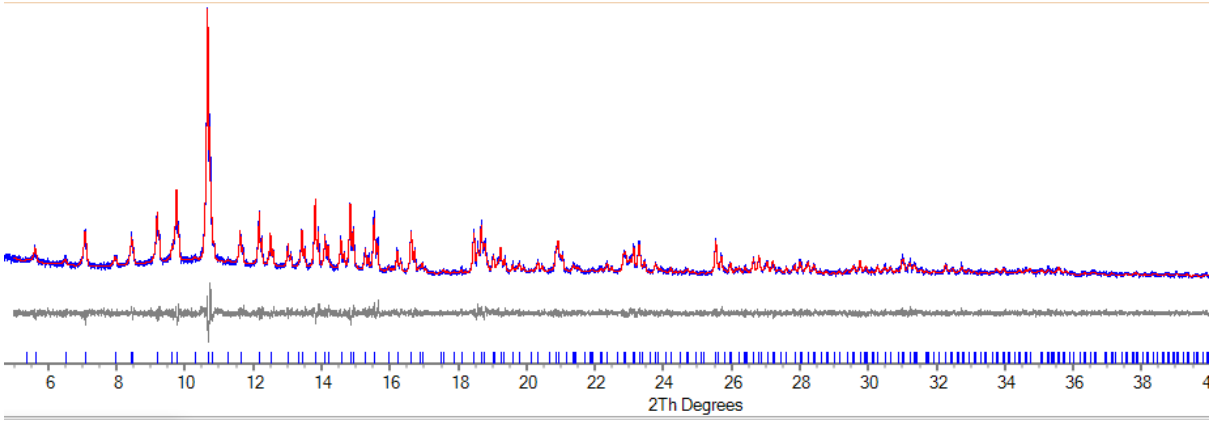

Figure 7-37: PXRD refinement and the crystal structure of ammonia adsorbed 0.5La13X. Comparison of the experiment data (blue line) and Rietveld refinement (red line) and the difference between them (grey line).

7.2.3.6. 1.5La13X

Table 7-35: Refined atomic parameters for 1.5La13X with ammonia at RT, recorded on Rigaku SmartLab diffractometer.

	x	y	z	occ	beq	Equivalent Positions
Al1	-0.05236 (39)	0.03817 (42)	0.12097 (42)	1	0.678(55)	96
Si1	-0.05793 (37)	0.12591 (35)	0.03486 (44)	1	0.678(55)	96
O1	-0.10347 (69)	-0.00302 (96)	0.11155 (70)	1	1.357(110)	96
O2	-0.00069 (83)	0.00185 (75)	0.13089 (38)	1	1.357(110)	96
O3	-0.03146 (36)	0.07833 (84)	0.07414 (92)	1	1.357(110)	96
O4	-0.07075 (43)	0.07514 (85)	0.17670 (89)	1	1.357(110)	96
Na1	0.01065 (99)	0.01065 (99)	0.01065 (99)	0.19394 (814)	11.013 (2.221)	32
Na3	0.39031 (244)	0.19152 (229)	0.21785 (256)	0.24182 (1872)	11.013 (2.221)	96
La1	0.06410 (11)	0.06410 (11)	0.06410 (11)	0.14463 (253)	2.142(100)	32
La2	0.55279 (246)	0.32034 (216)	0.30044 (208)	0.02520 (408)	2.142(100)	96
La3	0.76321 (15)	0.76321 (15)	0.76321 (15)	0.09444 (81)	2.142(100)	32
La4	0.20511 (86)	0.04489 (86)	0.20511 (86)	0.01910 (227)	2.142(100)	96
La5	0.24233 (583)	0.25636 (701)	0.06516 (523)	0.01013 (523)	2.142(100)	96
La6	0.35939 (396)	0.40027 (327)	0.14754 (194)	0.01853 (183)	2.142(100)	96
N1	0.33034 (58)	0.41966 (58)	0.91966 (58)	0.30717 (894)	5	32
N4	0.48703 (117)	-0.08125 (111)	0.04714 (87)	0.69900 (2623)	5	96

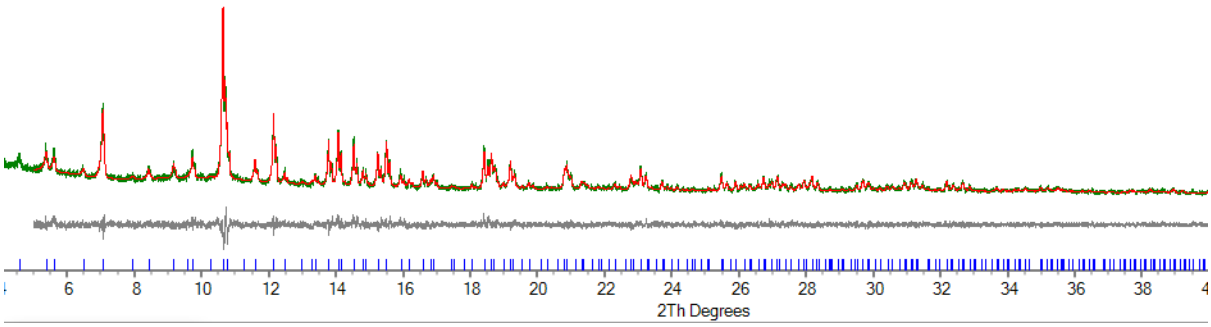

Figure 7-38: PXRD refinement and the crystal structure of ammonia adsorbed 1.5La13X. Comparison of the experiment data (green line) and Rietveld refinement (red line) and the difference between them (grey line).

7.3.Chapter 5 Supplementary Information

7.3.1. Comparison of Loading Methods

	Loading determined by IGA	Loading determined by Schlenk loading and TPD
Na13X	3.5 %	2.8 %
La13X	15.0 %	18.3 %